High Resolution Infrared Spectroscopy of Complex Polyatomic Molecules

by

P. Bryan Changala

S.B., Massachusetts Institute of Technology, 2013

A thesis submitted to the

Faculty of the Graduate School of the

University of Colorado in partial fulfillment

of the requirements for the degree of

Doctor of Philosophy

Department of Physics

2019

This thesis entitled:
High Resolution Infrared Spectroscopy of Complex Polyatomic Molecules
written by P. Bryan Changala
has been approved for the Department of Physics

Prof. Jun Ye

Prof. Carl Lineberger

Date

The final copy of this thesis has been examined by the signatories, and we find that both the content and the form meet acceptable presentation standards of scholarly work in the above mentioned discipline.

Changala, P. Bryan (Ph.D., Physics)

High Resolution Infrared Spectroscopy of Complex Polyatomic Molecules

Thesis directed by Prof. Jun Ye

Infrared spectroscopy is an essential tool for probing molecular structure and dynamics. Over the last decade, cavity-enhanced direct frequency comb spectroscopy (CE-DFCS) has emerged as a powerful technique for molecular spectroscopy in the mid-infrared region ($3-15$ μm). CE-DFCS combines the broad spectral bandwidth and high frequency resolution of frequency combs with the improved detection sensivity provided by high-finesse optical cavities. At room temperature, however, all but the simplest molecules suffer from severe spectral congestion, which obscures the detailed dynamics encoded in spectroscopic fine structure. To overcome this challenge, we demonstrate the integration of CE-DFCS with cryogenic buffer gas cooling, which provides continuous, cold samples of gas-phase molecules at rotational and translational temperatures as low as 10 K. By significantly reducing internal partition functions and Doppler broadening, we take full advantage of CE-DFCS to reveal the intricate rovibrational structure of complex polyatomic molecules.

The systems investigated in this thesis range from extremely anharmonic molecules to unprecedentedly large carbon cages, illustrating the diverse ways in which a molecule can be complex. One case study is free internal rotation in nitromethane, a model system for large amplitude nuclear motion. This work has motivated our development of new theoretical tools to predict the high resolution spectra of nitromethane and several other floppy molecules. We have also focused on large molecules outside the domain of traditional high resolution spectroscopy. The culmination of these efforts is the rotationally resolved spectrum of the C_{60} fullerene. C_{60} is now both the largest molecule and the first example of icosahedral symmetry for which rovibrational quantum state resolution has been achieved. In addition to CE-DFCS, we have constructed a cw-QCL-based spectrometer to probe and manipulate the quantum states of C_{60}. This work opens new avenues for fullerene research and for exploiting large molecules as platforms for quantum science.

Dedication

To my many teachers, with gratitude.

Acknowledgements

There are worse places than JILA to spend six years doing science. I have had a wonderful experience working in the Ye lab. Jun has been an inspiring and supportive advisor. I am grateful to him for not only teaching me what the highest quality research looks like, but for giving me the independence to explore my own interests while pushing together on scientific goals. Most of my graduate work in Jun's group was carried out closely with two outstanding post-docs, Ben Spaun (from 2014 to 2017) and Marissa Weichman (from 2017 to present). Apart from being brilliant scientists and hard-working colleagues, I have been grateful for their friendship and camaraderie in the lab. I would also like to thank past members of the mid-IR and XUV frequency comb groups, including Thinh Bui, Bryce Bjork, Oliver Heckl, Kana Iwakuni, Gil Porat, Stephen Schoun, Justin Niedermeyer, Christoph Heyl, Craig Benko, and Kevin Cossel, and wish continued success to current members including Jutta Toscano, Qizhong Liang, Chuankun Zhang, and Marissa. I've had the privilege of getting to know many others in the Ye group over the last several years – too numerous to list here but all excellent scientists and lab mates. I especially enjoyed my many office conversations with Shimon Kolkowitz.

Part of what makes JILA special is the outstanding administrative and technical staff. Travel, bureacratic issues, purchases, scheduling, etc. always went smoothly due to the hard work of Amy Allison, Agnieska Lynch, Krista Beck, the entire supply office staff, and many others. The instrument and electronics shops made crucial contributions to my experiments. I especially want to acknowledge Hans Green, Todd Asnicar, Terry Brown, and Carl Sauer.

I've had the opportunuity to contribute to many outstanding collaborations with scientists both inside and outside JILA. I've enjoyed working with Marie-Aline Martin-Drumel, Mike McCarthy, Barney Ellison, Branko Ruscic, David Bross, Jessie Porterfield, David Patterson, John Doyle, Kevin Lee, Lam Nguyen, Mitchio Okumura, Matt Nava, Allan Oliveira, Julia Lehman, Neil Reilly, and Carl Lineberger. Bob Field, who gave me my start in spectroscopy at MIT, has continued to act as a valued mentor and advisor. Josh Baraban was an excellent graduate student mentor to me when I worked in Bob's group. He moved to Boulder shortly after I did (to post-doc for Barney Ellison), which gave us the opportunity to continue working together on several theory projects as well as in the lab, using frequency combs with pyrolysis microreactor jets. Josh remains a close colleague and friend since starting his own group in Israel. John Stanton has served as an unofficial advisor of sorts. I am grateful for the many scientific opportunities he has provided me, including funding my travel to two conferences, and for being a generous promoter of my work. He and Barney have provided hours of entertainment over many enjoyable dinners at the Toad. (Barney also merits a special mention for delivering to me one of the only samples of dodecahedrane in the world after personally transporting it halfway across the country.)

I'd like to recognize my Comps and Defense committee members, including Carl Lineberger, David Nesbitt, Eric Cornell, Heather Lewandowski, and Cindy Regal, for their time and effort.

Lastly, I want to thank my family and friends, especially Gargi Datta and Kevin Gilmore; Amy Nkomo; Mom and Dad; my siblings Alissa, Danielle, and Matt, and siblings-in-law Oliver, Eoin, and Maggie (all "acquired" during my PhD); and my nephew Sebastian.

Contents

Chapter

Appendix

Tables

Table

Figures

Figure

Chapter 1

Introduction

Spectroscopy is the primary tool with which we study, probe, and manipulate matter at the molecular scale. The unique spectroscopic signatures of molecules permit detection and monitoring with a high degree of sensitivity and specificity. The patterns encoded in the spectrum itself reveal precise details of molecular structure and dynamics. By understanding the nature of this structure, we can harness molecules as highly controllable complex quantum systems. Advances in our ability to measure and interpret complex molecular spectra thus open new avenues for a wide range of problems in chemical and molecular physics.

The focus of this thesis is high resolution frequency domain spectroscopy of polyatomic molecules in the mid-infrared (MIR) spectral region (ca. 3 to 10 μm). MIR photons carry sufficient energy to excite one or more quanta of nuclear vibrational motion. As all polyatomic molecules possess at least one infrared (IR) active vibrational mode, IR spectroscopy is a universal and essential tool for probing molecular structure and dynamics. "High resolution," in this context, means resolving spectroscopic fine structure associated with changes in rotational, and even spin and hyperfine, quantum numbers that occur simultaneously with the primary vibrational transition. By reaching this level of resolution, it is possible to observe all internal molecular degrees of freedom in specific, well defined quantum states. The individual transition frequencies between these states can then be used to determine effective Hamiltonians that connect spectroscopic observations to molecular scale details, such as geometry, electronic structure, and potential energy surfaces.

Such precise insights have made high resolution infrared spectroscopy an important tool for studying molecular structure and dynamics. However, its applications have usually been restricted to small, light molecules. This is because at room temperature systems with even a few heavy atoms can already occupy millions of rotation-vibration quantum states, leading to severe spectral congestion. Targeting larger, more complex systems requires a high resolution and sensitive spectrometer coupled with a source of cold, dense molecular gases. This thesis discusses overcoming these experimental challenges by combining two powerful techniques: cavity-enhanced direct frequency comb spectroscopy (CE-DFCS) and cryogenic buffer gas cooling (CBGC). CE-DFCS exploits the simultaneous broadband and narrow-linewidth properties of infrared frequency combs by coupling them to high finesse optical cavities to yield high resolution and high sensitivity absorption spectra in a massively parallel fashion. CBGC efficiently quenches translational and internal motion in molecules to temperatures as low as a few kelvin, drastically reducing spectral congestion and linewidths, and enhancing absorption signal strengths. This thesis demonstrates harnessing these tools to obtain high resolution infrared spectra of unprecedentedly complex molecules. The culmination of this work is the first rotationally resolved spectrum of the C_{60} fullerene, now by far the largest molecule for which such measurements have been obtained.

The remaining chapters are organized as follows. Chapter 2 provides an introduction to CE-DFCS, the frequency comb sources and detection methods used in these studies, and the details of the frequency comb-buffer gas cooling apparatus. One of the first non-trivial molecules studied with the instrument was nitromethane, CH_3NO_2, which represents a unique example of completely unhindered internal rotation. Chapter 3 analyzes the spectroscopy of this system as a case study in large-amplitude nuclear motion. It also introduces theoretical tools developed to treat its unusual nuclear motion dynamics. Chapter 4 explores the limits of high resolution spectroscopy of large molecules near 3 μm. We examine the intrinsic challenges to rotationally resolved infrared spectroscopy in the CH stretch region of several large hydrocarbons, including naphthalene, adamantane, and diamantane. Shifting to the long wavelength infrared region, Chapter 5 presents the first rotationally resolved frequency comb spectra of C_{60} near 8.5 μm and discusses the changes in CBGC conditions required to successfully realize vibrational ground state cooling. The first

C_{60} experiments pose as many new spectroscopic puzzles as they solve, and Chapter 6 discusses on-going C_{60} experiments to address these questions using continuous wave quantum cascade laser spectroscopy. Finally, Chapter 7 provides a more comprehensive overview of the theoretical tools introduced in Chapter 3 and discusses several more of their recent applications for understanding the spectroscopy of complex polyatomic molecules.

Chapter 2

Cavity-enhanced direct frequency comb spectroscopy of buffer gas cooled molecules

All spectroscopic experiments consist of three primary components: a light source, a sample of matter that interacts with the radiation from the light source, and a detector that measures this interaction in some way. The many realizations and combinations of such components comprise the large, diverse set of modern spectroscopic techniques [1]. The nature of the physics one wishes to probe and its underlying spectroscopic signatures dictate the required parameters of a given spectroscopic experiment: wavelength coverage, frequency resolution and stability, detection bandwidth and sensitivity, sample density, temperature, pressure, amongst many others.

This chapter details the techniques employed in this thesis for high resolution rovibrational infrared spectroscopy of gas-phase polyatomic molecules. To appreciate the specific challenges of this goal, consider the simulated spectrum in Fig. 2.1 of vinyl bromide (C_2H_3Br), which in many ways represents a relatively simple "textbook" example of a molecule of its size (6 atoms) and mass (106 or 108 u, depending on the isotopologue). Figure 2.1a shows the three fundamental CH stretching vibrational bands, which span a 100 cm^{-1} window near 3050 cm^{-1} (3.3 μm), at a temperature of 15 K. The peak absorption cross sections are approximately 10^{-17} cm^2 per molecule. Even at this low temperature, each vibrational band exhibits considerable fine structure, as seen in Fig. 2.1b for the ν_3 band. Taking yet a closer look, Fig. 2.1c shows a small 1-cm^{-1}-wide portion of the ν_3 band with dense patterns associated with K_a sub-band structure, nuclear hyperfine effects, and isotopic mass splittings.

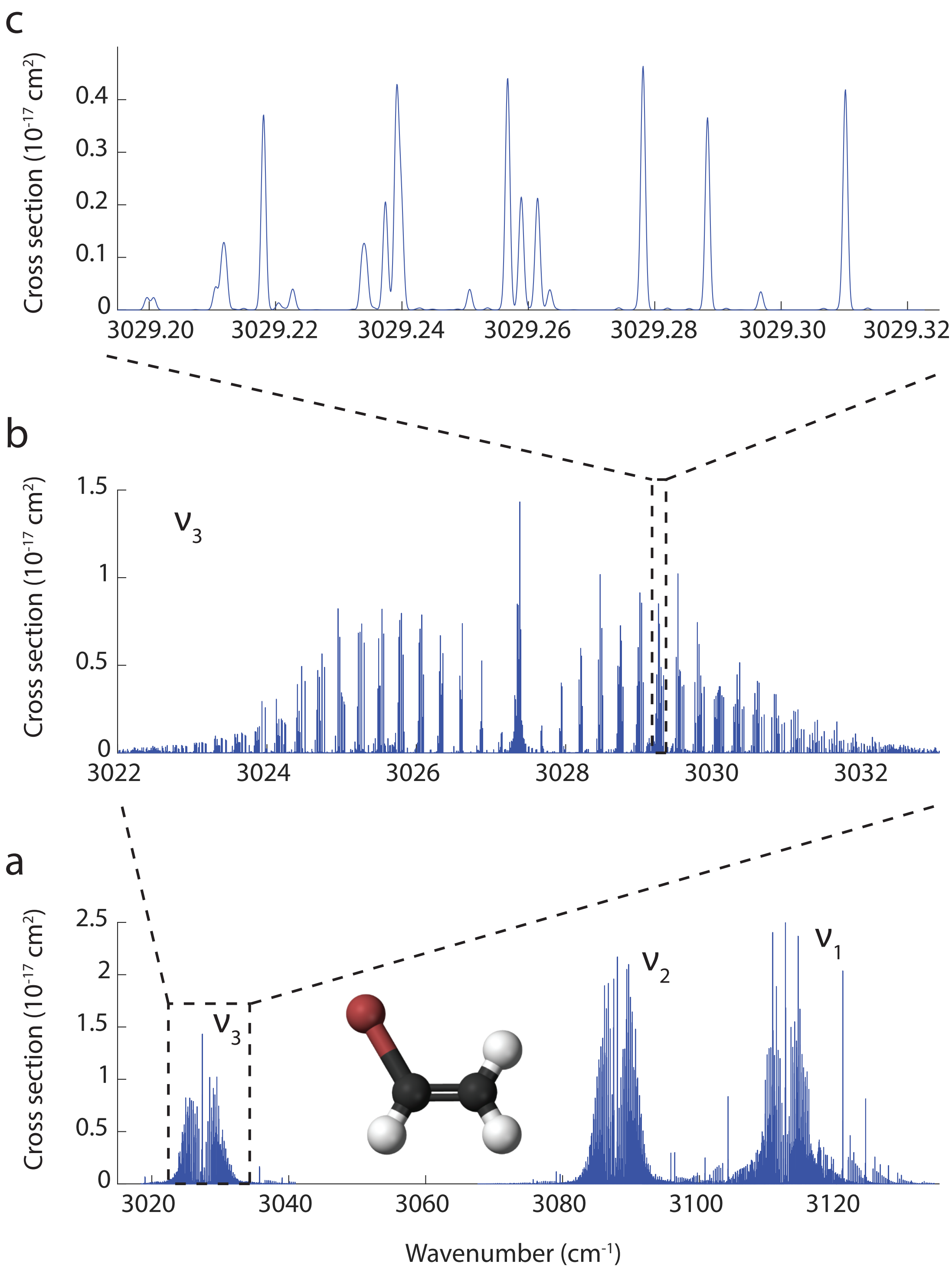

Figure 2.1: Simulated absorption spectrum of vinyl bromide in the CH stretch region. (a) The three fundamental CH stretch bands, conventionally labeled ν_1, ν_2, and ν_3, span a 100 cm^{-1} window. The spectrum is calculated for $T = 15$ K. (b) A zoom-in of the rotational fine structure of the ν_3 band. (c) A small 1 cm^{-1}-wide portion of the ν_3 band.

This example illustrates the general reality of high resolution rovibrational spectroscopy. Strong fundamental vibrational bands occur over the entire MIR region, with hydride stretching vibrations (e.g. CH and OH) at the short wavelength end (ca. 2.7 μm to 3.3 μm) and bending, twisting, and heavy atom streching vibrations at the long wavelength end (5 μm to 15 μm) and extending into the far-IR/terahertz regions ($>$ 15 μm). Efficiently probing a wide variety of molecules and multiple vibrational bands requires a light source with broad wavelength tunability and bandwidth. At the same time, each vibrational band can consist of thousands of individual rovibrational transitions, with line densities easily surpassing 10 to 100 per cm^{-1}, demanding high spectral resolution. Minimizing spectral congestion and line widths requires preparing cold, low pressure molecular gases. Furthermore, for linear absorption measurements, which are the focus here, high detection sensitivity is needed to overcome intrinsically small cross sections.

The general experimental challenges identified for “simple” polyatomic systems like C_2H_3Br become even more important for the complex polyatomic molecules that are the subject of this work. As we will see in later chapters, this complexity occurs as a matter of both kind and degree. An example of the former is large amplitude motion in nitromethane, CH_3NO_2 (Chapter 3). Here, unhindered internal rotation leads to a breakdown of the semi-rigid framework usually employed to model rovibrational spectra. Examples of the latter are the large hydrocarbon cages adamantane ($C_{10}H_{16}$) and diamantane ($C_{14}H_{20}$), as well as the C_{60} fullerene (Chapters 4-6). Despite being relatively rigid molecules, the sheer number of atoms and total mass of these systems leads to densities of internal states that are at the very frontier of what high resolution infrared spectroscopy can probe.

Returning to the three primary components of spectroscopic experiments, this chapter introduces the techniques of cavity-enhanced direct frequency comb spectroscopy and cryogenic buffer gas cooling, which provide the necessary light source, detection methods, and sample conditions to address the challenges of high resolution rovibrational spectroscopy of large, complex polyatomic molecules. Infrared frequency combs offer simultaneous high spectral resolution and wide spectral coverage, while cavity-enhanced detection coupled to broad bandwidth interferometric and dispersive readout provide high detection sensitivity. These spectrometer capabilities are fully realized with the cold, dense samples of gas-phase molecules provided by cryogenic buffer gas cooling. The remainder of this chapter discusses in detail each of these experimental components.

2.1 Mid-infrared frequency combs

The development of the optical frequency comb has dramatically advanced the fields of precision metrology and spectroscopy [2, 3]. While combs are now a common tool for frequency referencing, they can also be used to interact directly with samples under study, giving rise to a family of techniques known as direct frequency comb spectroscopy [4]. By coupling frequency combs to high-finesse optical cavities, cavity-enhanced direct frequency comb spectroscopy (CE-DFCS) provides simultaneously broad spectral bandwidth, high spectral resolution, and high detection sensitivity [5, 6]. The extension of CE-DFCS to the mid-infrared spectral region over the last ten years has enabled these advantages to be exploited for molecular rovibrational spectroscopy [7].

Frequency combs are commonly generated by mode-locked lasers that emit a train of ultrafast pulses of light with a regular period τ of the order of a few nanoseconds (Fig. 2.2a) [3]. Dispersion inside the laser oscillator cavity causes a pulse-to-pulse phase slip $\Delta\phi_{\mathrm{ce}}$ of the carrier field relative to the pulse intensity envelope. This regular time domain structure leads to the characteristic comb-like structure in the frequency domain (Fig. 2.2b). Each phase-coherent frequency comb mode is separated in optical frequency by the repetition rate $f_{\mathrm{rep}} = 1/\tau$. The spectral bandwidth of the comb is proportional to the inverse of the ultrafast pulse length, typically spanning at least 1 THz. The carrier-envelope phase slip $\Delta\phi_{\mathrm{ce}}$ shifts the entire comb spectrum by an offset frequency $f_0 = f_{\mathrm{rep}} \times \Delta\phi_{\mathrm{ce}}/2\pi$. The optical frequency of each comb mode is thus $\nu_n = n \times f_{\mathrm{rep}} + f_0$, where n is the integer comb mode index. Measuring the RF frequencies f_{rep} and f_0 determines the absolute frequency position of each optical mode in a calibration-free manner. Active feedback on these two comb parameters can be used to suppress frequency noise, yielding narrow-line-width comb modes.

MIR frequency combs are typically generated by non-linear wavelength conversion of near-IR (NIR) combs [8–16]. The latter are currently most commonly produced with fiber oscillators doped

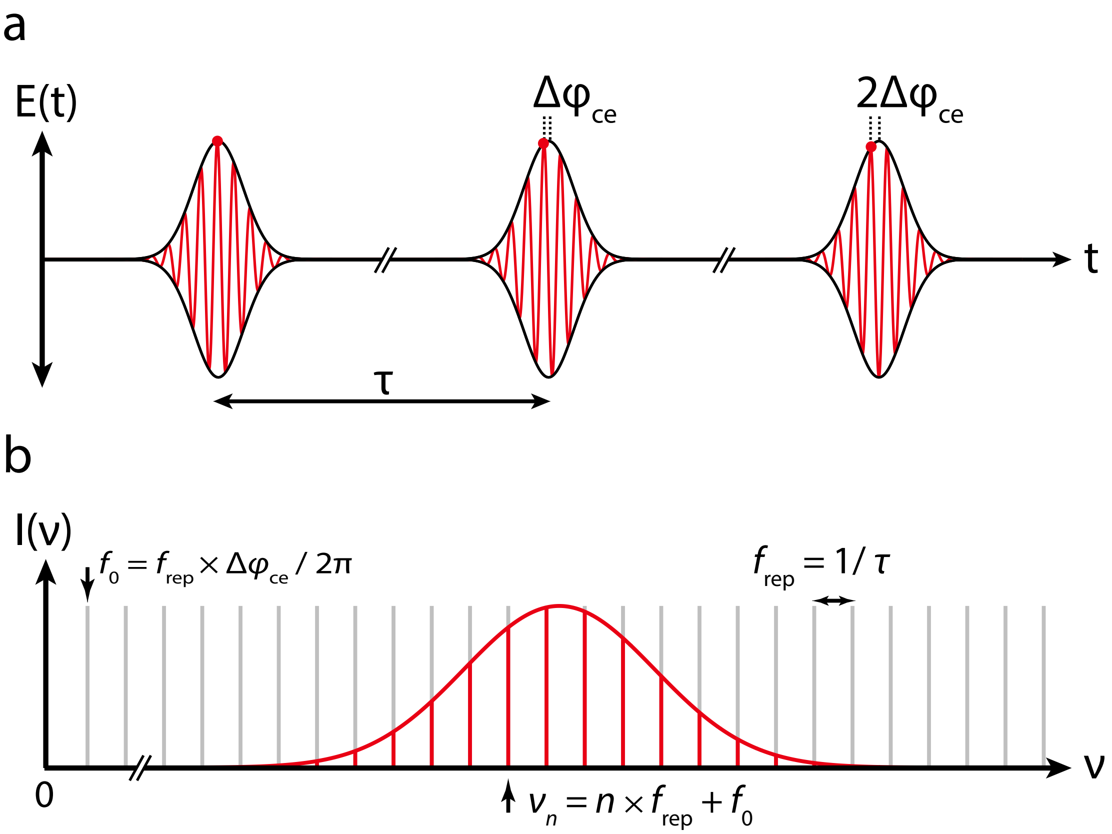

Figure 2.2: Time and frequency domain structure of an optical frequency comb. (a) Mode-locked fiber lasers produce ultrafast pulse trains with a repetition period of τ. The pulse-to-pulse carrier-envelope phase slip is $\Delta\phi_{\text{ce}}$. (b) In the frequency domain, the comb contains many optical modes, or "teeth," at frequencies separated by the repetition rate f_{rep} with a uniform frequency offset f_0.

with ytterbium, erbium, or thulium, which provide robust, passive mode-locked operation near 1.0, 1.5, or 2.0 μm, respectively, with repetition rates typically of the order of 100 MHz. Subsequent fiber amplification can deliver average optical powers of several watts. The correspondingly high peak intensity of the femtosecond pulses enables efficient non-linear frequency conversion. We use two MIR comb sources in this work: a 3-5 μm optical parametric oscillator (OPO) [11] (Fig. 2.3a) and a 6-11 μm difference frequency generation (DFG) comb [15] (Fig. 2.3b).

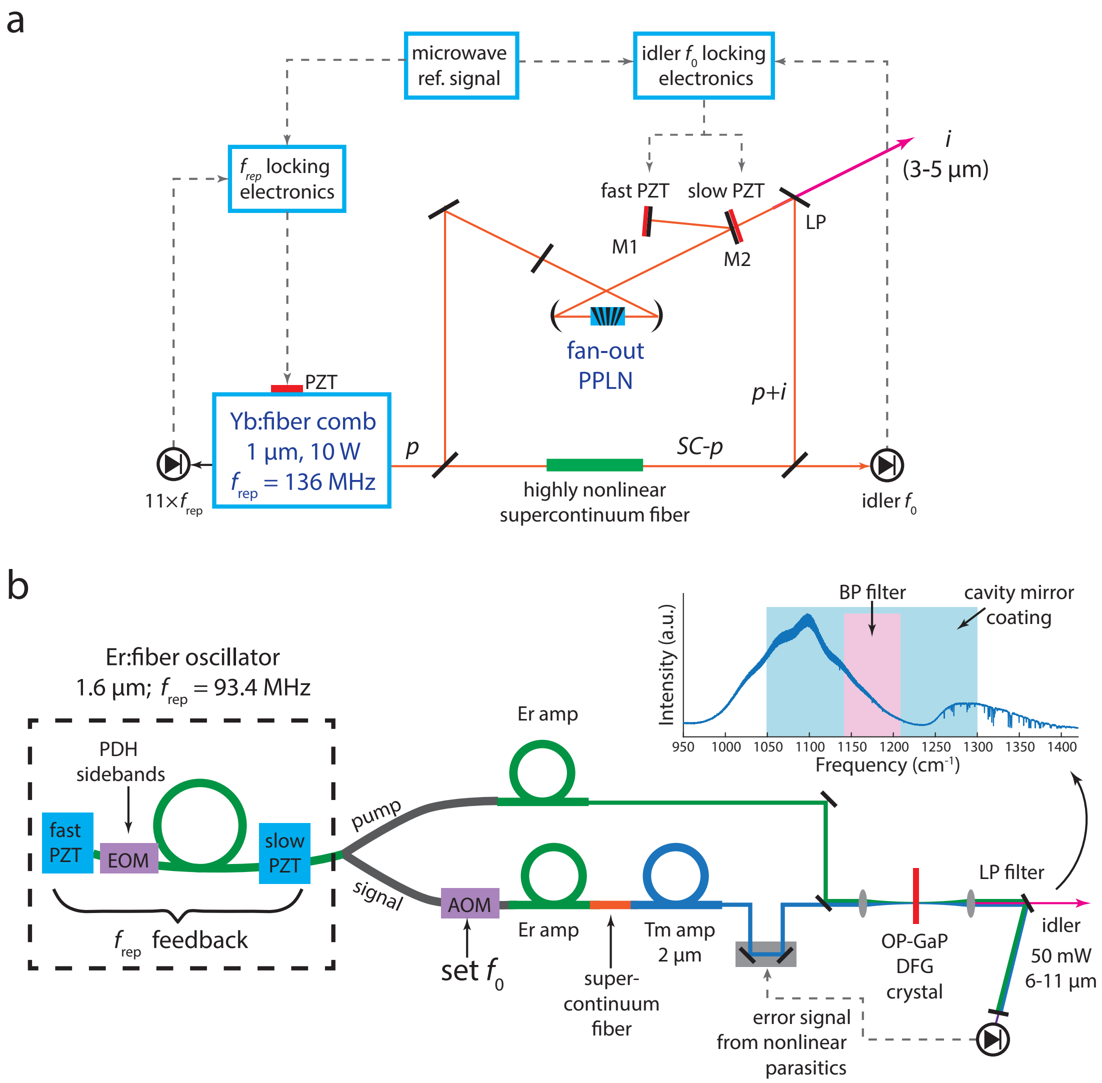

Figure 2.3: Mid-infrared frequency comb sources. (a) A high power OPO [11] is synchronously pumped by a 1 μm Yb:fiber comb. Idler light (i) from 3 μm to 5 μm is generated by tuning the poling period of a fan-out PPLN crystal. f_{rep} is monitored by an oscillator pick-off detector and actively stabilized by feedback onto oscillator cavity PZT elements. A portion of the pump light (p) is broadened in a highly nonlinear fiber. The supercontinuum output (SC-p) is co-aligned with parasitic pump-idler sum frequency light ($p+i$) and detected on a photodiode. The beat signal at the idler f_0 frequency is used to feed back onto PZT-actuated mirrors (M1, M2) in the OPO cavity. (b) The DFG comb [15] is generated by a single 1.6 μm Er:fiber oscillator. The oscillator output is split into two arms, broadened, amplified, and recombined in an OP-GaP crystal to generate MIR idler light. Adjusting the quasi-phase matching period in the OP-GaP crystal provides idler tuning from 6 μm to 11 μm. The idler f_0 is controlled by the AOM driver frequency. Frequency sidebands and f_{rep} feedback are generated by PZT-actuated mirrors and an EOM in the fiber oscillator. The time delay between the two DFG pump pulses is actively stabilized by monitoring parasitic nonlinear signals. (Inset) The broad idler spectrum is narrowed with a bandpass (BP) filter centered on C_{60} absorption band origin near 1185 cm^{-1}.

2.1.1 3–5 μm OPO comb

The high power MIR OPO was originally designed and built in the Ye lab a decade ago by Adler et al. [11]. The OPO is synchronously pumped by a 1 μm ytterbium (Yb) fiber comb that has a repetition rate $f_{\mathrm{rep}} = 136.6$ MHz and a maximum output power of 10 W. The OPO is based on a fan-out MgO-doped periodically poled lithium niobate (PPLN) crystal, which sits at the waist of a cavity that is singly resonant at the signal wavelength. By adjusting the quasi-phase matching period of the crystal, idler output is generated with a center wavelength tunable from 2.8 μm to 4.8 μm, a maximum average power of 1.5 W, and a simultaneous bandwidth up to 0.3 μm. We typically operate the OPO with idler light from 3.0 μm to 3.3 μm with an average power of 100 mW to 300 mW.

Stabilization of the optical frequencies of the idler comb requires active locking of the both the carrier-envelope offset frequency f_0 and the repetition rate f_{rep}. We lock f_{rep} by picking off a small portion of the 1 μm Yb:fiber comb and measuring its repetition rate directly on a fast photodiode. The seventh harmonic of the repetition rate $7f_{\mathrm{rep}} \approx 956$ MHz is mixed with a stable 1 GHz Wenzel quartz oscillator, slowly slaved to a 10 MHz cesium (Cs) clock. The resulting beat note is used to generate a phase error signal with respect to the RF output of a direct digital synthesizer (DDS), which is phase locked to the same RF oscillator. This error signal is then used to feed back simultaneously on a fast piezo (PZT)-actuated cavity mirror and a slower PZT fiber stretcher in the fiber laser oscillator.

The f_0 frequency of the MIR idler comb is measured by performing an optical beat note between the 1 μm pump light (p) and the parasitic sum frequency of the pump and idler ($p + i$) generated by the OPO crystal. A 150- to 200-mW portion of the pump light is picked off and coupled into a 15-cm-long piece of highly nonlinear supercontinuum fiber to broaden it to ~ 780 nm in order to be spectrally overlapped with the $p + i$ light. The output of the supercontinuum fiber and the $p + i$ light are then spatially and temporally overlapped onto a single photodiode to measure the $p - (p + i)$ optical beat note, which is equal to f_0 of the idler comb. This RF signal is used to generate a phase error signal with another DDS set to the desired f_0 value. The error signal is filtered and fed back onto PZT-actuated mirrors in the OPO cavity.

2.1.2 6–11 μm DFG comb

The DFG frequency comb system [15] was designed and built by our collaborators Kevin Lee and Martin Fermann. It is based on a 1.5 μm Er-doped fiber oscillator with a 93.4 MHz repetition rate. f_{rep} control is achieved with a fast piezo oscillator end mirror and a slow oscillator fiber stretcher. An intracavity electro-optic modulator (EOM) provides additional fast-bandwidth f_{rep} control. Oscillator light is split into two arms. The first is amplified in Er fiber to 1.6 W with 110 fs pulse duration. The second is pre-amplified with Er fiber, recompressed, broadened to 2 μm in a highly nonlinear fiber, and finally seeded into a Tm fiber amplifier generating 0.6 W with 60 fs pulse duration. The two arms are spatially and temporally overlapped and focused into an orientation patterned gallium phosphide (OP-GaP) crystal, which has several quasi-phase matching grating periods available to tune the spectrum of the DFG from 6 μm to 11 μm, with up to 60 mW of average power. A delay stage in the 2 μm drive arm is actively servoed by monitoring nonlinear parasitic output of the OP-GaP crystal. This feedback maintains optimal temporal overlap of the two driving pulses in the presence of slow thermal drifts.

The f_0 of the DFG frequency comb is equal to the difference of the f_0 of the two driving arms. In this design, both arms originate from the same oscillator and therefore cancel, yielding a DFG $f_0 = 0$ identically. To shift the f_0 to non-zero values, an acousto-optic modulator (AOM) is placed in one of the arms. By driving the AOM with a stable RF source, the desired f_0 can be simply dialed in and is passively stable. A small portion of the oscillator light is picked off and measured on a fast photodiode for f_{rep} monitoring. The eleventh harmonic at $11f_{\mathrm{rep}} \approx 1027$ MHz is mixed with a stable 1 GHz oscillator, and the beat note is used to generate an f_{rep} phase error with respect to a reference RF signal generated by a DDS (slaved to the same 1 GHz oscillator). This phase error can be fed back onto the oscillator cavity length piezos to lock f_{rep}.

2.2 Absorption spectroscopy with frequency combs

An infrared spectrum is obtained by directing comb light through a molecular sample and measuring how much each individual comb mode is absorbed. The transmitted intensity I of a given comb mode is determined by the standard linear absorption (Beer's Law) expression,

$$I = I_0 \exp(-N\sigma\ell), \tag{2.1}$$

where I_0 is the incident intensity, N is the number density of the absorbing species, σ is the absorption cross section, and ℓ is the sample path length. The cross section σ is frequency, temperature, and pressure dependent.

Obtaining the highest signal-to-noise ratio for the absorbed fraction of light $A = 1 - I/I_0$ requires increasing N, σ, or ℓ. For volatile species that are gaseous at room temperature, it is usually easy to reach large number densities N by using high pressure samples. However, collisional broadening will eventually dominate other contributions to the absorption line width, setting a practical upper limit. The collisionally broadened line width $\Delta\nu_{\mathrm{col}}$ is approximately linear with pressure, $\Delta\nu_{\mathrm{col}} = \gamma p$, where the broadening coefficient γ is typically $1 - 10$ MHz/Torr. At low pressures, the absorption line width is dominated by Doppler broadening, which has a contribution

$$\frac{\Delta\nu_{\mathrm{D}}}{\nu_0} = \sqrt{\frac{8k_{\mathrm{B}}T\ln 2}{mc^2}} = 7.16 \times 10^{-7}\sqrt{\frac{T/\mathrm{K}}{m/\mathrm{amu}}} \tag{2.2}$$

where $\Delta\nu_{\mathrm{D}}$ is the full width half maximum (FWHM) of the line, ν_0 is the center frequency, k_{B} is Boltzmann's constant, T is temperature, m is the molecular mass, and c is the speed of the light. For example, at 300 K methane has a Doppler line width of about 280 MHz in its strong 3 μm CH stretch region and a self-broadening coefficient $\gamma \approx 2$ MHz/Torr [17]. At this temperature, the useful upper density limit is about 10^{18} cm^{-3}. Heavier molecules and lower temperatures will result in smaller Doppler line widths, decreasing the useful density limit. Often, technical considerations of the absorption cell or a low sample vapor pressure will limit the achievable densities to even smaller values. The typical molecule density in our experiments is about 10^{12} cm^{-3} (see below).

The absorption cross section σ of a rovibrational transition is proportional to the intrinsic strength of the transition (i.e. the squared magnitude of the transition dipole moment), the lower state population, and the inverse of the line width [18]. The intrinsic line strength is strongest for vibrational transitions for which $\Delta v = 1$, where v is a vibrational quantum number. Therefore, most of the work here is focused on fundamental vibrational bands ($v = 1 \leftarrow v = 0$), though we will see some examples of relatively strong combination bands (involving a change in quantum number of more than one vibrational mode). The lower state population can be concentrated into fewer quantum states by minimizing the rovibrational partition function $Q_{\text{rot-vib}}$. Both $Q_{\text{rot-vib}}$ and the line width, which we assume to be Doppler-limited, increase with temperature. Thus achieving low temperatures, without unduly compromising number density, is a critical requirement for sensitive absorption spectroscopy. For the experimental conditions we typically use, we achieve peak cross sections of approximately 10^{-17} cm^2 (see also Fig. 2.1).

The last factor in absorption strength is the path length ℓ over which the frequency comb light interacts with the sample. Physical considerations often limit practical table-top cells to dimensions less than 1 m. The cell in our experiment has a sample path length of only 6 cm. Taking the typical values for N and σ discussed above, we can estimate an expected maximum single pass absorption loss of $N\sigma\ell = (10^{12}\ \text{cm}^{-3})(10^{-17}\ \text{cm}^2)(6\ \text{cm}) = 60$ ppm. Such a small fractional absorption requires stringently low noise baselines to achieve useful signal-to-noise ratios over practical acquisition times.

2.3 Cavity-enhanced frequency comb spectroscopy

Making significant improvements in N and σ is challenging. The most efficient way to increase the absorption sensitivity is thus to extend the effective path length of the sample. A simple way of implementing this is with a multipass cell, such as a White [19] or Herriott [20] configuration, where light is repeatedly reflected through the absorbing sample. Although the number of passes can in principle be quite large, technical difficulties often limit it to < 100. Moreover, cumulative losses from each reflection (e.g. about 1% per reflection on gold mirrors) severely attenuate the total power throughput.

Large path length enhancement factors and more efficient throughput can instead be achieved with high-finesse optical cavities [21]. In contrast to multipass cells, optical cavities rely on interference between reflected light to provide long effective path lengths with much less attenuation. Here we consider the simple case of a symmetric Fabry-Pérot cavity, formed by two identical, parallel mirrors separated by length ℓ (Fig. 2.4). Each mirror has a reflectivity R, transmission T, and loss L (including both absorptive and scattering losses), with $R + T + L = 1$. Light incident on the cavity is transmitted through the first mirror and reflects back and forth interfering with itself. If the cavity length ℓ and the wavelength λ are such that this interference is constructive, then the light will resonantly build up and transmit through the cavity. Longitudinal resonances occur at regularly spaced optical frequencies separated by the free spectral range, $\mathrm{FSR} = c/2n\ell$, where n is the index of refraction of the intracavity medium.[1] The regularly spaced mode structure of frequency combs is well suited to coupling into the similarly periodic resonance structure of optical cavities.

The line width of each cavity resonance is $\Delta\nu = \mathrm{FSR}/\mathcal{F}$, where $\mathcal{F}$ is the cavity finesse. Assuming we have high reflectivity mirrors ($1 - R = T + L \ll 1$), then the finesse is to a good approximation

$$\mathcal{F} \approx \frac{\pi\sqrt{R}}{1-R} \approx \frac{\pi}{T+L}. \tag{2.3}$$

When incident laser light is at a frequency several or more line widths away from a resonance, it is almost completely reflected back from the cavity. If tuned to a resonance, then it will couple into the cavity and be transmitted with a power throughput of

$$\tau_{\mathrm{cav}} = \left(\frac{T}{T+L}\right)^2. \tag{2.4}$$

The transmitted light experiences many round trips inside the cavity as it gradually leaks out through the end mirrors. The effective number of passes for light resonant with the cavity is $2\mathcal{F}/\pi$.

To illustrate the magnitude of these various cavity parameters, consider a typical MIR-

---

[1] Our cavities are typically in vacuum or filled with a low density of non-refractive gas such that $n = 1$ for all relevant wavelengths. An exception to this is near molecular absorption resonances where dispersive effects can be readily seen for sufficiently strong transitions.

coated dielectric mirror with $T = L = 250$ ppm, yielding a finesse of $\mathcal{F} \approx 6300$ and a transmission coefficient of $\tau_{\text{cav}} = 25\%$. Our cavity design, discussed in more detail below, has a mirror separation of about 54 cm, and therefore an FSR of 280 MHz and a line width of $\Delta\nu = \text{FSR}/\mathcal{F} = 44$ kHz. Most importantly, the effective path length enhancement factor is $2\mathcal{F}/\pi = 4000$. This provides a significant and crucial boost in absorption sensitivity.

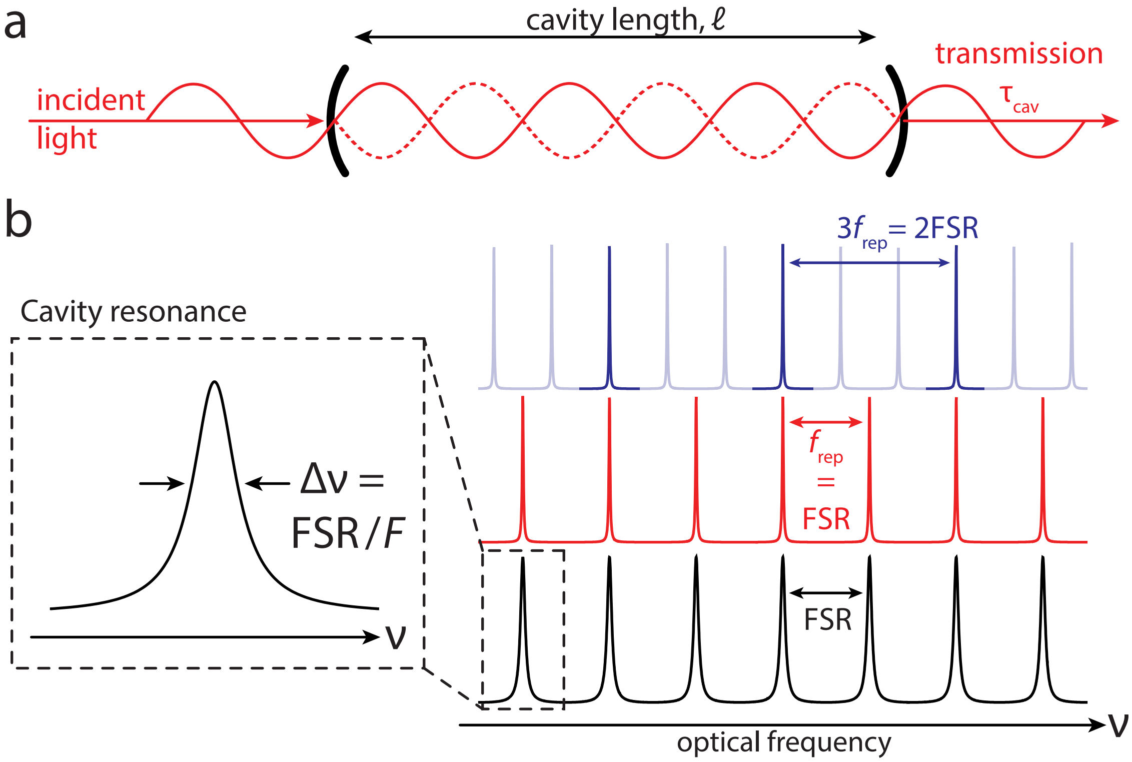

Figure 2.4: Cavity-comb coupling. (a) Frequency comb light is incident on a symmetric Fabry-Pérot cavity of length ℓ. When resonant, a fraction τ_{cav} of the light (Eq. 2.4) is transmitted through the cavity, making $\mathcal{F}/\pi$ round trips, where $\mathcal{F}$ is the cavity finesse. (b) The cavity transmission resonances (black trace) are spaced by the free spectral range, $\text{FSR} = c/2\ell$, with a line width (full width-half maximum) of $\Delta\nu = \text{FSR}/\mathcal{F}$. In one case, a frequency comb (red trace) has $f_{\text{rep}} = \text{FSR}$, such that each comb mode is resonant with the cavity. In a second case, a frequency comb (blue trace) with $3f_{\text{rep}} = 2\text{FSR}$ allows only every third comb mode to be resonant with the cavity, resulting in a larger effective f_{rep} for the transmitted light.

2.3.1 Cavity-comb coupling

Efficient cavity-comb coupling requires simultaneously matching the optical frequency of each comb mode with that of a cavity resonance [6]. This implies that f_{rep} and the cavity FSR must be related by some integer ratio, $m \times f_{\mathrm{rep}} = n \times \mathrm{FSR}$. In the simplest case where $m = n = 1$, each comb mode and cavity resonance are simultaneously coupled in a one-to-one fashion. For other integer ratios with m, n, or both greater than 1, only a subset of comb modes will be resonantly coupled to the cavity (Fig. 2.4b). The obvious disadvantage in this case is that not all the comb modes can be used for spectroscopy. However, this type of cavity filtering can also be useful. The transmitted comb has a higher effective f_{rep}, and it is therefore easier to individually resolve transmitted comb modes with a given detection apparatus. This idea is also used for frequency comb Vernier spectroscopy, where the cavity itself disperses comb modes one-by-one [22]. Details of our cavity filtering are discussed further in Section 2.4.

Just as dispersion in the comb laser oscillator cavity induces a non-zero f_0 offset frequency, dispersion from the enhancement cavity mirrors shifts the cavity resonances uniformly by f_{cav}. Therefore we also require that $f_0 = f_{\mathrm{cav}}$. In a typical setup, the f_{cav} value can be measured by tuning the comb f_0 until optimal coupling is observed. In the case of the MIR OPO discussed above, this value is then used as the reference frequency for the f_0 phase lock. For the DFG comb, the AO shifter drive frequency is simply set to f_{cav}. The value of f_{cav} depends on the static dispersive material properties of the mirror coatings, so that for a given wavelength, it is effectively fixed.

The optical frequencies of the comb modes and cavity resonances are equal to large integer multiples of the comb f_{rep} and cavity FSR, respectively. Therefore, fast relative fluctuations between f_{rep} and the FSR make active feedback necessary. A common tool to achieve tight comb-cavity locking is the Pound-Drever-Hall (PDH) technique [23]. Here, frequency sidebands are placed on the comb laser at a modulation frequency f_{mod} larger than the reference cavity line width. A fast photodiode is used to measure the reflected cavity light intensity signal, which is demodulated at f_{mod} to generate the PDH error signal. This error signal is linearly proportional to the comb-cavity frequency detuning over a frequency range approximately equal to the cavity line width. After passing the error signal through a proportional-integral (PI) filter, it is fed back onto the comb f_{rep} value. The error signal can also be further slowly integrated and fed back onto the cavity length via piezo actuators to compensate for long term drifts.

For the OPO comb, we generate frequency sidebands by driving a fast piezo actuated mirror in the fiber oscillator near its 760 kHz mechanical resonance frequency. The error signal is fed back onto the same fast piezo, as well as a tube piezo on the enhancement cavity that servoes its FSR.

For the DFG comb, we use an intracavity EOM in the fiber oscillator for the frequency sideband generation. In order to induce sufficient phase modulation in the EOM, a passive resonator is formed with a 100 μH inductor in series with the EOM electrode plates. The intrinsic capacitance of the EOM crystal ($C_{\text{EOM}} \approx 43$ pF) together with additional parasitics result in a resonance frequency of $f_{LC} = 1/2\pi\sqrt{LC} = 2.65$ MHz, with a Q of about 14. At frequencies below f_{LC}, the resonator passes feedback signals with unity gain. The PDH error signal is fed back onto both a fast piezo actuated oscillator mirror and a slow fiber stretcher. Additional feedback is placed on the oscillator EOM to achieve higher locking bandwidth. The PDH lock only ensures that the difference between f_{rep} and the cavity FSR (or suitable integer multiples) is zero. Once the PDH lock is actively slaving the comb to the cavity, the comb f_{rep} is measured using the 11^{th} harmonic as discussed above. Its phase error relative to a stable RF reference is fed back onto the enhancement cavity length to stabilize the absolute value of f_{rep}.

The PDH technique continuously locks the comb mode frequencies to their respective cavity resonances. However, the narrow line width and steep slope of the cavity transmission resonances can convert residual frequency noise into amplitude noise of the transmitted light. This FM-to-AM noise conversion can limit the absorption sensitivity. An alternative cavity locking scheme to PDH locking, called swept cavity locking [6], is relatively immune to FM-to-AM noise conversion and can provide significant sensitivity improvements. We implement a swept cavity lock by modulating the enhancement cavity length at 10 kHz via the cavity tube piezo. As the cavity length is swept, it passes through resonance with the comb light, permitting a transient buildup of power and transmission burst for each comb mode simultaneously. These transmission bursts occur at twice the cavity length modulation frequency, once for the forward sweep and once for the backward sweep. The relative time spacing between the transmission bursts when the cavity is being scanned forward versus backward determines the mean frequency offset of the cavity relative to the comb light. A small fraction of cavity transmission is picked off, measured on a photodiode, and demodulated at the cavity sweep frequency with a lock-in amplifier to generate an error signal that is fed back onto the cavity length piezo. The comb f_{rep} only needs to remain within the range of the cavity length sweep. Therefore the slow feedback bandwidth of the cavity piezo (~ 1 kHz) is sufficient to maintain the lock. In the swept cavity method, the amplitude of the transmission burst is determined by the relatively constant optical slew rate of the swept cavity resonance and insensitive to the cavity-comb optical detuning. Therefore it can provide cavity transmission with relatively low intensity noise at the cost of reduced duty cycle.

2.4 Comb detection

Two detection methods are used to acquire broadband comb spectra in these experiments. The first is the familiar technique of Fourier transfrom spectroscoscopy (FTS) and the second is based on spatial dispersion with a virtually image phased array (VIPA) etalon. This section discusses the details of each detector and their relative advantages and performance.

2.4.1 FTS detection

We perform FT spectroscopy using a home-built fast scanning interferometer [24] (Fig. 2.5a). Each arm of the interferometer is double-passed on a translating corner-cube reflector with a physical travel range of 0.7 m. This geometry provides $\ell = 4 \times 0.7 = 2.8$ m of optical path length difference and an instrument resolution of $\Delta\nu_{\text{FT}} = c/\ell = 110$ MHz (Fig. 2.5b,c). A complete cart scan (and return) takes $5 - 10$ s. If the input to the FTS were a continuous white light source, then $\Delta\nu_{\text{FT}}$ would determine the ultimate spectral resolution. In the case of a frequency comb, however, the FTS instrument line width is sufficiently narrow to resolve individual comb modes so long as the effective $f_{\text{rep}} < \Delta\nu_{\text{FT}}$. Once this limit is reached, the effective spectral resolution is determined only by the line width of the frequency comb ($\sim 1 - 10$ kHz), thereby providing high resolution measurements spaced by f_{rep} [25]. To fill in the "spectral gap" between the narrow comb modes, multiple measurements with different f_{rep} values are acquired and interleaved. For FTS experiments, we use enhancement cavity filtering that produces an effective f_{rep} in the $250 - 300$ MHz range, well into the comb-mode-resolved limit.

An important technical consideration is the instrument line shape of the FTS. We use a rectangular interferogram window, resulting in a sinc line shape function in the frequency domain. The outer lobes of the sinc function centered at a given comb mode in general overlap with the centers of neighboring comb modes, resulting in unwanted cross-talk [25]. We use an automated rewindowing process to relocate nodes of the instrument line shape function to coincide with the positions of neighboring comb modes, thereby eliminating cross-talk.

Given our typical FTS cart scanning velocity ($5 - 15$ cm/s) and optical wavelengths ($3 - 10$ μm), the interferogram signal carrier frequencies are in the $20 - 200$ kHz range. The noise baseline of the FTS in this region is dominated by the intensity noise of the incident comb light. We perform differential detection to suppress this noise. Each output port of the FTS beamsplitter is measured on a photodiode. The intensity noise is an in-phase common-mode signal on each photodiode, while the interferogram signal from one output port is 180° out-of-phase relative to the other port. By subtracting the signal of the two photodiodes, the interferogram signal is doubled and the common-mode intensity noise is canceled.[2] Effective common-mode noise rejection requires that the relative gain of the photodiode pair be tuned optimally. This is impractical to do manually because the average relative power incident on the photodiodes varies over the course of an FTS cart scan. (As the cart position changes, there are unavoidable drifts in the beam direction and size.) Therefore, we use a JILA-made autobalancing subtraction circuit that adjusts the gain of each photodiode to match their DC levels throughout a cart scan. We typically achieve 20 dB to

---

[2] Uncorrelated noise between the two detectors, such as shot and dark noise, are of course not canceled. They do benefit, however, from a $1/\sqrt{2}$ reduction in their relative amplitude because of the 2× enhancement factor of the interferogram signal.

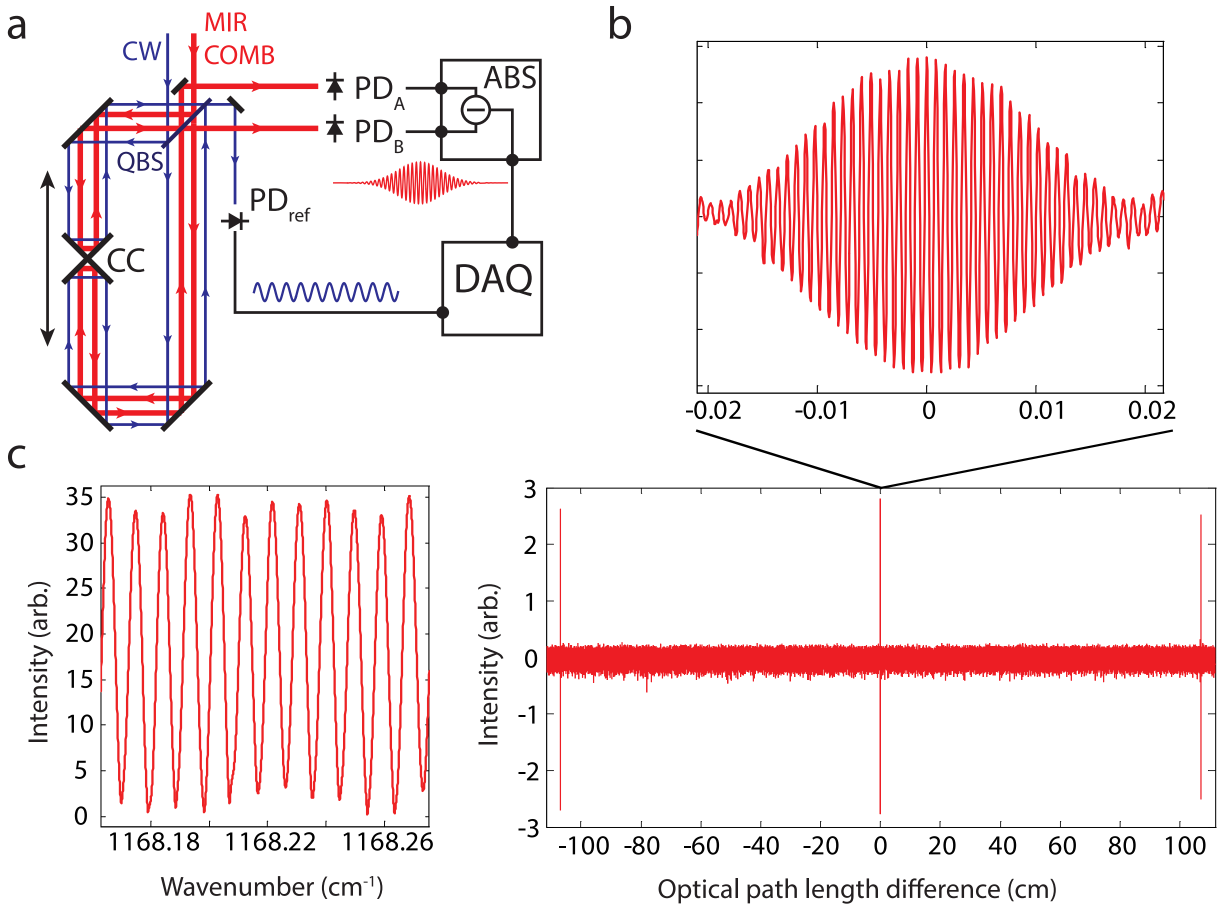

Figure 2.5: FTS detection of frequency combs. (a) MIR comb light and a 1 μm reference cw Nd:YAG NPRO laser are co-propagated in the FTS interferometer. A quadrant beam splitter (QBS) splits both inputs into two arms that are incident on a scanning corner-cube reflector (CC). The cw interferogram is measured on a photodiode ($\mathrm{PD_{ref}}$) for optical path length calibration. The two MIR QBS outputs are each measured on photodiodes ($\mathrm{PD_A}$, $\mathrm{PD_B}$). The difference signal from an autobalanced subtraction (ABS) circuit is acquired with a fast digitizer (DAQ). (b) An example comb interferogram shows a center burst at zero optical path length difference due to interference between one ultrafast pulse and itself. Two additional bursts on either side arise from interference between sequential pulses in time. The zoomed-in window shows the carrier wave of the MIR light in the center burst region. (c) A narrow portion of the Fourier-transformed spectrum from the comb interferogram in (b) shows individually resolved comb modes. The spacing between the peaks (0.009 cm^{-1}) is equal to the inverse of the optical path length difference between the interferogram center bursts (110 cm).

30 dB of common-mode noise rejection, which in some cases is sufficient to reach the shot-noise limit [26], though we are usually limited by residual non-shot-noise intensity fluctuations. For the 3-5 μm OPO system, we achieve a detection sensitivity of 4.4×10^{-8} cm^{-1} Hz$^{-1/2}$ for a single comb

mode. Given that the typical bandwidth of the FTS spectrum contains 3300 resolved comb lines, this corresponds to 7.6×10^{-10} cm^{-1} Hz$^{-1/2}$ per spectral element (PSE) [27]. For the DFG system operating near 8.5 μm, we achieve a sensitity of 2.2×10^{-7} cm^{-1} Hz$^{-1/2}$ for a single comb mode. The spectral bandwidth contains about 5000 resolved comb modes, corresponding to 3.1×10^{-9} cm^{-1} Hz$^{-1/2}$ PSE [28].

A conventional absorption measurement requires detecting the light intensity with (I) and without (I_0) the absorber to determine the absorption $A = 1 - I/I_0$. We typically forego acquiring two separate interferograms for such a measurement as the cavity-transmitted intensity of the comb light gradually drifts over the relatively long FTS acquisition time of $5 - 10$ s per interferogram. The absorption spectra for cold species are usually rather sparse with only a minor fraction of the comb modes being absorbed for a given f_{rep} value. Therefore, we can take the comb intensity envelope as a proxy for the reference intensity I_0. One approach could be to fit this envelope with a slowly varying polynomial or spline function. We take the even simpler route of high-pass filtering the cavity-transmitted spectrum. This processing is performed for the acquired comb spectrum for each f_{rep} value before interleaving them in the final composite spectrum.

2.4.2 VIPA spectrometer

Two important disadvantages of FTS detection are the relatively long acquisition times (up to ten seconds per interferogram) and the requirement of continuous incident light. The latter necessitates PDH comb-cavity locking, which as discussed above suffers from FM-to-AM noise conversion. An alternative to interferometric detection is to use a dispersive element to spatially separate comb modes and subsequently image the broadband spectrum on an infrared camera [6]. This general approach has the advantage of permitting fast, time-resolved, transient detection [29–32] (typically limited by the minimum camera integration time and maximum frame rate) and being compatible with the intermittent transmission of the swept-cavity locking scheme.

The primary challenge is constructing a dispersive spectrometer with sufficient resolution to spatially separate neighboring comb modes. The required resolving power for a diffraction grating is $R = mN = \lambda/\Delta\lambda \approx \nu/f_{\text{rep}} \sim 10^5 - 10^6$, where m is the diffraction order and N is the number of illuminated grooves. Standard MIR ruled gratings have groove densities on the order of 10^2/mm and operate at low diffraction order (often $m = 1$). A grating of this type would need to be about 10 m long to provide sufficient resolving power, which is obviously impractical for a table-top laboratory instrument. Recent advances in high-diffraction-order, high-refractive-index immersion gratings, however, have made this approach viable [33].

An optical element called a virtually imaged phased array (VIPA) etalon provides the high angular dispersion and resolution necessary for spatial separation of individual comb modes [34–36] (Fig. 2.6a). The setup consists of a thin glass parallel plate etalon. The back (output) surface has a high reflection coating ($\sim$ 95% or more), while the front (input) surface has a $\sim$ 100% coating. Input light is cylindrically focused and coupled into the etalon at a gap in the coating on the front face with a small incidence angle θ. The light bounces back and forth in the etalon, leaking through the output face at each bounce. The interference of the reflected beams forms collimated output light, where the output propagation angle is determined by the optical wavelength. (The angular dispersion is proportional to $n \cot\theta$, where n is the index of refraction of the etalon material.) The angular resolution is determined by the total loss per round trip in the etalon, and is therefore limited by the bulk material absorption and scattering. With our MIR etalons, VIPA line widths of $0.5 - 1.0$ GHz are achievable, corresponding to a resolving power of $\sim 10^5$ [29, 30, 37]. This represents a significant improvement over standard diffraction gratings. However, as our comb f_{rep} values are $\sim$ 100 MHz, some modest cavity filtering is still necessary for comb mode resolved spectroscopy [27, 38]

At a given output angle, light containing optical frequencies separated by the etalon FSR is overlapped. Our etalons have FSRs of about 50 GHz, and therefore the overlapping components are easily separated by placing a low-resolution reflective grating after the etalon at an orthogonal orientation. This creates a two-dimensional pattern of comb modes, which are then imaged onto a sensitive infrared camera (Fig. 2.6b). As with FTS spectroscopy, once the comb mode-resolved limit is reached, the effective resolution is no longer limited by the spectrometer (in this case, the

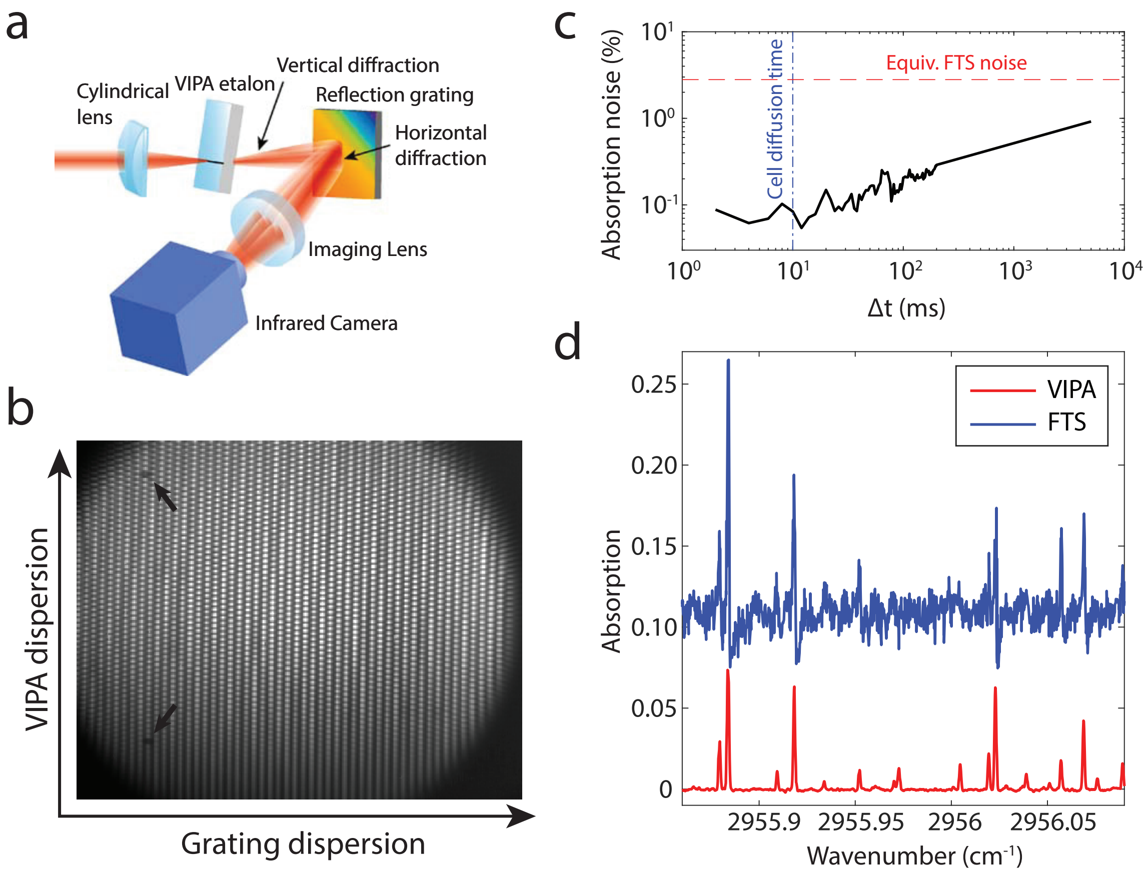

Figure 2.6: Frequency comb spectroscopy with a VIPA etalon. (a) Incident comb light is cylindrically focused into the VIPA etalon, which disperses light in the vertical direction. A low resolution reflection grating disperses overlapping etalon FSRs in the horizontal direction. The two-dimensional pattern of comb light is then imaged onto an infrared camera. (Figure reused by permission from Springer Nature: *Applied Physics B: Lasers and Optics*, "Cavity-enhanced direct frequency comb spectroscopy", M. J. Thorpe and J. Ye. [5]) (b) An example VIPA image showing resolved comb modes as individual bright spots. The vertical axis corresponds to VIPA dispersion, and the horizontal axis to grating dispersion. Each column fringe is a distinct VIPA order, separated from an adjacent fringe by the VIPA free spectral range (50 GHz). Along a given fringe, each comb mode spot is separated from its vertical neighbors by 1 GHz via cavity filtering. The two dark spots (indicated by arrows) correspond to the same absorbed comb mode appearing in the image in sequential VIPA orders. (c) Fast frame-to-frame subtraction of VIPA images improves the absorption noise baseline by removing incident comb light intensity fluctuations. At a $\Delta t = 10$ ms subtraction time, we observe a 30× improvement in sensitivity relative to FTS detection for the same total acquisition time. At shorter times, the noise baseline plateaus, indicating that the camera dark noise limit has been reached. The cell diffusion time of about 10 ms corresponds to the fastest rate at which the molecular absorber density in the cold cell can be efficiently modulated. (d) A comparision of FTS and VIPA spectra for a small region of the MIR absorption spectrum of cold CH_3NO_2.

VIPA etalon line width) and instead set by the frequency comb itself.

The VIPA spectrometer detection sensitivity is usually limited by the incident light intensity noise. Simultaneous differential detection to suppress comb mode intensity noise, as is performed with the FTS setup above, is in general difficult. While swept-cavity locking improves the baseline intensity noise by eliminating FM-to-AM noise conversion from the enhancement cavity [6], intrinsic (i.e. pre-cavity) intensity noise of the frequency comb light is not suppressed. To combat residual intensity noise, we take advantage of the fast frame rate (up to 500 Hz) of the detector camera, which permits a lock-in type measurement to be performed. Sequential camera frames are acquired, one with molecular absorption signal present and another without, and subtracted. This eliminates intensity noise contributions slower than the subraction rate, as shown in Fig. 2.6c. We modulate the molecular absorption signal by a fast mechanical shutter between the molecule source and the sample cell (see Section 2.5 below). The modulation rate is ultimately limited by the 10 ms diffusion time in the cell. At this diffusion-limited modulation rate, we are still able to reach the camera dark noise limit. For the $3 - 5$ μm OPO system, the combination of fast camera acquisition times and frame-to-frame intensity noise subtraction yield a 30-fold improvement in the cavity transmission noise floor relative to FTS detection normalized to equal acquisition time. It is important to realize, however, that the swept-cavity locking method reduces the effective path length of the light by a factor of 1/2 relative PDH locking due to differences in continous versus impulsive light-cavity coupling [6]. Therefore, the net absorption sensitivity of the VIPA setup is only about 15× higher than the PDH/FTS detection system (Fig. 2.6d), which is nonetheless a significant improvement [27].

2.5 Cryogenic buffer gas cooling

The MIR frequency comb techniques discussed in the previous sections provide powerful tools for probing molecular structure and dynamics. Taking full advantage of the high resolution capabilities of combs for molecular spectroscopy requires preparing molecules in a physical state such that the complex structure of their rovibrational spectra is fully revealed. For this reason, room temperature experiments have been largely limited to relatively small systems because molecules with even, say, half a dozen heavy atoms already occupy millions of rovibrational quantum states, yielding intractably congested and unassignable spectra. The ability to produce cold, dense samples of neutral molecules is therefore crucial to extending high resolution spectroscopy to more complex molecules.

We address this issue by combining CE-DFCS with cryogenic buffer gas cooling (CBGC) [39–42]. With this technique, a cryogenic cell with a wall temperature T_{wall} ranging from 10 K o 150 K is filled with an inert buffer gas, usually a noble gas such as helium, neon, or argon, which thermalizes to T_{wall}. Warm (room temperature or hotter) molecules are injected into the cell where they collide with the cold buffer gas atoms, approximately thermalizing their rotational and translational temperatures to T_{wall}. At these low temperatures, molecular spectra are drastically simplified relative to room temperature conditions, exhibiting reduced congestion, narrow Doppler line widths, and larger absorption cross sections. CBGC provides a continuous source of cold molecules with slow lab frame velocities and long interaction times with only modest pumping requirements. These represent distinct advantages over supersonic expansion cooling, which exhibits fast lab frame jet velocities and limited interaction times and poses a compromise between low duty cycle pulsed operation or managing non-trivially large gas loads. As will be discussed in later chapters, efficiently cooling complex polyatomic molecules with CBGC has permitted the measurement of rotationally resolved infrared spectra of unprecedentedly large molecules including adamantane ($C_{10}H_{16}$) in the 3 μm CH stretch region [27, 38] and buckminsterfullerene (C_{60}) near 8.5 μm [28].

2.5.1 Low-temperature CBGC system

We use one of two CBGC systems depending on the required cooling capacity and buffer gas load for the experiment. The low-temperature ($10 - 30$ K) device [27, 38] is based on a closed-cycle liquid-helium two-stage pulse tube cryostat (Cryomech PT410/CP2800), as diagrammed in Fig. 2.7a. The first stage has 40 W of cooling capacity at 40 K, and the second stage has 1 W of cooling capacity at 4 K. The pulse tube head is placed in a room temperature vacuum dewar with a base pressure of 1×10^{-6} Torr (when cold). A copper radiation shield mounted to the first stage reduces the blackbody radiative heat load on the second stage cooler. A hollow aluminum cold cell, shown in Fig. 2.8, with an interior volume of $6 \times 6 \times 6$ cm^3 is mounted to the second stage. Sensor diodes mounted to the cold cell, second stage, and radiation shield provide temperature monitoring. With no gas load, the cold cell reaches a baseline temperature of $3 - 4$ K. A small continuous flow (ca. 10 sccm) of helium buffer gas is pre-cooled to the 4 K stage before entering the cold cell through an annular slit inlet, resulting in a helium density of 10^{14} cm^{-3} to 10^{15} cm^{-3} inside the cell.

Helium leaking out of the cell is efficiently cryopumped by charcoal sorbs mounted to the 4 K stage. The details of the sorb design have a significant impact on their pumping performance [43,44], and it is worthwhile discussing these particulars here. Our "secret formula" comes from John Doyle's group [45, 46] via Dave Patterson, who collaborated with us on the construction of the CBGC system. We adhere activated coconut charcoal (Spectrum C1221, 8-30 mesh) to 1/8"-thick super-conductive OFHC (101) copper using Stycast 2850FT epoxy with catalyst 23LV (7.5% by weight).[3] Typically, three 3"×6" plates (both sides coated with charcoal) are installed, giving a total pumping area of about 700 cm^2. With a 10 sccm helium load, the background dewar pressure (measured outside the radiation shield) is about 2×10^{-5} Torr. Using this as an approximation for the helium pressure near the sorbs, we roughly estimate a pumping speed of 6000 L/s. The sorbs can run for 3 to 4 hours continuously, from which we also estimate a capacity of about 1500 L·Torr. Both of these estimates are consistent with the expected performance of coconut charcoal [43, 44].

Once saturated, the pumping speed drops and the background pressure gradually increases until it reaches about 1×10^{-4} Torr. At pressures higher than this, thermal contact to the room temperature dewar wall warms the sorbs, releasing helium and causing a runaway "crash". Usually, the helium is turned off before a crash is allowed to occur. To regenerate the sorbs, the pump out valve is opened and the refrigerator is turned off. Once the sorbs are above ca. 40 K almost all of

---

[3] For unknown reasons, the Ye group historically has used catalyst 23LV, while the Doyle group reports using catalyst 24LV [45, 46]. The two catalysts appear to have very similar physical properties [47].

the helium has been released, and they can be re-cooled for further use.

In the absence of contamination, we have successfully re-used the same sorbs continuously for over a year. Temporary “clogging” can occur from a vent or leak of atmosphere into the vacuum dewar. The sorbs can be restored by pumping on them at room temperature for several hours. (We suspect it helps that the air in Boulder, CO has a relatively low concentration of water vapor.) The chemical species we introduce into the cold cell are the most potentially problematic source of contamination. When the system is cold, these molecules are efficiently cryopumped by the metal surfaces of the cold cell and radiation shield, and it is likely only a very small fraction reaches the sorbs. However, when the system is eventually warmed up, these molecules are released and can come into contact with the sorbs. We have found that species that are gas-phase or have a high vapor pressure (at least tens of torr) at room temperature do not cause any observable degradation to the sorb. Conversely, highly non-volatile solids, such as C_{60}, remain solid after warming to room temperature and cause no problems (except for requiring frequent clean-up of the cold cell where the solid collects). The only permanent degradation we have observed is from certain sublimating solid and non-volatile liquid samples, such as hexamethylenetetramine and indole. After introducing these species into the cold cell and then warming up, the pumping speed of the sorbs was severely reduced. Attempts to revive poisoned sorbs by a 150°C bakeout overnight recovered only a small fraction of the peak pumping speed and helium capacity and were ultimately unsuccessful. Finally, it is important to note that only oil-free turbo and scroll pumps are used for the vacuum dewar, eliminating another potential source of sorb contamination.

Warm gas-phase molecules enter the cold cell (Fig 2.8) through a 1 cm aperture in the cell wall and quasi-thermalize to T_{wall} with a density of about 10^{12} cm^{-3} [27, 38]. For most small molecules, 10s to 100s of collisions are necessary to cool the internal and translational degrees of freedom. Buffer gas atom-molecule collisions occur with a mean collision period of $10 - 100$ μs, thereby requiring ca. 1 ms for thermalization. The molecules diffuse in the cell for $10 - 20$ ms before freezing out on the cell walls. Measured rotational and translational temperatures in this low-temperature cell are typically $10 - 20$ K (see Section 2.6). For volatile molecules with sufficient

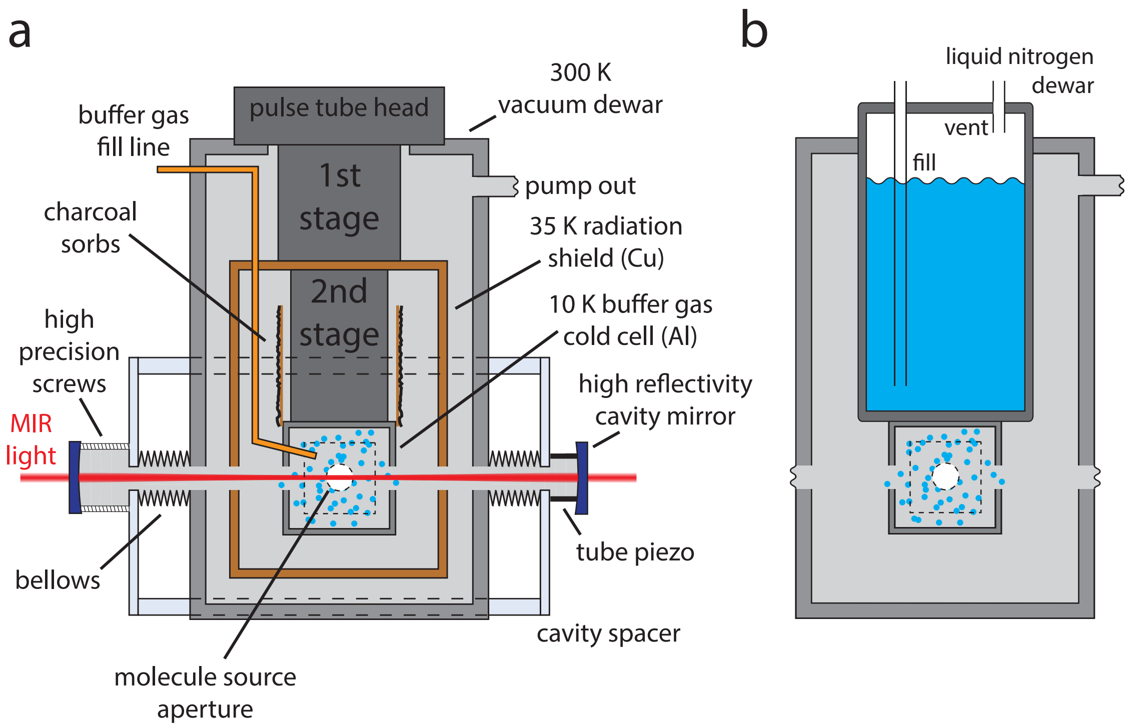

Figure 2.7: Cryogenic buffer gas cooling. (a) The low temperature CBGC apparatus is based on a two-stage liquid helium pulse tube refrigerator. The 35 K radiation shield is mounted to the first stage heat exchanger, while the 10 K cold cell is mounted to the second stage. Charcoal sorbs are also mounted to the second stage to provide high helium pumping speeds. A cavity spacer surrounding the dewar supports two high reflectivity mirrors that form the MIR enhancement cavity. Precision screws and a cavity tube piezo provide fine adjustment of the cavity alignment and length. The cavity optics are vibrationally isolated from the dewar by thin edge-welded bellows. (b) The high temperature system replaces the helium cold finger with an open liquid nitrogen dewar, and the blackbody radiation shield is removed. The cavity optics and hardware (not shown) are identical to those in (a).

.

vapor pressure at room temperature, a flow of $1-10$ sccm is introduced into the cell via a 1/4”-in stainless steel tube that terminates $1-2$ cm in front of the outer surface of the cell wall. For non-volatile molecules, a small copper oven (2 cm × 2 cm × 4 cm) is used to heat samples to produce sufficiently high vapor pressures. The oven, with an interior volume of 3 cm^3, is located *in vacuo* just outside the 35 K radiation shield, with a small tube outlet passing through the shield to guide molecules into the cold cell. The inner diameter (2 mm) and length (3 cm) of the outlet determine the output conductance of the oven and therefore what vapor pressure is necessary for

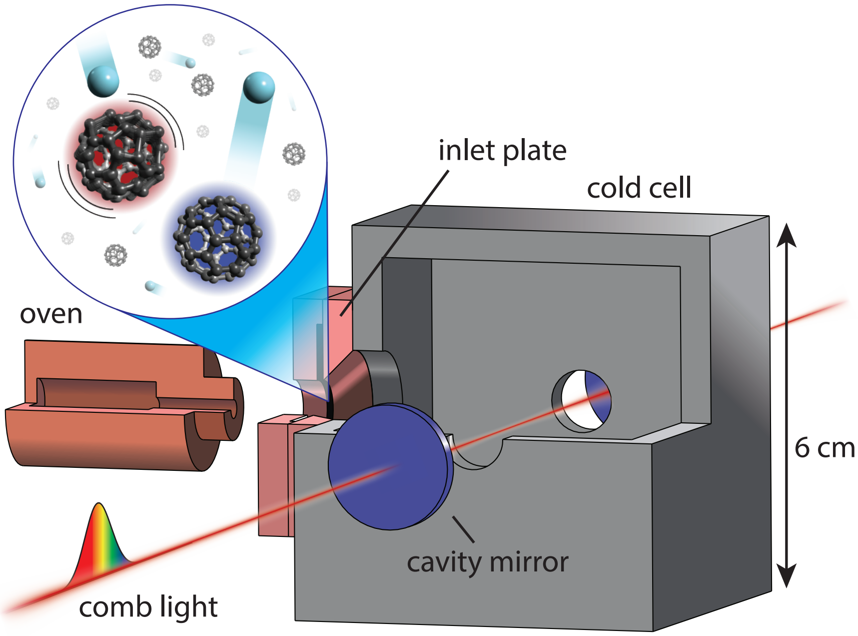

Figure 2.8: A detailed view of the cold cell. The cell is mounted to a either the liquid helium or liquid nitrogen cold finger. Pre-cooled buffer gas enters the cell through the annular slit inlet plate. Warm molecules from an oven source or tube inlet enter the cell and quasi-thermalize to the wall temperature via collisions with buffer gas atoms. Two high reflectivity mirrors (position not to scale) form a path length enhancement cavity that passes through two side apertures in the cold cell.

sufficient molecule output flow. The output conductance is high enough to require only modest oven temperatures (100 °C to 200 °C), but small enough to allow sufficient oven pressure buildup to provide stable vaporization/sublimation and prevent violent boiling. A small glass window permits visual monitoring of the interior of the oven while in use. The oven is resistively heated by two embedded cartridge heaters (50 W, 1/8" OD × 1.25") and temperature monitored by a type-K thermocouple.

A "molecule shutter" consisting of a thin aluminum paddle is placed between the molecule tube or oven outlet and the cold cell aperture in order to quickly turn on or off the molecule flow into the cold cell. The shutter is rotated into and out of the molecule flow with a small DC electric motor mounted to the 35 K shield. Short current pulses from a home-made driver circuit switch the shutter with an open/close time of 1 ms and a delay of 10 ms.

2.5.2 High-temperature CBGC system

In the high-temperature (80 – 150 K) setup (Fig. 2.7b), the helium cold finger is replaced with a liquid nitrogen (LN2) dewar without a blackbody radiation shield [28]. LN2 sets a minimum 77 K temperature limit for the cold cell, but is able to provide significantly higher cooling capacity, which permits using higher buffer gas flows and pressures relative to the low-temperature system (up to 100 sccm and 1 Torr background in the dewar). Charcoal cryopumping is replaced with a small turbo-molecular pump (300 L/s) that is typically choked to an effective pumping speed of less than 10 L/s. The high cooling capacity can handle commensurately high radiative heating, thus increasing the maximum operating temperature of the oven vaporization source. We constructed a second compact oven source capable of heating solid samples up to 1000 K. It consists of cylindrical copper body with a detachable heating collar clamped around it. The heating collar has two silicon nitride ignitors that each deliver a maximum heating power of ca. 1 kW, though they are typically operated at only 60 – 70% of their maximum power to achieve 1000 K oven temperatures. This is consistent with the estimated cooling power of the LN2 dewar based on the LN2 boil-off rate of 5 – 10 L/hr, from which we estimate a cooling power about 1 kW.

2.5.3 Absorption enhancement cavity

The absorption enhancement cavity consists of two parallel mirrors with high reflectivity (HR) coatings surrounding the cold cell [27]. Four 1"-thick stainless steel rods spanning either side of the cryostat dewar fix the gross cavity length (see Fig. 2.7a). The cavity mirrors are mechanically isolated from the dewar by a system of edge-welded bellows that form the vacuum connection between the cavity mirrors and the dewar. The position and alignment of each mirror are adjusted macroscopically by a set of fine precision screws. One of the cavity mirrors is fitted with a tube piezo for fine length adjustment and feedback control. The HR mirrors have broadband coatings with peak finesses of $\mathcal{F} \approx 3000 - 6000$. We typically achieve on-resonance cavity transmission efficiency of a few percent up to 25%, depending on the mirror losses, over a simultaneous transmission bandwidth of $50 - 100$ cm^{-1}, limited by the HR mirror dispersion. The cavity spacers limit the practical range of mirror separations to be $\ell = 50 - 70$ cm, yielding cavity FSRs in the range of 215 to 300 MHz. Cavity filtering is thus unavoidable given the f_{rep} values of our two frequency comb sources (136 MHz for the OPO system and 93.4 MHz for the DFG system). A small gas inlet is placed near each mirror to provide an optional purge flow that protects the mirrors from degradation. This was found necessary with the high-temperature CBGC setup to prevent deposits of C_{60} grains from forming on the mirror surface. The output of the enhancement cavity is routed to the detector systems for transmission read-out. Cavity reflection and transmission photodiodes are placed before and after the cavity to collect PDH and swept-cavity lock error signals, respectively.

2.6 CE-DFCS/CBGC system performance

This final section summarizes the technical performance of the combined CE-DFCS and CBGC apparatus. Returning to the example introduced at the beginning of the chapter, Fig. 2.9a shows the measured FTS absorption spectrum the ν_3 band of vinyl bromide acquired with the low-temperature CBGC cell. This spectrum can be compared to the simulation in Fig. 2.1b. (The negative-going signal in the measured absorption spectrum is an artifact of the filtering process applied to FTS spectra as described in Section 2.4.1.) The dense rotational structure is well resolved, as can be seen by the observation of hyperfine splittings (Fig. 2.9b) and K_a sub-band structure (Fig. 2.9c). The vibrational band contains well over a 1000 transitions from each isotopologue above the absorption noise baseline, essentially all of which have been successfully assigned. (Bromine occurs naturally as ^{79}Br and ^{81}Br in approximately 50:50 relative abundance. The results of a full effective Hamiltonian fit are available in Appendix B.)

The extracted rotational and translational temperature profiles from the vinyl bromide spectrum are shown in Fig. 2.10a,b. A small subset of rotational transitions was used to determine a rotational temperature of $T_{\text{rot}} = 17(3)$ K, while the Doppler-broadened line width indicates a translational temperature of $T_{\text{trans}} = 18(4)$ K. Similar measurements for nitromethane (CH_3NO_2)

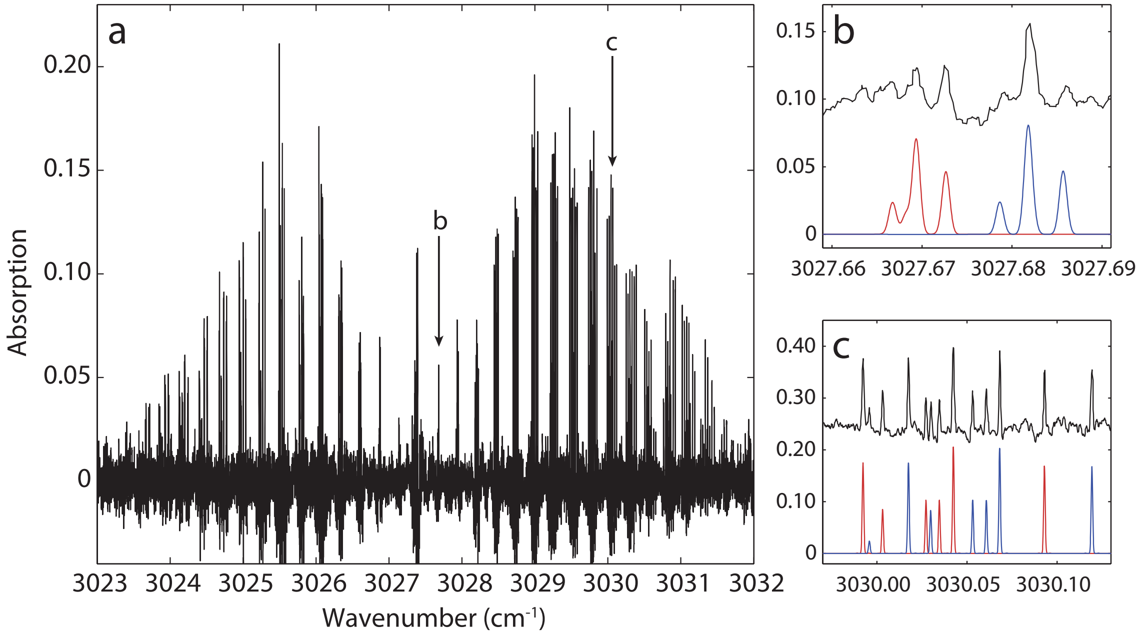

Figure 2.9: CE-DFCS absorption spectrum of the ν_3 band of vinyl bromide. (a) A survey of the entire ν_3 band, which spans about 10 cm^{-1} and contains over 1000 transitions above the noise baseline. Detailed views of the R(0) and R(9) transitions (marked with arrows) are shown in (b) and (c). (b) The measured R(0) transitions are shown in black (offset for clarity) and the simulations for $C_2H_3{}^{79}Br$ and $C_2H_3{}^{81}Br$ are shown in blue and red, respectively. The R(0) transition for each isotopologue is split by nuclear quadrupole effects into three hyperfine components corresponding to transitions from the $F'' = 3/2$ rovibrational ground state to $F' = 1/2$, $5/2$, and $3/2$ upper states, in order of increasing transition frequency. (c) The R(9) region shows clusters of transitions belonging to different $K_a \leq 4$ sub-bands.

yield $T_{\text{rot}} = 11(1)$ K and $T_{\text{trans}} = 16(1)$ K (Fig. 2.10c,d). These results are representative of almost all molecules we have cooled with the low-temperature CBGC cell. The translational and rotational temperatures do not always completely equilibrate, but they are reliably in the 10 K to 20 K range. Based on the integrated band strengths, we estimate the molecule densities to be in the range of $1 - 5 \times 10^{12}$ cm^{-3}.

The only molecule we could definitively *not* cool with the low-temperature CBGC system was buckminsterfullerene, C_{60}. The modest cooling power of the low-temperature system turns out to be no match for the high atom count (60 nuclei), molecular mass (720 u), and oven source temperature (950 K) of C_{60}, forcing us to rely on the much higher cooling capacity of the high-

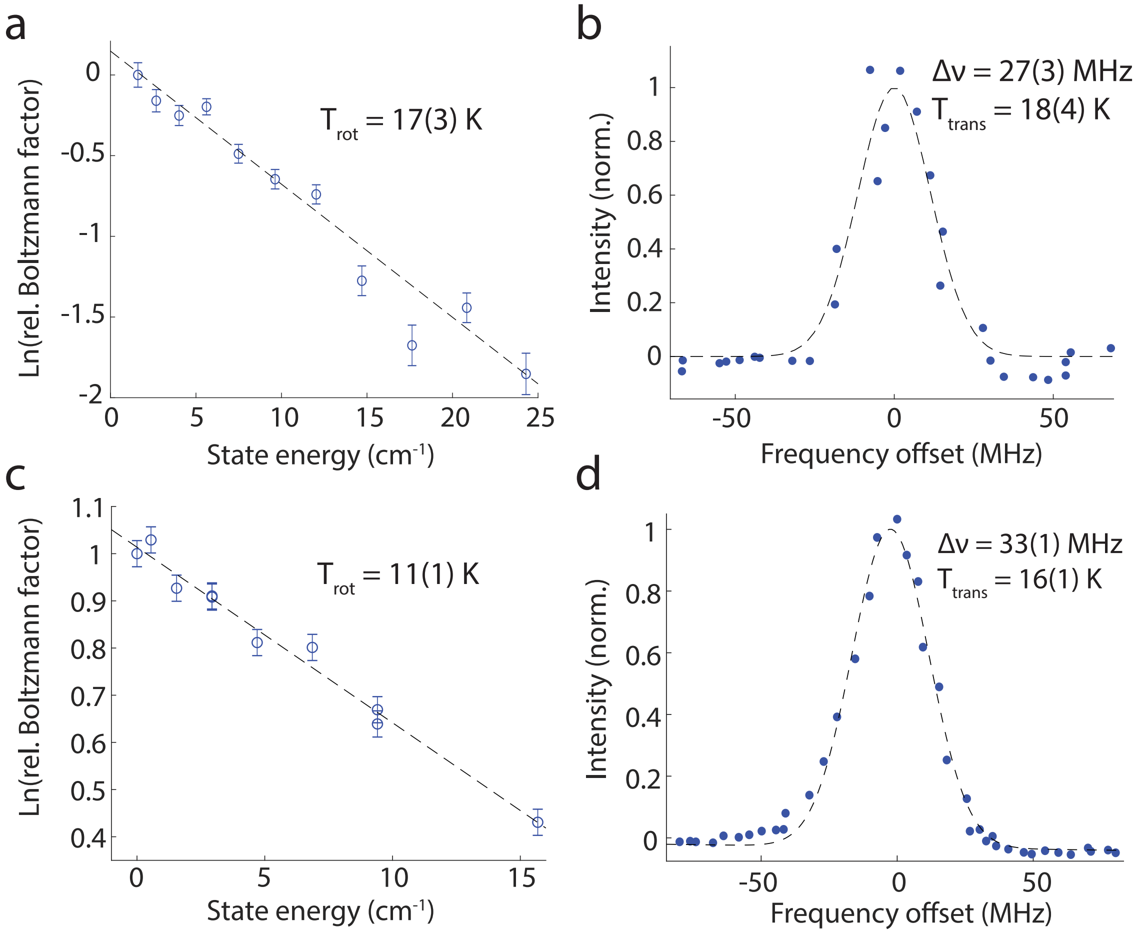

Figure 2.10: Rotational and translational temperatures of molecules in the low-temperature CBGC cell. (a) The natural logarithm of the inferred Boltzmann factors for the lower states of the $C_2H_3{}^{79}Br$ ν_3 ${}^{K_a''=0}$R-branch with $J'' = 3 - 13$. The Boltzmann factors are normalized relative to the $J'' = 3$ level. The fitted slope versus lower state energy indicates a rotational temperature of 17(3) K. (b) The R(9) transition of the same branch shows a Doppler line width of 27(3) MHz, corresponding to a translational temperature of 18(4) K. (All uncertainties are 2σ.) (c,d) Same as (a,b) for the $\nu_3 + \nu_6$ band of nitromethane, CH_3NO_2.

temperature LN2 cold finger. A full discussion of the challenges associated with C_{60} and the efforts to successfully cool it are deferred until Chapter 5. For now, Fig. 2.11 simply presents the final performance we achieved with the high-temperature CBGC system. The relative rotational state populations in Fig. 2.11a exhibit a Boltzmann distribution with an effective rotational temperature of 150(2) K. This is only slightly warmer than the measured wall temperature of 135 K, which is limited by the radiative heat load from the 950 K oven. (Subsequent tests with heat shields

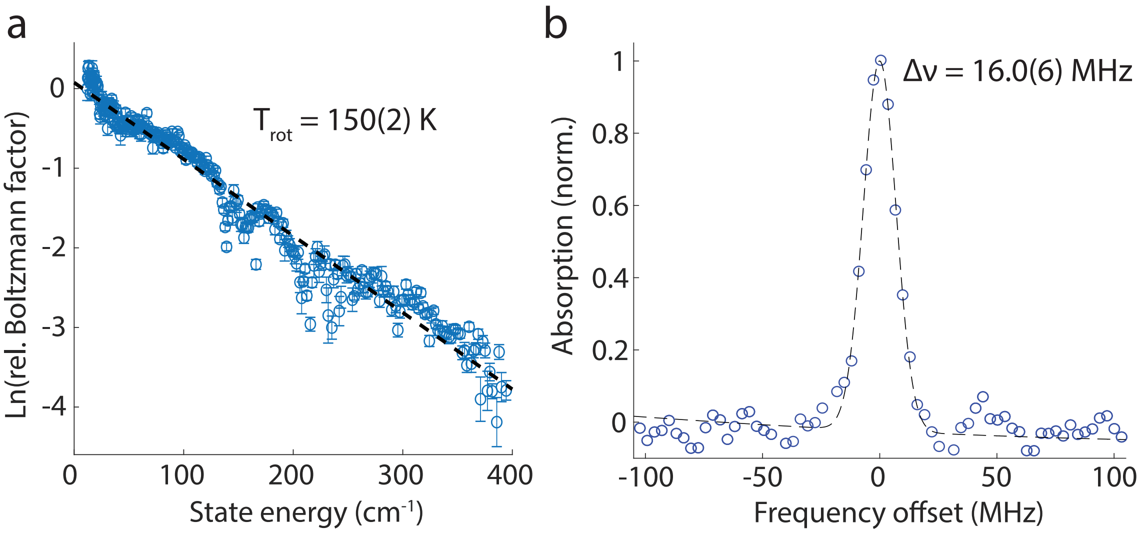

Figure 2.11: Cooling of C_{60} in the high-temperature CBGC cell. (a) The relative populations of the rotational sub-levels exhibit a Boltzmann distribution with $T_{\rm rot} = 150(2)$ K (with a measured cell wall temperature of 135 K). (b) The R(180) transition centered at 1186.2620 cm^{-1} has a line width of 16.0(6) MHz. This is slightly larger than the expected Doppler line width of 12 MHz – possible evidence of collisional broadening.

between the oven and cold cell suggest that the rotational temperatures as low as 100 K might be achievable.)

The absorption peak for the R(180) transition has a measured line width of 16.0(6) MHz, which is representative of the $15-20$ MHz range we observe over the entire vibrational band. This range is somewhat higher than the expected Doppler line width of 12 MHz (assuming that $T_{\rm trans}$ is equal to the measured $T_{\rm rot}$ value). We find it unlikely that the translational temperature could be so much higher than both the rotational and cell wall temperatures. Given the relatively high pressures in the cold cell (> 1 Torr), it is entirely plausible this excess line width is instead due to collisional broadening. Unfortunately, the observed signal-to-noise is insufficient to deconvolve the homogeneous versus inhomogeneous contributions to the line shape.

We conclude this section with a note on the frequency calibration and accuracy of the CE-DFCS spectra. For the 3 μm OPO system, both the FTS and VIPA frequency axes are calibrated by measuring CH_4 transitions whose precise frequencies are readily available [17]. The FTS calibration amounts simply to a uniform scaling of the FFT frequency axis, or equivalently, calibrating the wavelength of the reference cw laser that is copropagating with the MIR light in the interferometer. The VIPA calibration is more complex [27]. The reference CH_4 transitions are used to parameterize the 2D mapping of the comb modes in the camera image. Both the VIPA etalon FSR and effective vertical dispersion are determined in this fashion, and the calibration must be repeated each time the etalon or grating is re-aligned. The CH_4 calibration provides absolute optical frequency accuracy of about 30 MHz. Relative line center frequencies are accurate to within 10 MHz, limited by the f_{rep} scan step size and detection signal-to-noise.

Instead of relying on reference molecules, the frequency comb can also be calibrated by assigning the integer comb mode index and using the fundamental relationship between the comb optical frequencies and the f_{rep} and f_0 frequencies in the RF domain,

$$\nu_n = n \times f_{\text{rep}} + f_0. \tag{2.5}$$

This is the procedure we use for the 8.5 μm DFG comb. In this case, f_0 is simply equal to the AOM shifting frequency, while the f_{rep} value is fixed by the RF phase lock described in Section 2.1.2. A preliminary calibration is performed that takes advantage of absorption lines from trace intracavity H_2O [48]. These measurements provide sufficient accuracy to constrain the integer mode index n, at which point the final absolute optical frequency is determined by Eq. 2.5. The values of f_{rep} and f_0 are ultimately locked to an atomic time standard with a relative frequency offset error below 10^{-12}. The absolute frequencies determined in this fashion are verified by checking N_2O and D_2O line positions [49, 50] obtained in separate measurements. Of course, the actual uncertainty of our measured absorption line centers is dominated not by the absolute frequency calibration, but by the measured line width and signal-to-noise. For the DFG comb experiments, this (1σ) statistical uncertainty is 2.5×10^{-5} cm^{-1} or 0.75 MHz.

Chapter 3

Spectroscopic signatures of unhindered internal rotation in nitromethane

The traditional view of molecular structure is that of a quasi-static arrangement of atoms undergoing small amplitude fluctuations from a fixed reference geometry. This geometry is determined by the equilibrium configuration of the nuclei on the Born-Oppenheimer potential energy surface (PES). The equilibrium geometry is typically at the bottom of a deep, isolated well on the PES, which establishes a physical basis for the quasi-static picture. High resolution spectroscopy provides precise characterization of molecular structure by connecting spectroscopic observables to detailed properties of the PES in the vicinity of the equilibrium geometry.

Non-rigid molecules exhibiting large amplitude nuclear motion break this structural paradigm. They experience a relatively flat or shallow PES along one or more internal degrees of freedom. Even at 0 K, zero-point motion causes significant delocalization of the nuclear wavefunction. Such floppy, anharmonic systems lead to a breakdown of traditional spectroscopic models, posing practical difficulties for the analysis and interpretation of spectra. More fundamentally, they challenge the very notion of static molecular structure. Without the basis of a well defined equilibrium geometry, one is forced to take a step back and view a molecule as an intrinsically dynamic system.

This chapter explores large amplitude motion (LAM) of the unhindered methyl rotor in nitromethane, CH_3NO_2. Section 3.1 introduces the basic rovibrational models for such an internal rotor. We then report the first high resolution spectra of the CH stretch region near 3 μm in Section 3.2, including DC Stark measurements that reveal internal-rotation-induced "intramolecular alignment." The CH stretch vibrations are particularly complex as they couple small amplitude vibrational angular momentum with both total and internal rotation. Section 3.3 presents reduced dimension rovibrational calculations to better understand this intricate network of coupling. These calculations provide a useful, but still qualitative, physical picture of the internal rotation dynamics. Motivated by the lack of accurate and efficient quantitative methods for predicting the rovibrational structure of non-rigid molecules like CH_3NO_2, we have developed an *ab initio* method based on curvilinear vibrational Møller-Plesset perturbation theory [51]. This technique and its successful treatment of CH_3NO_2 are discussed in 3.4. This approach has proved to be a powerful tool for *ab initio* high resolution spectroscopy of non-rigid molecules in general, and we discuss several of its other recent applications later in Chapter 7.

3.1 Internal rotation in CH_3NO_2

Nitromethane contains a $-CH_3$ methyl group centrally bonded to an $-NO_2$ nitro group, making it the simplest organic nitro compound. With seven atoms, nitromethane has fifteen internal degrees of freedom, including fourteen small amplitude vibrations and one internal rotation angle, ρ (see Fig. 3.1a). The MIR frequency comb spectrum probes a subset of the small amplitude vibrations. Before considering these high energy excitations, we first review the structure of the low energy torsional and rotational degrees of freedom.

3.1.1 Pure torsion level structure

The simplest effective Hamiltonian describing the internal rotation, or torsion, motion is

$$H_{\mathrm{t}} = FJ_\rho^2 + V(\rho). \tag{3.1}$$

The kinetic energy term FJ_ρ^2 contains the torsional angular momentum operator $J_\rho = -i\partial_\rho$ and the inverse moment of inertia constant $F = \hbar^2/2I_\rho$. I_ρ is the reduced moment of inertia of the two coupled CH_3 and NO_2 rotors about the internal rotation axis, which is coincident with the principal a axis. Given $I_{\mathrm{CH_3}}/I_{\mathrm{NO_2}} < 0.1$, we expect $I_\rho \approx I_{\mathrm{CH_3}}$, and therefore F to be similar to the B constant of CH_4. Indeed, microwave spectroscopy has measured $F = 5.56\ \mathrm{cm}^{-1}$ [52, 53], while

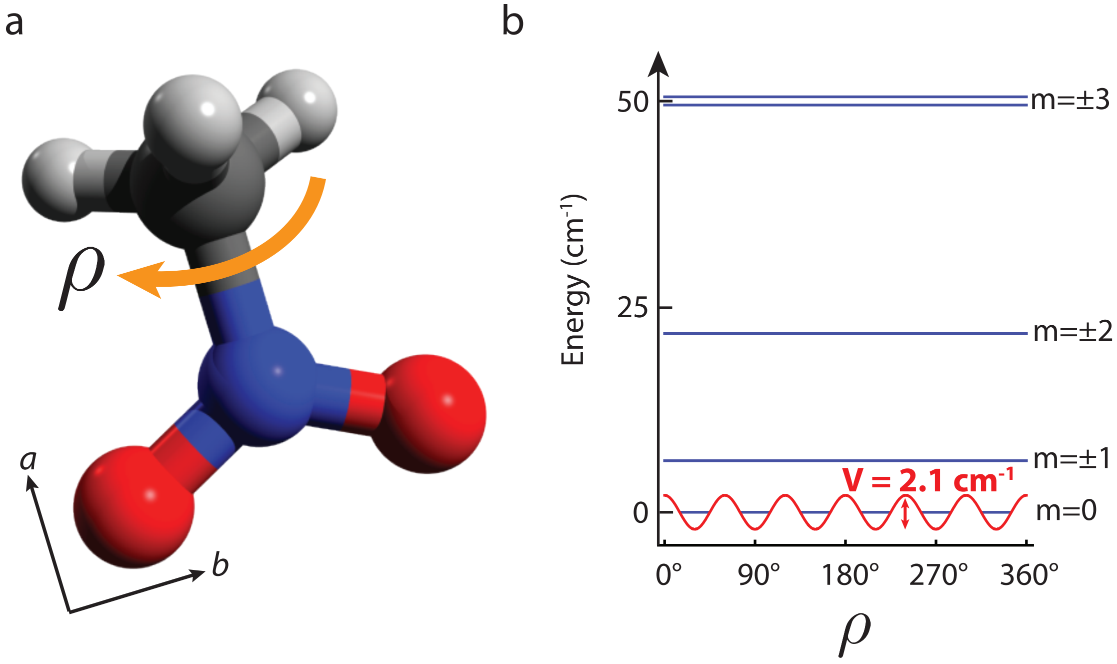

Figure 3.1: Internal rotation in CH_3NO_2. (a) The CH_3 methyl group rotates about the CN bond by the internal rotation angle ρ. The a and b principal axes, which lie in the plane of the CNO_2 frame, are shown. (b) The internal rotation potential energy curve has six-fold symmetry and a small barrier height of about 2 cm^{-1}. The energy levels are described approximately by the particle-on-a-ring expression $E_m = Fm^2$, where $m = 0, \pm 1, \pm 2, \ldots$ is the internal rotation quantum number. The rotor F constant is about 5 cm^{-1}. The degeneracy of the $|m| = 3n$ $(n > 0)$ levels is broken by the six-fold internal rotation barrier.

the B constant of CH_4 is 5.24 cm^{-1} [54].

In the completely unhindered limit, the torsional potential $V(\rho) = 0$. H_t then becomes equivalent to a particle-on-a-ring model containing only the kinetic energy term. Requiring 2π-periodicity in ρ, the eigenfunctions of the J_ρ^2 operator are the simple exponentials,

$$|m\rangle = \sqrt{\frac{1}{2\pi}} e^{im\rho}, \tag{3.2}$$

where the m is the torsion quantum number with $m = 0, \pm 1, \pm 2, \ldots$. The eigenenergies are

$$E_m = Fm^2, \tag{3.3}$$

such that states with $|m| > 0$ are doubly degenerate, reflecting the equivalence of clockwise and counter-clockwise torsion (Fig. 3.1b). In reality, the torsion potential is non-zero. Symmetry considerations [18] require that it have six-fold symmetry in ρ,

$$V(\rho) = \frac{V_6}{2}\cos(6\rho) + \frac{V_{12}}{2}\cos(12\rho) + \ldots, \tag{3.4}$$

where lowest order coefficient V_6 is dominant, and the remaining terms can be ignored. The $\cos(6\rho)$ operator serves to couple torsional levels with $\Delta m = \pm 6$, breaking the degeneracy of $|m| = 3n$ pairs. The $m = \pm 3$ states, in particular, split into non-degenerate $(|m = +3\rangle + |m = -3\rangle)$ and $(|m = +3\rangle - |m = -3\rangle)$ linear combinations separated in energy by $2 \times \langle m = +3|V|m = -3\rangle = V_6/2$. Measurement of this energy difference yields an effective barrier height of $V_6 = 2.10$ cm^{-1} [53]. Except for the $m = \pm 3$ case, the $\Delta m = \pm 6$ energy level differences are large relative to the small V_6 barrier height. Thus, the energy structure still closely resembles a free unhindered rotor, and m remains an approximately good quantum number. Fig. 3.1b shows the V_6 potential to scale with the particle-on-a-ring energy levels.

3.1.2 Rotation-torsion level structure

Rotation of the entire molecular frame leads to a combined rotation-torsion effective Hamiltonian,

$$H = H_{\mathrm{r}} + H_{\mathrm{t}} + H_{\mathrm{rt}}, \tag{3.5}$$

where H_{r} is the asymmetric top rigid rotor Hamiltonian,

$$H_{\mathrm{r}} = AJ_a^2 + BJ_b^2 + CJ_c^2, \tag{3.6}$$

H_{t} is as above, and the rotation-torsion coupling term is

$$H_{\mathrm{rt}} = -2A'J_\rho J_a. \tag{3.7}$$

The A, B, and C constants are equal to the inverse of the effective moments of inertia about the principal a, b, and c axes (see Fig. 3.1a) with one modification: the effective A constant only includes the a-axis moment of inertia of the CNO_2 frame and ignores that of the methyl hydrogen atoms. This arises because the methyl top and the heavy atom frame rotate freely with respect to each other [52, 55]. The rotation-torsion term H_{rt} accounts for Coriolis coupling between the a-axis component of the total angular momentum, J_a, and the torsion angular momentum, J_ρ. The coupling coefficient A' is equal to A in the rigid top limit (i.e. when all vibrations other than the torsion are frozen). In the actual non-rigid case, perturbative contributions from the small amplitude vibrations lead to a small difference between A and A' [53].

A convenient zeroth order basis for describing the combined rotation-torsion motion is a direct product of symmetric top rotational wavefunctions, $|J, k_a\rangle$, and the torsional wavefunctions, $|m\rangle$ (Eq. 3.2). J is the total angular momentum quantum number, and $k_a = -J, \ldots, +J$ is its projection on the body-fixed a axis. The symmetric top rotational factor obeys the usual eigenvalue relations,

$$\mathbf{J}^2|J, k_a\rangle = J(J+1)|J, k_a\rangle, \tag{3.8}$$

$$J_a|J, k_a\rangle = k_a|J, k_a\rangle, \tag{3.9}$$

where $\mathbf{J}^2 = J_a^2 + J_b^2 + J_c^2$. Ignoring the small torsional potential $V(\rho)$, we can rewrite the rotation-torsion Hamiltonian (Eq. 3.5) as

$$H = FJ_\rho^2 - 2A'J_aJ_\rho + \left(A - \frac{B+C}{2}\right)J_a^2 + \frac{B+C}{2}\mathbf{J}^2 + \frac{B-C}{2}\left(J_b^2 - J_c^2\right). \tag{3.10}$$

These five terms are written in order of approximately decreasing magnitude ($F \sim 5$ cm^{-1}, $A', A \sim 0.4$ cm^{-1}, $B \sim 0.35$ cm^{-1}, $C \sim 0.2$ cm^{-1}). The zeroth order rotation-torsion wavefunctions $|J, k_a\rangle|m\rangle$ are eigenfunctions of each term in H except for the last term proportional to $\left(J_b^2 - J_c^2\right)$. If we neglect this so-called *asymmetry term*, then the eigenenergies are

$$E(J, k_a, m) = Fm^2 - 2A'k_am + \left(A - \frac{B+C}{2}\right)k_a^2 + \frac{B+C}{2}J(J+1). \tag{3.11}$$

Note that in this limit there is a two-fold degeneracy between levels with $(k_a, m) \leftrightarrow (-k_a, -m)$.

Torsional levels of a given value of $|m|$ can be treated approximately separately from each other, with each supporting an independent manifold of rotational sub-levels. The ground torsional state, $m = 0$, behaves like a normal asymmetric top (albeit with a larger than expected A constant as discussed above) because the terms involving J_ρ are zero. Its low-J energy patterns are illustrated in Fig. 3.2a. The asymmetry term mixes states with $\Delta k_a = \pm 2$ and splits the two-fold degeneracy for states with $|k_a| > 0$.

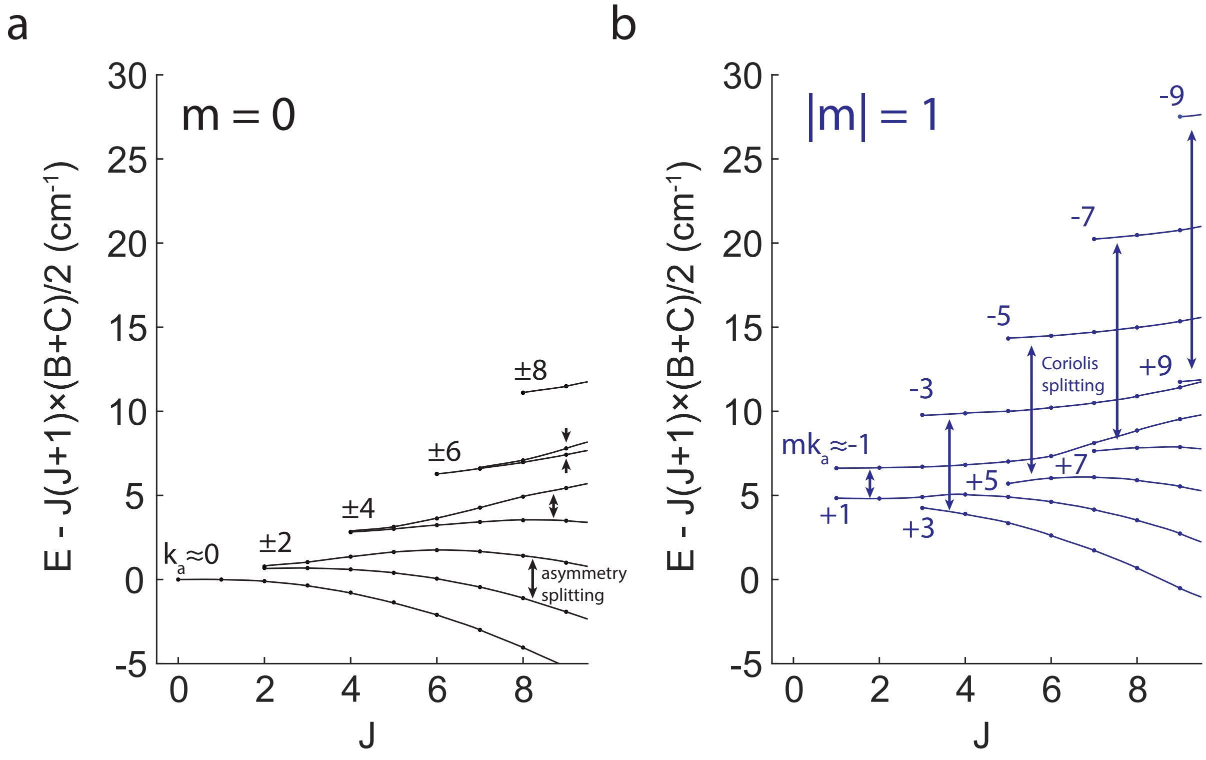

Figure 3.2: Rotational energy levels for the $m = 0, \pm 1$ torsional states. (a) In the $m = 0$ torsional ground state, nitromethane behaves like a normal asymmetric top. For low J values, the energy manifold is organized by the magnitude of the k_a quantum number. The asymmetry term splits the two-fold $\pm k_a$ degeneracy. (For clarity, the figure shows the total energy minus $J(J+1) \times (B+C)/2$.) (b) In the $m = \pm 1$ torsional states, Coriolis coupling organizes the rotational manifold by the product $m \times k_a$. Each energy level here is two-fold degenerate. Spin statistics of the two ^{16}O atoms mandate that only levels with $k_a + m = \mathit{even}$ exist when all small amplitude vibrations are in their ground state. Therefore, in (a) only $|k_a| = 0, 2, 4, \ldots$ states are shown, and in (b) only $|k_a| = 1, 3, 5, \ldots$ states are shown.

Excited torsional states, which have $|m| > 0$, have non-zero torsional angular momentum. Their energies are largely organized by the product of m and k_a because of the Coriolis coupling term $\propto J_a J_\rho$. An example for the $|m| = 1$ manifold is shown in Fig. 3.2b. Here, the asymmetry term does not split the two-fold degeneracy. This qualitative physical difference between the $m = 0$ and $|m| > 0$ manifolds, i.e. that the former is dominated by asymmetry splittings and the latter by

Coriolis splittings, has important effects on fundamental observables such as the lab frame dipole moment. We will examine this effect more closely in Section 3.2.

3.1.3 Symmetry, spin statistics, and selection rules

Characterizing the symmetry properies of the vibration-rotation-torsion states is necessary to predict nuclear spin degeneracy factors and infrared selection rules. Standard point group analysis is inadequate for treating the non-rigid molecules such as nitromethane, and we must use the more general molecular symmetry (MS) group, or Longuet-Higgins group, based on nuclear permutation-inversion operations [18]. Let the three hydrogen nuclei be labeled as H_1, H_2, and H_3, and the two oxygen nuclei as O_4 and O_5. The MS group appropriate for nitromethane is generated by three symmetry operations:

- (123), the cylic permutation of H_1, H_2, and H_3
- $(23)^*$, the permutation of H_2 and H_3, followed by inversion of all coordinates (nuclear and electronic) through a space-fixed origin
- (45), the permutation of O_4 and O_5

The group formed by products of these generators is called G_{12}. (It contains a total of twelve operations.) The group character table can be found in Table A-24 of Ref. [18]. G_{12} is isomorphic to the $\mathcal{D}_{3h}$ point group, and the same labels are used for their irreducible representations (irreps). There are four non-degenerate irreps: A_1', A_1'', A_2', and A_2''. The ${}^1/{}^2$ label gives the character under $(23)^*$ ($+1$ and -1, respectively), while the $'/''$ label gives the character under (45). The two doubly degenerate irreps are E' and E'', which have a similar meaning for the $'/''$ labels.

Using standard group theory procedures [18], one can show that the symmetric top rotational wavefunctions, $|J, k_a\rangle$, with $k_a = \mathit{even}$ span the $A_1' \oplus A_2'$ irreps, while those with $k_a = \mathit{odd}$ span $A_1'' \oplus A_2''$. The symmetries of the torsional wavefunctions are determined by the transformation properties of the torsion angle ρ, which are

$$\begin{aligned} (123)\rho &= \rho - 2\pi/3, \\ (23)^*\rho &= 2\pi - \rho, \\ (45)\rho &= \rho + \pi. \end{aligned} \tag{3.12}$$

The irreps of the $|m\rangle$ wavefunctions, Eq. 3.2, are summarized in Table 3.1. The combined torsion-rotation symmetry species is determined by the direct product of the individual torsion and rotation irreps.

Table 3.1: Symmetry species of torsional wavefunctions of nitromethane in the G_{12} MS group. (n is a non-negative integer.)

$\|m\|$	$\|m\rangle$ irrep.
0	A_1'
$6n \pm 1$	E''
$6n \pm 2$	E'
$6n + 3$	$A_1'' \oplus A_2''$
$6n + 6$	$A_1' \oplus A_2'$

We can now examine the nuclear spin weights of the normal isotopologue $^{12}CH_3{}^{14}N^{16}O_2$. Following section 8.4.1 of Ref. [18], the nuclear spin degeneracy ratios are $1:1:1:0:0:0$ for rovibronic symmetries $A_1' : A_2' : E' : A_1'' : A_2'' : E''$. The exclusion of $''$ species occurs because these are antisymmetric with respect to the (45) operation (permutation of the two ^{16}O nuclei, which are spin-0 bosons). Given that the ground states of the electronic and small amplitude vibrational degrees of freedom are all totally symmetry (A_1'), the net result is that $k_a + m$ must be *even* (see Fig. 3.2). In vibrationally excited states that transform as A_1'', A_2'', or E'', we must have $k_a + m = odd$.

Using a suitable choice of internal coordinates (see section 15.4.2 of Ref. [18]), the fourteen small amplitude vibrations have symmetry species

$$\Gamma_{\text{vib}} = 5A_1' \oplus 5A_1'' \oplus 4A_2''. \tag{3.13}$$

Each of these three irreps is IR active. A_1', A_1'', and A_2'' modes have a-, b-, and c-type rotational selection rules, respectively, as well as a strong $\Delta m = 0$ selection rule. A summary of the small amplitude vibrational modes is provided in Table 3.2. The infrared spectra of the ν_2, ν_6, and ν_7 bands have been previously studied at high resolution [56–60].

Table 3.2: Small amplitude vibrations of nitromethane. The mode labeling follows the convention of Ref. [18].

Mode	Description	Symmetry	Frequency (cm^{-1})
ν_1	Sym. CH stretch	A_1'	2974^a
ν_2	CN stretch	A_1'	918^a
ν_3	Sym. NO stretch	A_1'	1397^a
ν_4	Sym. CNO bend	A_1'	657^a
ν_5	Sym. NCH bend	A_1'	1380^a
ν_6	Asym. NO stretch	A_1''	1584^a
ν_7	In-plane NO$_2$ rock	A_1''	475^a
ν_9	Out-of-plane NO$_2$ wag	A_2''	605^a
$\nu_{10i,o}$	In-plane and out-of-plane CH stretches	$A_1'' \oplus A_2''$	$3042, 3076^b$
$\nu_{11i,o}$	In-plane and out-of-plane HCH bends	$A_1'' \oplus A_2''$	$1100, 1131^c$
$\nu_{12i,o}$	In-plane and out-of-plane NCH bends	$A_1'' \oplus A_2''$	1423^c

[a] Ref. [61]
[b] Ref. [62]
[c] Ref. [63]

3.2 High resolution spectra of CH_3NO_2 in the 3.3 μm region

3.2.1 Experimental setup and survey spectrum

We acquired CE-DFCS absorption spectra of nitromethane using the MIR OPO comb with FTS and VIPA detection (see Sections 2.1.1, 2.4.1, and 2.4.2). Cold gas-phase nitromethane samples were prepared with the low-temperature CBGC refrigerator, which provided rotational and translational temperatures of 11(1) K and 16(1) K, respectively (Fig. 2.10c,d). Two copper electrodes were installed in the cold cell for Stark effect measurements (Fig. 3.3) with DC electric fields up to 400 V/cm parallel to the cavity axis.

Figure 3.4 shows a 150-cm^{-1} wide survey spectrum of nitromethane from 2940 cm^{-1} to 3090 cm^{-1} (3.2 μm to 3.4 μm). This region is dominated by the strong $\nu_3 + \nu_6$ combination band near 2950 cm^{-1}. The symmetric CH stretching mode occurs near 2975 cm^{-1}, while the

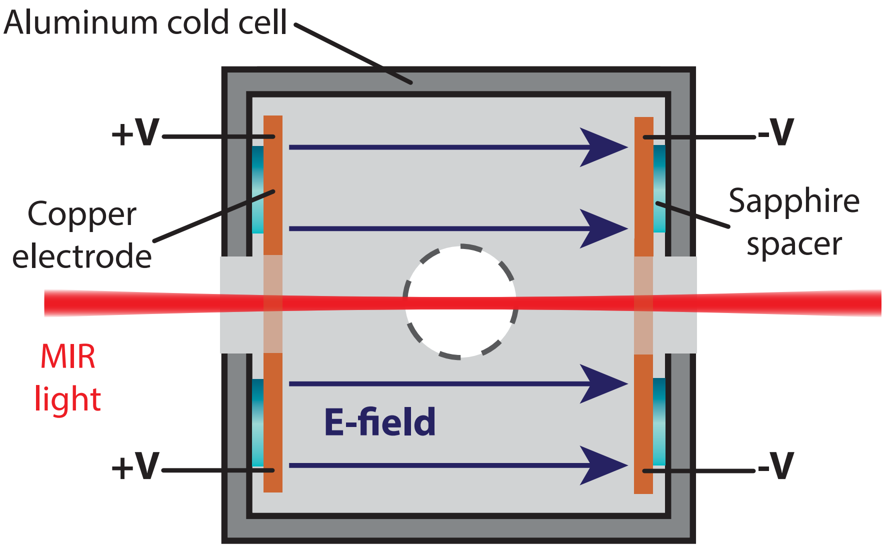

Figure 3.3: DC electrode geometry in the cold cell. A copper electrode is placed on each of the two cold cell walls perpendicular to the cavity axis. Sapphire discs electrically insulate the electrodes from the cell wall. A thin piece of indium is placed on either side of each sapphire disc to improve the thermal contact. Ceramic screws (not shown) are used to mount the electrodes, which generate a DC electric field up to 400 V/cm parallel to the cavity axis. The apertures in the electrode plates (ca. 1 cm diameter) and the finite extent of the plates themselves lead to a $\sim$ 10% field non-uniformity along the cavity axis.

two components of the asymmetric CH stretching mode, out-of-plane and in-plane, appear near 3055 cm^{-1} and 3085 cm^{-1}, respectively. Even at low rotational temperatures, this region contains thousands of individual rovibrational transitions above the noise baseline. The following sections discuss each vibrational band in more detail.

3.2.2 The $\nu_3 + \nu_6$ combination band

The $\nu_3 + \nu_6$ combination band involves simultaneous excitation of the symmetric and antisymmetric NO stretching modes. The excited state has A_1'' vibrational symmetry leading to b-type transitions with $\Delta K_a = \pm 1, \pm 3, \cdots$, $\Delta K_c = \pm 1, \pm 3, \cdots$, and $\Delta m = 0$ rotation-torsion selection rules. Using ground state combination differences derived from microwave data [52, 55], we have assigned several hundred transitions with $|m| \leq 1$. A full line list is included in Appendix A.

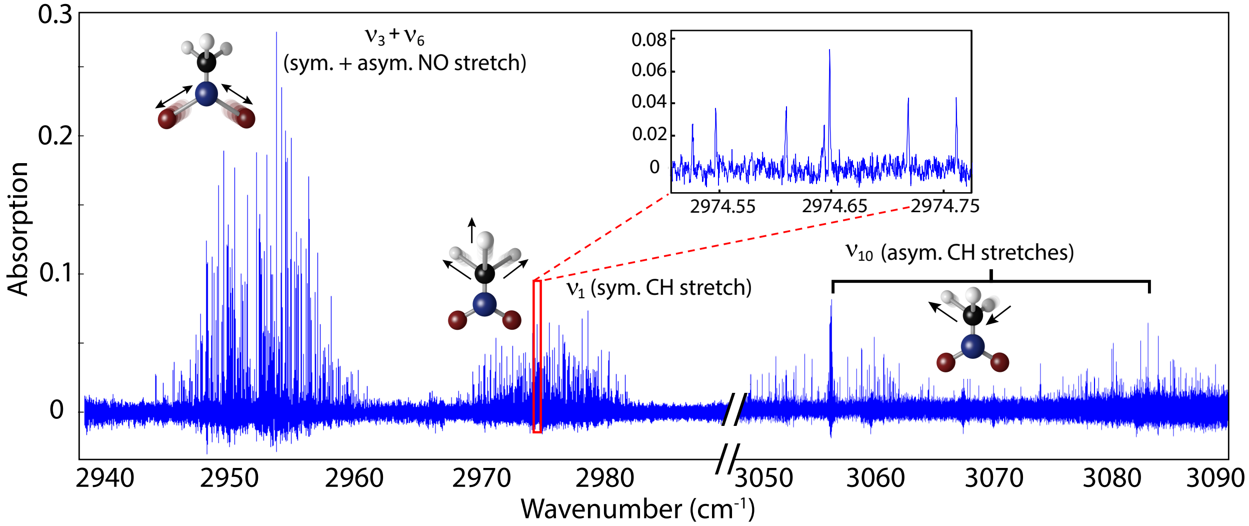

Figure 3.4: Absorption spectrum of nitromethane near 3.3 μm. This region is includes the $\nu_3 + \nu_6$ (sym. NO + asym. NO stretch) combination band as well as the ν_1 (sym. CH stretch) and ν_{10} (in-plane and out-of-plane asym. CH stretch) fundamental transitions. The inset shows well resolved rotational fine structure of a small portion of the ν_1 band.

The $m = 0$ transitions are the simplest to analyze as the associated energy levels are structured like a semi-rigid asymmetric top. Upper state term values (energies) were calculated using the measured transition frequencies and lower state rotation-torsion energies derived from previous studies [52,55]. A reduced term value plot is shown in Fig. 3.5, where a number of perturbations can be observed. For the $J_{K_aK_c} = 3_{13}$, 3_{12}, 4_{13}, 5_{14}, and 6_{16} states, the transition is split into a doublet, with two components of similar IR intensity. This indicates that there is complete mixing of each zeroth order bright state with a perturbing dark state. The magnitudes of the splittings range from 0.14 cm^{-1} to 0.18 cm^{-1}, which correspond to the value of the interaction matrix element. Given the high density of background dark states in this region of the spectrum, it is difficult to identify the character of the perturbing dark state.

Excluding the perturbed doublets, the remaining upper state term values were fitted to the

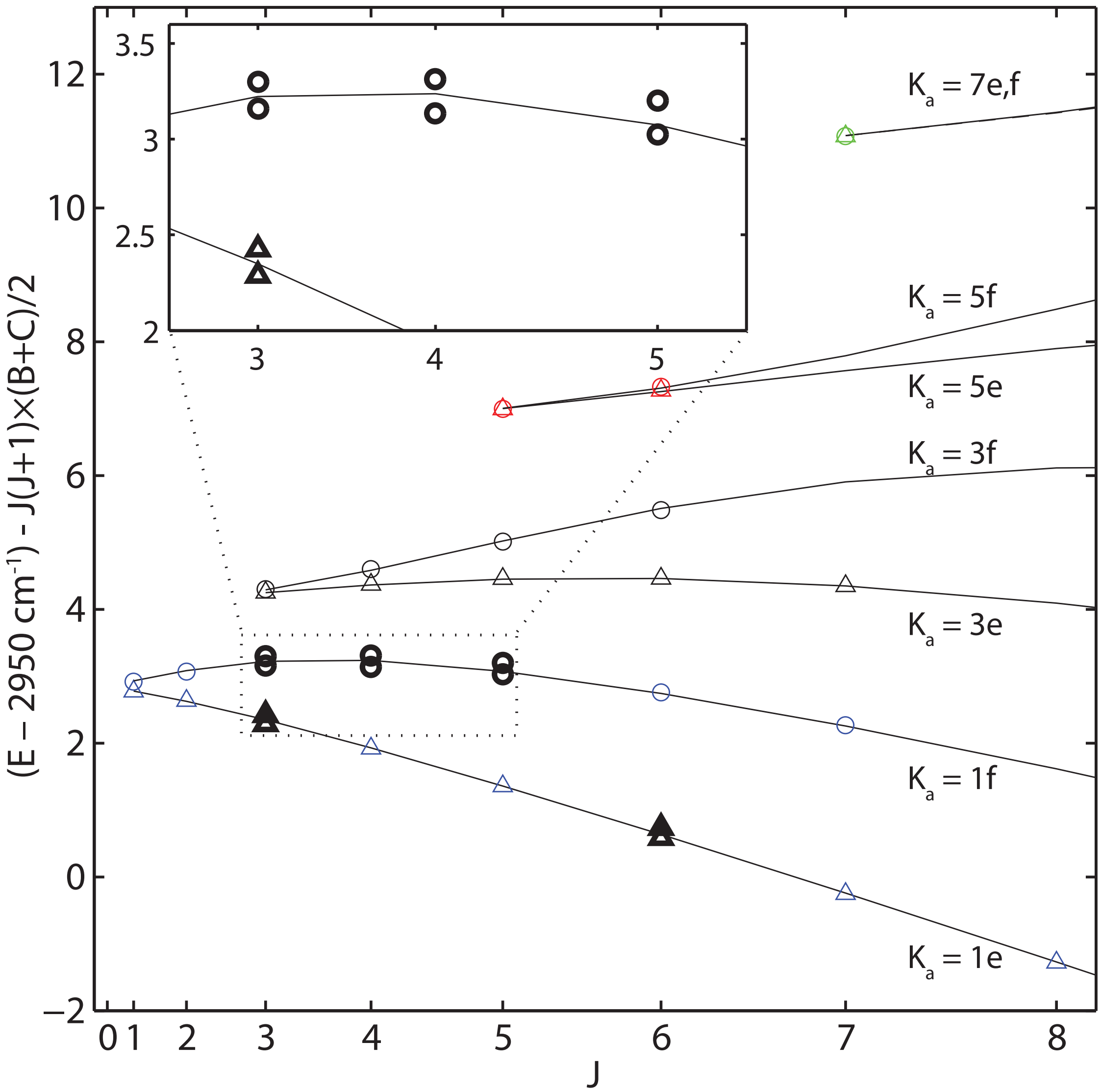

Figure 3.5: Reduced term values of the $m = 0$ states of $\nu_3 + \nu_6$. The quantity $J(J+1) \times \frac{B+C}{2}$ is subtracted from the absolute energy for clearer plotting. States of a given value of $K_a = |k_a|$ are connected with solid lines, which represent the eigenvalues of the fitted effective Hamiltonian, Eq. 3.14. Due to ^{16}O spin statistics, only $K_a = odd$ levels exist in the A_1'' vibrationally excited state. The e/f labels indicate the parity of each state. ($e(f)$ for levels that are $+(-)$ parity for $J = even$.) Black bold markers indicate perturbed states. (Inset) Symmetric doublets appear due to strong mixing of a zeroth order bright state with a perturbing dark state.

standard Watson A-reduced Hamiltonian (I^r representation) [64]:

$$\hat{H} = \nu_0 + AJ_a^2 + \frac{B+C}{2}\left(\mathbf{J}^2 - J_a^2\right) + \frac{B-C}{4}\left(J_+^2 + J_-^2\right) - \Delta_J \mathbf{J}^4 - \Delta_{JK}\mathbf{J}^2 J_a^2 - \Delta_K J_a^4 - \frac{1}{2}\left[\delta_J \mathbf{J}^2 + \delta_K J_a^2, J_+^2 + J_-^2\right]_+, \tag{3.14}$$

where $J_\pm = J_b \pm iJ_c$ and $[\cdots, \cdots]_+$ is an anti-commutator. This $m = 0$ Hamiltonian contains the non-torsion-dependent terms of the full torsion-rotation Hamiltonian, Eq. 3.10, along with the usual quartic centrifugal distortion terms [64]. The results of the least-squares fit for this Hamiltonian are shown in Table 3.3, with the corresponding energy eigenvalues shown as solid curves in Fig. 3.5. Due to the relatively low J values ($J \leq 8$) accessed in the cold spectrum, only the principal rotational constants (A, B, C) were fitted, with the quartic centrifugal distortion constants held fixed to their ground state values. Table 3.3 lists the rotational constants for the ground state [55] and ν_6 fundamental [58] for comparison with the $\nu_3 + \nu_6$ values measured in this work. The fit error for the $\nu_3 + \nu_6$ band is about 5× worse than for the ν_6 fundamental, suggestive of residual perturbations. There is a significant negative shift of the A, B, and C constants of $\nu_3 + \nu_6$ relative to both the ground state and the ν_6 fundamental. This effect can also be quantified by the inertial defect $\Delta_i = I_c - I_a - I_b$, where I_α is the effective moment of inertia about the $\alpha = a, b, c$ principal axis. Δ_i changes from $+0.203$ uÅ^2 in the ground state to -0.330 uÅ^2 in the $\nu_3 + \nu_6$ level. Such a large negative shift is consistent with an increase in the effective torsional barrier [65], as the methyl group becomes "locked-in" with respect to the C–NO$_2$ plane.

Table 3.3: Effective Hamiltonian fit for $m = 0$ levels of $\nu_3 + \nu_6$. All parameters are given in cm^{-1}. Those in brackets $[\cdots]$ are held fixed to their ground state values. RMSE is the root-mean-square fit residual. The inertial defect, $\Delta_i = I_c - I_a - I_b$, is given in uÅ^2.

Parameter	Ground state^a	$\nu_3 + \nu_6{}^b$	$\nu_6{}^c$
ν_0	0	2952.6854(45)	1583.81163(20)
A	0.445037	0.43990(18)	0.4449620(33)
B	0.351722	0.34772(30)	0.3516825(26)
C	0.195994	0.19495(14)	0.1960255(9)
$\Delta_J \times 10^6$	0.2048	[0.2048]	0.2431(23)
$\Delta_{JK} \times 10^6$	0.5921	[0.5921]	0.6822(103)
$\Delta_K \times 10^6$	−0.2515	[−0.2515]	−1.5701(93)
$\delta_J \times 10^6$	0.08229	[0.08229]	0.0717(11)
$\delta_K \times 10^6$	0.52536	[0.52536]	0.4573(34)
RMSE	—	0.0110	0.0023
Δ_i	+0.203	−0.330	+0.177

^{a} Ref. [55]
^{b} This work
^{c} Ref. [58]

We identified several $|m| = 1$ transitions in addition to those with $m = 0$. These assignments were facilitated by observation of their characteristic DC Stark effects. Fig. 3.6 shows an example of the different patterns for $m = 0$ vs. $m = \pm 1$ states. In the $m = 0$ case, the states involved are non-degenerate and have a vanishing dipole expectation value, $\langle \hat{\vec{\mu}} \rangle = 0$. Their DC Stark shifts rely on dipole coupling to other non-degenerate states, leading to a quadratic effect. The $m = \pm 1$ states are doubly degenerate, and each pair can be chosen to have non-zero $\langle \hat{\vec{\mu}} \rangle$ of opposite sign, leading to a linear effect that splits each transition symmetrically into two components.

This effect can be understood in detail by considering the relative sizes of the asymmetry term $\propto (J_b^2 - J_c^2)$ and the Coriolis coupling term $\propto J_a J_\rho$ in the rotation-torsion Hamiltonian, Eq. 3.10, for different rotation-torsion states. Consider, for example, the six rotation-torsion basis states $|m, k\rangle$ for $m = 0, \pm 1$ and $k = \pm 1$, which we abbreviate as $|0, +\rangle$, $|+, +\rangle$, $|-, +\rangle$, etc. Neglecting both the asymmetry term and the Coriolis coupling term, these states separate into two groups according to the value of $|m|$: a doubly degenerate set for $m = 0$ and a quadruply degenerate set for $m = \pm 1$ (Fig. 3.6c). The Coriolis term, $-2A' J_a J_\rho$, splits the $m = \pm 1$ quartet into two degenerate pairs according to the relative sign of m and k_a: $|+, -\rangle$ with $|-, +\rangle$ and $|+, +\rangle$ with $|-, -\rangle$. It has no effect on the $m = 0$ pair because the eigenvalue of J_ρ is zero. On the other hand, the asymmetry term, $\frac{B-C}{2}(J_b^2 - J_c^2)$, has a $\Delta k_a = \pm 2$ selection rule and mixes states with $k_a = +1 \leftrightarrow -1$ leading to non-degenerate linear combinations $\frac{1}{\sqrt{2}}(|m, +\rangle + |m, -\rangle)$ and $\frac{1}{\sqrt{2}}(|m, +\rangle - |m, -\rangle)$ for each value of m.

In the total Hamiltonian, competition between the Coriolis and asymmetry terms leads to the different character of the $m = 0$ and $m = \pm 1$ eigenstates. For $m = 0$, the Coriolis term is "turned off," so the final eigenstates have the asymmetry doublet structure with equal mixtures of $k_a = +1$ and $k_a = -1$ character. For $m = 1$, both Coriolis and asymmetry effects are present, but the former is dominant. ($2A'$ is an order of magnitude larger than $(B - C)/2$.) The $m = \pm 1$ eigenstates therefore have largely pure k_a character of either $+1$ or -1. The Stark effect operator $\hat{\vec{\mu}} \cdot \vec{E}$ has matrix elements (for $\Delta J = 0$) of the form $\langle m', k_a' | \hat{\vec{\mu}} \cdot \vec{E} | m, k_a \rangle \propto \mu_a k_a \delta_{k_a k_a'} \delta_{mm'}$ [66], where μ_a is the permanent body-frame a-axis dipole moment. The diagonal matrix element of

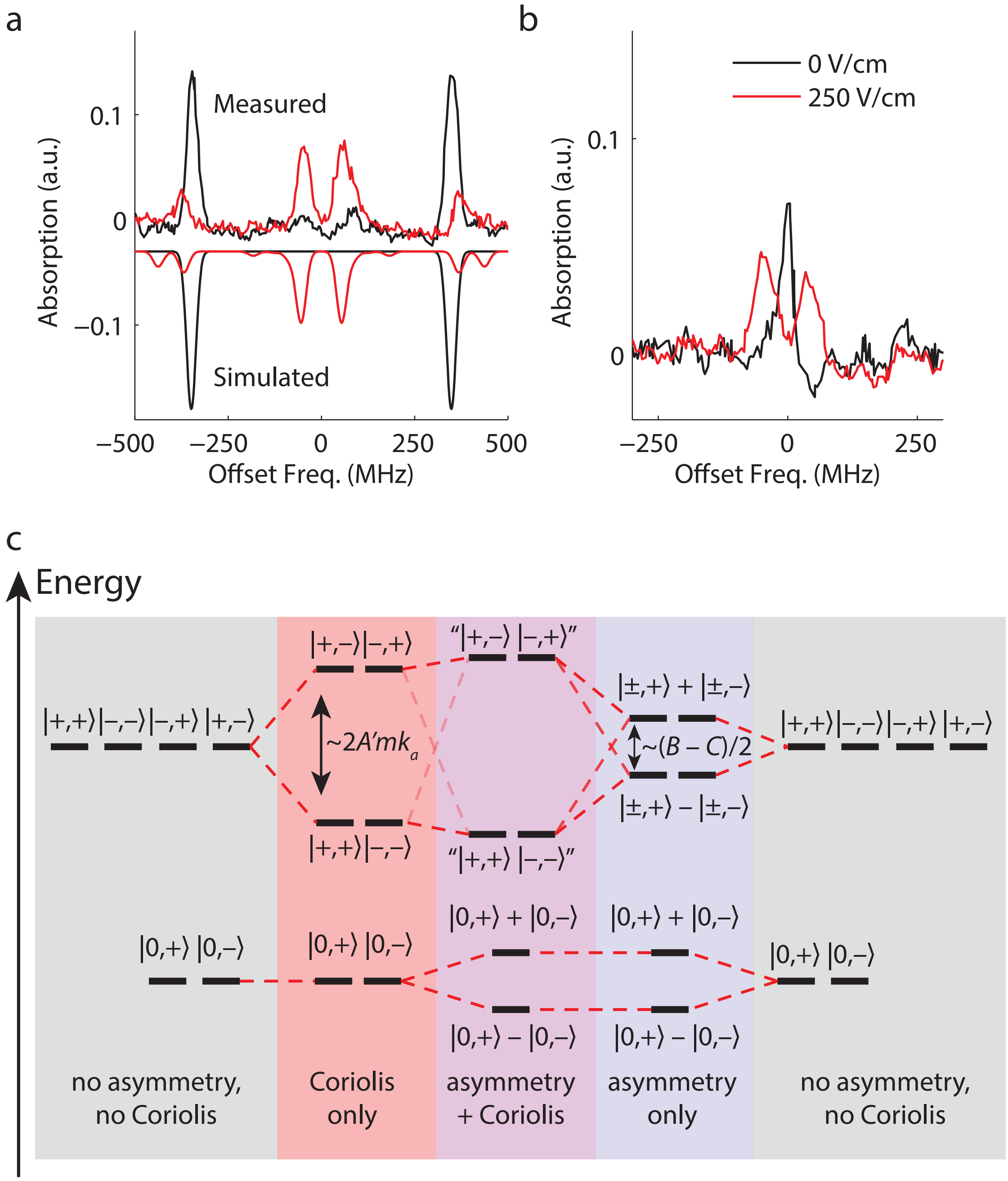

Figure 3.6: DC Stark effect patterns in nitromethane. (a) The $J_{K_a} = 5_5 \leftarrow 4_4$ $(m = 0)$ parity doublet transitions in zero field (black) and 250 V/cm (red). The simulated spectrum is based on the experimental effective Hamiltonians and a permanent body-frame dipole moment of $\mu_a = 3.46$ Debye [66]. (b) The $J_\tau = 2_1 \leftarrow 3_1$ $(m = 1)$ transition splits symmetrically and linearly under an applied field. (c) Competition between Coriolis coupling and asymmetry splitting leads to different DC Stark effects for $m = 0$ and $m = \pm 1$ torsion-rotation states, $|m, k_a\rangle$. See text for details.

the asymmetry doublet states for $m = 0$ have contributions that cancel exactly, leading to zero first-order effect. The diagonal matrix elements of the Coriolis-split states for $m = \pm 1$ are non-zero, leading to a linear DC Stark shift.

The essential physics is that Coriolis coupling between the internal torsion motion and the total-body rotation leads to an internal alignment of angular momentum in the body-fixed frame, analogous to rotational motion of a symmetric top. In the absence of Coriolis coupling, the asymmetry term quenches this alignment, as in any ordinary semi-rigid asymmetric top. This is an example of the unique effects associated with large amplitude motion in polyatomic molecules.

The number of observed $|m| = 1$ transitions is too small to perform a complete rotational fit due to the cold experimental temperatures. The subset of observed levels, however, already indicates there is significant disruption of the rotation-torsion structure in the excited $\nu_3 + \nu_6$ state compared to the ground state. For example, Fig. 3.7 compares the observed $m = 0$ and $|m| = 1$ upper state energies with calculated predictions based on the ground state rotation-torsion parameters, including the kinetic energy parameter F, the Coriolis coupling constant A', and the six-fold torsion barrier height V_6. The $m = 0$ levels are the same as in Fig. 3.5 and show good agreement with the empirical effective Hamiltonian. This is not the case for the observed $|m| = 1$ levels, which all belong to the $mk_a \approx +2$ branch. These energies exhibit a downward shift relative to the predictions, with an average difference of about 0.7 cm^{-1} for the higher J values. This is evidence of one of several possibilities in the excited vibrational state: (i) it has a higher barrier to internal rotation, which lowers all $|m| = 1$ energies; (ii) it has a significantly larger Coriolis constant A', which pushes $\pm mk_a$ branches further apart; or (iii) there is some interloping dark state repelling the observed states downward. Reduced dimension torsion-rotation calculations, discussed below in Sec. 3.3, providing compelling quantitative evidence for case (i).

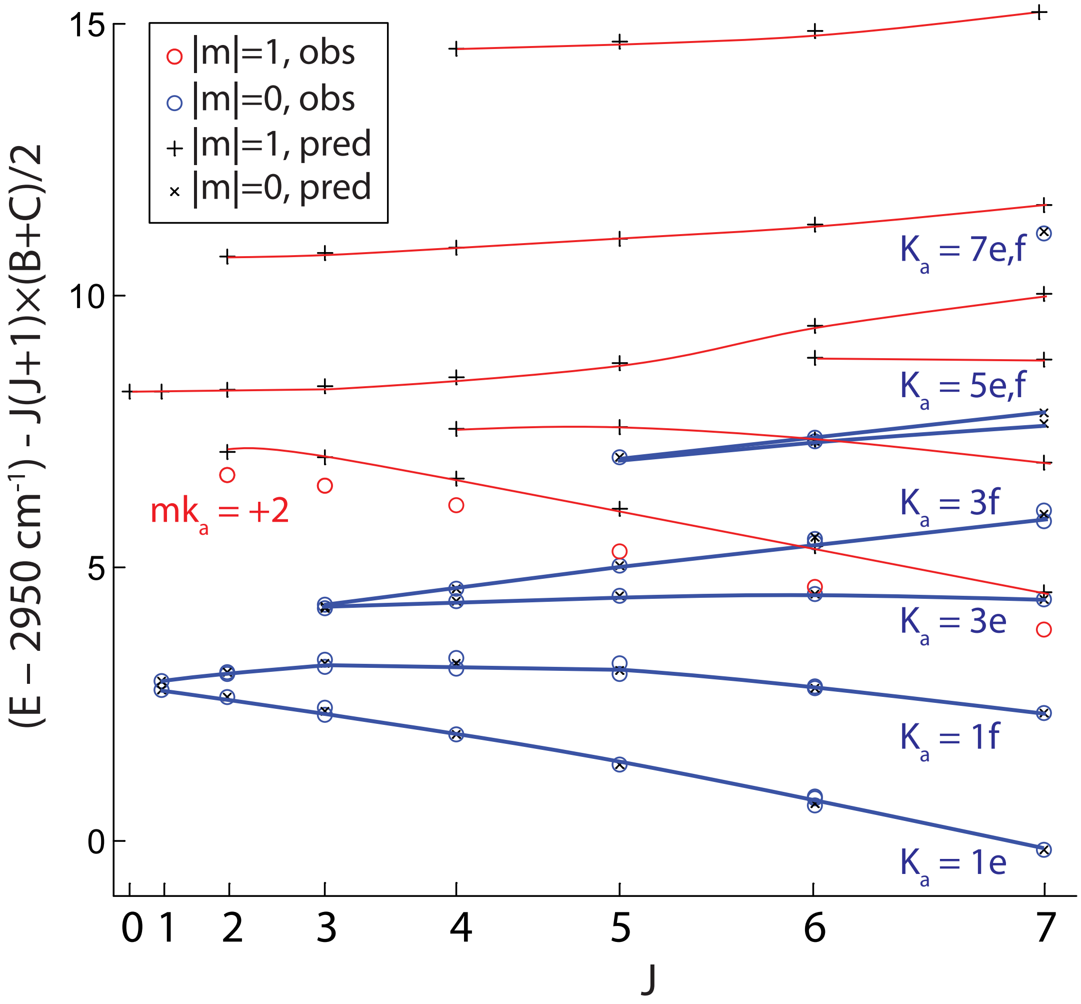

Figure 3.7: Observed and predicted energies for the $m = 0, \pm1$ levels of the $\nu_3 + \nu_6$ vibrational state. The measured $m = 0$ levels (blue ○) are shown for $K_a(= |k_a|) \leq 7$, as in Fig. 3.5. The measured $|m| = 1$ levels (red ○) are shown only for the nominal $mk_a = +2$ branch. All predicted $m = 0$ (black ×) and $|m| = 1$ (black +) energies are shown up to $J = 7$. (Note that the $\nu_3 + \nu_6$ state has A_1'' vibrational symmetry such that only $m + k_a = odd$ levels have non-zero nuclear spin weight.) The observed $|m| = 1$ levels show a substantial discrepancy with the predictions calculated using ground state rotation-torsion parameters.

3.2.3 CH stretching modes

All three CH stretching modes of CH_3NO_2 are IR active. The totally symmetric A_1' mode ν_1 is the strongest and has the lowest frequency, with a band origin near 2975 cm^{-1}. The two asymmetric modes are the out-of-plane component ν_{10o} near 3055 cm^{-1} and the in-plane component ν_{10i} near 3085 cm^{-1}. The identification of out-of-plane vs. in-plane can be made by the spectroscopic signatures of the two resulting vibrational symmetries [62]. The out-of-plane mode has A_2'' symmetry and therefore c-type rotational selection rules, resulting in dense Q-branch transitions near the band origin (clearly visible in the survey spectrum, Fig. 3.4). The in-plane mode has A_1'' symmetry with b-type rotational selection rules and lacks such a strong Q-branch feature.

In total, we have identified nearly a thousand individual rovibrational transitions in the three bands. Less than 10% of these, however, have been successfully rotationally assigned via ground state combination differences. Complex zeroth order structure and seemingly widespread perturbations are reponsible for this low fraction of assignments, line lists for which are provided in Tables A.3–A.4 (see Appendices).

For the ν_1 band, we identified P and R branches accessing the upper state $K_a' = 0e$ manifold and P, Q, and R branches accessing the $K_a' = 2f$ manifold (Fig. 3.8). These transitions provide sufficient data to fit the band origin and the rotational constants A and $(B+C)$ for the ν_1 state (for $m = 0$). The results of this fit are summarized in Table 3.4. There is a substantial (6%) decrease in the effective A parameter. As with $\nu_3 + \nu_6$, this may be evidence of a corresponding increase in the effective torsional barrier height. However, given that only two K_a' manifolds are being fitted to, it is unclear how significant this value is. Moreover, the relatively high fit residuals (RMSE $= 0.066$ cm^{-1}) suggest there are important interactions unaccounted for, likely involving $|m| > 0$ states. Although the DC Stark spectra have revealed many $|m| > 0$ transitions, their assignment has thus far remained elusive.

The $m = 0$ transitions of the out-of-plane CH stretch band ν_{10o} proved easier to assign than those for ν_1. Upper state energies were obtained for $K_a' \leq 5$ (both parity components) and

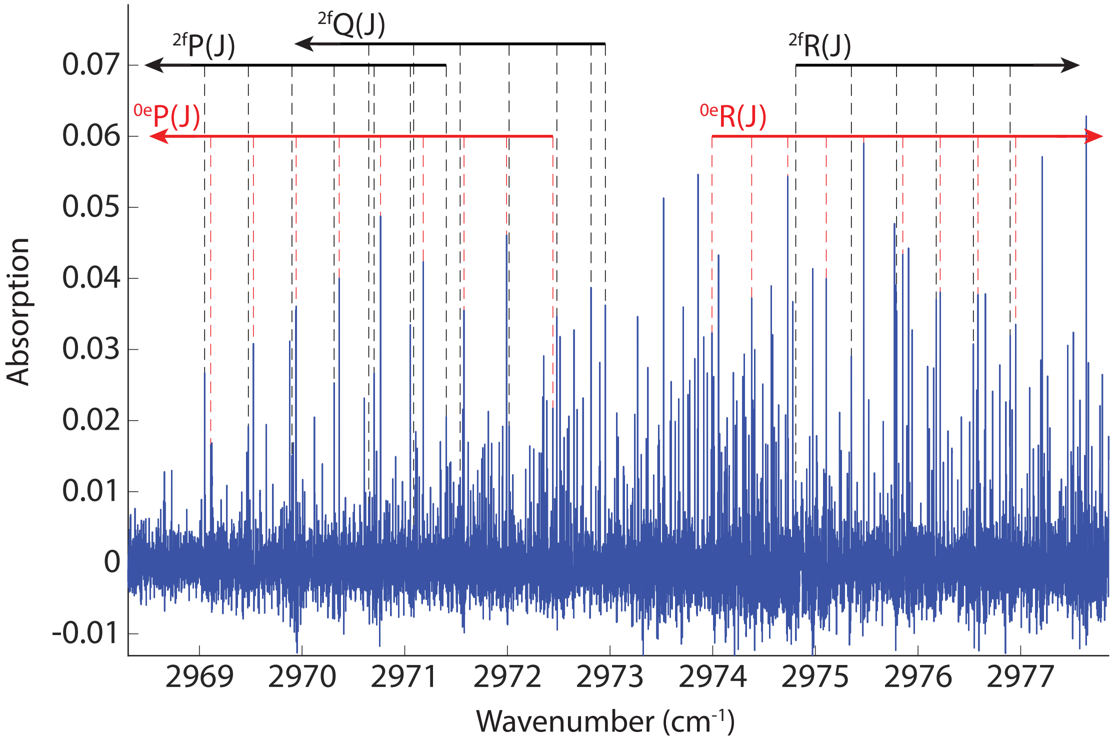

Figure 3.8: Assigned transitions of the ν_1 $(m = 0)$ band of CH_3NO_2. The P/Q/R branches are labeled with tie lines, where the superscript denotes the upper state K_a quantum number and the usual e/f parity label. (All transitions follow an a-type $\Delta K_a = 0$ selection rule.)

Table 3.4: Rotational parameters of the ν_1 and ν_{10o} $(m = 0)$ bands of CH_3NO_2. All values are given in cm^{-1}. The difference $B - C$ was constrained to the corresponding ground state value for the ν_1 fit. Quartic centrifugal distortion terms were included for all states, but held fixed to their ground state values (see Table 3.3).

Parameter	Ground state[a]	ν_1[b]	ν_{10o}[b]
ν_0	0	2973.35(3)	3053.08(2)
A	0.445037	0.4187(71)	0.4602(19)
B	0.351722	0.3521(7)	0.3520(17)
C	0.195994	0.1963(7)	0.1944(13)
RMSE	—	0.066	0.055

[a] Ref. [55]
[b] This work.

$J' \leq 6$, permitting a fit of all three effective rotational constants (Table 3.4). The fit residuals for this state are large (RMSE $= 0.055$ cm^{-1}) and similar to those of ν_1. As above, this suggests that certain interactions are unaccounted for in the effective Hamiltonian. For the ν_{10} modes, in particular, torsionally mediated interactions are expected to be important because the torsion motion transforms the in-plane and out-of-plane coordinates into each other, resulting in strong Coriolis-like coupling [62, 65].

The in-plane CH stretch band ν_{10i} exhibits the most complicated spectrum of all those considered in this chapter. Using ground state combination differences, we have assigned transitions to several $m = 0$ upper states. The resulting upper state energies, however, bear little resemblance to the expected rigid asymmetric top zeroth order structure and no attempt at fitting them has been successful. We speculate that the rotation-torsion structure here is even more severely perturbed by torsion-vibration interactions than for the lower-energy out-of-plane band. This is because the in-plane component is near-resonant with $|m| > 0$ states (and excited rotational states) of the out-of-plane component, leading to a severe reorganization of the zeroth order structure. We examine these dynamics further with model calculations in the next section.

3.3 Reduced-dimension calculations of the rotation-torsion structure and CH stretching vibrations

Under the Born-Oppenheimer approximation, rotation-vibration energies correspond to the eigenvalues of the nuclear motion Hamiltonian H_{nuc}. Calculating the eigenvalues (and eigenfunctions) of H_{nuc} is a highly non-trivial task as the computational expense in general grows exponentially with the number of degrees of freedom. One way to address this problem is to consider a simpler, reduced-dimension Hamiltonian H_{red} obtained by "freezing" a subset of degrees of freedom, i.e. constraining certain nuclear coordinates to fixed values. The spectrum of H_{red} can be computed efficiently and accurately at the cost of approximating the dynamics of the full molecular system. For cases in which the active and constrained degrees of freedom are approximately separable, reduced dimension approaches are a useful means for understanding zeroth order nuclear motion dynamics. In this section, we take advantage of reduced-dimension models to interpret the observed spectroscopic signatures of internal rotation and CH stretching vibrational dynamics in CH_3NO_2.

3.3.1 Method overview

The first step of a reduced-dimension calculation is to construct the appropriate Hamiltonian,

$$H_{\text{red}} = T + V(\mathbf{q}), \tag{3.15}$$

where T is the reduced-dimension kinetic energy operator (KEO) and $V(\mathbf{q})$ is the nuclear potential energy surface (PES). We defer a detailed discussion of calculating the KEO for Chapter 7. For now, we simply assert that we can obtain a numerically exact KEO for arbitrary reduced-dimension models with general curvilinear coordinates including all vibration, rotation, and Coriolis contributions. The PES $V(\mathbf{q})$ is a scalar function of the coordinates included in the reduced-dimension calculation. It can be obtained by fitting a surface to a set of energies obtained by a some electronic structure method or by constructing a simple model potential.

Once H_{red} is specified, its eigenvalues and eigenfunctions are computed variationally by diagonalizing its matrix representation in a suitably large basis set. We accomplish this with large-scale iterative eigensolver methods [67] in combination with direct-product grid discrete variable representation basis sets [68]. Again, the details of these methods can be found in Chapter 7. For the problem sizes considered here, these techniques provide numerically exact energies and wavefunctions for the H_{red} models of interest.

3.3.2 Effect of the torsion barrier height on torsion-rotation energies

The rotational analysis of the $\nu_3 + \nu_6$ combination band (Section 3.2.2) revealed two related facts. First, the effective A constant of the excited vibrational state is 1.2% smaller than that of the ground state (a relatively large shift). Second, the $(|m| = 1) - (m = 0)$ energy difference in the excited vibrational state is about 0.7 cm^{-1} smaller than in the ground state. Both of these effects can be explained by an increase in the effective torsional barrier height in the excited vibrational state. Are the effective barrier heights inferred from these shifts mutually consistent? Reduced-dimension calculations can help us answer this question.

We consider a (1+3)-dimensional model that includes the torsion angle ρ (see Fig. 3.1) and the three body-frame rotations. The remaining fourteen small amplitude internal coordinates are held fixed to their (ρ-averaged) equilibrium values. The PES $V(\rho)$ is only dependent on the torsion angle ρ and is represented with a single six-fold term (see discussion above):

$$V(\rho) = \frac{V_6}{2}\cos(6\rho), \tag{3.16}$$

where V_6 is the internal rotation barrier height. For a given value of V_6, we calculate the reduced-dimension torsion-rotation energies and extract the lowest torsion excitation energy $E(1-0)$ and the effective rotational A constant. Figure 3.9 shows the barrier height dependence of these two observables from a series of such calculations. The plots are normalized to their free internal rotation limit ($V_6 = 0$). Each curve shows a similar sigmoidal transition. The torsion excitation energy $E(1-0)$ starts at the free value determined by the torsion F constant (5.6 cm^{-1}) and becomes exponentially small as the rotor moves into the high-barrier tunneling limit. The effective rotational A constant starts as the inverse moment of inertia of the NO_2 frame and changes to that of the entire CH_3NO_2 molecule as the torsion becomes locked in the high-barrier limit. The ratio of these two moments of inertias is equal to the limiting value of $A/A_{\text{free}} \approx 0.92$. The turnover of both curves occurs when the barrier height becomes equal to the energy difference between the $m = 0$ ground state and the $m = \pm 6$ excited states, which are the first that the six-fold potential can couple to the $m = 0$ state. Thus, we expect the turnover at $V_6 \sim F \times 6^2 \approx 200$ cm^{-1}.

The two barrier-dependence curves allow us to correlate changes in the torsional excitation energy with changes in the rotational A constant. In the ground vibrational state, the effective V_6 parameter equals 2.10 cm^{-1} [53], such that the torsion energy and A are approximately equal to their free-rotor-limit values. In the excited $\nu_3 + \nu_6$ vibrational state, A decreases to a relative value of

$$\frac{A_{\nu_3+\nu_6}}{A_{\text{free}}} \approx \frac{A_{\nu_3+\nu_6}}{A_0} = \frac{0.43990\ \text{cm}^{-1}}{0.44504\ \text{cm}^{-1}} \approx 0.988$$

(see Table 3.3). This value is marked as a horizontal dashed line in the bottom plot of Fig. 3.9. The corresponding effective barrier height is $V_6 \approx 117$ cm^{-1}, marked as vertical dashed line in

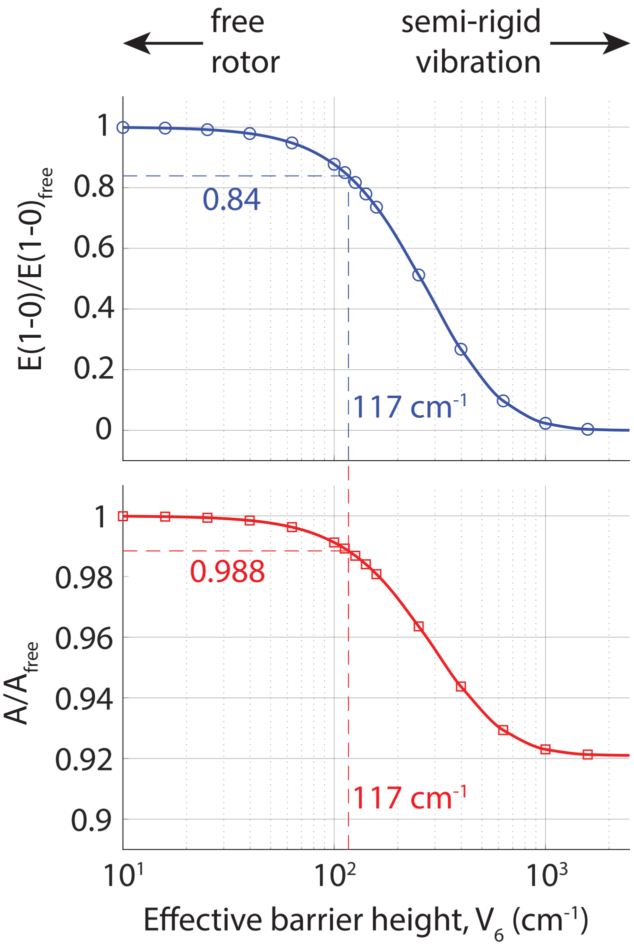

Figure 3.9: Torsion excitation energy and rotational A constant as a function of the effective barrier height V_6. The dependence of each observable is shown normalized to its value in the free rotor limit ($V_6 = 0$). The observed value of $A/A_{\text{free}} = 0.988$ for the $\nu_3 + \nu_6$ vibrational state is marked with a horizontal dashed line (bottom plot). The corresponding effective barrier height is $V_6 = 117$ cm^{-1}. This implies a decrease of the torsion excitation energy to 0.84 times its free rotor value (top plot).

the same plot. Given this V_6 value, we expect the torsional excitation energy to decrease to 0.84 times its free rotor (ground state) value, i.e. to shift down by $(1 - 0.84) \times F_0 \approx 0.89$ cm^{-1}, where $F_0 \approx 5.56$ cm^{-1} is the ground state internal rotor constant [53]. This value is in reasonably good agreement with the experimental $|m| = 1$ energy shift of 0.7 cm^{-1} in the $\nu_3 + \nu_6$ vibrational state. One can conclude that the observed torsion-rotation parameters for $\nu_3 + \nu_6$ are roughly consistent with an increase in the effective barrier height V_6 to slightly more than 100 cm^{-1}, placing it within the intermediate region between the low- and high-barrier limits.

3.3.3 Torsion-mediated coupling of the CH stretch vibrations

We can extend the (1+3)-D torsion-rotation calculation by adding the three CH bond length coordinates, r_1, r_2, and r_3, to model the CH stretching vibrations (see Fig. 3.10) and to understand the torsion-mediated interactions between them. The PES is now a function of ρ and the three bond lengths. To ensure the PES has proper permutational symmetry, it is convenient to introduce symmetrized bond length coordinates,

$$\begin{aligned} q_1 &= \frac{1}{\sqrt{3}}\left(r_1 + r_2 + r_3\right), \\ q_{10a} &= \frac{1}{\sqrt{6}}\left(2r_1 - r_2 - r_3\right), \\ q_{10b} &= \frac{1}{\sqrt{2}}\left(r_2 - r_3\right). \end{aligned} \tag{3.17}$$

The q_1 coordinate is totally symmetric (A_1') and corresponds to the ν_1 mode. q_{10a} and q_{10b} transform as a degenerate E' pair. They describe asymmetric CH stretching motions that have a fixed orientation relative to the local CH$_3$ frame. We must perform a ρ-dependent transformation to generate "in-plane" and "out-of-plane" coordinates [18],

$$\begin{aligned} q_{10i} &= q_{10a}\cos\rho - q_{10b}\sin\rho, \\ q_{10o} &= q_{10a}\sin\rho - q_{10b}\cos\rho. \end{aligned} \tag{3.18}$$

The in-plane coordinate q_{10i} transforms as A_1'', and the out-of-plane coordinate q_{10o} transforms as A_2''. These correspond to the ν_{10i} and ν_{10o} vibrational modes, respectively. Using these coordinates, we define a model 4-D torsion-vibration PES as

$$V = \frac{V_6}{2}\cos(6\rho) + \frac{1}{2}k_1 q_1^2 + \frac{1}{2}k_{10i}q_{10i}^2 + \frac{1}{2}k_{10o}q_{10o}^2. \tag{3.19}$$

The V_6 parameter is chosen to equal the ground state value of 2.1 cm^{-1}. The three force constants k_1, k_{10i}, k_{10o} are tuned to match the reduced-dimension vibrational frequencies to the experimental anharmonic frequencies.

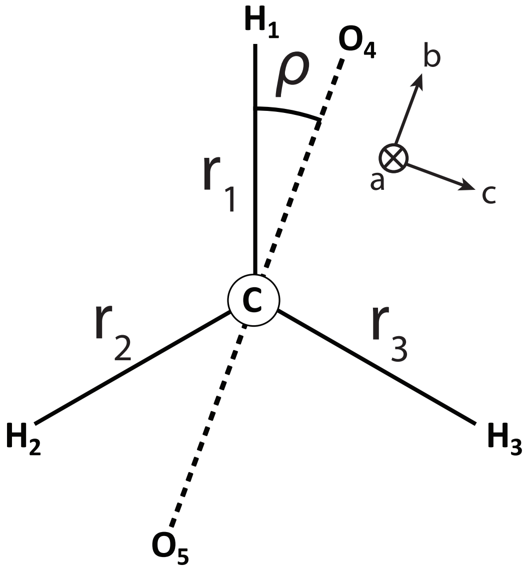

Figure 3.10: CH bond length coordinates for nitromethane. The three stretching coordinates r_1, r_2, and r_3 are defined as the respective C−H$_i$ internuclear distances. $\rho = 0$ is defined as the C−H$_1$ bond being parallel to the O−N−O plane. (The N atom is eclipsed by the C atom in the drawing.)

The calculated vibration-torsion manifolds for the three CH stretching modes are shown in Fig. 3.11a. The $m = 0$ levels are the pure vibrational energies of the three modes: symmetric stretch (black), out-of-plane stretch (blue), and in-plane stretch (red) in increasing energy order. For each vibrational state there is a progression of excited torsional sub-levels whose energies increase quadratically with m. This quadratic dependence is nearly perfect for the symmetric stretch, while the two asymmetric stretches show deviations. These are more clearly seen in Fig. 3.11b, where the nominal Fm^2 torsion energy contribution has been subtracted (with $F \sim 5.6$ cm^{-1} as expected).

The repulsive pattern between the in-plane and out-of-plane manifolds can be modeled with a simple Hamiltonian in the vibrational angular momentum basis. Define the $|+\rangle$ and $|-\rangle$ vibrational states as

$$|\pm\rangle = \frac{1}{\sqrt{2}}\left(|\nu_{10i}\rangle \pm i|\nu_{10o}\rangle\right), \tag{3.20}$$

and the vibrational angular momentum operator $\hat{\Lambda}$ such that

$$\hat{\Lambda}|\pm\rangle = \pm|\pm\rangle. \tag{3.21}$$

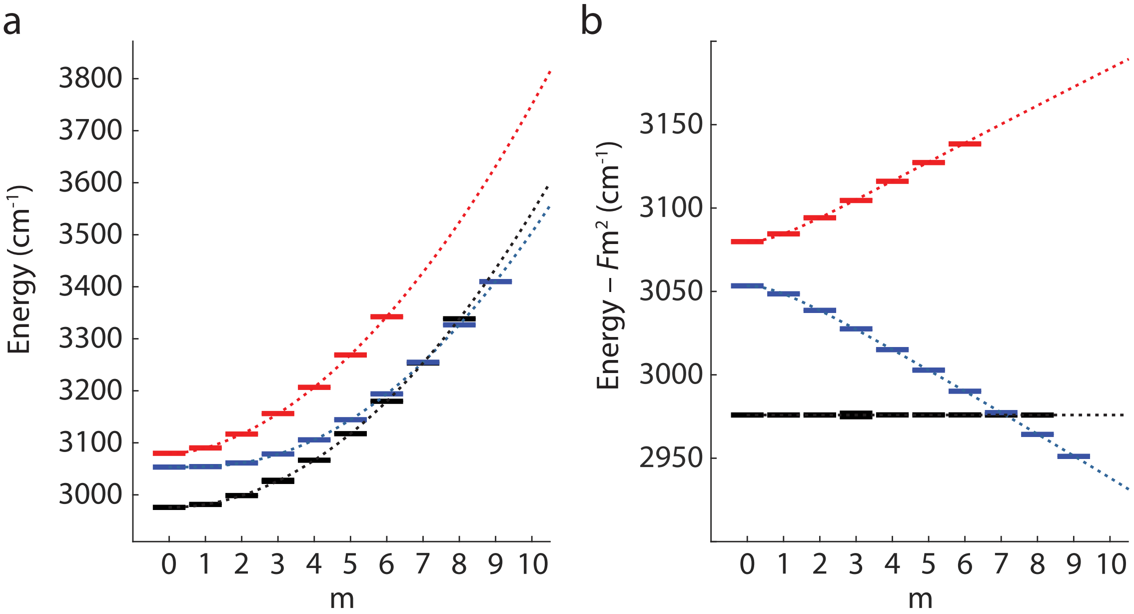

Figure 3.11: Reduced-dimension torsion-vibration energies of the CH stretching modes of nitromethane. (a) The absolute torsion-vibration energies are plotted for the symmetric stretch (black), out-of-plane asymmetric stretch (blue), and in-plane asymmetric stretch (red) vibrational modes as a function of the torsion quantum number m. The dashed curves are the fitted model Hamiltonian eigenenergies, Eq. 3.24. (b) The same as (a) with the pure torsion energy contribution Fm^2 subtracted away.

This vibrational angular momentum is a result of small orbital motions of the H atoms about their local equilibrium positions. It is distinct from the angular momentum associated with large amplitude motion of the entire methyl rotor unit. Now consider the following Hamiltonian,

$$\begin{aligned} H = \overline{\omega} + \frac{\delta\omega}{2}\big(|+\rangle\langle-| + |+\rangle\langle-|\big) \\ + F\hat{J}_\rho^2 + \zeta_\rho \hat{\Lambda}\hat{J}_\rho. \end{aligned} \tag{3.22}$$

$\overline{\omega}$ is the mean vibrational frequency of the two asymmetric modes. $\delta\omega$ describes the static interaction of the methyl top with the NO_2 group, which breaks the degeneracy of the in-plane vs. out-of-plane frequencies. The $F\hat{J}_\rho^2$ term is the usual kinetic energy contribution of the methyl rotor. The last term $\zeta_\rho\hat{\Lambda}\hat{J}_\rho$ accounts for coupling between the small-amplitude vibrational angular momentum and the large amplitude torsional angular momentum. This is similar to standard Coriolis coupling, except that in this case the two angular momenta are both internal motions and the body-frame angular momentum does not appear.

The model H is block diagonal in the torsion quantum number. For each value of m, there is a 2×2 block of the form

$$H_m = \begin{pmatrix} \varpi + Fm^2 + \zeta_\rho m & \delta\omega/2 \\ \delta\omega/2 & \varpi + Fm^2 - \zeta_\rho m \end{pmatrix}, \tag{3.23}$$

with energy eigenvalues

$$E^{\pm}(m) = \varpi + Fm^2 \pm \sqrt{\left(\frac{\delta\omega}{2}\right)^2 + (\zeta_\rho m)^2}. \tag{3.24}$$

For example, for $m = 0$ the diagonal elements become equal. The resulting eigenvalues are the pure vibrational energies $\varpi \pm \delta\omega$ and the eigenvectors revert to the expected in-plane $|\nu_{10i}\rangle$ and out-of-plane $|\nu_{10o}\rangle$ vibrational states. As m increases such that the $\zeta_\rho \hat{\Lambda} \hat{J}_\rho$ interaction is dominant over the static $\delta\omega$ splitting, the vibrational states have approximately pure $|\pm\rangle$ angular momentum character. This is analogous to the rotation-torsion Coriolis interaction that results in pure k_a character states (Fig. 3.6), but on a larger energy scale.

Fitting Eq. 3.24 to the reduced-dimension torsion-vibration energies yields

$$\begin{aligned} \varpi &= 3067 \text{ cm}^{-1}, \\ |\delta\omega| &= 26.5 \text{ cm}^{-1}, \\ F &= 5.6 \text{ cm}^{-1}, \\ |\zeta_\rho| &= 12.2 \text{ cm}^{-1}. \end{aligned}$$

The corresponding $E^{\pm}(m)$ curves are plotted as red and blue dashed lines in Fig. 3.11. This simple model shows excellent agreement with the torsion-vibration energies. The parameter of most interest is the torsion-vibration angular momentum coupling constant ζ_ρ. Its relatively large value of 12.2 cm^{-1} indicates that this interaction must be taken into account to understand the rotation-torsion fine structure of the asymmetric CH stretch bands. The reduced-dimension estimate of its magnitude should prove useful for making progress with this analysis.

3.4 Torsion-rotation Hamiltonians via curvilinear vibrational Møller–Plesset perturbation theory

The calculations presented in the previous section are useful tools for understanding the zeroth order structure, dynamics, and interactions at play in nitromethane. The reduced-dimension approximation, however, is simply too severe to make predictions of spectroscopic accuracy. This is especially true of rotational parameters (e.g. A, B, C constants and centrifugal distortion parameters) measured by microwave and millimeter-wave spectroscopy to high degrees of precision. In this context, accurate full-dimensional *ab initio* calculations are necessary both to facilitate interpretation of experimental results and to provide usefully predictive spectroscopic constants [69].

Direct variational rovibrational calculations of the type employed above became intractably expensive for molecules the size of nitromethane, which has only seven atoms, due to the exponential scaling of the computational complexity. Therefore, we must turn to non-variational perturbative methods that decrease the cost of the calculation without unduly compromising its accuracy. The standard approach to rovibrational perturbation theory (VPT) is based on a harmonic zeroth order approximation to the rectilinear Watson Hamiltonian [70, 71]. VPT fails in two ways for floppy molecules that undergo large amplitude motion. First, such systems are highly anharmonic. (The torsional motion in nitromethane has zeroth order dynamics that are nothing like a harmonic oscillator.) Second, rectilinear (Cartesian) coordinates poorly describe the motion of floppy molecules. (Torsion in nitromethane is best described by the curvilinear rotation angle of the methyl group, not by fixed rectilinear displacement vectors required by VPT.) The inadequacy of a second-order VPT (VPT2) treatment of nitromethane is demonstrated by the wildly inaccurate predictions of some of its ground state torsion-rotation parameters, summarized in Table 3.5.

Motivated by the failure of VPT to treat floppy molecules exhibiting large amplitude motion, we have developed an alternative approach based on second order vibrational Møller-Plesset perturbation theory (VMP2). The key concept is to use a more flexible zeroth order picture that properly accounts for anharmonic, curvilinear dynamics. This zeroth order wavefunction $|\Psi_0\rangle$ is a

Hartree product of anharmonic 1-D wavefunctions for each vibrational coordinate,

$$|\Psi_0\rangle = \phi_1(q_1)\phi_2(q_2)\phi_3(q_3)\cdots . \tag{3.25}$$

The q_i are general curvilinear coordinates, chosen to maximize the separability of the total vibrational Hamiltonian. The anharmonic 1-D functions ϕ_i are optimized variationally by minimizing the expectation value $\langle\Psi_0|H|\Psi_0\rangle$. This leads to a set of mean-field equations, which are solved iteratively until self-consistency is reached, hence the term vibrational self-consistent-field theory (VSCF) [72–74]. The zeroth-order VSCF wavefunction can be refined by applying second-order Rayleigh-Schrödinger perturbation theory to account for vibrational correlation effects beyond the mean-field description. In analogy with electronic structure theory [75], this method is termed vibrational Møller–Plesset perturbation theory (VMP2) [76]. We have extended curvilinear VMP2 to include rotational and rovibrational terms in the nuclear motion Hamiltonian, thereby generating effective rotational Hamiltonians in addition to anharmonic vibrational frequencies [51] (see Chapter 7).

The two main inputs into a VMP2 calculation are the PES and the choice of curvilinear coordinate system. We employ the full-dimensional CCSD(T)-F12b/HaDZ PES recently constructed by Wang, Carter and Bowman [77]. A minimum energy isomerization path coordinate system suitable for large amplitude torsion is used as the internal coordinate system. (More details can be found in Ref. [51]). The primary results of the application to the ground state rotation-torsion structure of nitromethane are shown in Table 3.5. The curvilinear VMP2 results show uniformly excellent agreement with the experimental rotation-torsion parameters, including the principal rotational constants (A, B, and C), the internal rotor constants (A' and F), and the quartic centrifugal distortion parameters (Δ_J, Δ_{JK}, Δ_K, δ_J, δ_K). (These constants are defined in the effective Hamiltonians in Eqs. 3.10 and 3.14.) This is in striking contrast to VPT2, which is particularly problematic for quantities involving the a-axis (A, Δ_{JK}, Δ_K, and δ_K) because it is coincident with the internal rotation axis. Moreover, VPT2 cannot provide predictions at all for the internal rotor constants F and A'. These issues can be traced back to the use of rectilinear coordinates and a harmonic zeroth-order description, which are physically inappropriate for large amplitude motion.

Table 3.5: *Ab initio* torsion-rotation parameters of nitromethane. Predictions based on curvilinear VMP2 and standard rectilinear second-order VPT (VPT2) are compared to experimental values. VPT2 entries marked * are especially unphysical. All values are given in GHz.

Parameter		VMP2	VPT2	Expt.
A		13.33	12.19*	13.34[a]
B		10.51	10.46	10.54[a]
C		5.86	5.85	5.88[a]
F		166.9	—	166.7[b]
A'		13.25	—	13.28[a]
Δ_J	$\times 10^6$	5.50	5.67	6.14[a]
Δ_{JK}	$\times 10^6$	17.84	952.73*	17.75[a]
Δ_K	$\times 10^6$	-10.66	-949.39*	-7.54[a]
δ_J	$\times 10^6$	2.24	2.30	2.47[a]
δ_K	$\times 10^6$	15.77	-268.95*	15.75[a]

[a] Ref. [55]
[b] Ref. [52, 53]

The success of curvilinear VMP2 for providing accurate ground state constants for nitromethane is encouraging. Similar calculations can be performed for excited vibrational states. Effects such as torsion-vibration angular momentum coupling, as discussed in the previous section, are fully captured with this approach. These predictions will aid in the continued analysis of the complex rotation-torsion structure of the CH stretching vibrations.

3.5 Conclusions

The combination of comb spectroscopy and cold molecules results in a remarkable quantity of detailed spectroscopic information. Analysis of this data distills a "phonebook" of line positions into specific structural and dynamical insights, as demonstrated in this chapter for nitromethane. Although many conclusions are to a greater or lesser degree particular to this example, they also reveal patterns and general physical concepts that can be applied to related molecular systems. Similarly, analytical and computational tools developed to understand the spectroscopy of nitromethane, such as the curvilinear VMP2 methods introduced in this chapter, can be applied to a variety of other problems. (Examples of such applications are presented in Chapter 7.) As large amplitude motion remains an incompletely understood phenomenon, high resolution infrared spectroscopy continues to contribute to our understanding of its consequences on molecular structure and dynamics.

Chapter 4

Limits to rotationally resolved MIR spectroscopy of large hydrocarbons

High resolution gas-phase spectroscopy is an essential tool for molecular detection and identification. This is especially true for applications in extraterrestrial and astronomical chemistry, where spectroscopic detection is the primary, and often only, means of identification [78]. Most astronomical observations of molecules are made via pure rotational transitions in the microwave and millimeter-wave regime [79], but this requires the presence of a permanent dipole moment. Many molecules of potential astrochemical importance, such as large polyaromatic hydrocarbons (PAHs) [80] or fullerenes (see Chapter 5), lack a permanent dipole moment by symmetry. One must instead turn to optical techniques, i.e. vibrational or electronic spectroscopy.

Rotationally resolved infrared studies of large molecules are relatively few in number compared to those of small- to medium-sized molecules of less than about a dozen atoms. One contributing factor is the difficulty of producing gas-phase samples of large, heavy molecules that are rotationally and vibrationally cold. Even if this can be achieved in the laboratory, the spectra are often intrinsically congested and complex due to the high density of rovibrational states at the internal energies excited by infrared photons. These systems are thus an ideal challenge for the combined capabilities of cryogenic buffer gas cooling and cavity-enhanced direct frequency comb absorption spectroscopy.

This brief chapter contains several studies of large hydrocarbon molecules of increasing size and mass. We present rotationally resolved infrared spectra in the CH stretching region (ca. 3 μm) of naphthalene ($C_{10}H_8$), adamantane ($C_{10}H_{16}$), and hexamethylenetetramine (HMT, $C_6N_4H_{12}$, not strictly a hydrocarbon). We also report our inability to observe rotational structure in the spectrum of cold diamantane ($C_{14}H_{20}$), and discuss the general implications of these results for rotationally resolved spectroscopy of large molecules in the context of intramolecular vibrational energy redistribution (IVR) [81].

4.1 Experimental details

All spectra discussed in this chapter were recorded using the 3 μm OPO comb with FTS and VIPA-based detection. Cold (10 to 20 K) samples of each molecular species were prepared with the low-temperature CBGC cell with He buffer gas. Details of these apparatus are provided in Sections 2.1.1, 2.4, and 2.5.1 and will not be repeated here.

The target species are crystalline solids at room temperature, requiring an oven source to produce a sufficient flux of gas-phase molecules. The oven temperature range used in each case is listed in Table 4.1. For each species, the temperature is below its respective melting point. Sublimation is sufficiently rapid to produce the necessary flux.

Table 4.1: Oven temperatures used to introduce solid samples into CBGC cell.

Species	Oven Temperature (°C)
Naphthalene	60 – 70
Adamantane	45 – 65
HMT	120 – 125
Diamantane	110 – 120

4.2 Results

Naphthalene, $C_{10}H_8$, contains two fused benzene rings making it the simplest PAH. As such, it has received significant spectroscopic attention in both the infrared [82–84] and ultraviolet [85,86] regions. The ν_{29} CH stretch band, which has previously been studied with skimmed-molecular-beam optothermal experiments [84], is shown in Fig. 4.1. This CE-DFCS measurement is the first rotationally resolved spectroscopy in this wavelength region for naphthalene via direct absorption. We assigned over 150 rovibrational transitions (Table A.5) and used these to determine the asymmetric-top rotational parameters of the ν_{29} state (Table 4.2). The upper state energies and fitted curves are shown in the inset of Fig. 4.1. Fitting just the three principal rotational constants A, B, and C results in small residuals (RMSE $= 4.3 \times 10^{-4}$ cm$^{-1} \approx 14$ MHz) on the order of the line position uncertainty.[1] The band intensity profiles are consistent with a rotational temperature of 10(3) K.

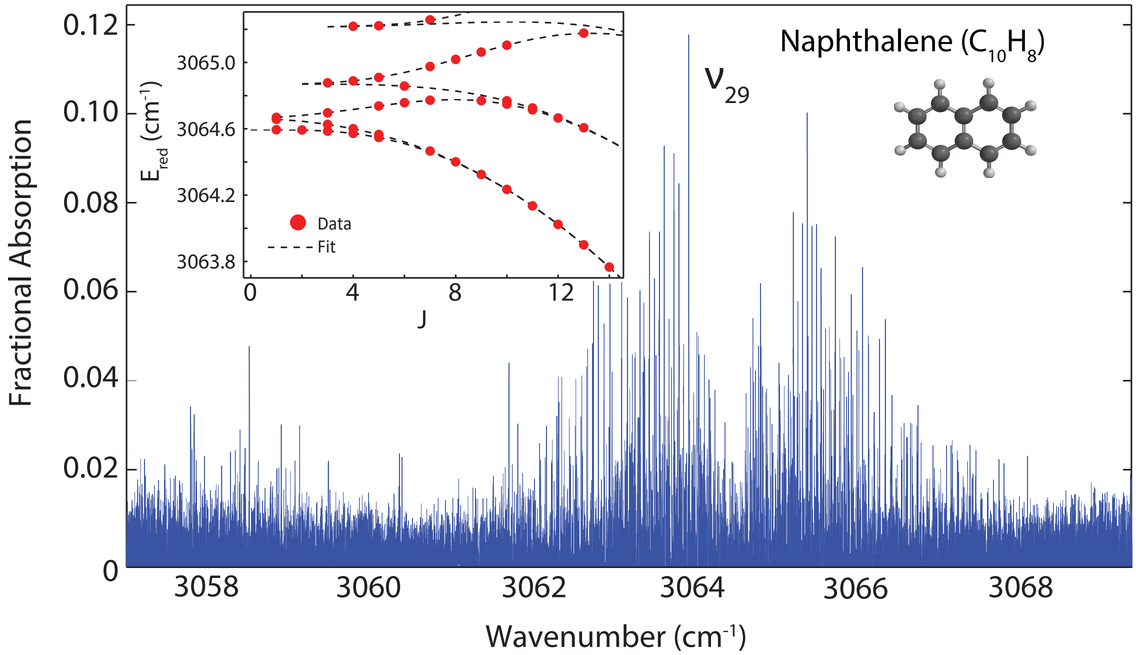

Figure 4.1: The ν_{29} band of cold naphthalene. Extensive rotational fine structure is resolved in the buffer-gas-cooled CE-DFCS spectrum. (Inset) Reduced term energies of ν_{29} rotational sub-levels plotted versus J. The fitted effective rotational Hamiltonian (Table 4.2) shows excellent agreement with the measured rovibrational energies.

Adamantane, $C_{10}H_{16}$, is the simplest member of the diamonoid family of molecules, so-named for their tetrahedral carbon-cage structure that forms the building block of bulk diamond. Figure 4.2 shows a 100-cm^{-1}-wide portion of its spectrum centered around 3.4 μm. This region contains five strong vibrational bands: the three IR active CH stretch modes (ν_{20}, ν_{21}, and ν_{22}) as well as two unassigned bands near 2853.1 cm^{-1} and 2904.6 cm^{-1}. Each of these bands contains

---

[1] Although we achieve similar residuals as the fit based on skimmed-beam data by Hewett et al. [84], our rotational constants disagree by several σ. After comparing combination differences of both sets of data with accurate ground state energies [82], we speculate that the line positions reported by Hewett et al. suffer from a calibration error.

Table 4.2: Rotational fit of the ν_{29} band of naphthalene. The quartic centrifugal distortion constants for the upper state were held fixed to the ground state values of Ref. [82]. All values are given in cm^{-1}.

Parameter		Ground state^a	${\nu_{29}}^b$	${\nu_{29}}^c$
ν_0		0	3064.5942(5)	3064.58(2)
A		0.104051836(124)	0.104198(30)	0.104013(17)
B		0.04112733(37)	0.0411173(38)	0.0411023(45)
C		0.029483552(140)	0.02942455(9)	0.0294062(20)
Δ_J	$\times 10^9$	0.528(49)	[0.528]	—
Δ_{JK}	$\times 10^9$	1.206(145)	[1.206]	—
Δ_K	$\times 10^9$	5.648(112)	[5.648]	—
δ_J	$\times 10^9$	0.1752^d	[0.1752]	—
δ_K	$\times 10^9$	1.951^d	[1.951]	—
RMSE	$\times 10^4$	3.1	4.3	6.3

a. Ref. [82]. δ_J and δ_K are calculated values.
b. This work
c. Ref. [84]

extensive rotational fine structure. The Doppler-broadened rovibrational transitions have a line width of 23(2) MHz, indicating a translational temperature of 17(1) K (Fig. 4.2b). The narrow line width provides sufficient resolution to reveal intricate tetrahedral centrifugal distortion splittings of this heavy spherical top (Fig. 4.2c). HMT, $C_6N_4H_{16}$, is a heterocycle cage formed from adamantane by replacing the four carbon atoms at the vertices of a tetrahedron with nitrogen atoms. Figure 4.3 shows a small portion of its cold absorption spectrum centered near the ν_{17} CH stretch band. We observe similarly well resolved and narrow rovibrational transitions as for adamantane.

The next largest diamonoid after adamantane is diamantane, $C_{14}H_{20}$. Its absorption spectrum is shown in Fig. 4.4. Although acquired under nearly identical conditions to the previous examples, this spectrum shows a quasi-continuous absorption profile with 5-cm^{-1}-wide vibrational bands centered around the CH stretch fundamental frequencies. Upon close examination, a limited number of narrow absorption features can be detected that appear at approximately regular intervals of $0.04 - 0.05$ cm^{-1} (Fig. 4.4 inset). This spacing is about equal to $2B$, suggesting that these features are vestiges of some underlying rotational structure. These transitions have line widths of $20 - 30$ MHz. Assuming this to be a Doppler-broadened feature, that corresponds to

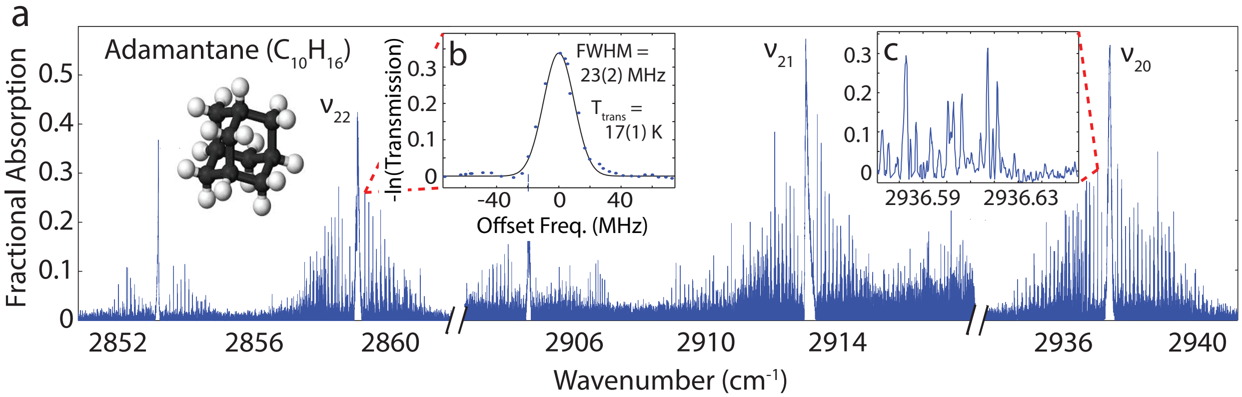

Figure 4.2: Survey absorption spectrum of cold adamantane, $C_{10}H_{16}$. (a) The region spanning $2850-2950$ cm^{-1} contains three very bright IR active CH stretch bands (ν_{20}, ν_{21}, ν_{22}) as well as two unassigned bands near 2853.1 cm^{-1} and 2904.6 cm^{-1}. (b) The narrow Doppler profiles demonstrate translational cooling to a temperature of $T_{\mathrm{trans}} = 17(1)$ K. (c) Rovibrational transitions of this spherical top appear in dense clusters due to tetrahedral fine structure splittings.

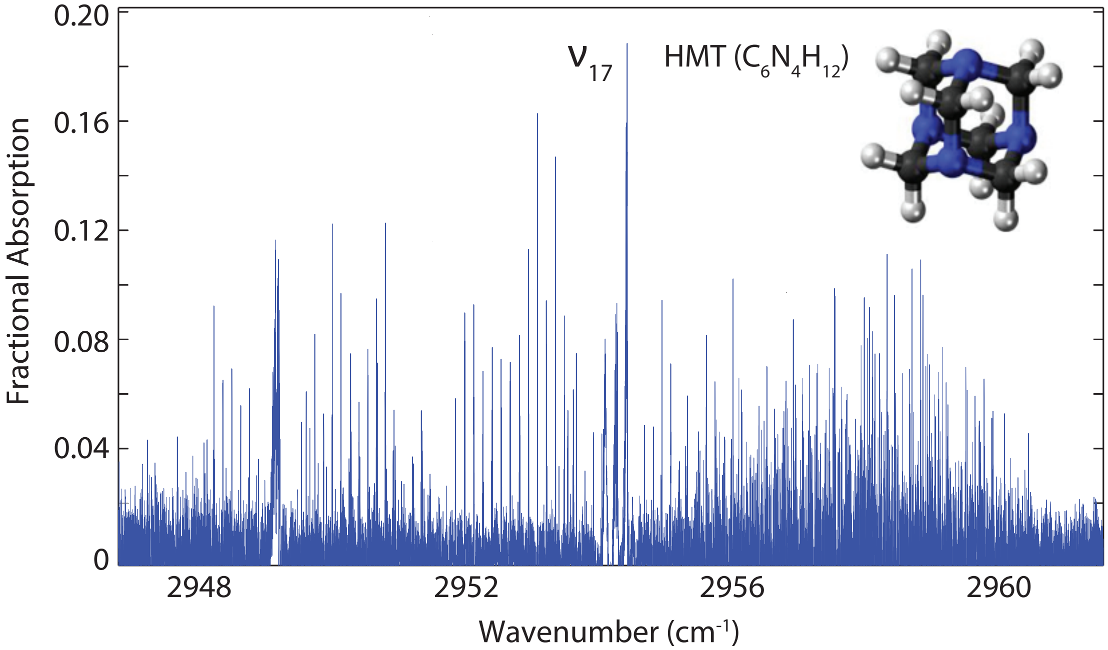

Figure 4.3: The CE-DFCS absorption spectrum of HMT in the vicinity of the ν_{17} CH stretch band. This spectrum has a similar appearance to that of adamantane (Fig. 4.2) due to the related structure and identical symmetry of the two molecules.

translational temperatures of 20 K. The width of the rotational contours is also consistent with a rotational temperature of $10 - 30$ K. This indicates that diamantane is approximately thermalized with the He buffer gas bath, and that the continuous absorption profile is an intrinsic feature of its spectrum.

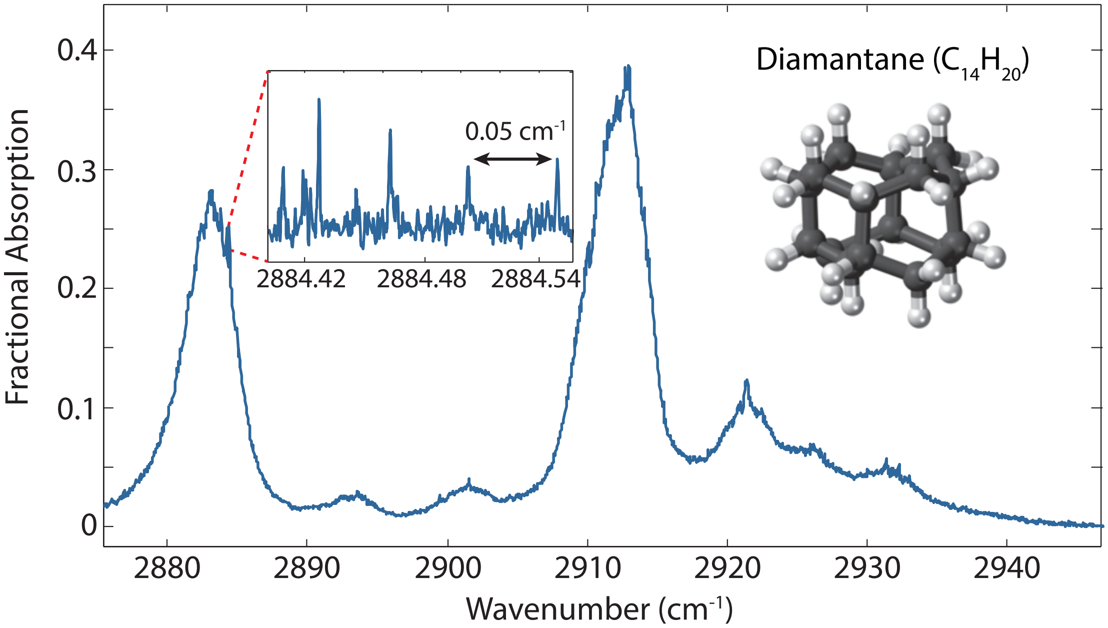

Figure 4.4: Absorption profile of diamantane, $C_{14}H_{20}$. In lieu of the rotational fine structure observed for other examples, diamantane exhibits a quasi-continuous absorption profile in the CH stretch region. The strongest vibrational bands are each about 5 cm^{-1} wide. (Inset) Small portions of the spectrum contain narrow, regularly spaced features suggestive of underlying rotational structure. These features are only $20 - 30$ MHz wide.

4.3 Discussion and conclusion

The observations above represent the largest molecules for which rotationally resolved spectra in 3 μm region have been reported [87, 88], demonstrating the effectiveness of the combined cold molecule-frequency comb spectrometer. From a practical perspective, the system provides very high data throughput, collecting millions of individual frequency elements in a short amount of time. (Altogether, the spectra above required a total of only three hours of data collection.) Gas-phase infrared measurements of comparable bandwidth and resolution are otherwise possible only with ultra-long FTIR instruments, which typically require the use of synchrotron facilities [82, 83, 87, 89, 90] and are not suited to table-top experiments.

While our results show just how far high resolution infrared spectroscopy of large molecules can be taken, they also suggest intrinsic limits to such experiments, as evidenced by the CH stretch spectrum of diamantane. We interpret its quasi-continuous absorption profile as evidence of intramolecular vibrational energy redistribution (IVR) between the zeroth-order CH stretch bright states and the manifold of background dark states [81]. The density of vibrational states at the $\sim$3000 cm^{-1} internal energies probed by the infrared photon is about 10× larger for diamantane than for molecules for which well resolved rotational fine structure is observed, such as adamantane and naphthalene (see Fig. 4.5). Various studies on IVR rates in hydrocarbons [91–96] suggest an approximate background state density threshold of $\rho \sim 10^2/\mathrm{cm}^{-1}$ before the onset of severe spectral fractionation [81]. Diamantane, with $\rho \approx 10^3/\mathrm{cm}^{-1}$ at 3000 cm^{-1}, is well above this limit. Based on this rule of thumb, one might expect that adamantane and naphthalene should also suffer from IVR effects. However, it is important to take into account the ameliorating role of symmetry [97–99], which reduces the extent of IVR coupling, especially in highly symmetric molecules like adamantane.

IVR presents a general obstacle for high resolution spectroscopy of large molecules. Continued progress mandates a shift away from the 3 μm CH stretch region. At the lower internal energies probed by longer wavelength IR photons, the density of background vibrational states decreases exponentially. This motivates the development of LWIR frequency comb sources, such as the $6-11$ μm DFG system described in Section 2.1.2. These tools will enable the exploration of even larger and more complex molecular systems with rotationally resolved spectroscopy.

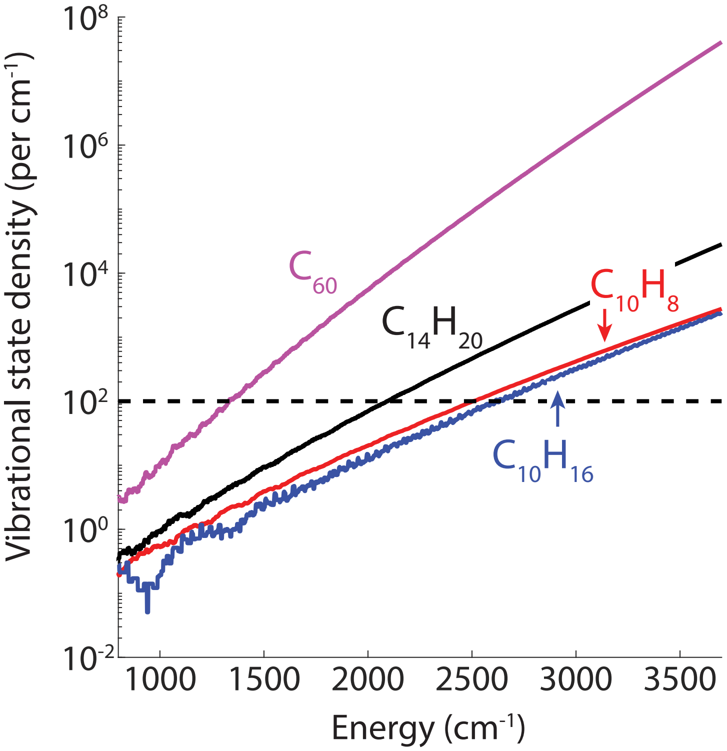

Figure 4.5: Vibrational state density for several large carbon-containing molecules, including adamantane ($C_{10}H_{16}$, blue), naphthalene ($C_{10}H_8$, red), diamantane ($C_{14}H_{20}$, black), and buckminsterfullerene (C_{60}, pink). The curves were calculated using a direct count algorithm [100] with vibrational frequencies from Refs. [101–106]. The approximate IVR threshold of 10^2 states per cm^{-1} [81] is indicated with a dashed horizontal line.

Chapter 5

Rovibrational quantum state resolution of the C_{60} fullerene

The previous chapter provided specific examples of the general limitations placed on high resolution infrared spectroscopy by large, heavy polyatomic molecules. Some problems are of a purely technical and, some might say, shallow variety: having sufficiently narrow lasers and molecular line widths can eventually reveal even the most congested of spectra. Congestion, however, is merely a symptom of a deeper and more essential obstacle. The inseparability of the ever multiplying degrees of freedom in large molecules (i.e. IVR) suggests that frequency domain spectroscopy and an eigenstate-by-eigenstate perspective will have diminishing usefulness in understanding the dynamics and structure of such complex many-body systems.

This chapter provides a counter-example to this trend in the form of buckminsterfullerene, C_{60} (Fig. 5.1). As we will see, the remarkable symmetry and rigidity of C_{60} make a description of its rovibrational spectrum and structure at the level of individual quantum states possible. To the best of the author's knowledge, C_{60} represents not only the largest molecule for which a rotationally resolved spectrum has been obtained, but also the most symmetric, C_{60} being an example of the relatively rare icosahedral (I_h) point group. Section 5.1 provides an overview of the structure and thermodynamics of C_{60}, illustrating why its size and mass make rotationally resolved spectroscopy so formidable. As demonstrated in prior chapters, these challenges are overcome with a combination of CBGC and CE-DFCS. However, unlike previous experiments, the particularly difficult task of cooling C_{60} requires the high-temperature, high cooling power CBGC setup introduced in Chapter 2. Section 5.2 describes in more detail the production of cold, dense samples of gas-phase C_{60} with this device and the DFG frequency comb used to measure its infrared spectrum. An effective rovibrational Hamiltonian model is introduced in Section 5.3. We use this to extract detailed molecular scale insights into C_{60}. Finally, the chapter concludes with a discussion of some remaining spectroscopic puzzles presented by these first frequency comb experiments.

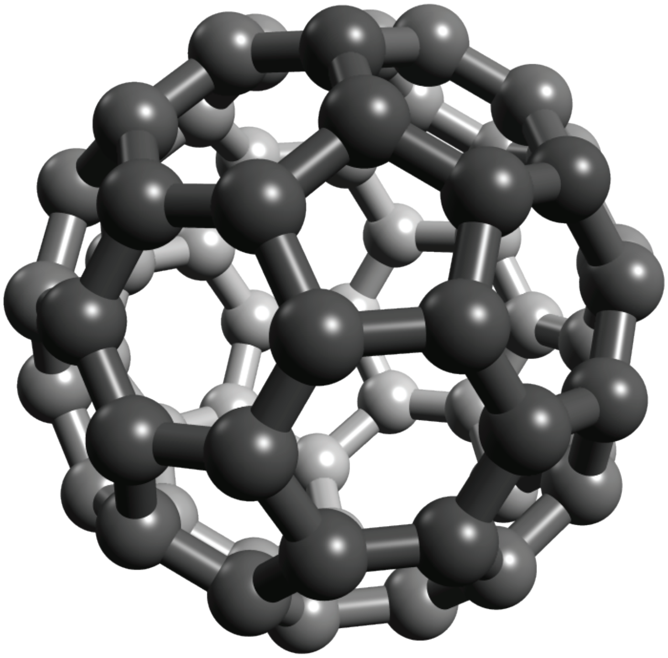

Figure 5.1: The structure of buckminsterfullerene, C_{60}. Sixty carbon atoms lie at the vertices of a truncated icosahedron (a soccer ball shape), making C_{60} an example of the icosahedral I_h point group. Each carbon atom site is chemically indistinguishable to all others.

5.1 An introduction to C_{60}

The existence of a stable, hollow cage of sixty carbon atoms was first postulated and studied theoretically in the 1970s and early 1980s by several groups independently [107–110]. However, it was not until 1985 that the seminal mass spectrometry experiments of Kroto et al. provided clear evidence for C_{60} [111]. The apparent stability of the molecule quickly led to the conjecture that it formed a closed spherical cage with 20 hexagonal faces and 12 isolated pentagonal faces, i.e. the truncated icosahedral structure shown in Fig. 5.1, which inspired the name "buckminsterfullerene," and soon thereafter "buckyball," in honor of the geodesic structures of the architect Buckminster Fuller [112]. Subsequent infrared and ^{13}C-NMR studies of isolated C_{60} in the early 1990s confirmed its highly symmetric I_h structure [113–118]. Since then, a wide variety of spectroscopic and analytical techniques, including x-ray and electron diffraction [119, 120], optical Raman and neutron scattering [121–127], matrix and helium droplet isolation spectroscopy [128–133], and photoelectron spectroscopy [134–136], have greatly contributed to our understanding of this unique molecule. Spectroscopy in particular has played an essential role in the astronomical identification of C_{60} and its derivatives [132, 137–141], and high resolution laboratory data may help resolve current uncertainty regarding its astrophysical state [132]. However, despite intense interest, no rotationally resolved spectrum of gas-phase C_{60} has been reported to date.

The high degree of symmetry exhibited by C_{60} makes it relatively difficult to probe with electromagnetic radiation. Like all spherical tops, C_{60} possesses no permanent dipole moment,[1] and therefore has no pure rotational microwave spectrum. Although centrifugal distortion effects in some spherical tops, like tetrahedral CH_4, permit very weak pure rotational transitions [143], even these are strictly electric dipole forbidden in icosahedral tops such as C_{60} due to the presence of a center of symmetry. We must therefore turn to the optical regime, i.e. electronic or vibrational spectroscopy. The first strong electronic absorption features only appear relatively high in the singlet excitation manifold [144]. Vibronic coupling within the singlet manifold and fast intersystem crossing to triplet states [145, 146] will potentially obscure spectroscopic fine structure, but nonetheless would be very interesting to explore. Lower lying states have either orbital- or spin-forbidden (or both) transitions from the ground electronic state and have very weak oscillator strengths [144].

This leaves IR spectroscopy as the most viable approach to make the first observations of rovibrational quantum state-resolved structure in C_{60}. With $N = 60$ atoms, each molecule has $3N - 6 = 174$ vibrational modes. Under the I_h point group (the character table for which is provided

---

[1] In fact, the lowest rank multipole moment allowed for C_{60} is the 64-pole (a hexacontatetrapole) [142].

in Appendix C), only those modes that transform as the T_{1u} irreducible representation are IR active. There are four such sets of T_{1u} vibrations, each comprised of three triply degenerate modes. These four T_{1u} bands are readily observed in low resolution condensed- or gas-phase experiments and occur at 7.0, 8.5, 17.4, and 19.1 μm [131]. We choose to focus on the 8.5 μm band, which has a modest integrated band intensity of 9.4 km mol^{-1} [131] and is conveniently located in the center of the operating range of our DFG frequency comb.

The remaining obstacle to obtaining rotationally resolved spectra of C_{60} is its formidable thermodynamics. The vibrational and rotational degrees of freedom pose complementary challenges. Although the rigidity of the C_{60} carbon frame leads to relatively high vibrational frequencies for a molecule of its size (spanning 260 to 1600 cm^{-1} [106]), the sheer number of vibrational modes results in a steep rise in the density of states with increasing internal energy. Conversely, while there are only 3 rotational degrees of freedom, the large moment of inertia, ca. 6×10^3 uÅ^2, results in a very small rotational energy level spacing. (The fundamental $J = 0 - 1$ spacing is approxiately $h \times 170$ MHz.) Both of these contribute to a large internal partition function, particularly the vibrational contribution Z_{vib}, which is shown in Fig. 5.2. At the temperature of our C_{60} oven, which approaches 1000 K, there are $Z_{\mathrm{vib}} \approx 10^{29}$ thermally occupied vibrational states! Even at 300 K, Z_{vib} is greater than 10^3. It is necessary that most of the population is cooled to the vibrational ground state, i.e. $Z_{\mathrm{vib}} \sim 1$, to avoid spectral congestion from hot band transitions. This requires internal temperatures of 150 K or lower. Concomitant with the rapidly increasing partition function is the large internal energy stored in the vibrational modes. At 1000 K, each C_{60} molecule contains 60000 cm^{-1} (7.5 eV) of vibrational energy. To achieve vibrational ground state cooling, all of this energy must be efficiently removed.

5.2 Generating cold C_{60}

We turn once again to CBGC to generate cold samples of gas-phase C_{60}. The reader is referred back to Fig. 2.8, which shows the geometry of the C_{60} oven source and cryogenic cold cell. A $1 - 10$ mg min^{-1} flow of C_{60} molecules thermalized to the source temperature of 950 K exits

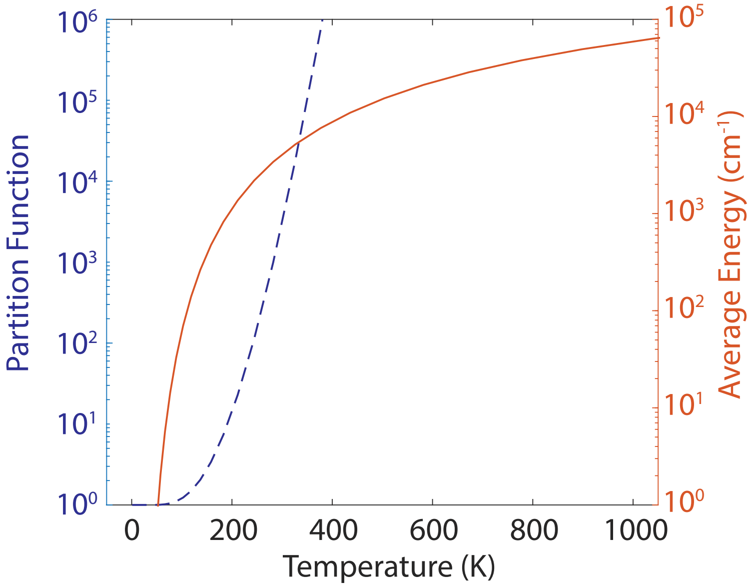

Figure 5.2: Thermodynamical functions for C_{60} vibrations. The vibrational partition function (blue dashed line, left vertical axis) increases super-exponentially with temperature as more and more vibrational modes "unfreeze." The corresponding average vibrational energy (red solid line, right vertical axis) reaches several tens of thousands of cm^{-1} by 1000 K, reflecting the large heat capacity per molecule.

the oven into cold cell. The cell intersects the axis of the optical enhancement cavity, which has a finesse of 6000 and a FSR of 280 MHz. DFG comb light tuned to cover the 8.5 μm absorption band of C_{60} is continously coupled into the optical cavity and monitored with the FTS spectrometer.

Our first attempts to cool vibrationally hot C_{60} molecules used the low-temperature helium CBGC setup (see Section 2.5.1), which successfully cooled all attempted species in the past. Although deposits of vaporized material from the oven clearly indicated that material was entering the cell, there was no detectable absorption signal from C_{60}, or any other absorber, above a 1 ppm single pass loss baseline. While a variety of explanations could account for the absence of signal, including thermal degradation of C_{60} into amorphous carbon, the primary suspect was insufficiently high buffer gas density, which leads to inadequate cooling for both translational and internal states. With poor translational cooling, C_{60} molecules ballistically travel from the oven to the cold cell walls and freeze out, instead of slowly diffusing throughout the cell, thereby inhibiting a build-up of C_{60} density. With poor internal state cooling, too many excited vibrational states are occupied, leading to broadening, congestion, and dilution of the absorption cross-section. Indeed, in recently attempted supersonic jet absorption spectroscopy experiments, inefficient vibrational cooling was also speculated to be the reason for the lack of detectable C_{60} absorption [147]. The large mass difference between C_{60} and the buffer gas helium atoms likely further reduces the collisional cooling efficiency in our experiment.

A serendipitous accident in lab provided support for the "collisionally starved" explanation and a path forward for C_{60} cooling. One afternoon, an undetected short of a thermocouple lead on the C_{60} oven resulted in a temperature reading that was about one-half of the actual oven temperature. This led us to signficiantly overheat the oven, and the resulting radiative heat load warmed the cryo-sorbs responsible for pumping helium buffer gas. They quickly experienced a hard crash, releasing a significant amount of desorbed helium. In a few seconds, the dewar background pressure increased from less than 10^{-4} Torr to about 10^{-1} Torr, and a strong, broad absorption signal immediately appeared in the FTS comb spectrum, as shown in Fig. 5.3. This signal was strongly dependent on the oven temperature and located at the expected band origin position [131], indicating C_{60} – in some form – was almost certainly the carrier. Using different buffer gas species, we were able to reproduce the signal, with the band center being unaffected by the buffer gas species, while the shape and width did exhibit some slight dependence. The optimal dewar pressure was between 80 and 500 mTorr, depending on buffer gas. In order to run the low-temperature CBGC cell at these high background pressures, the helium refrigerator had to be turned off and we relied on mechanical vacuum pumps. The traces in Fig. 5.3b were collected after the cold cell had warmed to a temperature of 100 K.

The physical state of C_{60} giving rise to the broad absorption feature is still uncertain. One hypothesis is that it is from a C_{60}-buffer gas van der Waals complex or even a $(C_{60})_n$ "super-cluster" [148, 149]. Although we cannot entirely rule out these possibilities, we believe the simplest and most likely case is that it is simply from "warm" C_{60}, i.e. partially cooled from the initial oven temperature, but not completely thermalized to the buffer gas bath (ca. 100 K). This reasoning

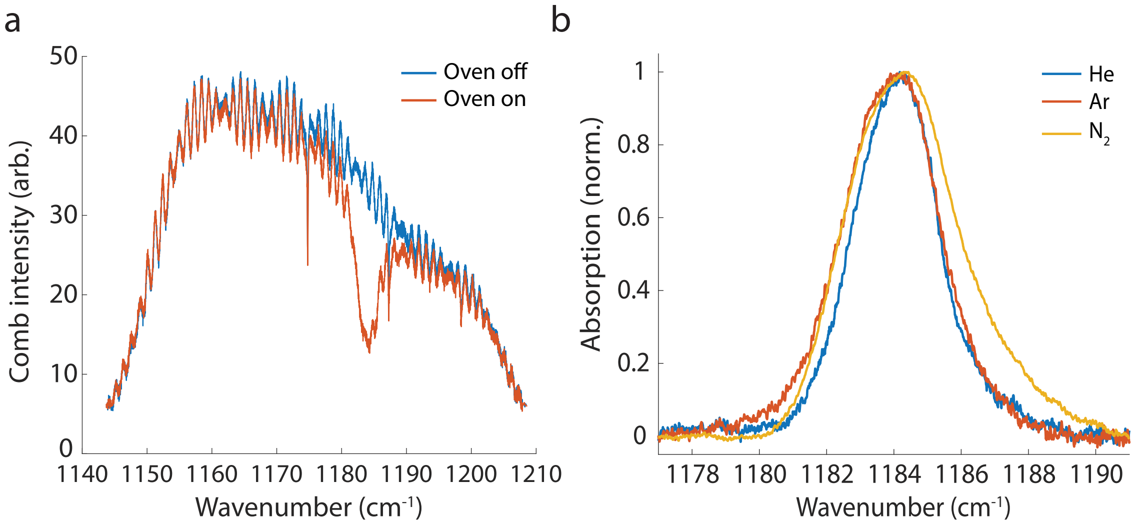

Figure 5.3: Absorption from the 8.5 μm band of C_{60}. (a) The raw comb spectral intensity envelope shows a clear absorption dip from C_{60} centered near 1185 cm^{-1}. The periodic fringes are due to etalons, while the handful of sharp absorption peaks are from ambient water vapor. (b) The normalized absorption profiles in "warm" conditions for several buffer gas species including helium, argon, and molecular nitrogen. The buffer gas temperature is 100 K.

suggests that increasing not only the number of buffer gas-C_{60} collisions but also the average energy transfer per collision will help drive the hot C_{60} molecules to thermalization with the cold buffer gas.

After extensively exploring a variety of buffer gas parameters, including the input flow rate, the background dewar pressure (controlled independently of input flow rate by adjusting the pumping speed), the position of the oven relative to the annular slit inlet plate (see Fig. 2.8), and the buffer gas species, we were eventually able to observe narrow absorption resonances in place of the broad absorption envelope. Figure 5.4 illustrates these signatures for several different buffer gas species. The strongest signal was obtained with argon buffer gas, suggesting it is the most efficient collisional cooling partner for C_{60}. (Note that the spectra in Fig. 5.4 were acquired with a single f_{rep} position, and only a fraction of the C_{60} absorption resonances overlap with the 280 MHz-spaced cavity resonances.)

As indicated above, the small cooling capacity of the helium refrigerator is insufficient to operate at such high buffer gas pressures for any extended period of time. We addressed this

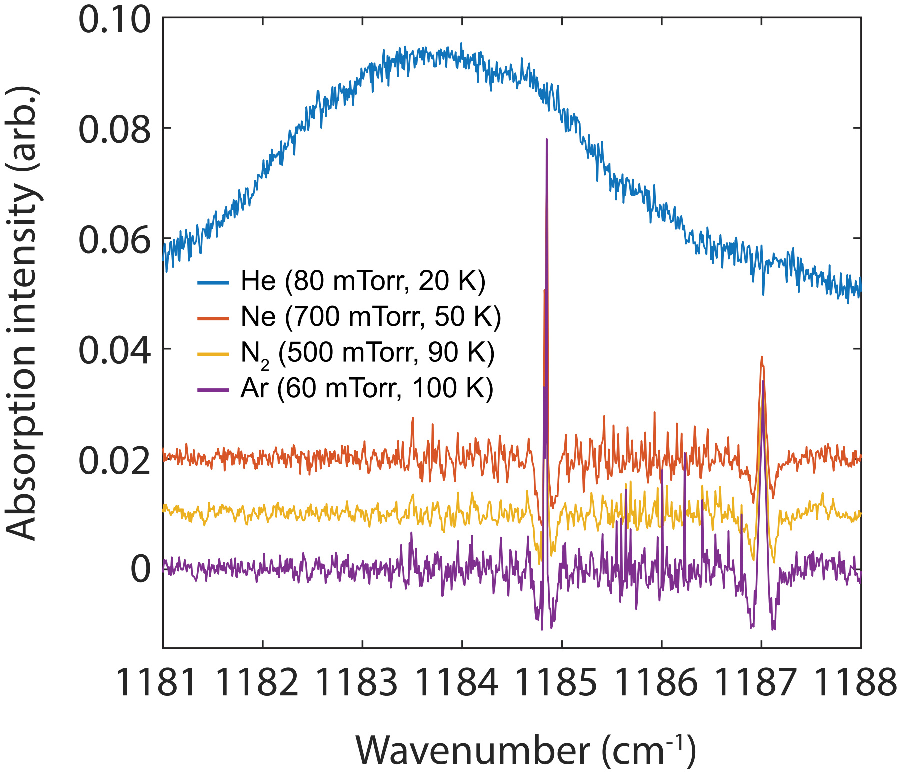

Figure 5.4: The first cold C_{60} signals. The broad, continuous absorption observed with helium buffer gas is compared to optimized signals obtained with neon, nitrogen, and argon buffer gas. The traces are offset for clarity. With the last three buffer gas species, narrow, well resolved absorption resonances were observed. The strong peak near 1185 cm^{-1} is the Q branch of the C_{60} vibrational band. The broad line near 1187 cm^{-1} is from ambient water. The remaining "weeds" are transitions from the C_{60} R and P branches. These spectra were all obtained at a single comb f_{rep} value, such that the absorption spectrum is only sampled at the 280 MHz spacing provided by the enhancement cavity. (The negative over-shoot is an artifact of the filtering process applied to the FTS comb spectra.)

issue by constructing the high-temperature CBGC system described in Section 2.5.2. The primary difference is the replacement of the helium refrigerator with an LN2 cold finger, which provides sufficient cooling capacity to run indefinitely at the required buffer gas pressures, enabling repeated f_{rep} scans and averaging. Of course, this also restricts the minimum achievable temperature to the 77 K boiling point of LN2.

A survey spectrum of the full C_{60} band acquired with the high-temperature CBGC cell is shown in Fig. 5.5. The cold spectrum contains data acquired over 20 hours of total averaging time. The 280 MHz comb mode spacing set by the cavity FSR was split into 89 subdivisions such that the final optical frequency step size in the spectrum was about 3 MHz. The optimum cooling conditions were found to be an argon buffer gas flow rate of $50-100$ sccm and a 250 mTorr background dewar pressure. The oven was placed $0.5-1.0$ cm from the cold cell inlet aperture. The extracted rotational temperature is 150(2) K, only slightly warmer than the measured cell wall temperature of 135 K (see Fig. 2.11). A comparison of the warm and cold spectra in Fig. 5.5 shows a clear red shift of the warm spectrum relative to the band origin of the cold spectrum (located at the strong Q branch). This is consistent with the warm spectrum being assigned to vibrationally hot C_{60}, as hot bands are usually red shifted due to vibrational anharmonicity [131]. The strongest absorption in the cold spectrum (the peak of the Q branch) corresponds to a single-pass absorption of 25 ppm.

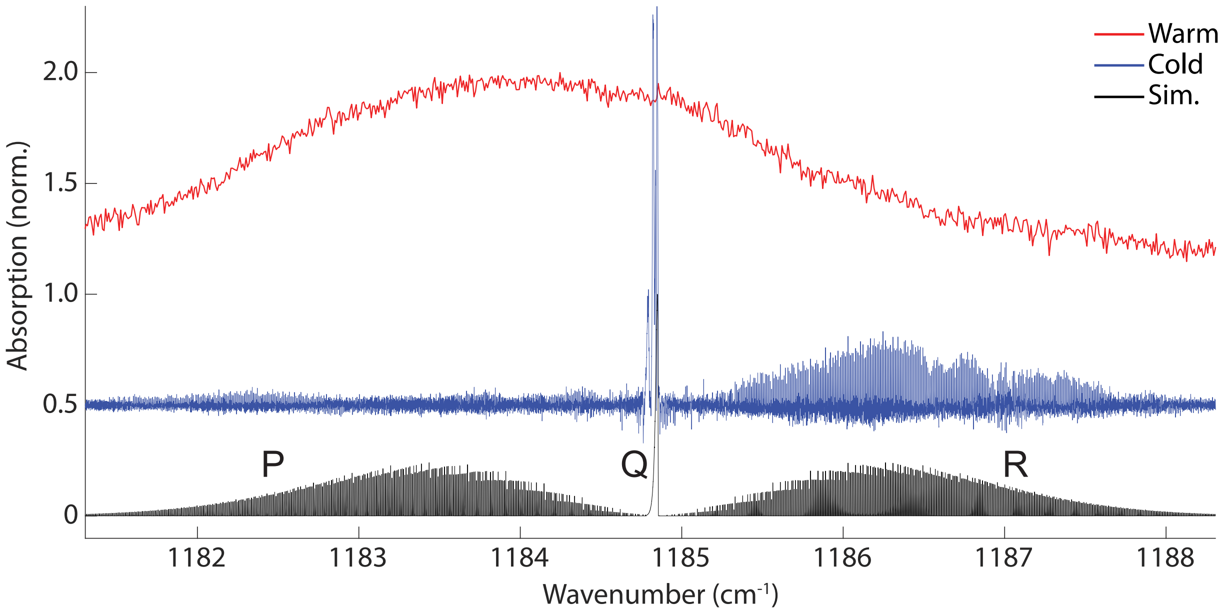

Figure 5.5: Survey spectrum of cold C_{60} near 8.5 μm (1185 cm^{-1}). Under optimized conditions (see text), the broad, continuous absorption from warm C_{60} (red, top trace) collapses to a narrow, well-resolved vibrational band from cold C_{60} in its vibrational ground state (blue, middle trace). A zeroth order simulation (black, bottom trace) shows the extended rotational fine structure of the P, Q, and R branches. (The simulation temperature is 150 K.)

5.3 Rotationally resolved C_{60} spectroscopy

5.3.1 Rovibrational wavefunctions

The rotational fine structure observed in the cold spectrum encodes a wealth of details about the quantum structure of C_{60}. To lowest order, the rotations of C_{60} are those of a spherical top with total angular momentum operator $\mathbf{J}$. These can be described with the symmetric top wavefunctions $|J, k, m\rangle$, which obey the standard eigenvalue relations

$$\mathbf{J}^2|J,k,m\rangle = J(J+1)|J,k,m\rangle, \tag{5.1}$$

$$J_z|J,k,m\rangle = k|J,k,m\rangle, \tag{5.2}$$

$$J_Z|J,k,m\rangle = m|J,k,m\rangle, \tag{5.3}$$

where factors of $\hbar$ have been suppressed. $J = 0, 1, 2, \ldots$ is the total angular momentum quantum number. J_z is the body-fixed z-axis projection operator of $\mathbf{J}$, and $k = -J, \ldots, +J$ is the body-fixed projection quantum number. Similarly, J_Z is the lab-frame Z-axis projection operator of $\mathbf{J}$, and $m = -J, \ldots, +J$ is the corresponding lab-frame projection quantum number.

The triply degenerate T_{1u} vibrational mode that gives rise to the 1185 cm^{-1} absorption band can be described with the vibrational normal coordinates q_x, q_y, and q_z. To lowest order, these three vibrational modes are equivalent to a 3D isotropic harmonic oscillator with vibrational angular momentum $\boldsymbol{\ell}$. The components of $\boldsymbol{\ell}$ are defined as

$$\ell_x = q_y p_z - q_z p_y, \tag{5.4}$$

with cyclic permutations for ℓ_y and ℓ_z. $p_{x,y,z}$ are the conjugate vibrational momenta of the coordinates $q_{x,y,z}$. The vibrational quantum states describing this triplet of T_{1u} modes are $|n, \ell, k_\ell\rangle$, where n is the total number of vibrational quanta, $\ell = n, n-2, n-4, \ldots$ is the vibrational angular momentum quantum number, and $k_\ell = -\ell, \ldots, +\ell$ is the body-fixed projection quantum number for $\boldsymbol{\ell}$. The vibrational angular momentum operator obeys the expected eigenvalue relations

$$\boldsymbol{\ell}^2|n,\ell,k_\ell\rangle = \ell(\ell+1)|n,\ell,k_\ell\rangle, \tag{5.5}$$

$$\ell_z|n,\ell,k_\ell\rangle = k_\ell|n,\ell,k_\ell\rangle. \tag{5.6}$$

Combined rovibrational wavefunctions can be written in an uncoupled representation by taking the direct product $|J,k,m\rangle|n,\ell,k_\ell\rangle$. These functions are simultaneously eigenfunctions of $\mathbf{J}^2$, J_z, J_Z, $\boldsymbol{\ell}^2$, and ℓ_z. As might be expected when encountering multiple angular momenta, it is useful to define a composite vector, the so-called "pure rotational" angular momentum,

$$\mathbf{R} \equiv \mathbf{J} - \boldsymbol{\ell}. \tag{5.7}$$

Eigenfunctions of $\mathbf{R}$ can be constructed from the uncoupled basis $|J,k,m\rangle|n,\ell,k_\ell\rangle$ using standard angular momentum coupling relations [150]. The coupled functions are $|R,k_R,J,\ell,n,m\rangle$, where R is the angular momentum quantum number for $\mathbf{R}$ and $k_R = -R,\ldots,+R$ is its body-fixed projection. The allowed values of R satisfy the usual triangle inequality, $|J-\ell| \le R \le J+\ell$. The lower state of the observed infrared band is the vibrational ground state with $n=\ell=0$. Thus, in the ground state, $R=J$. The upper state of the infrared band is the first excited state of the T_{1u} mode, with $n=\ell=1$. Here, R takes the values J and $|J\pm1|$.

5.3.2 Zeroth order effective Hamiltonians and energies

The rotational energy levels of each vibrational state are determined by an effective rotational Hamiltonian. For the ground vibrational state, the simplest zeroth order Hamiltonian is that of rigid spherical top,

$$\hat{H}_{\mathrm{gr}} = B''\mathbf{J}^2, \tag{5.8}$$

where B'' is the ground state rotational constant. The ground state wavefunctions $|R=J,k_R,J,0,0,m\rangle$ are eigenfunctions of this Hamiltonian,

$$\hat{H}_{\mathrm{gr}}|R=J,k_R,J,0,0,m\rangle = E_{\mathrm{gr}}(J)|R=J,k_R,J,0,0,m\rangle, \tag{5.9}$$

where

$$E_{\mathrm{gr}}(J) = B'' J(J+1). \tag{5.10}$$

At first glance, this may appear similar to the rotational level structure of a diatomic or linear molecule, which also has the simple $J(J+1)$ dependence. However, it is important to note that a spherical top contains an extra rotational degree of freedom and associated degeneracy relative to a linear rotor. In addition to the usual $g_J = (2J+1)$ degeneracy of the lab-frame projection quantum number m, there is an additional $g_R = (2R+1)$ degeneracy factor of the body-fixed projection quantum number k_R. For the ground state with $J = R$, the total degeneracy factor is $g_J g_R = (2J+1)^2$.

In the vibrationally excited state, the presence of non-zero vibrational angular momentum leads to a slightly more complicated effective Hamiltonian,

$$\hat{H}_{\mathrm{ex}} = \nu_0 + B' \mathbf{J}^2 - 2B'\zeta(\mathbf{J} \cdot \boldsymbol{\ell}), \tag{5.11}$$

where ν_0 is the vibrational band origin and B' is the excited state rotational constant. B' differs very slightly from B'' due to changes in the molecule's effective moments of inertia upon vibrational excitation. The last term in Eq. 5.11 accounts for Coriolis coupling between the total angular momentum $\mathbf{J}$ and the vibrational angular momentum $\boldsymbol{\ell}$. The strength of this coupling is determined by the Coriolis constant ζ, which encodes the geometric details of the vibrational mode and can take values $-1 \leq \zeta \leq 1$ [150]. By making use of the definition Eq. 5.7, we can rewrite the coupling term as

$$\begin{aligned} -2\mathbf{J} \cdot \boldsymbol{\ell} &= (\mathbf{J} - \boldsymbol{\ell})^2 - \mathbf{J}^2 - \boldsymbol{\ell}^2 \\ &= \mathbf{R}^2 - \mathbf{J}^2 - \boldsymbol{\ell}^2. \end{aligned} \tag{5.12}$$

(Note that $\mathbf{J}$ and $\boldsymbol{\ell}$ commute with each other.) The coupled wavefunctions for the upper state $|R = \{J, |J \pm 1|\}, k_R, J, 1, 1, m\rangle$ are now clearly eigenfunctions of $\hat{H}_{\mathrm{ex}}$ with eigenvalues

$$E_{\mathrm{ex}}(R, J) = \nu_0 + B' J(J+1) + B'\zeta \left[R(R+1) - J(J+1) - \ell(\ell+1) \right]. \tag{5.13}$$

The three possible values of $R = J, J \pm 1$ sort the excited state energies naturally into three manifolds with distinct J-dependencies

$$\begin{aligned} E_{\mathrm{ex}}^{(+)}(J) &= E_J + 2B'\zeta J, & R &= J+1 \\ E_{\mathrm{ex}}^{(0)}(J) &= E_J - 2B'\zeta, & R &= J \\ E_{\mathrm{ex}}^{(-)}(J) &= E_J - 2B'\zeta(J+1), & R &= J-1, \end{aligned} \tag{5.14}$$

where $E_J = \nu_0 + B'J(J+1)$ is the pure vibrational and rigid rotor contribution to the total energy. Physically, these three manifolds, which we label $T_{1u}^{(+)}$, $T_{1u}^{(0)}$, and $T_{1u}^{(-)}$, correspond to states where $\mathbf{J}$ and $\boldsymbol{\ell}$ are mutually antiparallel, perpendicular, and parallel, respectively. As in the ground vibrational state, each excited state level has a total degeneracy of $g_J g_R = (2J+1)(2R+1)$.

5.3.3 Spherical top rovibrational selection rules

We now examine the rovibrational selection rules for C_{60} to predict the expected transitions between the energy levels derived in the previous section. As with all atoms and molecules there is the usual $\Delta J = 0, \pm 1$ total angular momentum selection rule for electric dipole transitions (the only type we consider here). The high symmetry of spherical tops leads to another approximate, but typically quite strong, selection rule for the R and k_R quantum numbers. If we assume that the body-fixed dipole moment can be expanded only linearly in the T_{1u} vibrational coordinates, i.e.

$$\vec{\mu}_{\mathrm{bf}} \propto \vec{q}, \tag{5.15}$$

where $\vec{q} = (q_x, q_y, q_z)^T$, then it can be shown (see Appendix D) that the following commutation equalities hold between any *body-frame* component of $\boldsymbol{\ell}$ or $\mathbf{J}$ and any *lab-frame* component of the dipole moment operator $\vec{\mu}_{\mathrm{L}}$:

$$[\ell_\alpha, \mu_i] = [J_\alpha, \mu_i], \tag{5.16}$$

where $\alpha = x, y, z$ is a body-frame axis, and $i = X, Y, Z$ is a lab-frame axis. We therefore have

$$[R_\alpha, \mu_i] = 0, \tag{5.17}$$

and in particular

$$[\mathbf{R}^2, \mu_i] = 0, \tag{5.18}$$

$$[R_z, \mu_i] = 0. \tag{5.19}$$

These final two commutation relations mean that in T_{1u} fundamental vibrational bands in spherical tops, the eigenvalues of $\mathbf{R}^2$ and R_z cannot change, yielding the spherical top IR selection rules

$$\Delta R = \Delta k_R = 0. \tag{5.20}$$

Combined, the R- and J-selection rules result in a highly constrained set of transitions between the ground state and excited T_{1u} state. For a given lower state $|R = J, k_R, J, n = \ell = 0\rangle$ (omitting the m quantum number) there are at most three allowed transitions, one P-type ($\Delta J = -1$), one Q-type ($\Delta J = 0$), and one R-type ($\Delta J = +1$),

$$\begin{aligned}
|R = J, k_R, J, n = \ell = 0\rangle &\rightarrow |R = J, \quad k_R,\ J-1,\ n = \ell = 1\rangle,\\
|R = J, k_R, J, n = \ell = 0\rangle &\rightarrow |R = J, \quad k_R,\ J, \qquad n = \ell = 1\rangle,\\
|R = J, k_R, J, n = \ell = 0\rangle &\rightarrow |R = J, \quad k_R,\ J+1,\ n = \ell = 1\rangle.
\end{aligned}$$

For the edge case of the lower state $|R = J = 0\rangle$, there is only a single (R-type) transition to the $|R = 0, J = 1\rangle$ upper state.

These transitions are summarized in the level diagram shown in Fig. 5.6. Note that a given rotational level of the excited vibrational state is accessed via an IR transition from only a single rotational level of the ground vibrational state. This restriction is due to the spherical top R-selection rule. In most molecules, which are less symmetrical, the situation is different: a given upper state is accessed by transitions from multiple lower states. This means that we are unable to determine ground state combination differences via the zeroth order allowed transitions in spherical tops. This in turn reduces the number of parameters in the effective Hamiltonians that are determinable from the measured spectrum.

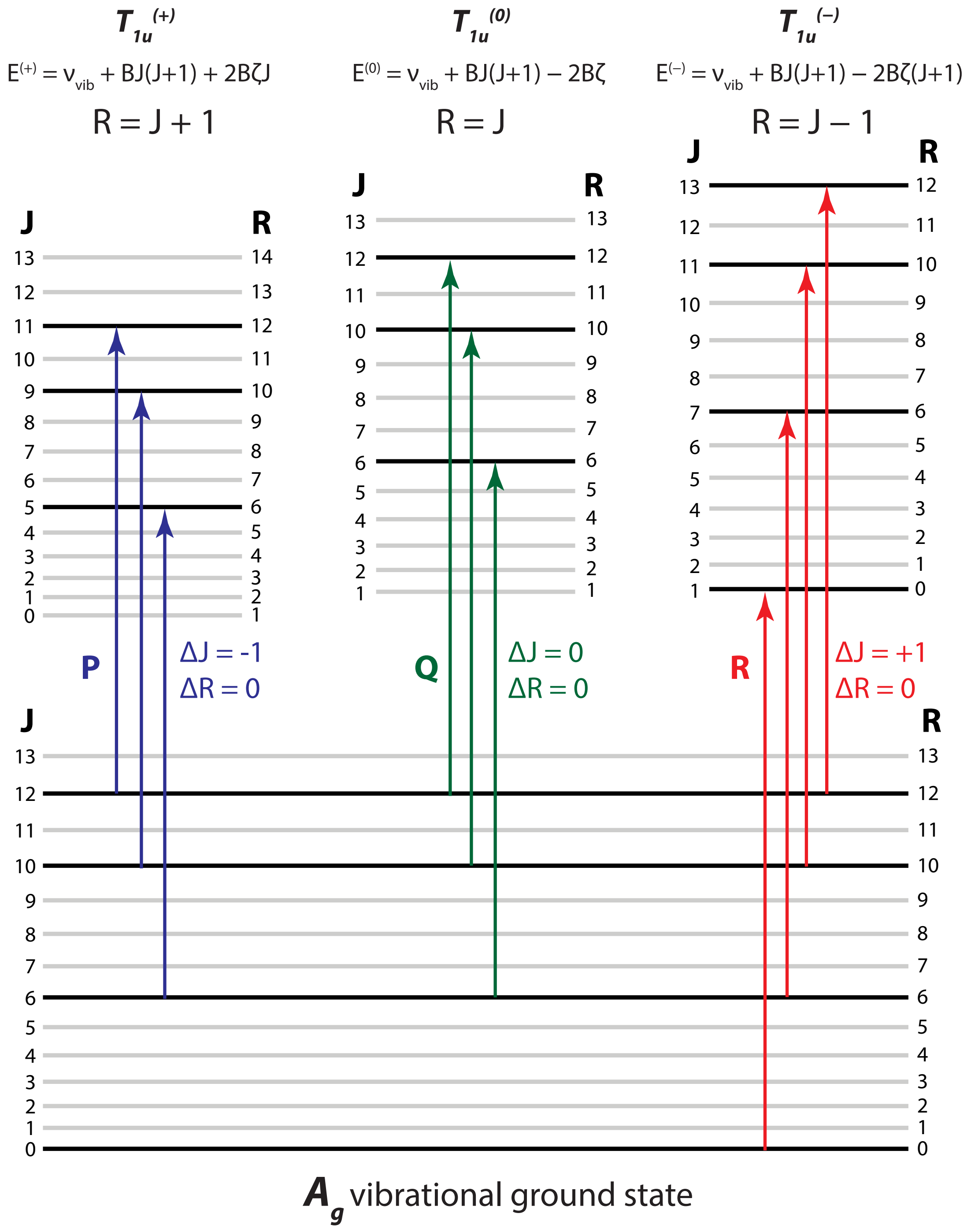

Figure 5.6: Spherical top energy levels and IR transitions. The lower half of the diagram shows rotational levels of the ground vibrational state. The upper half shows those for the excited vibrational state, sorted into three Coriolis manifolds ($T_{1u}^{(+)}$, $T_{1u}^{(0)}$, and $T_{1u}^{(-)}$) according to the relative values of the R and J quantum numbers. Example P, Q, and R transitions are shown. Solid black lines indicate rotational levels that have non-zero nuclear spin degeneracy factors, while gray lines indicate rotational levels that have nuclear spin degeneracy factors of zero (for $^{12}C_{60}$).

5.3.4 Nuclear spin statistics

An unpurified sample of C_{60} contains many isotopologues due to the large number (i.e. sixty) of possible carbon substitution sites. Taking only the ^{12}C and ^{13}C nuclear isotopes to have non-negligible abundance, the $^{12}C_{60-n}{}^{13}C_n$ isotopologue fraction is

$$P_n = (1-p)^{60-n} p^n \binom{60}{n}, \tag{5.21}$$

where $p = 1.1\%$ is the natural abundance of ^{13}C [151]. Therefore, only about 52% of natural C_{60} is pure $^{12}C_{60}$, 34% is singly substituted $^{12}C_{59}{}^{13}C$, and 11% is doubly substituted $^{12}C_{58}{}^{13}C_2$. The remaining 3% is more highly substituted. Note that there is only a single isotopomer of $^{12}C_{59}{}^{13}C$ (which has C_s symmetry) because each carbon site of the truncated icosahedron is structurally equivalent. There are several $^{12}C_{58}{}^{13}C_2$ isotopomers owing to the different relative positions of two substitution sites.

The nuclear spin statistics of each of these isotopologues have important effects on their rovibrational structure and spectra by modifying the g_R degeneracy factor. We consider first the major $^{12}C_{60}$ isotopologue, which contains sixty identical spin-0 ^{12}C nuclei. A permutation P of any subset of these bosonic nuclei must leave the total molecular wavefunction $|\Psi_{\text{tot}}\rangle$ unchanged,

$$P|\Psi_{\text{tot}}\rangle = +|\Psi_{\text{tot}}\rangle. \tag{5.22}$$

Pure rotation point group elements, such as E (identity) and C_n (a rotation of $2\pi/n$ about some axis), correspond to permutations of ^{12}C nuclei and must follow Eq. 5.22. Point group elements i (body-frame inversion), S_n (improper rotations), and σ (reflections) correspond to permutation-inversion operations P^*, i.e. they involve a pure permutation P combined with inversion of all coordinates through some space-fixed origin. These operations must follow

$$P^*|\Psi_{\text{tot}}\rangle = \pm|\Psi_{\text{tot}}\rangle \tag{5.23}$$

depending on whether $|\Psi_{\text{tot}}\rangle$ is a state of total + parity or total − parity, respectively. Inspection of the I_h character table (Table C.1) shows that the only irreducible representations of I_h that meet these requirements are A_g (for + parity states) and A_u (for − parity states). We therefore require that $|\Psi_{\text{tot}}\rangle$ belong to one of these two irreducible representations.

The total molecular wavefunction can be factored into electronic, rotation-vibration, and nuclear spin factors,

$$|\Psi_{\text{tot}}\rangle = |\psi_{\text{el}}\rangle|\psi_{\text{rovib}}\rangle|\psi_{\text{nuc}}\rangle. \tag{5.24}$$

We consider here only the electronic ground state, which is closed-shell and has A_g symmetry. Each ^{12}C nucleus is spin-0, and therefore the total nuclear spin wavefunction is trivially A_g as well. This means that the symmetry of the total molecular wavefunction is determined by that of the rovibrational factor, i.e. the $|R, k_R, J, \ell, n, m\rangle$ wavefunctions.

To determine the rovibrational symmetry of the $|R, k_R, J, \ell, n, m\rangle$ wavefunctions, let us review some fundamental results from the interface of angular momentum theory and group theory. Recall that the set of all rotations about *lab-fixed* axes forms a group isomorphic to SO(3) [18, 152]. We label this particular version of the rotation group $\text{SO}(3)_\text{L}$ (‘L’ for ‘lab-fixed’). For a given value of total angular momentum J, the $2J + 1$ wavefunctions $|R, k_R, J, \ell, n, m\rangle$ with $m = -J, \ldots, J$ span the $D^{(J)}$ irreducible representation of $\text{SO}(3)_\text{L}$. All the symmetry properties with respect to $\text{SO}(3)_\text{L}$ are determined by the values of J and m.

In a similar fashion, we define a second group by the set of all rotations about *molecule-fixed* axes and call it $\text{SO}(3)_\text{M}$ (‘M’ for ‘molecule-fixed’). For a fixed orientation of the molecular frame in space, there is a one-to-one equivalency between the elements of $\text{SO}(3)_\text{L}$ and $\text{SO}(3)_\text{M}$. However, this mapping changes if the orientation of the molecule in space changes, and the two groups have distinct meanings.[2] Just as J and m determine the lab-frame symmetry properties, R and k_R determine the molecule-frame symmetry properties. In particular, for a given value of R, the $2R+1$ wavefunctions $|R, k_R, J, \ell, n, m\rangle$ with $k_R = -R, \ldots, R$ span the $D^{(R)}$ irreducible representation of $\text{SO}(3)_\text{M}$.

---

[2] For example, if the x, y, z molecule-fixed axes are aligned with the X, Y, Z lab-frame axes, respectively, then a rotation of $\pi/2$ about z, say, which is an element of $\text{SO}(3)_\text{M}$, is the same as a rotation of $\pi/2$ about Z, an element of $\text{SO}(3)_\text{L}$. If the molecule is reoriented in space such that the z-axis is parallel to lab frame X-axis, then that same element of $\text{SO}(3)_\text{M}$ is equal to a different element of $\text{SO}(3)_\text{L}$ (i.e. $\pi/2$ about X).

For a perfectly spherical molecule, $\mathrm{SO}(3)_\mathrm{M}$ would indeed be the true rotational symmetry group. C_{60} is of course not a perfect sphere, and its rotation group is the icosahedral group I, which is a sub-group of $\mathrm{SO}(3)_\mathrm{M}$. (The full molecular symmetry group I_h is just a direct product of I with the inversion group $\{E, i\}$.) We can determine the icosahedral symmetries of the $|R, k_R, J, \ell, n, m\rangle$ wavefunctions by using the correlations of the irreducible representations of $\mathrm{SO}(3)_\mathrm{M}$ and I [153]. This procedure is carried out in Appendix C and the results summarized in Table C.2. The additional g/u label for the full I_h group is determined by the character under the i operation, which comes only from the electronic and vibrational factors (in this case, the parity of ℓ). All rotational levels of the groud vibrational state are g, and all rotational levels of the excited T_{1u} vibrational state are u.

We can now take all these results together. Bose-Einstein statistics imply that only rovibrational states with $A_{g/u}$ symmetry are allowed. Table C.2 tells us which $|R, k_R, J, \ell, n, m\rangle$ wavefunctions correlate to $A_{g/u}$. For $R = 0, 6, 10, 12, 15, 16, 18, 20-22$, and $24-28$, we can construct only a single linear combination of k_R states that transform as $A_{g/u}$. All other values of $R < 30$ have no linear combination of k_R states that transforms as $A_{g/u}$ and thus do not exist. For $R > 30$, we can always find at least one linear combination of k_R states that transform as $A_{g/u}$, but this is far fewer than the original $g_R = 2R + 1$ degeneracy. In the high-R limit, only 1 in 60 states is allowed. These extreme nuclear spin statistics are accounted for in Fig. 5.6, where levels that do not exist in ${}^{12}\mathrm{C}_{60}$ are faded out. For low values of R, "holes" appear in the spectrum where missing lines would be expected in the absence of spin statistics. For higher values of R, the degeneracy factors result in characteristic integer-ratio intensity patterns.

A single ${}^{13}\mathrm{C}$ substitution destroys the indistinguishability of the remaining fifty-nine ${}^{12}\mathrm{C}$ nuclei, as they can now be "labeled" by their position relative to the unique ${}^{13}\mathrm{C}$ nucleus. Therefore, there are no spin-statistical effects expected in the ${}^{12}\mathrm{C}_{59}{}^{13}\mathrm{C}$ spectrum. Of the several ${}^{12}\mathrm{C}_{58}{}^{13}\mathrm{C}_2$ isotopomers, most are asymmetric and do not exhibit any statistical effects. Those in which the two ${}^{13}\mathrm{C}$ nuclei are in symmetrical positions will have some non-trivial spin statistics (similar to those of ortho/para $\mathrm{H}_2\mathrm{O}$), though not as extreme as for the case of ${}^{12}\mathrm{C}_{60}$. We do not consider those here.

5.3.5 Rovibrational spectrum simulation

Taking the results of the last several sections, namely the zeroth order rovibrational energies, selection rules, and spin statistics, leaves the simulated infrared spectrum plotted in black in Fig. 5.5. The spectrum consists of a strong central Q branch, composed of many overlapped transitions, surrounded by extended P and R branches containing transitions evenly spaced by approximately $(B''+B')(1-\zeta) \approx 0.0078\ \mathrm{cm}^{-1}$. Visual inspection of the survey spectrum shows that the simulated Q and R branches qualitatively agree with the appearance of the observed spectrum, while the P branch does not. The following sections will examine each region of the spectrum in more detail.

5.4 Rotational analysis of the 8.5 μm band

5.4.1 R branch

The observed R branch contains a highly uniformly spaced progression of well resolved rovibrational transitions. We observe about three hundred individual features above the absorption noise baseline, a subset of which are illustrated in Fig. 5.7a. As discussed above, the R(J) transitions correspond to those from the ground vibrational state to the "$R = J - 1$" manifold of the excited vibrational state (Fig. 5.6), with $\Delta J = +1, \Delta R = 0$ selection rules. Using the zeroth order energies, we expect these transitions to occur at frequencies

$$\begin{aligned}\nu[\mathrm{R}(J)] &= E_{\mathrm{ex}}^{(-)}(J+1) - E_{\mathrm{gr}}(J)\\ &= \nu_0 + B'(J+1)(J+2) - 2B'\zeta(J+2) - B''J(J+1)\\ &= \nu_0 + (2\bar{B} + \Delta B)(1-2\zeta) +\\ &\qquad J[2\bar{B}(1-\zeta) + \Delta B(2-\zeta)] +\\ &\qquad J^2\Delta B, \end{aligned} \tag{5.25}$$

where $\bar{B} = (B' + B'')/2$ is the mean of the ground and excited state rotational constants and $\Delta B = B' - B'' \ll \bar{B}$ is their difference. The primary J-dependence is through the linear term,

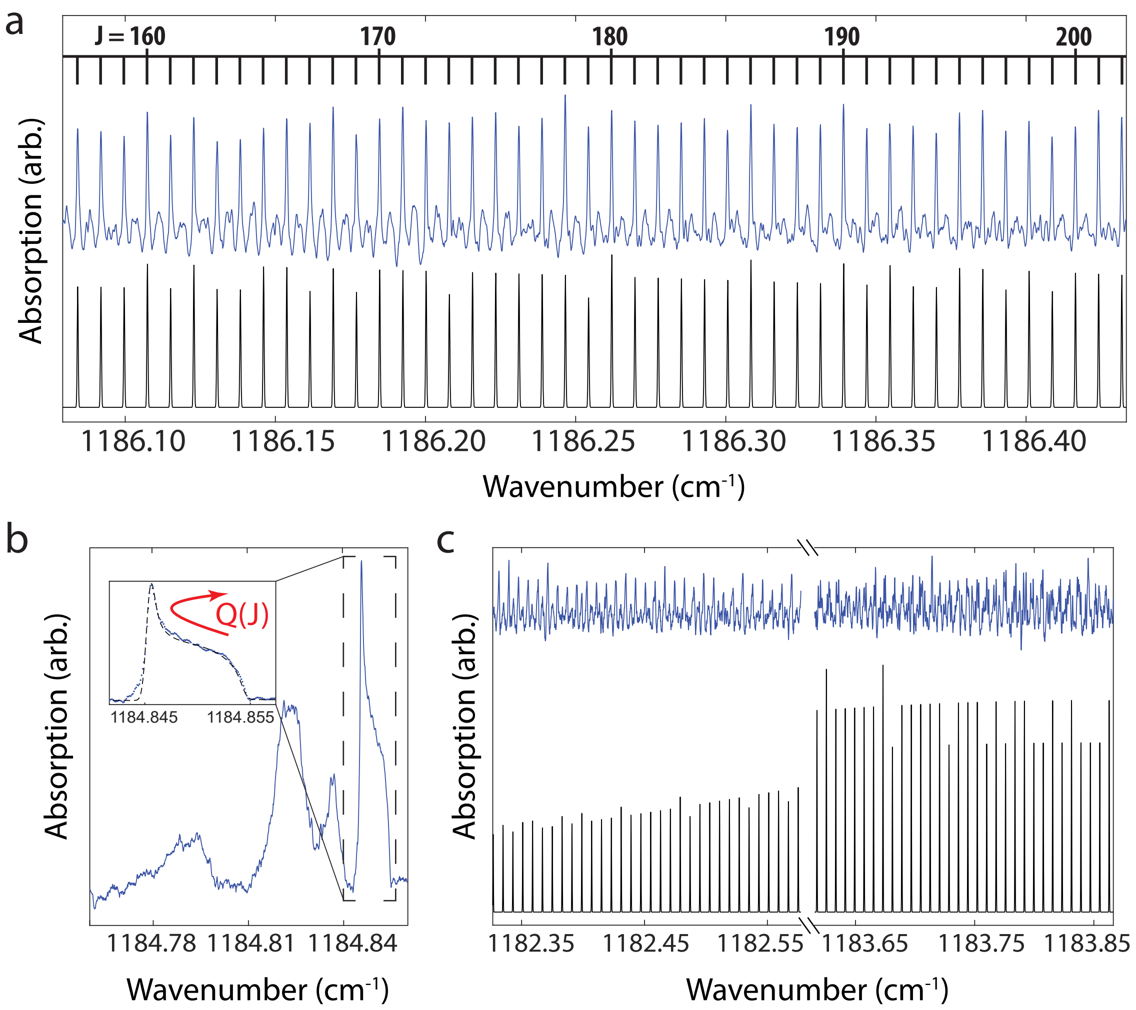

Figure 5.7: Detailed views of the 8.5 μm band of C_{60}. (a) The measured (blue, top) and simulated (black, bottom) R(J) transitions are shown from $J = 160$ to 200. The characteristic intensity alternation patterns are a signature of $^{12}C_{60}$ nuclear spin statistics. (b) The band origin region shows several features, including the $^{12}C_{60}$ Q branch extending from 1184.845 to 1184.855 cm^{-1}. The inset shows a fit to Q branch contour using a quartic centrifugal distortion model (see text). The remaining features are speculatively assigned to $^{12}C_{59}{}^{13}C$. (c) The P branch region contains weaker and more congested transitions that are in qualitatively disagreement with the zeroth order simulation. This is possible evidence of icosahedral fine structure or dark state perturbers.

whose coefficient is dominated by the $2\bar{B}(1-\zeta)$ contribution. The spacing between adjacent R(J) transitions should be approximately equal to this quantity. There is also a small quadratic dependence on J proportional to ΔB.

Approximately three hundred R(J) transitions with $J \approx 60 - 360$ were assigned and fitted (see Fig. 2.11b) to determine their center frequencies. These frequency positions were then used to fit the parameters in Eq. 5.25. The frequencies and fit residuals are shown in Fig. 5.8, and the fitted spectroscopic constants are summarized in Table 5.1. The complete line list and raw spectrum is available in a permanent online data repository [154].

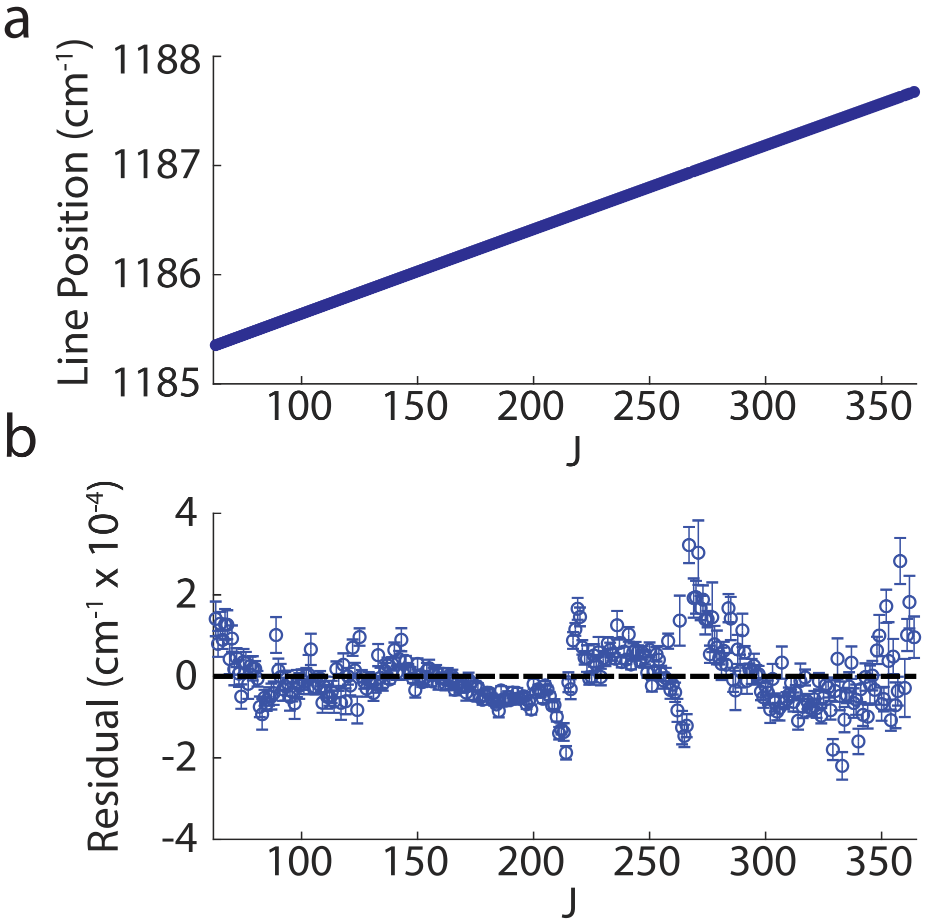

Figure 5.8: Fit of the C_{60} R branch. (a) The R(J) line positions are shown for $J \approx 60 - 360$. They exhibit a nearly linear dependence on J. (b) The residuals from fitting to Eq. 5.25 have a root-mean-square value of 7.4×10^{-5} cm^{-1} and show at least two possible avoided crossings near $J = 220$ and $J = 270$. The individual error bars are the 1σ line center uncertainties, which have a mean value of 2.5×10^{-5} cm^{-1}.

We confirmed the correct J assignment in two ways. First, the fitted spectroscopic parameters were used to extrapolate the R(J) line positions to the fictitious "R(-1)" transition. This should occur at $\nu[\mathrm{R}(-1)] = \nu_0 - (2\bar{B} + \Delta B)\zeta$, which is coincident with the zeroth order Q(1) position

Table 5.1: Fitted spectroscopic parameters of the C_{60} R branch with Eq. 5.25. The fit residuals have a total root-mean-square error of 7.4×10^{-5} cm^{-1}. The 1σ uncertainty in the fitted parameters is shown in parentheses in units of the last digit.

Parameter	Value (cm^{-1})
$\nu_0 + (2\bar{B} + \Delta B)(1 - 2\zeta)$	1184.86196(3)
$2\bar{B}(1 - \zeta) + \Delta B(2 - \zeta)$	0.0078300(3)
ΔB	$-2.876(6) \times 10^{-7}$

up to small differences of $\mathcal{O}(\Delta B)$. This agreement is shown in Fig. 5.9. A second confirmation is provided by the nuclear spin statistics intensity patterns, which have a very strict and characteristic dependence on J. As can be seen in Fig. 5.7a, the observed intensity patterns are in agreement with those predicted by the symmetry analysis described in Section 5.3.4. Based on both frequency and intensity information, we can have confidence in the correct J assignment and therefore the validity of the spectroscopic constants in Table 5.1.

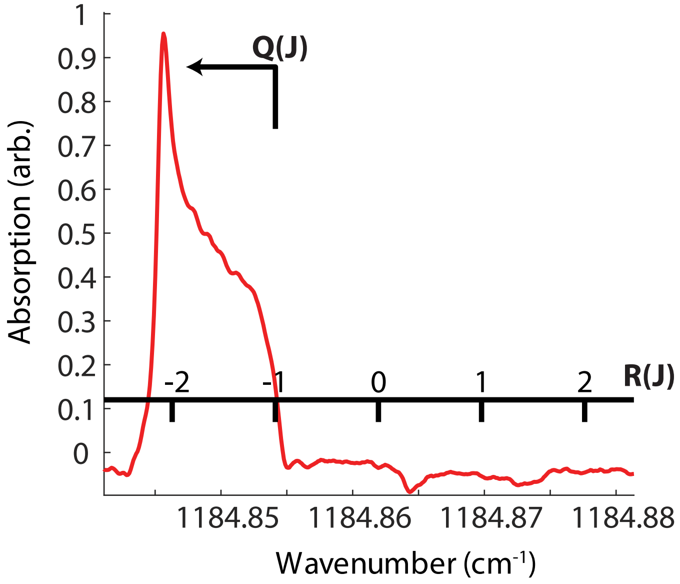

Figure 5.9: J assignment via R(J) extrapolation. The extrapolated position of the fictitious R(-1) transition coincides with the onset of the Q branch near 1184.855 cm^{-1}, confirming the correct R branch J assignment.

The rotational fine structure of the R branch spectrum provides detailed structual information about isolated C_{60} molecules. Our initial analysis does not allow an indepenent determination of B'' and ζ due to the restrictive $\Delta R = 0$ spherical top selection rule. However, if we assume a range of $\zeta = -0.30$ to -0.45 based on theoretical calculations [155], we can estimate $B'' = \frac{1}{hc}\frac{\hbar^2}{2I} \approx 0.0027$ to 0.0030 cm^{-1}, where I is the effective moment of inertia of the ground vibrational state. For a spherical shell of mass m and radius r, the moment of inertia is $I = \frac{2}{3}mr^2$, yielding a C_{60} radius in the range of $r = 3.4$ to 3.6 Å. This is consistent with a previous gas-phase electron diffraction measurement of 3.557(5) Å, which includes thermal averaging effects that lengthen the measured radius relative to that of the vibrational ground state [119]. Further analysis of the rotational fine structure of $^{12}C_{60}$ (and eventually $^{12}C_{59}{}^{13}C$) will be necessary to constrain B'' and ζ independently and completely determine the gas-phase structural parameters. High resolution spectra in combination with the large range of observed J values provide highly precise spectroscopic constants, which will ultimately provide an equally precise structure determination. Our measured value of ΔB implies that the effective C_{60} radius increases by only 0.005% upon excitation of the observed vibrational mode, which is primarily of a surface-tangent C$-$C bond stretching character. Furthermore, the narrow IR transition linewidths (mostly Doppler-limited to about 20 MHz) to the excited vibrational state provide a lower bound for its IVR lifetime of at least 8 ns, despite being embedded in a dense manifold of dark vibrational states (see Fig. 4.5).

5.4.2 Q branch

The Q branch region of the 8.5 μm band is shown in Fig. 5.7b. This 0.1 cm^{-1}-wide window contains several features with complex rotational contours. We assign the blue-most feature, shown in the inset Fig. 5.7b, to $^{12}C_{60}$. The Q(J) transitions access the central Coriolis manifold of the excited vibrational state, which consists of rotational states satisfying $R = J$ (Fig. 5.6). According to the zeroth order energy expressions (Eqs. 5.10,5.14), these Q(J) transitions should occur at frequencies

$$\begin{aligned}\nu[\mathrm{Q}(J)] &= E_{\mathrm{ex}}^{(0)}(J) - E_{\mathrm{gr}}(J)\\ &= \nu_0 + B'J(J+1) - 2B'\zeta - B''J(J+1)\\ &= \nu_0 - (2\bar{B} + \Delta B)\zeta + \Delta B\, J(J+1). \end{aligned} \tag{5.26}$$

Due to the small quadratic J-dependence proportional to ΔB, these transitions lie close to one another, resulting in an unresolved rotational branch contour. According to the zeroth order model, the Q(J) frequencies should be monotonically red-degraded (as $\Delta B < 0$). However, the observed contour shows a clear band head associated with an initial red degradation towards lower frequencies and then a reversal back towards higher frequencies, suggesting the presence of centrifugal distortion (CD) effects, which arise from the flexibility of the carbon skeleton.

The simplest addition to the zeroth order effective Hamiltonians is a quartic scalar CD operator, $-D\mathbf{J}^4$, which contributes $-DJ^2(J+1)^2$ to the total rovibrational energy. The quartic CD constant can take different values for the ground and excited vibrational states, D'' and D' respectively, and their difference contributes a new quartic term to the Q(J) transition frequencies

$$\nu[\mathrm{Q}(J)] = \nu_0 - (2\bar{B} + \Delta B)\zeta + \Delta B\, J(J+1) - \Delta D\, J^2(J+1)^2, \tag{5.27}$$

where $\Delta D = D' - D''$. A rotational temperature T_{rot} and a line width must also be included to fit the intensity profile of the Q branch contour. Using such a model, a contour can be successfully fitted to the measured profile (dashed line shown in the inset of Fig. 5.7b). Here, the values of the band origin, ΔB, and the line width are fixed their values determined in the R branch fit, while ΔD and T_{rot} are optimized by a non-linear least squares fit to $-2.27(1) \times 10^{-12}$ cm^{-1} and 103(1) K, respectively. However, it is unclear how meaningful the fitted value of T_{rot} is. For example, the rotational temperature from a fit to the R branch intensities yields $T_{\mathrm{rot}} = 150(2)$ K (Fig. 2.11). This latter value is expected to be more reliable as it is derived from the relative intensities of many individually resolved transitions, rather than the total contour of the many unresolved Q(J) transitions. If T_{rot} is held fixed to the R branch-derived value, the fitted value of ΔD from the Q branch contour changes slightly to $-2.10(3) \times 10^{-12}$ cm^{-1}. For a fixed value of ΔB, the value of ΔD is largely determined by the width of the Q branch contour, explaining why ΔD is relatively insensitive to T_{rot} in the fit. Therefore, a ΔD value in the range of -2.0 to -2.5×10^{-12} cm^{-1} seems like a reasonable conservative estimate.

Canonical rovibrational perturbation theory indicates that the quartic CD constant should be of the order of magnitude of B^3/ω^2, where ω is a vibrational frequency [156]. Taking $B \sim 0.003$ cm^{-1} and $\omega \sim 500$ cm^{-1} yields $D \sim 10^{-13}$ cm^{-1}. To confirm this order of magnitude prediction, we computed the density functional theory (DFG) harmonic force constants of C_{60} using the B3LYP functional with a 6-31g basis set, as implemented in the NWChem package [157]. This calculation predicts $D = 5.8 \times 10^{-13}$ cm^{-1}. The R branch transition frequencies also provide information on the magnitude of D. Here, the presence of quartic CD manifests in a J^3 dependence of the line positions. An attempt to include a cubic term in the R branch fit shows that there is no statistically significant J^3 dependence over the $J = 60 - 360$ range to within our frequency measurement uncertainty, suggesting an upper bound of $|D| < 1 \times 10^{-11}$ cm^{-1}, consistent with the theoretical estimates. If we assume the DFG prediction to be correct for the ground state constant D'', then the Q branch contour implies that the upper state value D' is several times larger in magnitude than D'' and of opposite sign. This situation is certainly plausible, but would imply that local perturbations or higher order CD effects cause a significant change to the effective Q branch D' value. Unfortunately, it is difficult to explore these details with only the relatively crude contour information of the unresolved Q branch. Nonetheless, it is clear from the observed structure that effects beyond the simple zeroth order rigid spherical top are important.

As can be seen in Fig. 5.7b, there are three features red-shifted from the $^{12}C_{60}$ Q branch contour. While there are multiple explanations for them, including vibrational hot bands, we believe the most likely possibility is that they belong to the $^{12}C_{59}{}^{13}C$ isotopologue, which occurs at a 2:3 abundance relative to the pure ^{12}C isotopologue. A single ^{13}C substitution breaks the triple degeneracy of the T_{1u} vibrational mode, resulting in three closely spaced vibrational origins of comparable intensity [158]. The lack of clear $^{12}C_{59}{}^{13}C$ signatures in the R branch region, on the other hand, can be explained by the spectroscopic splittings that result from the inequivalent moments of inertia. This has a relatively smaller effect on the already unresolved Q branch contours. We do not attempt a detailed analysis of the putative $^{12}C_{59}{}^{13}C$ features here due to the significantly more complex rotational fine structure expected for this asymmetric isotopologue [158].

5.4.3 P branch

In contrast to the simple structure of the R branch, the P branch exhibits a less regular, more congested pattern of transitions. Both the number and position of absorption features in the observed spectrum disagree with the zeroth order simulation, which is based on the spectroscopic parameters determined from the R branch fit. In the survey spectrum of this band (Fig. 5.5), there is an obvious asymmetry in the absorption intensity envelope of the P branch relative to the R branch. Beginning at the band origin near 1184.9 cm^{-1} and moving down in frequency, some low-J features do begin to appear, though they are relatively weak and irregular as shown in the right half of Fig. 5.7c. As one continues through the P branch, the absorption intensity vanishes before re-emerging at the high-J tail (left half of Fig. 5.7c). In this last portion, the absorption lines have approximately the same spacing as in the R-branch, but are offset from the positions expected from the R branch fit. The apparent decrease in the integrated absorption cross section may in fact just be an artifact of the high-pass filtering performed on the cold C_{60} FTS spectrum (see Section 2.4.1), which removes any broad, quasi-continuous component. Therefore, one explanation for the appearance of the P branch is that whatever mechanism is responsible for the splitting of the low-J transitions continues to intensify in the middle of the branch. Here, the congestion is so severe that the spectrum is continuous and unresolvable, and thus subtracted from the high-pass filtered signal. As J increases into the tail of the branch, the splitting mechanism causes the transitions to re-coalesce with their neighbors (a “rotational echo” of sorts), explaining why they have a similar spacing as, but a systematic offset from, the zeroth order simulation.

5.5 Discussion

One of the clearest results of our initial spectroscopic analysis is the confirmation of the characteristic $^{12}\mathrm{C}_{60}$ rotational intensity patterns, representing the most extreme example of nuclear spin statistical effects in a molecular system. This observation illustrates the consequences of symmetry in C_{60} in a fundamentally different way than previous spectroscopic studies. In the latter case, the icosahedral symmetry of C_{60} has been established based on observed selection rules and energetics [113–118, 159]. However, these effects are classical in nature and boil down to certain matrix element integrals being equivalent to each other or to zero at the level of experimental sensitivity. In contrast, nuclear spin statistics effects are fundamentally quantum mechanical in nature, deriving from the simultaneous indistinguishability of all sixty $^{12}\mathrm{C}$ nuclei and the perfect icosahedral symmetry of their geometrical arrangement.

The most glaring spectroscopic puzzle uncovered so far is the qualitatively different behavior of the R and P branches of the 8.5 μm band. The R branch exhibits no deviation from the simplest possible zeroth order structure, except for what appear to be very weak, local avoided crossings. This in and of itself is a remarkable fact given the very high values of angular momentum observed in the spectrum, i.e. $J \sim 360$. This "textbook" regularity of the R branch structure makes it difficult to find a consistent explanation for the much more complex structure observed in the P branch. As shown in Fig. 5.6, the spherical top IR selection rules imply that the P, Q, and R branch transitions all access mutually exclusive sets of upper states. It is therefore possible that some effect perturbs the P branch (connected to the $T_{1u}^{(+)}$ manifold) while sparing the R branch (connected to the $T_{1u}^{(-)}$ manifold). Such a perturbation could fall into one of two cases: (i) a local perturbation caused by resonant interactions with one or a few accidentally degenerate dark state(s) or (ii) non-local perturbations with the entire rovibrational manifold that manifest as high order Coriolis and centrifugal distortion terms in each vibrational state's effective Hamiltonian. In case (i), it is difficult to imagine that any state that interacts strongly enough to so thoroughly perturb the $T_{1u}^{(+)}$ manifold does not also do so to the $T_{1u}^{(-)}$ manifold. The total spin-rovibronic symmetry of each excited state sub-level is A_u, and therefore there is no rigorous symmetry selection rule that protects one manifold, but not the other.

In case (ii), the icosahedral symmetry severely restricts the form that high order terms can take in effective rovibrational Hamiltonians [18, 160]. In the ground vibrational state, where $\ell = 0$, the rotational Hamiltonian only contains powers of the total angular momentum $\mathbf{J}$ and its body-fixed components. The simplest high order contributions are of the form $(\mathbf{J}^2)^n$, representing the quartic ($n = 2$), sextic ($n = 3$), etc. spherical centrifugal distortion operators.[3] These operators have rank-0 tensor character under $\mathrm{SO}(3)_\mathrm{M}$, and the Wigner-Eckart theorem prevents them from breaking the degeneracy of the $2J + 1$ body-fixed projections of $\mathbf{J}$ [152, 161].

Splittings of rovibrational transitions must come from non-spherical operators (rank $k > 0$). We still require that these transform as the totally symmetric representation A_g. The correlation properties between $\mathrm{SO}(3)_\mathrm{M}$ and I_h (Table C.2) tell us that the first allowed non-spherical operator has rank-6 character. It takes the form

$$\Omega^{(6)} = \frac{\sqrt{11}}{5}\Omega_0^{(6)} + \frac{\sqrt{7}}{5}\left(\Omega_5^{(6)} - \Omega_{-5}^{(6)}\right), \tag{5.28}$$

where $\Omega_q^{(k)}$ is the q^{th} component of a spherical tensor operator of rank k [162,163]. The eigenvalues of this operator, and therefore the expected first-order energy splittings caused by it, are independent of the physical details of the molecule. They are determined only by the algebraic tensor structure of $\Omega^{(6)}$. Figure 5.10 illustrates the patterns of such icosahedral splittings for C_{60} rotational states.

The $\Omega^{(6)}$ term is the simplest non-spherical tensor operator one can consider. In the vibrationally excited state, the presence of non-zero vibrational angular momentum $\boldsymbol{\ell}$ introduces many additional operators resulting in a complicated menagerie of icosahedral splitting patterns. Numerical exploration of the allowed possibilities, however, suggests that none affects the spectrum in such a way that the R branch is left unperturbed over the entire observed $J = 60 - 360$ range while simultaneously accounting for the P branch behavior. Observation of low-J lines, which are below the comb spectrum noise baseline for $J < 60$, will undoubtedly assist in sorting out these

---

[3] Only even powers of $\mathbf{J}$ can appear to preserve time-reversal symmetry [18].

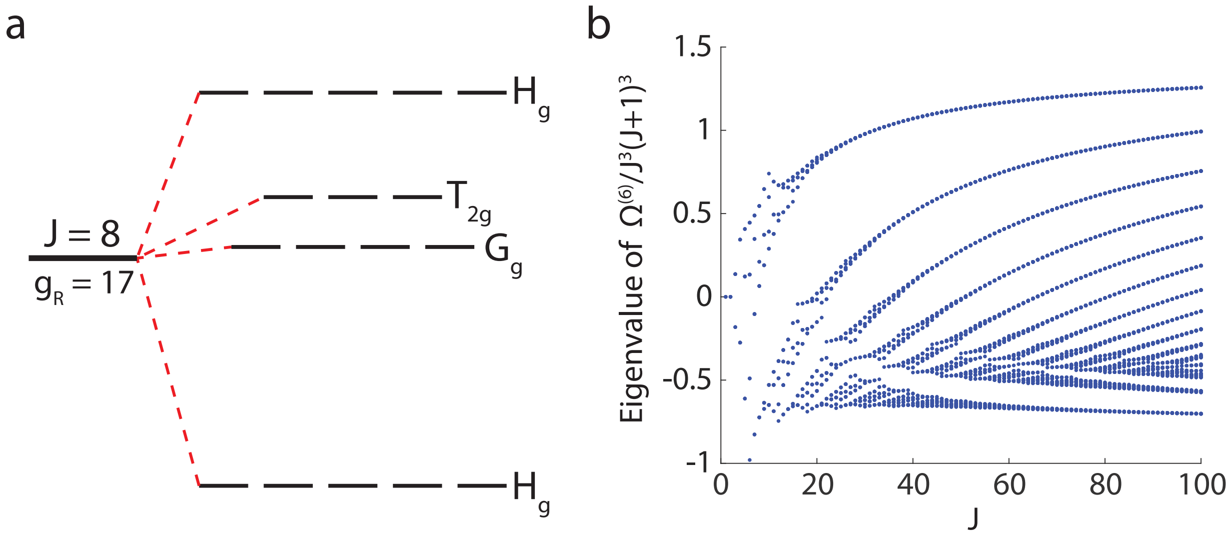

Figure 5.10: Icosahedral splitting patterns of C_{60} via the $\Omega^{(6)}$ operator. (a) Under spherical symmetry, the $J = 8$ rotational level would contain $g_R = 2J + 1 = 17$ degenerate components, corresponding to the different projections of **J** in the body-fixed frame. These split into multiplets of reduced degeneracy according to the symmetry correlations between $\mathrm{SO}(3)_\mathrm{M}$ and I_h (see Table C.2). (b) The complete eigenvalue structure of $\Omega^{(6)}$ as a function of angular momentum quantum number J. The characteristic clustering patterns are related to the semi-classical rotational energy surfaces of a deformable icosahedral top [162, 163].

complications.

5.6 Conclusions

The high resolution spectroscopy reported in this chapter provides a first glimpse at the unique rovibrational structure and symmetry of C_{60}. Beyond the detailed spectroscopic aspects particular to C_{60}, rovibrational quantum state resolved measurements establish the possiblity of using fullerenes as platforms to explore quantum science. For example,

- Small fullerenes straddle the border between molecular-scale structure and bulk materials [164]. What can the vibrational and electronic structure of C_{60} tell us about phonons and electronic transport in extended systems?
- C_{60} in its rest frame and ground rovibrational state represents a perfect atomic lattice at

absolute zero temperature. The pure $^{13}\mathrm{C}_{60}$ isotopologue is therefore a pristine instance of a spherical spin-1/2 lattice [165, 166]. Can rovibrational quantum state control of single $^{13}\mathrm{C}_{60}$ molecules be used to study and manipulate the many-body dynamics of a large spin network?

- Fullerenes present the unique capability of encapsulating atoms and small molecules within their hollow core [167]. Can such endo-fullerenes be used to functionalize C_{60} in useful ways, such as for cooling and trapping? Can such systems be used as models for understanding the interactions, dynamics, and energy flow between small molecules and an extended bath system?

Precision spectroscopy lays the ground work for these and other exciting new avenues in molecular science.

Chapter 6

Quantum cascade laser spectroscopy of C_{60}

6.1 Introduction

Frequency comb spectroscopy enables the rapid acquisition of high resolution, broadband measurements with a high detection sensitivity. The large ratio between the comb bandwidth and repetition rate (ca. 10^3–10^5:1), however, results in an average power per comb mode that is typically quite small, even when accounting for intracavity build up. This often restricts low-power MIR combs to act as passive spectroscopic probes. Single-frequency continous-wave (cw) lasers, on the other hand, provide complementary capabilities to frequency combs. By concentrating intensity into a single optical frequency, cw lasers can efficiently pump MIR transitions to transfer population between rovibrational quantum states. Moreover, one can take advantage of a large variety of cavity-enhanced cw-laser spectroscopy techniques for ultrasensitive detection [21] . These benefits, of course, come at the cost of reduced spectral bandwidth.

This chapter summarizes our on-going exploration of C_{60} spectroscopy with the development of a MIR quantum cascade laser (QCL)-based spectrometer operating near 8.5 μm. Section 6.2 describes the technical aspects of our QCL device and our initial attempts at frequency stabilization. Cavity ring-down experiments are then discussed in Section 6.3. In Section 6.4, we move our attention to true cw spectroscopy via optical feedback stabilization, resulting in the discovery of saturation of C_{60} rovibrational transitions, described in Section 6.5. Finally, Section 6.6 presents some concluding remarks on future experimental directions.

6.2 MIR QCL frequency noise

QCLs are semi-conductor laser devices with a one-dimensional quantum well structure that permits the lasing wavelength to be engineered over a wide range of the MIR region [168, 169]. We use a distributed feedback (DFB)-QCL [170] (Alpes Lasers) that provides stable single-mode operation near 8.5 μm with an average output power of up to 30 mW. The laser output is temperature/current tunable from 1183 to 1189 cm^{-1}, which covers most of the C_{60} vibrational band (Fig. 5.5). Unlike traditional diode lasers, frequency tuning of DFB-QCLs is performed by thermal tuning of the refractive index of the active region, which ultimately limits the wavelength modulation response bandwidth to less than 100 kHz (see below).

Figure 6.1a shows the free-running frequency noise density of the QCL measured using the side of an N_2O absorption peak as a frequency discriminator. The derived optical line width is about 1 MHz, which is significantly broader than the 50 kHz line width of the optical enhancement cavity used for the absorption measurements. The effect of these frequency fluctuations as the laser wavelength is scanned over a cavity resonance can be seen in both the cavity transmission and PDH reflection signals shown in Fig. 6.1b.

The free-running laser frequency must be stabilized to avoid detrimental relative laser-cavity noise. We initially attempted to feed back on the laser frequency via current modulation using a PDH error signal from the spectroscopy cavity. This strategy proved unsuccessful due to the limited frequency feedback bandwidth of the QCL. As shown in Figs. 6.2a and b, the QCL frequency modulation response drops by 50% (relative to DC) by 100 kHz, where it has already acquired 30° of phase delay. This results in simply not enough feedback bandwidth to narrow a 1 MHz free-running line width to a 50 kHz cavity. We also tried an intermediate approach using a short pre-stabilization cavity with a line width of 1 MHz, comparable to that of the laser. The QCL could be successfully locked to the pre-stabilization cavity, demonstrating a significant reduction in its low-frequency wavelength jitter (Fig. 6.2c). Nevertheless, this feedback loop was still bandwidth-limited to about 50 kHz due to the slow thermal frequency response of the laser. The remaining

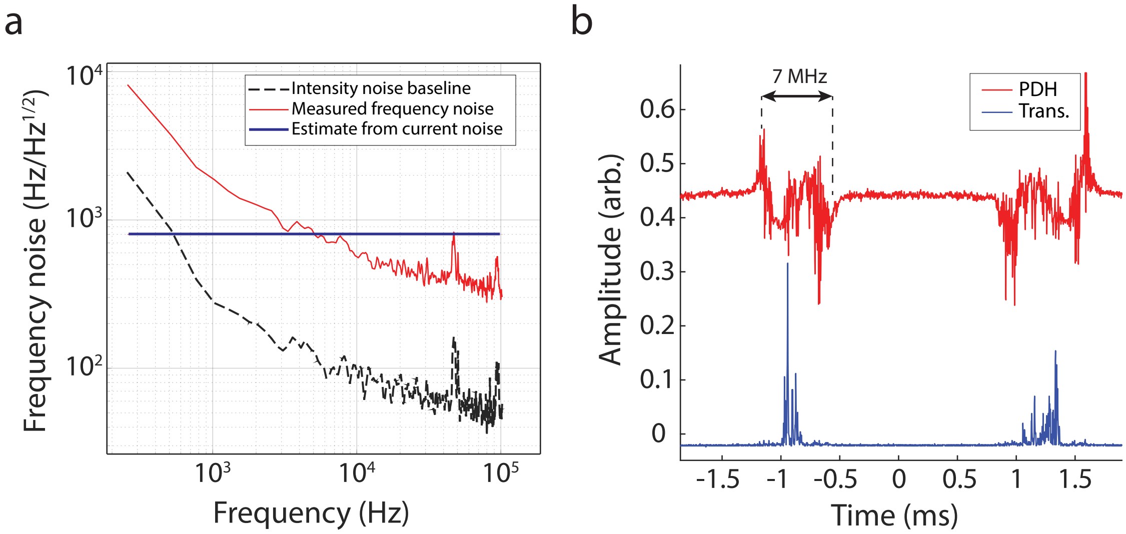

Figure 6.1: Frequency noise of the free-running QCL. (a) The frequency noise spectral density (red) is measured using an N_2O absorption line as a frequency discriminator. The blue horizontal line indicates the expected frequency noise assuming that it is determined only by the current driver noise (which, as can be seen, it is not). (b) Cavity transmission and reflected PDH signals during a laser frequency scan. The PDH sidebands at ±3.5 MHz provide a horizontal frequency calibration scale.

laser frequency noise above 50 kHz results in essentially no change to the short-time line width and therefore no improvement in the laser-spectroscopy cavity coupling performance.

6.3 Cavity ring-down spectroscopy

Cavity ring-down spectroscopy (CRDS) [171] offers a way to work around QCL frequency fluctuations. During the ring-down measurement, the laser does not interact with the cavity, and the signal is therefore immune to relative laser-cavity frequency noise, as well as laser intensity noise. We configured the QCL setup for CRDS operation as shown by the diagram in Fig. 6.3a. Laser light is repeatedly injected into the cavity by sweeping either the cavity length or QCL current. The average cavity-laser offset is stabilized by a swept-cavity lock feedback loop (see Section 2.3.1). As laser light comes into resonance, it builds up in the cavity and is detected by a transmission photodiode. A pulse detector circuit monitors when the cavity build-up reaches a given threshold value. At this point, the laser is switched off resonance by a short current square pulse, and the

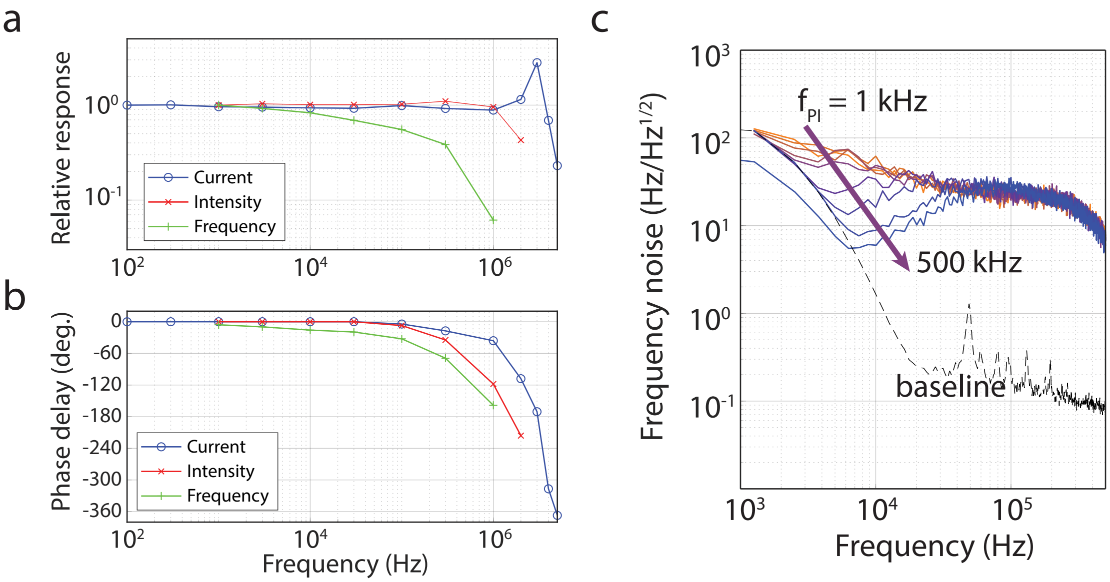

Figure 6.2: QCL current modulation response and PDH frequency stabilization. (a) This plot shows the amplitude response of the QCL current driver output, the QCL optical output intensity, and the QCL optical frequency as a function of the current driver modulation input signal frequency. All traces have been normalized to their respective DC response. The intensity response is flat out to 1 MHz, while the frequency response begins to roll off steeply past 10 kHz. (b) The phase response curves associated with (a). (c) The in-loop QCL frequency noise for the PDH lock to the pre-stabilization cavity ($\Delta\nu_{\mathrm{cav}} = 1$ MHz). Several curves are shown for PI corner frequencies ranging from 1 to 500 kHz. The feedback loop bandwidth is approximately 50 kHz, which is limited by the frequency response function measured in (a).

free ring-down curve is acquired by a fast digitizer (Keysight LXI-L4532A) and transferred to a PC.[1] The ring-down signal is fitted to a single exponential to extract the cavity lifetime τ, which is converted to the single-pass cavity loss. A slow current scan is applied to the QCL to acquire the CRDS spectrum over a small frequency window.

The CRDS spectrum of the Q-branch region of $^{12}\mathrm{C}_{60}$ is shown in Fig. 6.3b. The maximum additional loss above the empty cavity baseline is about 25 ppm, consistent with the previous direct absorption CE-DFCS measurements. The CRDS Allan deviation, shown in Fig. 6.3c, exhibits an optimal averaging time of 10–20 s before the onset of slow baseline drifts. The corresponding single-pass absorption sensitivity is 2.5×10^{-8} Hz$^{-1/2}$. By comparison, the DFG comb system

---

[1] Ideally, instead of a current pulse, one would use an AOM acting as a fast shutter to block the laser from the cavity. Our commercial 8.5 μm AOM, however, exhibits a shut-off time of > 1.5 μs, which is not short enough compared to the 3 μs ring-down time of the cavity.

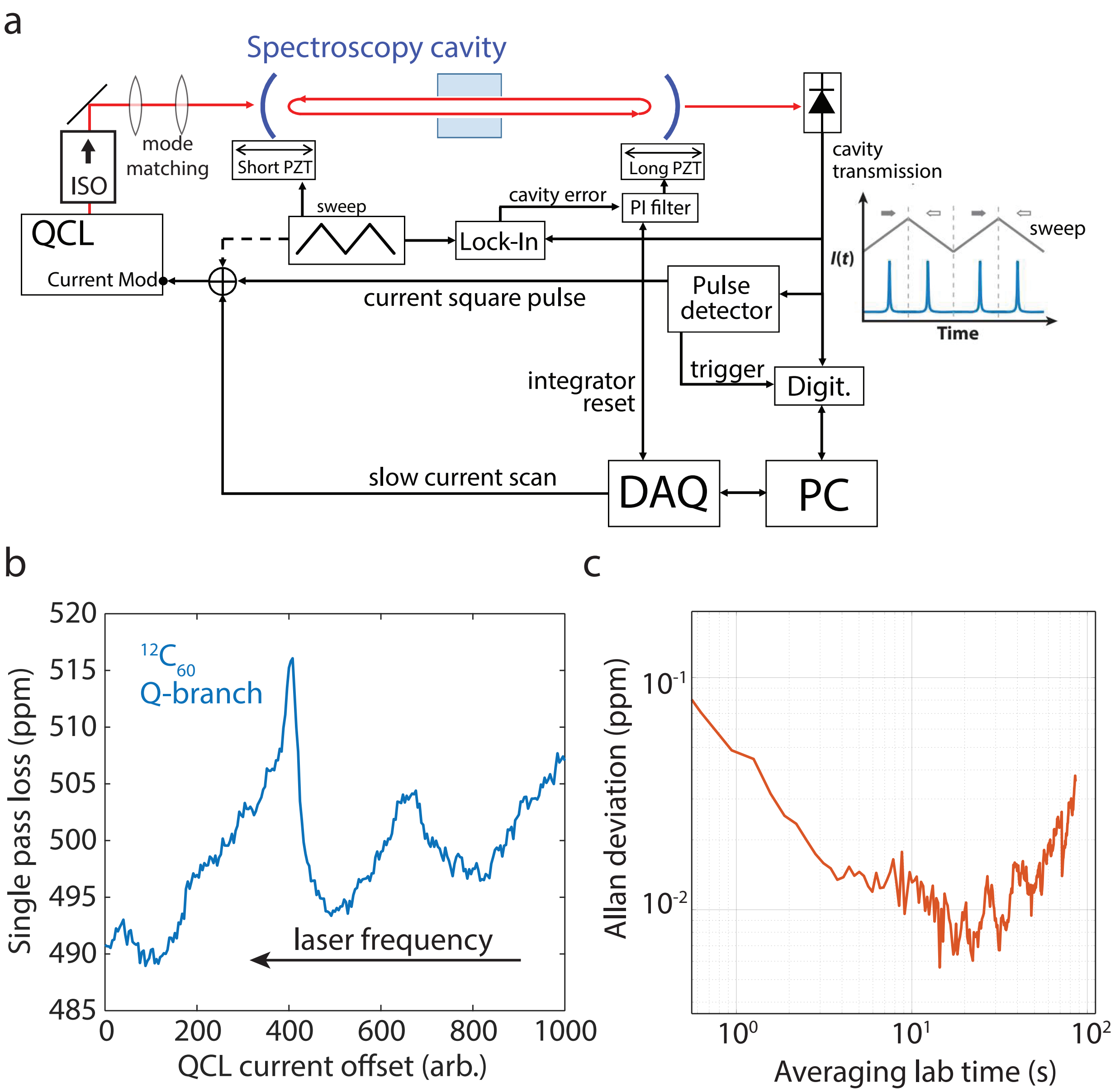

Figure 6.3: QCL cavity ring-down spectroscopy (CRDS). (a) Diagram of the CRDS setup. QCL light is routed through an optical isolator (ISO) and mode matching optics before being injected into the enhancement cavity. The average laser-cavity frequency offset is stabilized with a swept-cavity feedback lock. Ring-down events are triggered by a pulse detector monitoring the cavity transmission. The detector circuit sends a square pulse to the QCL current to quickly move the laser off resonance with the cavity. The ring-down signals are acquired by a fast digitizer and transferred to a PC for processing and fitting. A DAQ device controls the slow current scans and resets the swept-cavity lock integrator when the scan needs to hop to the next cavity mode. (b) The CRDS spectrum of the $^{12}C_{60}$ Q branch. The strongest feature is the Q-branch head, corresponding to an additional 25 ppm of intracavity loss. The plot spans an optical frequency window of about 1 GHz. (c) Allan deviation curve for the CRDS measurements. The optimal averaging time is about 10–20 s, after which the measurement becomes sensitive to slow drifts in the cavity lifetime.

achieves 3.1×10^{-9} cm^{-1} Hz$^{-1/2}$ PSE (Section 2.4.1), which with a 6-cm cold cell translates to 1.9×10^{-8} Hz$^{-1/2}$ PSE, about 20% better than the CRDS measurement. One drawback of CRDS is the low duty cycle. The cavity light has a lifetime of $\tau \approx 3 - 4$ μs and ring-downs can only be acquired (in our setup) at a rate of about 1 kHz. Furthermore, the peak transmitted power during the ring-down is only about 1% of the saturation limit of the photodiode, resulting in an integrated power duty cycle of less than 0.01%. This limits the maximum achievable sensitivity. In principle, one would hope to reach the shot noise limit, which at the saturation power of our photodiodes (~200 μW) and cavity finesse ($\mathcal{F} = 6000$) translates to a single-pass absorption sensitivity of 4×10^{-12} Hz$^{-1/2}$, a full three orders of magnitude better than the CRDS performance. The point, of course, is that one should not waste any photons, and this can only be achieved with a cw measurement.

6.4 Optical feedback stabilization QCL spectroscopy

As demonstrated above, the limited frequency modulation bandwidth of the QCL renders electronic feedback insufficient for a tight cw laser-cavity lock. An alternative solution is to use *optical* feedback, which can provide significantly faster feedback bandwidth. Although optical feedback is usually detrimental to the performance and stability of semiconductor lasers, under certain circumstances it can used advantageously to perform self-locking of the laser to an external cavity [172–175]. A simplified diagram of the optical feedback stabilization (OFS) setup is illustrated in Fig. 6.4a. The key requirements for successful self-locking to the cavity are to (i) minimize optical feedback from light that is non-resonant with the cavity and (ii) control the optical phase of the feedback. The first requirement is met by replacing our usual two-mirror cavity with a three-mirror V-shaped cavity. QCL light is coupled into the cavity at the apex mirror. Because the incident beam is not perperpendicular to the mirror, the non-resonant cavity reflections are deflected away, while intracavity circulating light is able to retrace the optical path back to the laser. The optical phase is optimized by controlling the physical distance between the QCL and the cavity at the sub-λ scale. This is accomplished with a combination of a fast, short-throw, bullet-mount piezo

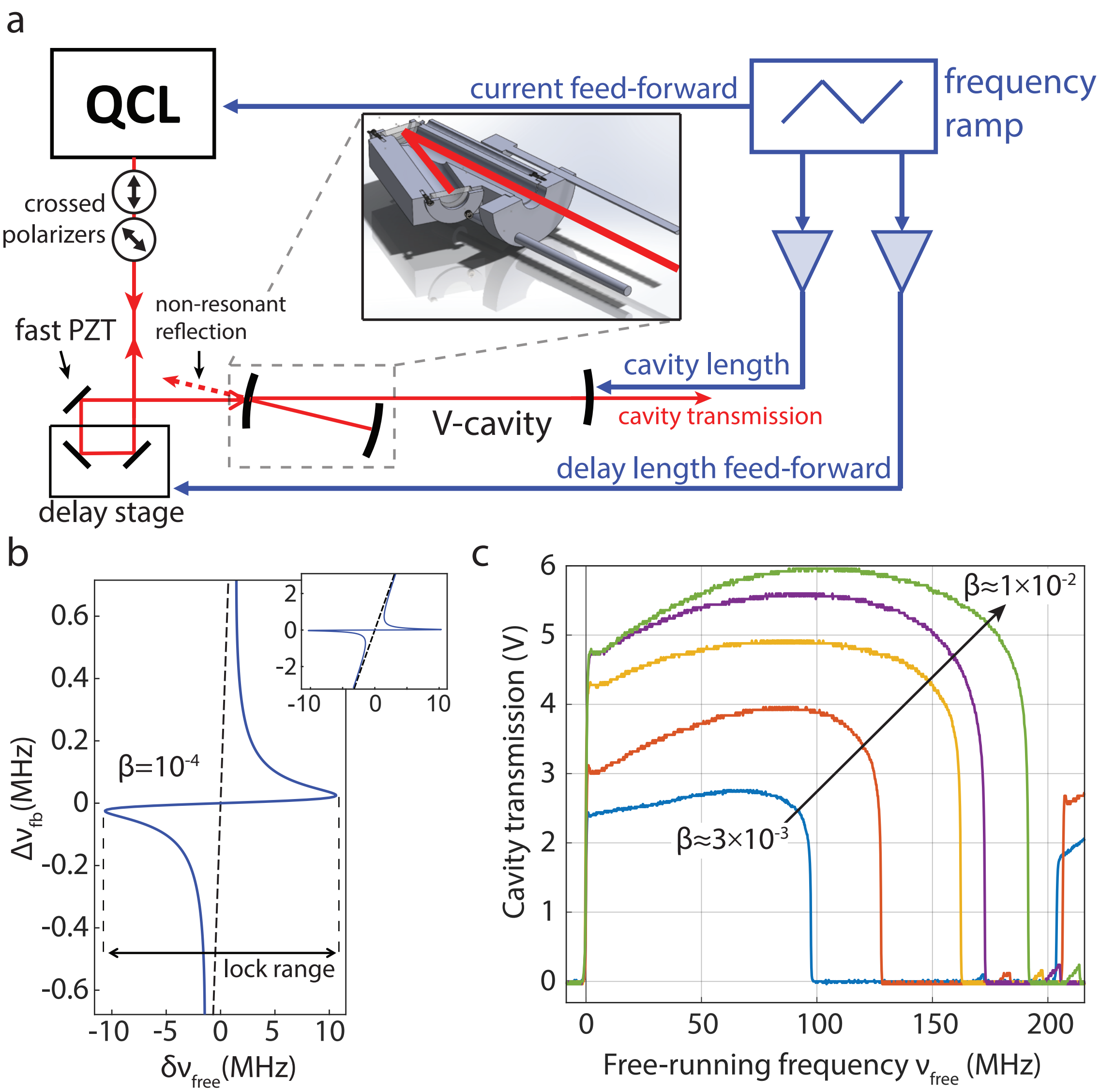

Figure 6.4: QCL optical feedback stabilization (OFS) and self-locking. (a) A simplified diagram of the QCL-OFS setup. The V-cavity geometry permits resonant cavity light to return to the laser, while deflecting non-resonant reflections. The inset shows the custom V-shaped vacuum mount that holds the two closer-spaced cavity mirrors. The feedback power ratio is controlled with a pair of crossed polarizers, which act as a variable attenuator. A fast PZT-mounted mirror and a slow delay stage together provide control of the optical feedback phase. When the OFS lock is active, a frequency scan is performed by ramping the cavity length, with simultaneous feed-forward signals sent to the QCL current and delay-length piezos. (b) The relationship between the free-running laser-cavity detuning $\delta\nu_{\mathrm{free}}$ and the output frequency detuning $\Delta\nu_{\mathrm{fb}}$ in the presence of optical feedback with a power ratio of $\beta = 10^{-4}$. The OFS locking range extends between the two turning points of the curve. The dashed line corresponds to the $\Delta\nu_{\mathrm{fb}} = \delta\nu_{\mathrm{free}}$ turning curve without optical feedback. The inset shows a zoomed-out view. (c) The measured cavity transmission during a QCL current scan for several values of β in the range 3×10^{-3} to 1×10^{-2}. The horizontal axis is calibrated to the free-running frequency ν_{free}, with each curve offset such that the capture-point is at $\nu_{\mathrm{free}} = 0$.

mirror [176] and a slow, long-throw, piezo-actuated delay stage.

One of the key parameters controlling OFS is the ratio $\beta = P_{\text{fb}}/P_{\text{tot}}$ between the power of the feedback light P_{fb} recoupled into the QCL laser mode and the total laser output power P_{tot}. Figure 6.4b shows the relationship between the free-running optical frequency of the laser ν_{free} and the actual output frequency ν_{fb} in the presence of optical feedback, simulated for $\beta = 10^{-4}$ and assuming that the QCL laser cavity has an optical length of $n\ell = 5$ mm and a finesse of 5 [173]. (We do not know the actual parameters of the QCL laser cavity. These are simply reasonable guesses.) Over the OFS locking range, which is $\propto \beta^{1/2}$, the laser frequency is pulled to center of the cavity resonance and free-running frequency fluctuations are suppressed. The self-locking effect is easily observed by scanning the QCL current (i.e. the free-running frequency) and monitoring the cavity transmission signal. This is shown in Fig. 6.4c for several values of β (tuned by adjusting a pair of crossed polarizers between the laser and external cavity). As ν_{free} enters the capture range of the OFS, it quickly locks to the cavity resonance with a sharp turn-on in the cavity transmission. As ν_{free} continues to scan through the lock range, it moves from one side of the cavity resonance to the other, passing through a transmission maximum when the actual detuning $\Delta\nu_{\text{fb}}$ relative to the cavity resonance is zero. Once ν_{free} reaches the end of the lock range, it quickly falls out of resonance and the cavity transmission drops to zero. At our maximum achievable feedback power ratio, which we estimate to be $\beta = 10^{-2}$, the locking range is about 190 MHz, i.e. 95% of the cavity FSR = 200 MHz. This performance is similar to other recent demonstrations of OFS with QCLs [177–180].

We actively stabilize the optical feedback phase by applying a $f = 20 - 35$ kHz dither to ν_{free} via QCL current modulation. The cavity transmission signal is then demodulated to isolate the $1f$ component, which is filtered and fed back onto the fast delay PZT, maintaining optimal OFS conditions. The residual intensity noise (RIN) spectrum of the cavity transmission with an active OFS lock is shown in Fig. 6.5a, along with the RIN spectrum of the incident cavity light ("Reference") with and without optical feedback. At frequencies below 1 kHz, residual laser-cavity frequency fluctuations add intensity noise to the cavity transmission, but at frequencies between 1 kHz and the cavity half-width of 35 kHz, the incident and transmitted cavity light have comparable amplitude noise. It is also evident that as the optical feedback corrects for free-running frequency fluctuations, it imprints intensity noise onto the laser output. DC cavity transmission has a baseline RIN of about 2×10^{-4} Hz$^{-1/2}$, corresponding to a single-pass absorption sensitivity of 1×10^{-7} Hz$^{-1/2}$ (the V-cavity has a finesse of about 3000). By adding another stage of modulation to perform wavelength-modulation spectroscopy, the detection band could be moved to the 1–10 kHz window, where the detection sensitivity would be as low as 5×10^{-10} Hz$^{-1/2}$, about a factor of 40× better than the CE-DFCS or QCL-CRDS sensitivities.

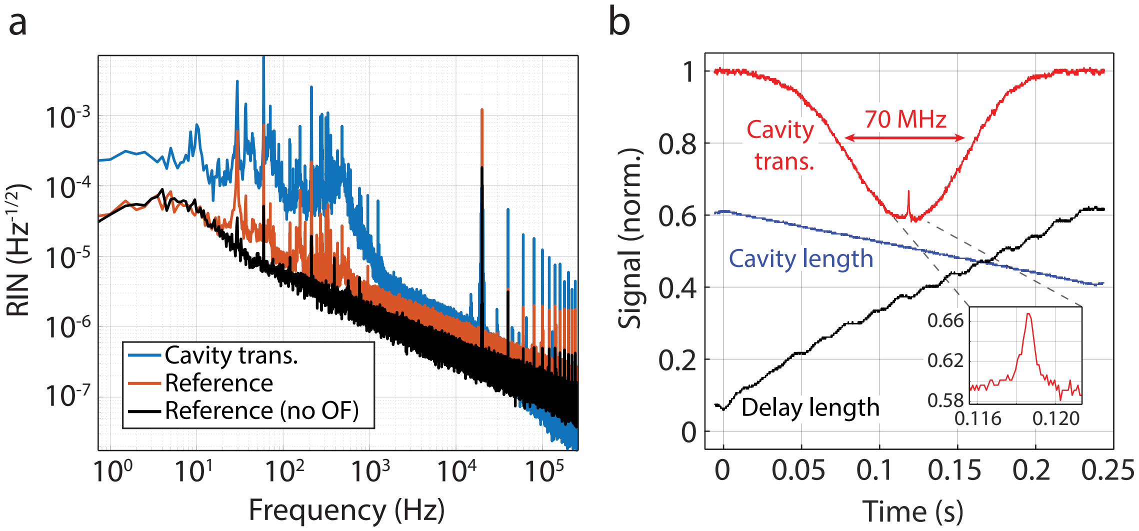

Figure 6.5: OFS-locked intensity noise and frequency ramp. (a) RIN spectra are plotted for the cavity transmission (blue), reference incident cavity light (red), and incident cavity light without optical feedback (black). The cavity roll-off (half-width) frequency is 35 kHz. The narrow spikes are from a 20 kHz current dither used for the delay-length stabilization servo. (b) An OFS-lock frequency ramp containing an N_2O absorption line. The cavity transmission (red) shows the 70 MHz-wide Doppler profile with a narrow 700 kHz Lamp dip (inset). The cavity length ramp (blue) and delay-length feed-forward signal (black) are also plotted.

A slow ramp is applied to the optical cavity length to perform a frequency scan. The OFS-lock forces the laser frequency to follow the moving cavity resonance, while the $1f$ dither lock maintains the optimal feedback phase. Feed-forward signals are applied to both the QCL current and delay-length piezos to keep their respective locks within their operation range. The maximum cavity ramp range is about 220 MHz (limited by the throw of the slow delay-length piezo). This is larger than the 200 MHz FSR of the cavity, so by hopping the laser between sequential cavity resonances, a wider spectral window can be continuously stitched together. Figure 6.5b shows a single OFS-locked cavity ramp containing a strong N_2O absorption peak. The cavity transmission signal, the cavity length ramp, and the delay length feed-forward signal are plotted. The transition is partially saturated revealing a narrow Lamb dip feature, which has a FWHM of 700 kHz, limited by transit time and power broadening.

6.5 Saturation of C_{60} rovibrational transitions

Upon the demonstration of successful frequency ramps with N_2O, we immediately searched for C_{60} transitions. Spectrally broad absorption, observed as attenuation of the DC cavity transmission, was detected and attributed to the warm C_{60} "blob" (see Fig. 5.5). However, there were no detectable signatures of narrow transitions from cold C_{60}, not even from the strong Q-branch head. After the possibility of frequency calibration errors was quickly ruled out, we were left to suspect that the C_{60} molecules were not being properly cooled, which could explain why only broad background absorption was detected. We spent several weeks investigating this issue, focusing on the C_{60} oven and buffer gas annular slit inlet. These components were modified and re-built multiple times. The buffer gas flow rates and pumping speeds were also carefully recalibrated. None of these actions resulted in any change in the observed signal.

After eliminating all other possibilities, we considered the prospect that cold C_{60} transitions might be saturated, given that our typical OFS operating conditions result in an intracavity circulating power of up to 700 mW. Indeed, by attenuating the QCL light incident on the cavity, narrow absorption resonances were recovered. Figures 6.6a and b show an R(J) transition near 1186.2 cm^{-1}. Increasing the intracavity circulating power from $P_{\text{cav}} = 40$ mW to 160 mW results in the complete disappearance of the absorption signal. The C_{60} Q branch is shown in Figs. 6.6c and d. At $P_{\text{cav}} = 15$ mW, the expected Q-branch contour begins to take shape, but this structure already begins to wash out at $P_{\text{cav}} = 30$ mW. The effective single-pass loss for the Q-branch head

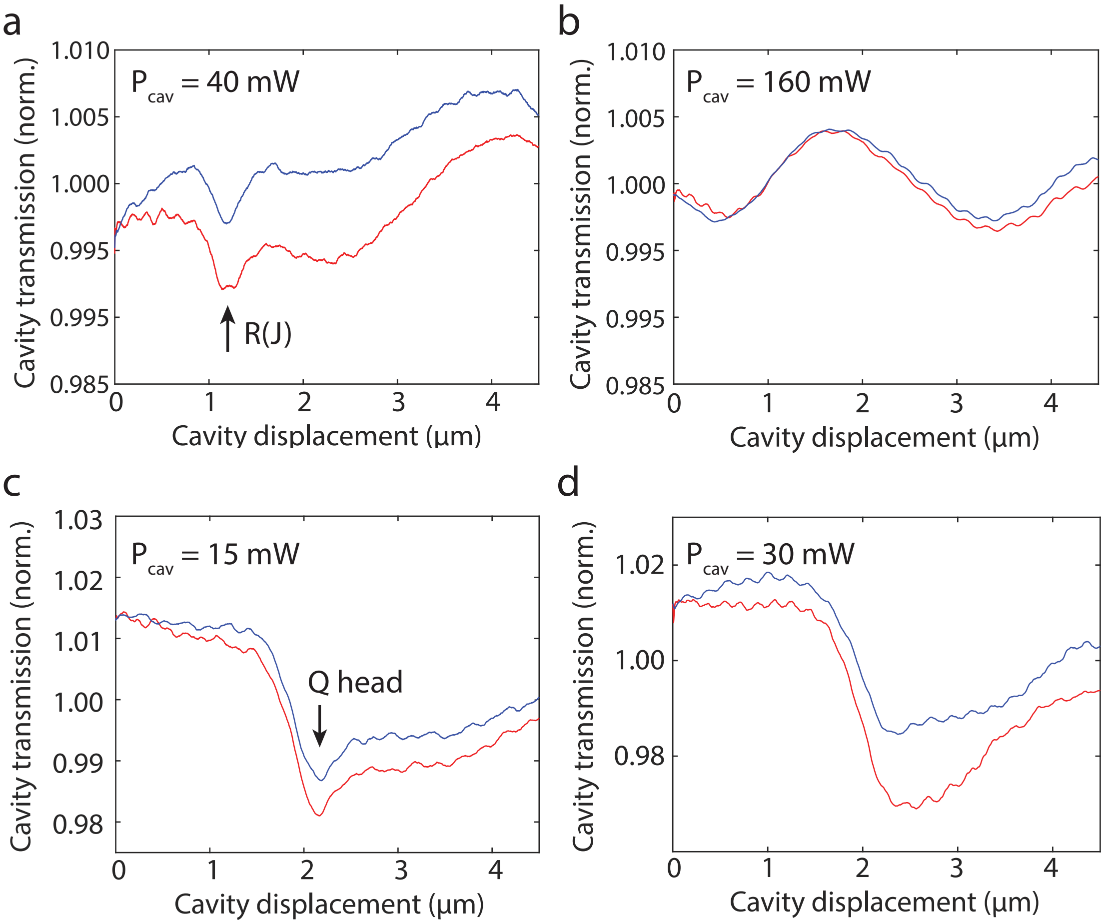

Figure 6.6: Saturation of cold C_{60} rovibrational transitions. (a) An OFS-locked cavity scan with $P_{\text{cav}} = 40$ mW shows absorption from an R($J \approx 170$) transition near 1186.2 cm^{-1}. The two traces are from the upward (red) and downward (blue) portions of the cavity length ramp. (b) Same as (a) with $P_{\text{cav}} = 160$ mW. (c) A scan near 1184.85 cm^{-1} with $P_{\text{cav}} = 15$ mW shows the partially resolved Q-branch head. (d) Same as (c) with $P_{\text{cav}} = 30$ mW, showing a washed out Q-branch contour.

at $P_{\text{cav}} = 15$ mW is only about half the expected magnitude, suggesting that it is still partially saturated.

Although the observation of C_{60} saturation came as a surprise, in hindsight it might have been anticipated. The integrated intensity of the 8.5 μm band is about 9.4 km mol^{-1} [131], corresponding to a vibrational transition dipole of 0.05 D. The CE-DFCS data suggests that the IR transitions are collisionally broadened to about 20 MHz implying a saturation intensity of $\sim 10^2$ W/cm^2. The maximum $P_{\text{cav}} = 700$ mW with a cavity waist of $w_0 = 1.5$ mm^2 yields a peak intensity of $I = 2P_{\mathrm{cav}}/\pi w_0^2 \approx 20$ W/cm^2. This back-of-the-envelope calculation suggests that saturation effects should not have been entirely unexpected with cw OFS-locking. On the other hand, the peak intensities in the CRDS measurements are 25–50× lower, and in the CE-DFCS measurements about $10^4\times$ lower (per comb mode), explaining why no saturation effects are observed in those experiments.

6.6 Conclusions and future directions

The discovery of C_{60} saturation ultimately opens up new experimental possibilities. For example, efficient vibrational population transfer is a pre-requisite for hole-burning and double-resonance techniques. In the near-term, however, it represents a significant experimental barrier for intracavity absorption measurements. Engineering low intracavity powers with an OFS lock is practically difficult. The OFS process fundamentally relies on laser power being coupled into the external cavity and then back into the laser cavity. Attenuating light before it enters the external cavity or decreasing the build-up factor of the cavity compromises OFS performance. One way to overcome this challenge is to take advantage of sideband spectroscopy. The ideal technique is probably NICE-OHMS [181], which requires frequency sidebands at a modulation frequency equal to the cavity FSR (200 MHz). Unfortunately, the limited frequency response bandwidth of QCLs makes this impractical to accomplish with direct current modulation, and external phase modulators such as EOMs are not widely available at 8.5 μm. A compromise approach is to use AM sidebands. While this strategy sacrifices various advantages of FM spectroscopy, it is relatively straightforward to current modulate a QCL at 200 MHz. Only a small fraction of the total power (probably $< 1\%$) needs to be placed in the AM sidebands. The high intensity carrier interacts with one cavity mode generating a stable OFS lock, while AM sidebands on either side couple to adjacent cavity modes to perform a linear absorption measurement below the saturation intensity. This approach is currently being implemented in the Ye lab and promises to help us take the next step in C_{60} QCL spectroscopy.

Chapter 7

High accuracy rovibrational calculations of small molecules

7.1 Introduction

Gas-phase, frequency domain spectroscopy probes the molecular eigenstates associated with electronic, vibrational, and rotational motion. The interpretation, assignment, and analysis of such spectra, ranging from the microwave to optical regions, is aided enormously by accurate *ab initio* calculations. Reliable predictions of anharmonic vibrational frequencies and rotational constants are only the starting point: treatment of higher order effects such as centrifugal distortion, Coriolis interactions, tunneling splittings, and various types of perturbations is often necessary to successfully describe a high resolution spectrum [182]. Certain quantities of interest are intractable or impossible to extract directly from experimental spectra alone and require theoretical input. For example, calculated nuclear zero-point motion effects are crucial to equilibrium structure determination [183, 184] and high-level thermochemistry protocols [185–187].

Ab initio approaches are often based on solving the time-independent Schrödinger equation (SE) for the total molecular Hamiltonian,

$$H_{\mathrm{mol}}(\mathbf{r}_{\mathrm{e}}, \mathbf{R}_{\mathrm{n}}) = H_{\mathrm{elec}}(\mathbf{r}_{\mathrm{e}}; \mathbf{R}_{\mathrm{n}}) + \left[T_{\mathrm{nuc}}(\mathbf{R}_{\mathrm{n}}) + U_{\mathrm{nuc}}(\mathbf{R}_{\mathrm{n}})\right].$$

H_{mol} contains an electronic part $H_{\mathrm{elec}}(\mathbf{r}_{\mathrm{e}}; \mathbf{R}_{\mathrm{n}})$, which depends on both the electronic $\mathbf{r}_{\mathrm{e}}$ and nuclear $\mathbf{R}_{\mathrm{n}}$ coordinates, and a nuclear part that includes the nuclear kinetic energy $T_{\mathrm{nuc}}(\mathbf{R}_{\mathrm{n}})$ and internuclear Coulomb repulsion $U_{\mathrm{nuc}}(\mathbf{R}_{\mathrm{n}})$. The Born-Oppenheimer approximation [188] splits the molecular problem into two halves by adiabatically separating the electronic and nuclear degrees of freedom. In this framework, one first solves an electronic SE,

$$H_{\mathrm{elec}}(\mathbf{r}_{\mathrm{e}};\mathbf{R}_{\mathrm{n}})|\psi_{\mathrm{e}}(\mathbf{r}_{\mathrm{e}};\mathbf{R}_{\mathrm{n}})\rangle = E_{\mathrm{e}}(\mathbf{R}_{\mathrm{n}})|\psi_{\mathrm{e}}(\mathbf{r}_{\mathrm{e}};\mathbf{R}_{\mathrm{n}})\rangle, \tag{7.1}$$

which depends parametrically on $\mathbf{R}_{\mathrm{n}}$. The solution to this problem constitutes the extensive field of electronic structure theory and quantum chemistry.

We focus here on the second step, namely the nuclear motion SE,

$$H_{\mathrm{nuc}}|\psi_{\mathrm{nuc}}(\mathbf{R}_{\mathrm{n}})\rangle = \left[T_{\mathrm{nuc}} + V(\mathbf{R}_{\mathrm{n}})\right]|\psi_{\mathrm{nuc}}(\mathbf{R}_{\mathrm{n}})\rangle = E_{\mathrm{nuc}}|\psi_{\mathrm{nuc}}(\mathbf{R}_{\mathrm{n}})\rangle, \tag{7.2}$$

which describes rovibrational dynamics occuring on an effective potential energy surface (PES) $V(\mathbf{R}_{\mathrm{n}}) = E_{\mathrm{e}}(\mathbf{R}_{\mathrm{n}}) + U_{\mathrm{nuc}}(\mathbf{R}_{\mathrm{n}})$. In polyatomic molecules, this is a high-dimensional, many-body problem. Its solution is especially complex for non-rigid, floppy systems that exhibit extreme anharmonicity and large-amplitude nuclear motion. Many molecules of fundamental physical and chemical interest, including reactive transients, radicals and ions, and exotic astrochemical species, fall into this category.[1] We have already encountered one example earlier in Chapter 3 on the infrared spectrocopy of nitromethane. Automated "blackbox" tools, such as those based on standard vibrational perturbation theory [70, 191], fail – often catastrophically so – for these types of systems [51]. The development of accurate and efficient alternative methods to tackle them remains a challenge.

This chapter discusses the computational methods we use to understand and interpret the rovibronic spectra of small- to medium-sized polyatomic molecules. Section 7.2 describes these tools, which include implementations of relatively well established techniques along with newly developed approaches and extensions. In Section 7.3, we explore several applications to floppy, anharmonic molecules including the methide anion [192], disilicon carbide [193–195], hydrogen peroxide [196, 197], and *gauche*-1,3-butadiene [198]. Each of these examples is framed by the goal of interpreting and quantitatively understanding measured spectra. Indeed, most of these projects are the result of close collaboration with experimental spectroscopists. Ultimately, we hope to demonstrate the important benefits of close contact between experiment and theory [182].

---

[1] An excellent survey of this topic can be found in two recent special issues of the *Journal of Molecular Spectroscopy* organized in honor of the late Jon Hougen [189, 190], who made numerous fundamental contributions to this field.

7.2 Methods

In this section, we give an overview of the construction of nuclear motion Hamiltonians and the determination of their energy eigenvalues and eigenfunctions. The Hamiltonian has two parts: the kinetic energy operator (KEO) and the potential energy surface (PES). The KEO is determined only by the choice of coordinates used to describe the nuclear degrees of freedom, while the PES is built from fitting high-dimensional functions to data sets of quantum chemical electronic energies. The strategies employed to determine the spectrum of the Hamiltonian include both variational and perturbative techniques. The former involves iterative eigensolvers combined with sparse direct-product grid representations of the Hamiltonian. For systems that are too large to treat with this approach, we have developed a version of rovibrational perturbation theory based on curvilinear vibrational mean-field theory. The software used to perform each of these various parts of a nuclear motion calculation has been organized into a freely available package called NITROGEN [199].

7.2.1 Direct-product grid variational calculations with iterative eigensolvers

The most general way to compute the spectrum of a rovibrational Hamiltonian is via variational methods [200, 201]. In this approach, wavefunctions are represented as linear combinations of a set of basis functions. The matrix representation of the Hamiltonian operator in this basis set is diagonalized to compute its eigenvalues (energies) and eigenvectors (wavefunctions). By systematically increasing the size of the basis set, numerically exact energies and wavefunctions can be converged. The calculation is limited only by the size of the Hamiltonian matrix one can build and diagonalize.

The most straightforward basis set for multi-dimensional wavefunctions is a direct product of one-dimensional basis functions for each degree of freedom [201, 202]. These take the general form

$$\Phi_{i_1 i_2 \cdots i_n}(\vec{q}) = \phi^{(1)}_{i_1}(q_1)\phi^{(2)}_{i_2}(q_2)\cdots\phi^{(n)}_{i_n}(q_n), \tag{7.3}$$

where each vibrational coordinate q_k, $k = 1 \ldots n$, has its own independent set of 1-D basis functions $\phi^{(k)}_{i_k}(q_k)$. (We consider rotational motion later.) The desired many-body wavefunctions are represented as an n-index sum over the direct product basis,

$$\Psi(\vec{q}) = \sum_{i_1} \sum_{i_2} \cdots \sum_{i_n} c_{i_1 i_2 \cdots i_n} \Phi_{i_1 i_2 \cdots i_n}(\vec{q}), \tag{7.4}$$

where the coefficients $c_{i_1 i_2 \cdots i_n}$ are equal to the components of the eigenvectors of the Hamiltonian matrix. As the number of basis functions $\phi_{i_k}^{(k)}$ for each coordinate approaches completeness in 1-D, so does the many-dimensional direct-product basis.

The challenge with this approach is that the number of direct-product basis functions grows exponentially with the number of coordinates. For example, each 1-D basis set typically needs a minimum of 10 functions for accurate results, yielding a total of 10^n direct-product basis functions. A five-atom molecule, such as CH_4, has $n = 3N - 6 = 9$ internal coordinates, so its minimum basis set contains 10^9 functions. Most importantly, the Hamiltonian operator in this basis is a $10^9 \times 10^9$ matrix, which would require about 10^{10} gigabytes of memory to store on a computer. Even if this were possible, direct diagonalization methods of $m \times m$ matrices scale as $\mathcal{O}(m^3)$ and are impractical for such large matrices. Furthermore, only the lowest energy eigenvalues are typically desired, which represent a very small fraction of the complete eigenvalue spectrum of the Hamiltonian matrix. Calculating the entire set of eigenvalues is therefore a vast waste of resources.

The problem of calculating and storing the Hamiltonian matrix is avoided by using iterative diagonalization methods [203–205], in particular the Lanczos algorithm [206], which is applicable to Hermitian matrices. Iterative methods focus the computational effort on calculating the lowest energy eigenvalues and not the entire unnecessary spectrum. They also require only that one calculate the Hamiltonian matrix-vector product, $w = Hv$, where v is an arbitrary vector of basis function coefficients. The key point is that matrix-vector products (MVPs) can be calculated without the explicit construction of the matrix H itself. This drastically reduces the memory requirements, making the direct-product basis approach viable. We forgo a detailed discussion of iterative diagonalization algorithms here. We most often employ the so-called thick-restart Lanczos method, details of which can be found in Ref. [67].

In general, the efficiency of iterative techniques is determined by the cost of MVPs with

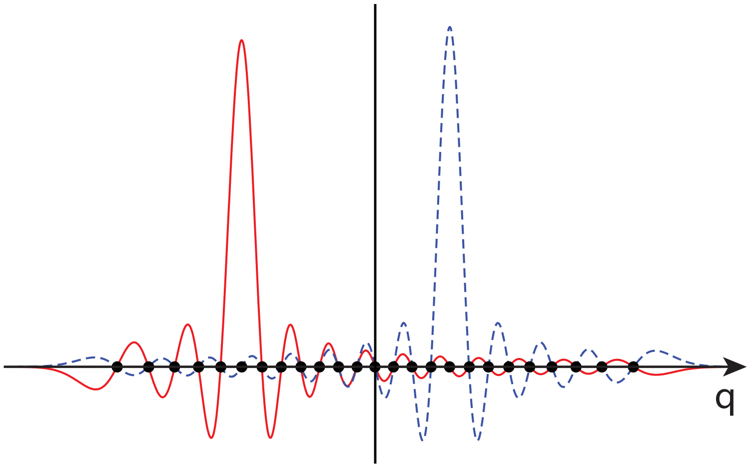

Figure 7.1: Discrete-variable representation (DVR) basis functions. The two DVR functions (red solid line and blue dashed line) are associated with a one-dimensional grid of twenty-five points (black dots). Each DVR function is highly localized about its respective grid point and has a node at all other grid points.

the Hamiltonian. Discrete-variable representation (DVR) basis sets [68, 207–209] are an essential tool for reducing the computational expense of this step. DVRs are coordinate-representation basis functions that are highly localized about discrete values (i.e. grid points) of the coordinate variable [68] (see Fig. 7.1). One definition of DVRs is the eigenfunctions of the coordinate operator in a finite basis set of orthogonal polynomials, and therefore they may be thought of as finite basis approximations of Dirac delta functions. Indeed, a fundamental property of DVRs is that matrix representations of scalar functions are approximately diagonal,

$$\int dq\, \phi_i^*(q) f(q) \phi_j(q) \approx \delta_{ij} f(q_i), \tag{7.5}$$

where ϕ_i (ϕ_j) is the DVR basis function centered on grid point q_i (q_j). This diagonal approximation is related to Gaussian quadrature of integrals, and the associated error rapidly decreases as the number of DVR basis functions (i.e. the number of grid points) increases [68].

Using DVR basis sets with iterative diagonalization is advantageous for two reasons. First, the diagonal property results in a highly sparse Hamiltonian matrix with a small fraction of non-zero matrix elements. Second, these matrix elements can be calculated without performing expensive integrals. The only information needed is the values of the PES and KEO coefficients at the DVR grid points. These properties make MVPs and iterative diagonalization simple and efficient. Additional techniques such as pre-conditioned spectral transformations [205, 210, 211] and symmetry-adapted Lanczos [212] can further improve the computational efficiency.

The above discussion focuses on the pure vibrational problem ($J = 0$). Rotations are easily included by attaching a set of symmetric top rotational basis functions to each DVR grid point. Other than modifying the Hamiltonian MVP routine to account for rotational and rovibrational terms in the KEO, the iterative diagonalization algorithm is essentially unchanged. Both the size of the combined rovibrational direct-product basis and the cost of MVPs are proportional to $2J + 1$, the number of symmetric top functions for a given value of J.

7.2.2 Rovibrational perturbation theory based on curvilinear vibrational mean-field theory

Although iterative techniques and DVRs make direct-product-basis variational calculations orders of magnitude more efficient than direct matrix construction and diagonalization, their cost still scales exponentially with the number of coordinates, limiting them to small molecules of up to four or five atoms. (We note that recent advances [213–215] have substantially pushed this dimensionality limit for some cases.) For medium-sized molecules, it it advantageous to use approximate methods that are even more efficient while retaining enough accuracy to be useful for spectroscopy.

One of the most popular approximate methods is second-order vibrational perturbation theory (VPT2) [69, 70, 191]. The zeroth-order description in VPT2 is a set of uncoupled harmonic oscillator vibrations and rigid-top rotations. Perturbative corrections from anharmonicity and rotation-vibration coupling are used to generate anharmonic vibrational frequencies and effective rotational parameters. Although VPT2 is based on the formally exact Watson Hamiltonian [71], it relies on rectilinear normal coordinates and single-reference Eckart embedding [216]. This renders it best suited for molecules that undergo small harmonic displacements from a single, well defined equilibrium configuration. VPT2 thus fails for floppy or highly anharmonic molecules [51, 191].

This section introduces a more general rovibrational perturbative method that goes beyond the Watson Hamiltonian/VPT2 framework. Non-rigid systems demand the use of curvilinear coordinates, general representations of the PES and KEO beyond power series/Taylor expansions, and more flexible quasi-Eckart frame embeddings not tied to a single reference geometry (which in cases like nitromethane (Chapter 3) may not even be well defined). Prior work on perturbative [217, 218] and hybrid variational-perturbative [219, 220] approaches have addressed some of these issues. We base our approach on vibrational self-consistent field theory (VSCF) [72–74, 221] and second-order vibrational Møller–Plesset perturbation theory (VMP2) [76, 222]. VMP2 corrects a zeroth-order VSCF mean-field wavefunction for vibrational correlation effects using Rayleigh-Schrödinger perturbation theory, in analogy to electronic structure MP2 [75]. While VSCF-based methods were originally developed for the rectilinear Watson Hamiltonian, they have since been applied to a variety of curvilinear coordinate systems [223–230]. The contribution of the present work is to extend the curvilinear VSCF/VMP2 approach by accounting for the rotational and rotation-vibration coupling terms of the nuclear motion Hamiltonian [51]. Rotational and rovibrational effective Hamiltonians are calculated by applying a second-order contact, or Van Vleck, transformation [231] to the zeroth order VSCF Hamiltonian.

The zeroth-order VSCF wavefunction ansatz is a Hartree product for the n vibrational coordinates,

$$\Psi_0(\vec{q}) = \psi_1(q_1)\psi_2(q_2)\cdots\psi_n(q_n), \tag{7.6}$$

or in ket notation,

$$|\Psi_0\rangle = |1\rangle|2\rangle\cdots|n\rangle = \prod_k |k\rangle. \tag{7.7}$$

Variational optimization of $|\Psi_0\rangle$ leads to a 1-D Schrödinger equation for each degree of freedom,

$$\hat{h}_k|k\rangle = \varepsilon_k|k\rangle, \tag{7.8}$$

where

$$\hat{h}_k = \left(\prod_{l \neq k} \langle l | \right) H_\mathrm{v} \left(\prod_{l \neq k} | l \rangle \right) \tag{7.9}$$

is the one-body Hamiltonian for vibrational coordinate k, computed by averaging the full vibrational Hamiltonian H_v over the other degrees of freedom $l \neq k$. As in other mean-field theories, this set of equations is solved iteratively until self-consistency is reached. We use underlying DVR basis sets for each of these 1-D problems.

Second-order vibrational Møller–Plesset perturbation theory (VMP2) is used to correct the VSCF wavefunction $|\Psi_0\rangle$. The VMP2 energy is computed using standard Rayleigh-Schrödinger perturbative corrections,

$$E_0^{\mathrm{VMP2}} = E_0^{(0)} + E_0^{(2)}, \tag{7.10}$$

$$E_0^{(0)} = \langle \Psi_0 | H_\mathrm{v} | \Psi_0 \rangle, \tag{7.11}$$

$$E_0^{(2)} = \sum_{|v\rangle \neq |\Psi_0\rangle} \frac{|\langle \Psi_0 | H_v | v \rangle|^2}{E_0^{(0)} - E_v^{(0)}}, \tag{7.12}$$

where the second-order sum is over virtual excitation wavefunctions $|v\rangle$ formed from higher-energy eigenfunctions of the one-body problems, Eq. 7.8. (These form a direct-product basis set that completely spans the one-body functional space.) The zeroth order wavefunction $|\Psi_0\rangle$ is not necessarily the ground state. Excited vibrational states can be targeted equally as well.

This approach provides approximate wavefunctions and energies for the pure vibrational Hamiltonian $H_\mathrm{v} = T_\mathrm{v} + V$, where T_v is the vibrational KEO and V is the PES. To calculate rovibrational states with $J > 0$, one must consider the full nuclear motion Hamiltonian $H = H_\mathrm{v} + T_\mathrm{r} + T_\mathrm{rv}$, which contains additional KEO terms for rotational motion (T_r) and rotation-vibration coupling (T_rv). These terms are typically several orders of magnitude smaller than the vibrational part of the Hamiltonian and therefore may be folded into the perturbative treatment. This procedure is formally carried out with a contact or Van Vleck transformation [231], with the final product being a rotational or rovibrational effective Hamiltonian for the state(s) of interest [232, 233].

We provide only a brief overview here of contact transformations. (Further details can be found, for example, in Appendix C of Ref. [234].) We first define the zeroth-order Hamiltonian using the VSCF wavefunctions as

$$H^{(0)} = \sum_v E_v^{(0)} |v\rangle\langle v|, \tag{7.13}$$

where $E_v^{(0)} = \langle v|H_{\text{v}}|v\rangle$ are the zeroth-order energies. Letting $\Delta H = H_{\text{v}} - H^{(0)}$, we partition H as

$$\begin{aligned} H &= H^{(0)} + \Delta H + T_{\text{rv}} + T_{\text{r}} & (7.14) \\ &= H^{(0)} + \lambda H', & (7.15) \end{aligned}$$

where the perturbation term $H' = \Delta H + T_{\text{rv}} + T_{\text{r}}$ appears with an order-sorting parameter λ, which is formally equal to 1.

Consider the Hamiltonian matrix representation with zeroth-order rovibrational wavefunctions $|v\rangle|r\rangle$. $|v\rangle$ is a VSCF wavefunction ($|\Psi_0\rangle$ or an excited virtual state), while $|r\rangle$ is some rotational basis function (usually a symmetric top wavefunction, but the actual choice does not matter). A schematic drawing of H in this basis is shown in Fig. 7.2. The Hamiltonian is organized into vibrational blocks $\langle v|H|v\rangle$ along the diagonal. Off-diagonal coupling from H' between different vibrational blocks is of $\mathcal{O}(\lambda)$. A contact transformation is a unitary transformation of the original Hamiltonian to form a modified Hamiltonian $\tilde{H}$ of the form,

$$\tilde{H} = e^{-i\lambda \mathbf{S}} H e^{i\lambda \mathbf{S}}, \tag{7.16}$$

where $\mathbf{S}$ is a Hermitian operator. $\mathbf{S}$ is chosen to make $\tilde{H}$ approximately block-diagonal by eliminating off-diagonal coupling up through some given order in λ. Here, we go to second-order such that the off-diagonal coupling is reduced to $\mathcal{O}(\lambda^2)$. The new diagonal block $\langle v|\tilde{H}|v\rangle$ is also modified from the original $\langle v|H|v\rangle$ by changes of $\mathcal{O}(\lambda^2)$. At this point, the remaining small off-diagonal coupling is neglected, and the isolated block for the vibrational state of interest is numerically diagonalized to generate rovibrational energy eigenvalues and wavefunctions. The size of each diagonal vibrational block is only $(2J+1) \times (2J+1)$, so its direct diagonalization is inexpensive. In practice, the transformation operator $\mathbf{S}$ is never explicitly constructed. Simple equations relate the matrix elements of the effective Hamiltonian $\tilde{H}$ in terms of those of the original Hamiltonian H (see Refs. [51, 233, 234]).

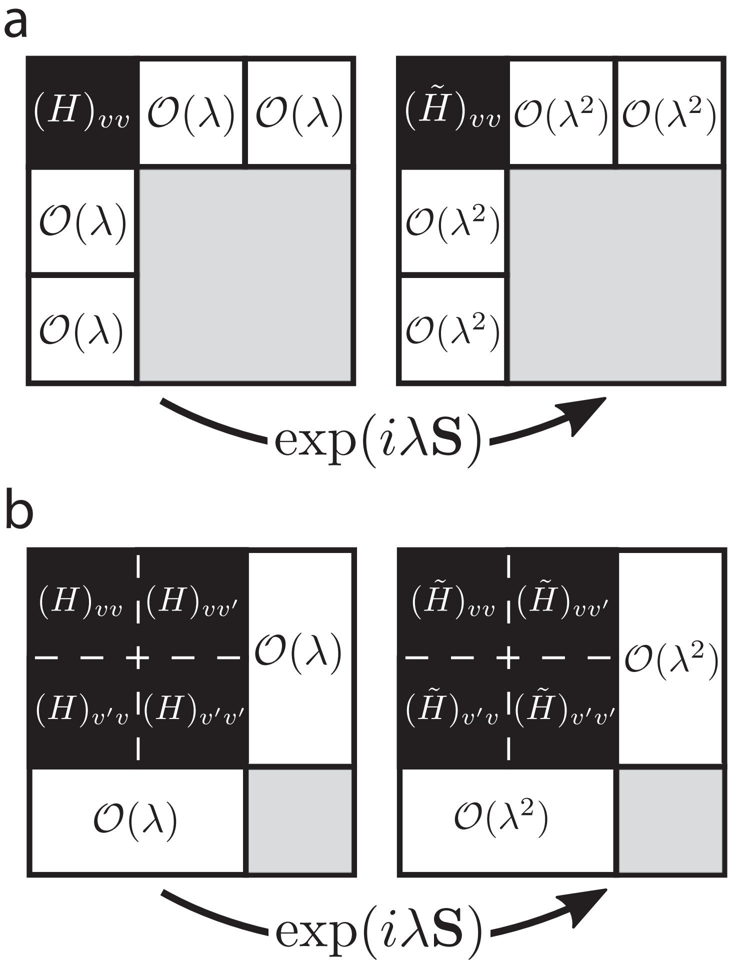

Figure 7.2: Contact transformations of the rovibrational Hamiltonian. (a) A unitary transformation with $\exp(i\lambda\mathbf{S})$ eliminates off-diagonal coupling through λ and transforms the diagonal block $(H)_{vv}$ into the effective Hamiltonian $(\tilde{H})_{vv}$. (b) Resonantly interacting vibrational states are grouped together into a multi-state block. The contact transformation generates a larger effective Hamiltonian that accurately treats the non-perturbative interactions between the resonant states.

This basic procedure works well when individual vibrational states are well-separated in energy and only interact weakly with each other. Large-amplitude motion, however, often results in low-lying vibrationally excited states that have energy differences on the same scale as rotational excitations. This leads to non-perturbative, resonant rotation-vibration interactions. An excellent example is the rotation-torsion manifold in nitromethane (Chapter 3). In this case, the resonantly interacting vibrational states can be grouped together into a multi-state block. The contact transformation eliminates coupling between this enlarged block and the rest of the rovibrational manifold, resulting in a multi-state effective Hamiltonian (Fig. 7.2b). This effective Hamiltonian accurately treats the non-perturbative interactions among the resonant vibrational states. We will see another example of the need for multi-state effective Hamiltonians in the section below about tunneling *gauche*-butadiene.

7.2.3 Kinetic energy operators

We now consider the detailed form of the curvilinear Hamiltonians used in the variational and perturbative methods discussed above. Relative to rectilinear coordinates, which form the basis of the Eckart-Watson Hamiltonian [71], curvilinear coordinates provide an improved treatment of molecular vibrations and large-amplitude motion. These benefits come at the cost of a significantly more complex analytical form of the nuclear motion KEO [235–238]. However, the use of DVR basis functions, which require only numerical evaluation of the KEO instead of close-formed analytical expressions, obviates these drawbacks [239–242].

We define a curvilinear coordinate system for an N-atom molecule by specifying the Cartesian positions $\vec{x}_i$ of each nucleus $i = 1 \ldots N$ in a body-fixed, center-of-mass frame as a function of n internal vibrational coordinates q_k, $k = 1 \ldots n$. For full-dimensional problems, $n = 3N - 6$, though one can also consider reduced-dimension models that use only a subset $n < 3N - 6$ of the available degrees of freedom. The n internal coordinates are collectively denoted as $\vec{q}$. The body-frame Cartesian position functions $\vec{x}_i(\vec{q})$ generate an associated metric tensor $\mathbf{g}$, an $(n + 3) \times (n + 3)$

symmetric matrix with elements given by

$$g_{kl} = \sum_i^N m_i \partial_k \vec{x}_i \cdot \partial_l \vec{x}_i, \tag{7.17}$$

$$g_{\alpha l} = \sum_i^N m_i (\hat{e}_\alpha \times \vec{x}_i) \cdot \partial_l \vec{x}_i, \tag{7.18}$$

$$g_{\alpha\beta} = \sum_i^N m_i (\hat{e}_\alpha \times \vec{x}_i) \cdot (\hat{e}_\beta \times \vec{x}_i). \tag{7.19}$$

Here and throughout, k, l, m, etc. are vibrational indices taking values $1 \ldots n$, and α, β, γ, etc. are rotational indices, taking values x, y, and z (i.e. the three body-fixed axes). ∂_k is shorthand for $\partial/\partial q_k$, $\hat{e}_\alpha$ is a unit vector parallel to the body-fixed α axis, and m_i is the mass of the i^{th} atom. We also define the determinant $g = \det(\mathbf{g})$ and inverse $\mathbf{G} = \mathbf{g}^{-1}$ of the metric tensor.

Following Podolsky [243], the rovibrational KEO can then be written as

$$T = T_\mathrm{v} + T_\mathrm{r} + T_\mathrm{rv}, \tag{7.20}$$

which includes a vibrational term,

$$T_\mathrm{v} = \frac{\hbar^2}{2} \sum_{kl} g^{-1/4} \partial_k^\dagger G_{kl} g^{1/2} \partial_l g^{-1/4}, \tag{7.21}$$

a rotational term,

$$T_\mathrm{r} = \frac{-\hbar^2}{4} \sum_{\alpha\beta} G_{\alpha\beta} \left[\frac{iJ_\alpha}{\hbar}, \frac{iJ_\beta}{\hbar} \right]_+, \tag{7.22}$$

and a rotation-vibration coupling term,

$$T_\mathrm{rv} = \frac{-\hbar^2}{2} \sum_{k\gamma} (-\partial_k^\dagger G_{k\gamma} + G_{k\gamma} \partial_k) \frac{iJ_\gamma}{\hbar}, \tag{7.23}$$

where the operator J_α is the body-frame projection of the total angular momentum $\mathbf{J}$ along the α-axis. (The Hermitian conjugate derivatives $\partial_k^\dagger$ act to the left.) Matrix elements of this KEO are calculated using the so-called Dirac volume element $dq_1 dq_2 \cdots dq_n$ [243, 244] instead of the usual Euclidean volume element that includes the Jacobian determinant of the curvilinear coordinate system, i.e. the normalization convention is

$$\int \cdots \int dq_1 \cdots dq_n \psi^*(\vec{q}) \psi(\vec{q}) = 1. \tag{7.24}$$

The above form of the KEO is convenient for the iterative direct-product DVR grid approach (Section 7.2.1). Matrix elements of complicated expressions such as $g^{-1/4}\partial_k^\dagger G_{kl} g^{1/2} \partial_l g^{-1/4}$ are simple to evaluate by repeated insertion of the truncated identity operator and use of the diagonal-DVR approximation [239].

For the VSCF-based methods, it turns out to be useful to push the derivative operators appearing in T_v to the edges of each term (i.e. ∂_k all the way to right and $\partial_k^\dagger$ to the left). Doing so rearranges T_v into an equivalent form [229, 230],

$$T_\mathrm{v} = \frac{\hbar^2}{2} \sum_{kl} \partial_k^\dagger G_{kl} \partial_l + \frac{\hbar^2}{2} \sum_l \left(U_l \partial_l + \partial_l^\dagger U_l \right) + V_T, \tag{7.25}$$

where the single-derivative coefficients are

$$U_l = -\frac{1}{4} \sum_k \left(\frac{\partial_k g}{g} \right) G_{kl}, \tag{7.26}$$

and the kinetic pseudo-potential is

$$V_T = \frac{\hbar^2}{32} \sum_{kl} \left(\frac{\partial_k g}{g} \right) \left(\frac{\partial_l g}{g} \right) G_{kl}. \tag{7.27}$$

The determinant derivative is conveniently evaluated using the relation $(\partial_k g)/g = \mathrm{tr}(\mathbf{G} \partial_k \mathbf{g})$.

The VSCF calculations require that matrix element integrals of the various functions in the KEO, such as G_{kl}, U_l, and V_T, as well as the PES, be computed between Hartree product basis states. These KEO coefficients in general depend on all n internal coordinates, leading to very high dimensional integrals. For example, molecules as large as butadiene, considered below, would require 24-dimensional sums, which are simply impractical to compute. A common method to address this problem is to expand the various high-dimensional functions in a many-body (or "n-mode") expansion [221, 229]. For some scalar function $F(q_1, q_2, \ldots, q_n)$, this exansion is

$$F(q_1, \ldots, q_n) = f_0 + \sum_k f_k(q_k) + \sum_{k<l} f_{kl}(q_k, q_l) + \sum_{k<l<m} f_{klm}(q_k, q_l, q_m) + \cdots, \tag{7.28}$$

where

$$
\begin{aligned}
f_0 &= F(q_1^{\mathrm{ref}}, \ldots, q_n^{\mathrm{ref}}), \\
f_k &= F(q_1^{\mathrm{ref}}, \ldots, q_k, \ldots, q_n^{\mathrm{ref}}) - f_0, \\
f_{kl} &= F(q_1^{\mathrm{ref}}, \ldots, q_k, q_l, \ldots, q_n^{\mathrm{ref}}) - f_k - f_l - f_0, \\
f_{klm} &= F(q_1^{\mathrm{ref}}, \ldots, q_k, q_l, q_m. \ldots, q_n^{\mathrm{ref}}), \\
&\quad - f_{kl} - f_{km} - f_{lm} - f_k - f_l - f_m - f_0,
\end{aligned}
\tag{7.29}
$$

and so on. $(q_1^{\mathrm{ref}}, \ldots, q_n^{\mathrm{ref}})$ is a reference geometry about which the expansion is computed (usually the equilibrium configuration). Many-body expansions break up a complicated high-dimensional function into smaller parts of lower dimensionality. By taking the expansion to include all terms up to n-body contributions, the exact original function F is recovered, but nothing is gained. It is often accurate, however, to truncate the expansion at three- or four-body terms, which drastically reduces the dimensionality of the matrix element integrals of F. The small errors introduced by the many-body expansion can be systematically controlled by checking that computed energies are converged with respect to the maximum number of n-body terms.

7.2.4 Coordinate systems and body-fixed frame embedding

The procedures above allow us to construct the numerically exact KEO for an arbitrary set of internal coordinates $\vec{q}$ and body-fixed frame embedding (implicitly defined by the Cartesian position functions $\vec{x}_i(\vec{q})$). The question remains, how do we choose these coordinates optimally?

For iterative direct-product DVR grid calculations, we often use primitive valence coordinates such as internuclear distances, bond angles, and dihedral angles [237]. Simple orthogonal coordinate systems like Jacobi and Radau coordinates are also convenient [245, 246]. For reduced-dimension calculations it is of course necessary to choose coordinates that accurately describe the dynamics of the sub-system of interest. The computational efficiency and accuracy of full-dimensional direct-product grid calculations, however, is not strongly dependent on the choice of coordinates as long as they compactly span the energetically relevant regions of configuration space.

On the other hand, the choice of coordinates is critically important for VSCF-based calculations. In general, one wants to find a coordinate system that minimizes coupling and leads to an approximately separable vibrational Hamiltonian, $H_v(\vec{q}) \approx h_1(q_1) + h_2(q_2) + \cdots$. This ensures that the VSCF Hartree product is an accurate zeroth-order wavefunction and that the various many-body expansions will be accurate for low expansion orders. For molecules with a single equilibrium configuration, the ground and lowest excited vibrational states are usually best described with the normal coordinates associated with the PES minimum. These are found by a (curvilinear) GF harmonic analysis [247]. Systems with more than one dynamically accessible minimum, which describes most of the examples below, require a more elaborate treatment such as a reaction path (RP) coordinate system [224, 248–252]. A RP coordinate system is based on the steepest descent trajectory that connects neighboring minima through intermediate saddle points on the PES. At each point along the steepest descent RP, a modified GF calculation is performed to determine the "instantaneous" normal modes orthogonal to the RP at that position. In this way, the RP coordinate system smoothly interpolates between the different normal mode coordinates associated with each local minimum. It provides an approximately globally separable coordinate system, which is crucial to making VSCF/VMP2 efficient and accurate.

In addition to choosing a coordinate system that minimizes the coupling between different vibrations, VSCF/VMP2 requires that the body-fixed frame embedding results in small rotation-vibration coupling terms T_{rv}. This embedding is defined by how the molecular body-fixed frame is rotated in space for a given value of the internal coordinates $\vec{q}$. For most cases, the best choice of embedding is the Eckart frame [216], which eliminates rotation-vibration coupling near the equilibrium geometry. Implementing Eckart frame embedding for arbitrary curvilinear Hamiltonians is in general a complicated, non-trivial problem [241, 242, 253–256]. The approach we take is based on the elegant quaternion algebra method recently introduced by Krasnoshchekov et al. [257]. It allows for the simple numerical evaluation of exact Eckart-frame KEOs. Further algorithmic details can be found in Ref. [51].

7.2.5 Potential energy surfaces

Last but not least, an accurate potential energy surface based on high-level quantum chemical methods is the foundation for any nuclear motion calculation. The techniques discussed above require the PES to be evaluated over coordinate grids that can contain up to millions of points. Performing an individual electronic structure calculation at each of these grid points is impractical, and the usual approach is to instead fit an analytical representation of the PES to a smaller data set of pre-computed electronic energies, of which perhaps only thousands to tens of thousands are necessary. We rely on single-reference coupled-cluster (CC) theory – in particular its CCSD(T) variant [258] – in combination with the Dunning correlation-consistent basis sets [259] or the atomic natural orbital (ANO) basis sets of Almlöf and Taylor [260], which perform well for vibrational frequency calculations [261]. All electronic structure calculations for our in-house PES's are performed with the CFOUR package [262].

One advantage of DVR basis sets is that the PES only needs to be numerically evaluated on grid points. The coordinates used to describe the PES are therefore entirely independent of the "dynamical" coordinates used in the nuclear motion calculation itself, providing substantial flexibility in the underlying analytical representation of the PES. A high-dimensional polynomial in some set of internal coordinates is typically fit via linear-least-squares to a set of electronic energies. The method of permutationally invariant polynomials (PIPs) is particularly useful for generating surfaces that rigorously enforce nuclear permutation symmetry [263]. We make extensive use of this approach and have developed a suite of tools for constructing, fitting, and coding PIP surfaces combined with automated differentiation [199, 264].

7.3 Applications

The first half of this chapter introduced methods for high accuracy *ab initio* rovibrational calculations. In the second half, we apply these to several molecular systems. Most of these projects were carried out in close coordination with experimental collaborators, as acknowledged in each section, as well as two essential theory collaborators, Josh Baraban (Ben-Gurion University) and John Stanton (University of Florida).

7.3.1 Photoelectron spectroscopy of the methide anion, CH_3^-

The methide anion, CH_3^-, is the simplest carbanion species [265]. As the conjugate base of CH_4, it plays an important role in constraining thermochemical cycles that determine the gas-phase acidity of CH_4, itself an important thermochemical reference [266]. CH_3^- is isoelectronic to NH_3 and H_3O^+ and shares with them a non-planar, trigonal pyramidal structure with tunneling inversion between the two equivalent enantiomers [267]. Characterizing this fundamental structural motif is, however, challenging due to the difficulty in isolating this reactive species in the gas phase [268–270].

This section discusses the high-resolution photoelectron spectra of CH_3^- (and CD_3^-) recently measured in the Lineberger lab as part of an intra-JILA collaboration [192]. The experiment measures the electron kinetic energy (eKE) of photo-detached electrons generated via $CH_3^- + h\nu \to CH_3 + e^-$, where $h\nu$ is represents a photon from a pulsed nanosecond laser source. The derived electron binding energies ($\text{eBE} = h\nu - \text{eKE}$) provide a map of the vibrational energy levels of the anion and neutral species. The experimental spectrum (Fig. 7.3a) exhibits an extended Franck–Condon progression in the ν_2 umbrella mode associated with the large change in geometry between the pyramidal C_{3v} anion and the planar D_{3h} neutral. The goal of the calculations is to accurately simulate this spectrum, particularly features associated with the inversion tunneling splitting in the anion.

We used a reduced-dimension treatment to calculate the vibrational levels of CH_3^- and CH_3. The umbrella inversion angle ϕ and the three C–H bond lengths were included, while the HCH bond angles were constrained to be equal. A 4-D anion potential energy surface was constructed initially at the CCSD(T)/d-aug-pVTZ level of theory. This surface was further refined with corrections for a variety of higher order effects including triple augmentation, core correlation, triples and non-iterative quadruples correlation, diagonal Born-Oppenheimer corrections, scalar relativistic corrections, and zero-point motion in the neglected HCH bend angles (see supplementary infor-

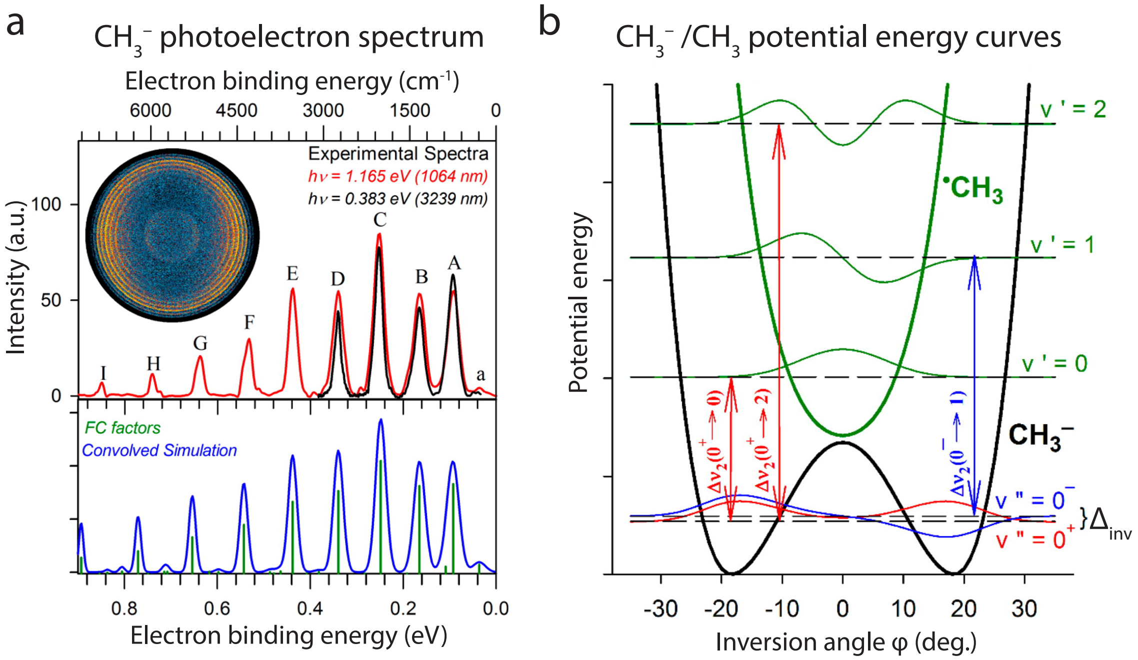

Figure 7.3: Photoelectron spectra and potential curves of CH_3^-/CH_3. (a) Upper panel: the photoelectron spectra are shown for two photon energies, 1.165 eV (red) and 0.383 eV (black). The inset shows a raw velocity-mapped photoelectron image (see Ref. [192] for details). Lower panel: The simulated Franck–Condon spectrum. (b) The potential energy curves (not to scale) of CH_3^- (black) and CH_3 (green) as a function of the umbrella inversion angle ϕ. The vertical arrows indicate Franck–Condon-allowed transitions from the $v = 0^+$ (red) and $v = 0^-$ (blue) anion tunneling states, which are split in energy by Δ_{inv}. (Figures adapted with permission from A. Oliveira et al., *J. Am. Chem. Soc.* 137:12939 (2015). Copyright 2015 American Chemical Society.)

mation of Ref. [192] for details). For the neutral, we used the *ab initio* force field calculated by Schwenke [271]. The reduced-dimension vibrational levels of the anion and neutral were calculated on these surfaces using the iterative diagonalization direct-product DVR grid method.

Figure 7.3a demonstrates the excellent agreement between the experimental photoelectron spectrum with a simulation using the Franck–Condon overlap factors between the calculated anion and neutral vibrational wavefunctions. Peaks “A” through “I” correspond to transitions from the $v = 0^+/0^-$ ground state tunneling doublet of the anion to successively higher overtones of the ν_2 umbrella inversion mode of the neutral. The calculated spectrum also confirms the assignment of peak “a” as a hot band from the $v = 1^+$ anion vibrational level. Figure 7.3b illustrates the contrasting level structure of the double-well anion potential curve vs. the single-well neutral. The energy splitting Δ_{inv} between the $v = 0^+$ and $v = 0^-$ tunneling levels of the anion corresponds to the frequency of interconversion between the two enantiomer wells. From the positions of the experimental peaks, this tunneling splitting is determined to be $\Delta_{\text{inv}} = 21(5)$ cm^{-1}, consistent with the calculated value of 25.0 cm^{-1}. (Similar results are obtained for the deuterated CD_3^- species [192].)

The inversion tunneling splitting for CH_3^- is intermediate to those of NH_3 (0.79 cm^{-1}, the famous ammonia maser transition [272, 273]) and H_3O^+ (55.34 cm^{-1} [274]). These only very roughly correlate with the corresponding effective 1-D inversion barrier heights: 661 cm^{-1} for CH_3^- as inferred from our 4-D surface vs. 650 cm^{-1} for H_3O^+ and 1782 cm^{-1} for NH_3 [275]. This illustrates why concepts such as 1-D effective barrier heights should be considered with a grain of salt. Tunneling dynamics are sensitive to the complete multi-dimensional potential energy surface. Vibrational motion calculations that account for such multi-dimensional dynamics, such as those reported here, are ultimately necessary for spectroscopically accurate *ab initio* results.

7.3.2 Laboratory and astronomical discovery of disilicon carbide, Si_2C

Small silicon- and carbon-containing molecules are key building blocks for the formation of interstellar dust [276] and thought to be important intermediates in the generation of solid SiC [277]. Of the four triatomics containing only silicon and carbon (Si_mC_n, $m + n = 3$), the least well-studied is disilicon carbide, Si_2C, despite evidence of it being unusually stable [278] and an abundant Si-bearing species in space [279]. Quantum chemical studies predict Si_2C to have a bent geometry with an Si–C–Si bond angle of about 115°, but a low barrier to linearity of only ~ 800 cm^{-1} [280–282]. The highly anharmonic rovibrational structure of such "quasi-linear" molecules is of considerable fundamental interest [283]. There has been no prior spectroscopic characterization of Si_2C, however, with the exception of limited matrix-IR [284, 285] and low-resolution electronic excitation spectra [286].

This gap has recently been addressed by a series of spectroscopic studies carried out in the McCarthy lab at the Harvard-Smithsonian Center for Astrophysics characterizing the rovibrational structure of the ground electronic state of Si_2C [193,194]. As part of a joint theoretical-experimental collaboration, we carried out extensive *ab initio* calculations to aid in the assignment, analysis, and prediction of these spectra. The project originated with observations of the ground $^1A_1$ electronic state of Si_2C acquired by laser-induced dispersed fluorescence (DF) from excited electronic states in the 380–395 nm region. The DF spectra, shown in Fig 7.4, exhibit extended Franck–Condon progressions in the ν_2 bending mode consistent with the large change in geometry between the near-linear excited state and the bent ground state ($\angle$SiCSi $= 115°$, see Fig. 7.5a). Weaker stretch-bend combinations are also observed. We constructed an Si_2C PES at the frozen-core CCSD(T)/PVQZ level of theory and used this to compute the lowest 200 vibrational states, which extend up to about 4000 cm^{-1} above the vibrational ground state, as well as rotational sub-levels up to $J \leq 3$ for vibrational states below 2500 cm^{-1}. With guidance from these calculations, essentially all emission lines in the DF spectra could be assigned with excellent agreement between the observed and calculated vibrational energies (see supplementary material of Ref. [193]).

The barrier to linearity reveals itself spectroscopically by the observed decrease and then increase of the effective bending frequency as the barrier energy is approached and then exceeded. This "Dixon-dip" behavior is readily seen in plots of the bending interval as a function of the vibrational energy, where a minimum occurs in the vicinity of the linear saddle point [287] (Fig. 7.5b). From the $(v_1 = 0, v_2 = n, v_3 = 0)$ bending progression, we extract an experimental effective barrier height of 783(48) cm^{-1} [288], in good agreement with theory (802(9) cm^{-1}). Excitation in the symmetric Si–C stretching mode ν_1 decreases the effective barrier by about 300 cm^{-1}, while excitation in the antisymmetric stretch ν_3 increases it by about 360 cm^{-1}. These changes are consistent with the changes in the calculated harmonic frequencies at the saddle-point. The spectroscopic signatures of the barrier to linearity are also apparent in the experimental and calculated eigenvalue lattices for the (K_a, ν_2) levels, shown in Fig. 7.5c. (K_a is the usual a-axis rotational quantum number.) As the ν_2 bending mode is excited up to and beyond the barrier to linearity, the K_a-dependence transitions from quadratic to linear. This is a quintessential example of quantum monodromy, where a critical point in the Hamiltonian due to the linear saddle point prevents the

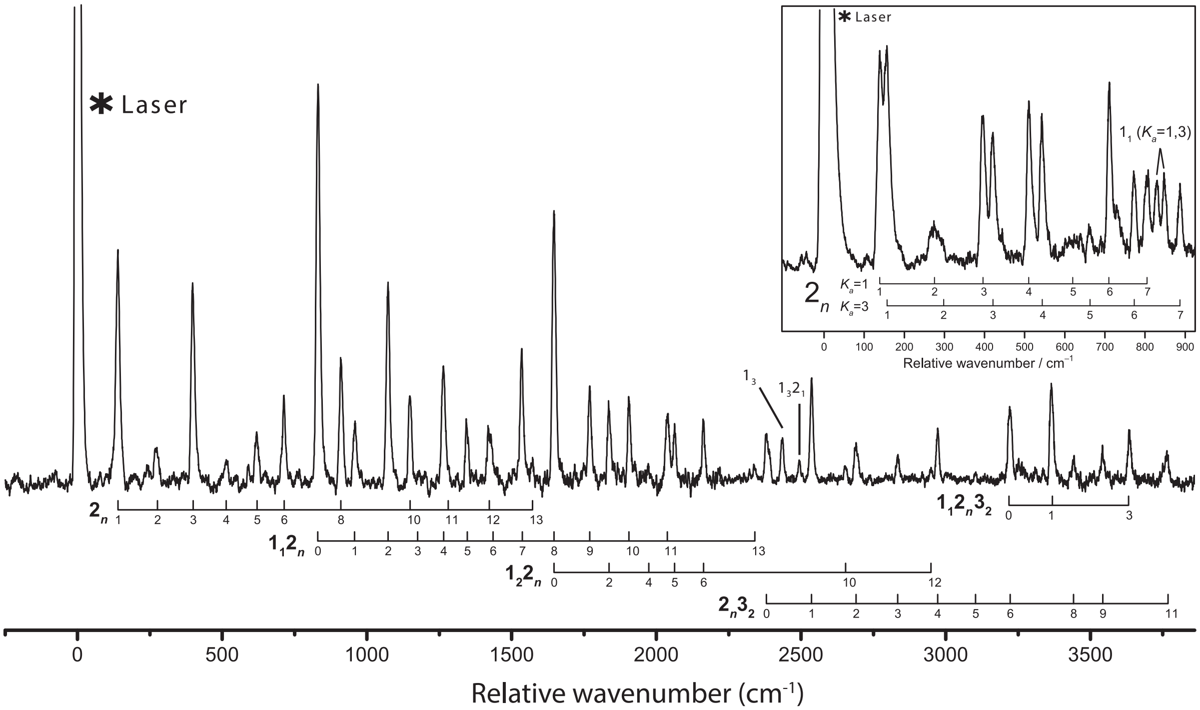

Figure 7.4: Dispersed fluorescence (DF) spectra of Si_2C. The main plot shows the DF spectrum after excitation at 25515 cm^{-1} of a parallel transition within the K_a sub-level. Essentially all features can be assigned with guidance from variational nuclear motion calculations. Vibrational assignments are summarized in Table S1 of Ref. [193]. Inset: DF spectrum of Si_2C at 26242 cm^{-1} excitation. This is a perpendicular transition with emission to $K_a = 1$ and 3 sub-levels, which diverge as the barrier to linearity is approached. (Figure reproduced from N. Reilly et al., *J. Chem. Phys.* 142:231101 (2015), with the permission of AIP Publishing.)

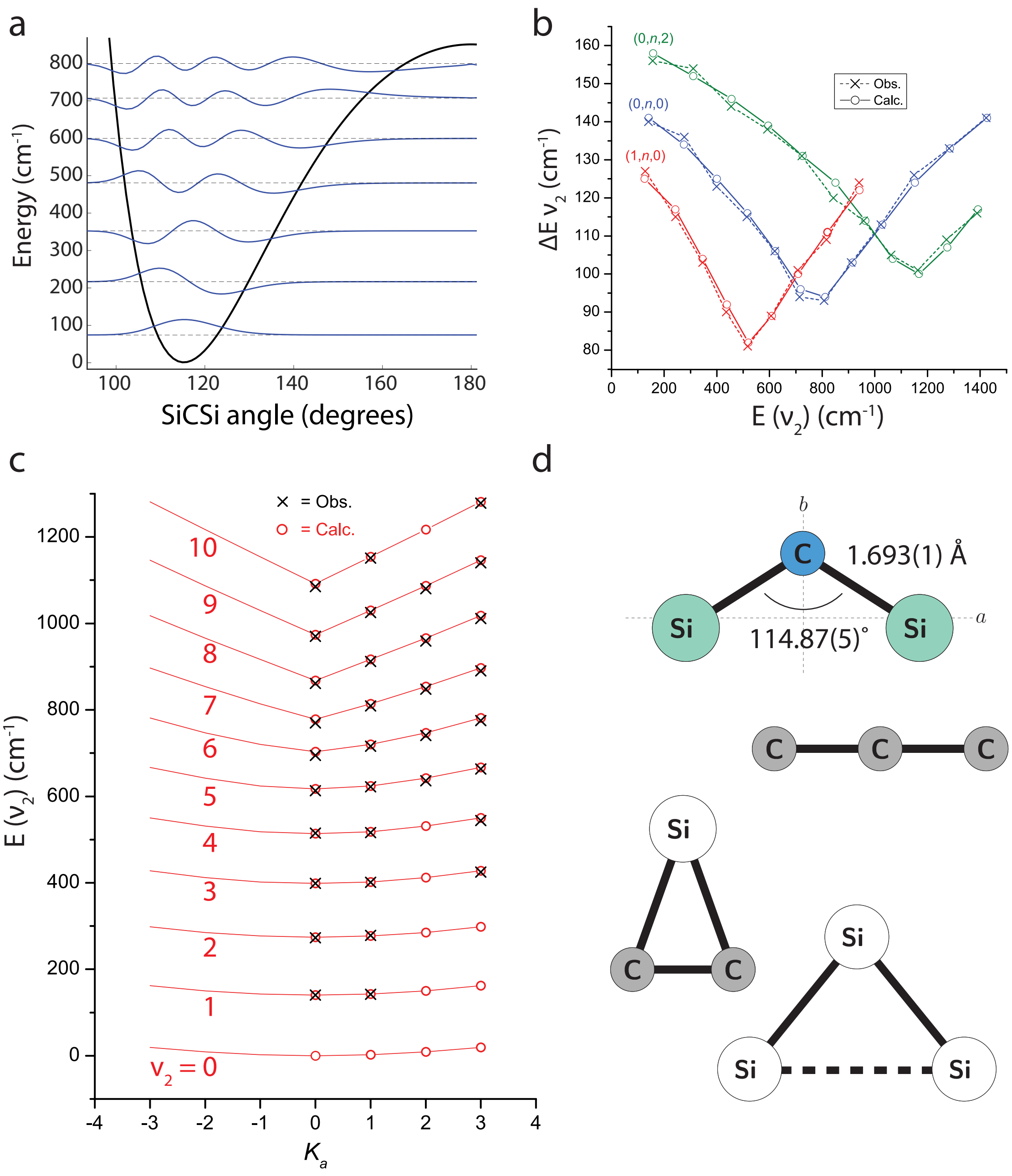

Figure 7.5: Potential energy surface, energy levels, and structure of Si_2C. (a) The potential energy surface as a function of the Si–C–Si bending angle, with a minimum near 115° and a barrier to linearity of ca. 800 cm^{-1}. The 1-D bending wavefunctions for states below the barrier are shown. (b) The bending energy level interval, representative of the effective bending frequency, is plotted versus vibrational energy for the pure bending progression $(v_1, v_2, v_3) = (0, n, 0)$, as well as for the symmetric stretch $(1, n, 0)$ and antisymmetric stretch $(0, n, 2)$ combinations. A characteristic dip occurs at the energy of the barrier. (c) (v_2, K_a) eigenvalue lattice for $v_2 \leq 10$ and $K_a \leq 3$. The transition from quadratic to linear K_a-dependence near $v_2 = 7$ is a signature of quantum monodromy. (d) The structures of Si_2C (this work) and the three other silicon carbides Si_mC_n with $m + n = 3$. (Figures b,c reproduced from N. Reilly et al., *J. Chem. Phys.* 142:231101 (2015), with the permission of AIP Publishing; Figure d adapted with permission from M. McCarthy et al., *J. Phys. Chem. Lett.* 6:2107 (2015). Copyright 2015 American Chemical Society.)

existence of a uniquely defined set of global quantum numbers [289].

Guided by the accurate rovibrational variational calculations, a new search was conducted by our collaborators for the pure rotational spectrum of Si_2C using Fourier transform microwave (FTMW) spectroscopy [194]. Detection of Si_2C by FTMW has proven challenging because of its sparse rotational spectrum (with half the levels missing from nuclear spin statistics) and the sensitivity of its rotational constants to small changes in its geometry, especially the obtuse Si–C–Si bending angle. Our calculations predicted a strong rotational transition ($2_{0,2} \rightarrow 1_{1,1}$) near 38 GHz for the $Si^{13}CSi$ isotopologue, which was quickly found in the laboratory. Two additional lines were detected at exactly the predicted frequencies for the ^{29}Si and ^{30}Si isotopic shifts, confirming the carrier to be Si_2C. Ultimately, between eight and twelve transitions from each of $^{28}Si_2{}^{12}C$ and the ^{13}C, ^{29}Si, and ^{30}Si singly substituted isotopologues were measured, permitting a fit of their ground state rotational constants. The experimental rotational constants were then corrected with calculated zero-point motion shifts to obtain semi-experimental equilibrium constants, which were then used to derive the precise semi-experimental equilibrium structure shown in Fig. 7.5d. By comparing this structure to other triatomic silicon carbides, it can be inferred that when silicon is the central atom, it prefers a small bending angle ($< 90°$), while a central carbon atom prefers only slightly bent or linear geometries. These structural patterns illustrate the predominantly single bonding nature of silicon via p orbitals vs. the multiple bonding of carbon via sp or sp^2 hybridization [194].

The laboratory identification of Si_2C immediately led to its astronomical discovery in the carbon-rich star IRC+10216 [195]. These observations have shown that, along with SiC_2, Si_2C is the most abundant species containing a Si–C bond in the dust formation region of this star, indicating that it plays a key role in the formation of dust grains. Since this initial discovery, additional astronomical and laboratory observations have been made [290], including rotational satellite transitions from vibrationally excited Si_2C, which greatly benefited from our variationally calculated vibration-rotation constants [276]. Rapid progress continues to be made on the spectroscopy of Si_2C, including the first rotationally resolved infrared measurements of the ν_3 band recently reported by Witsch et al. [291].

7.3.3 The ionization energy and equilibrium structure of hydrogen peroxide, H_2O_2

In the past fifteen years, the advent of Active Thermochemical Tables (ATcT) [292, 293] has dramatically improved the accuracy of fundamental thermodynamic quantities of small molecules. The ATcT approach relies on thermochemical networks, which explicitly account for the high degree of interdependency between the thermodynamics of even very different molecules. All available information, including both experimental and high-level theoretical data (with calibrated uncertainties), is taken into account by the network to provide self-consistent, accurate values of bond energies, enthalpies of formation and reaction, etc. with meaningful uncertainties. In some cases, computational results are used to reanalyze published data for inclusion in ATcT. In this section, we discuss such an example for the ionization energy (IE) of hydrogen peroxide, H_2O_2. This work was carried out in collaboration with the "ATcT Task Force" led by Branko Ruscic (Argonne National Laboratory).

The IE of H_2O_2 has potentially important impact on the ions of compounds involved in hydrogen combustion chemistry, as well as several other key chemical species [197, 294]. In 2016, Schio et al. studied H_2O_2 via threshold photoelectron spectroscopy (TPES), reporting an IE of 10.685 ± 0.005 eV [294]. This value disagrees by many σ with the (then current) ATcT value of 10.637 ± 0.006 eV [295], the largest contributors to which a photoionization mass spectrometry (PIMS) measurement, 10.631 ± 0.007 eV [296], and an early photoelectron spectroscopy measurement, 10.62 ± 0.02 eV [297]. The TPES value is based on the assignment of peak "a" in Fig. 7.6b to a vibrational hot band involving the torsional mode, placing the vibrational origin (the 0–0 transition) between peaks "a" and "b". This assignment is largely based on harmonic Franck–Condon simulations carried out by the authors of Ref. [294]. The ground state of H_2O_2, however, exhibits large-amplitude nuclear motion (Fig. 7.6a) and a simple harmonic simulation is inadequate.

We have reanalyzed the TPES spectrum using simulations based on variational anharmonic vibrational wavefunctions and energies of the neutral molecule and cation. For the neutral, we use the potential energy surfaces previously reported by Koput et al. [298, 299], while for the cation we constructed a new surface at the FC-EOMIP-CCSD/ANO0 level of theory [260, 300]. We converged full-dimensional vibrational wavefunctions with the iterative diagonalization direct-product DVR grid method. Franck–Condon factors were calculated with the overlap integrals of the computed wavefunctions. The resulting photoelectron spectrum simulation is shown in Fig. 7.6b. The simulated spectrum has been shifted so that the origin band coincides with peak "a". In the low-energy region of the spectrum, the first unresolved feature actually contains the 4^0_1 hot band (ν_4 is the torsional mode) and the origin band. Features up to 11.1 eV can also be assigned (see Table 2 of Ref. [197]). The excellent qualitative agreement with experimental spectrum confirms the correct origin assignment. This alternative interpretation of the TPES spectrum leads to a revised IE of 10.649 ± 0.005 eV.

In the older PIMS measurement by Litorja and Ruscic [296], the reported IE of 10.631 ± 0.007 was based on the half-height of the first step in the onset of the photoionization efficiency (PIE) curve, shown in Fig. 7.6c. The anharmonic simulations suggest, however, that the strong 4^0_1 hot band is probably biasing this determination to too small a value. In light of this, we have reanalyzed the PIMS PIE curve in comparison to the integrated Franck–Condon simulation at 300 K (convoluted with the appropriate instrument line shape). The simulations indicate that the PIMS value should be slightly increased to 10.645 ± 0.010 eV, which is now consistent with the revised TPES value of 10.649 ± 0.005 eV.

A careful analysis of the experimental spectra also requires one to consider shifts due to assymetric rotational envelopes. A completely quantitative analysis of this effect requires knowledge of the the photoelectron partial wave amplitudes, which is outside the scope of this study. However, an analysis of the rotational contours under various scenarios suggests that the peak of the origin band contour will indeed be blue-shifted by about 7 meV relative to the true IE, though with a large uncertainty of ±6 meV. This shift is mostly due to the large difference in the value of $(B+C)/2$ in the cation (1.01 cm^{-1}) and neutral (0.86 cm^{-1}). Taking this into account leaders to further refinement of the PIMS and TPES IE values: 10.638 ± 0.012 eV and 10.642 ± 0.008 eV,

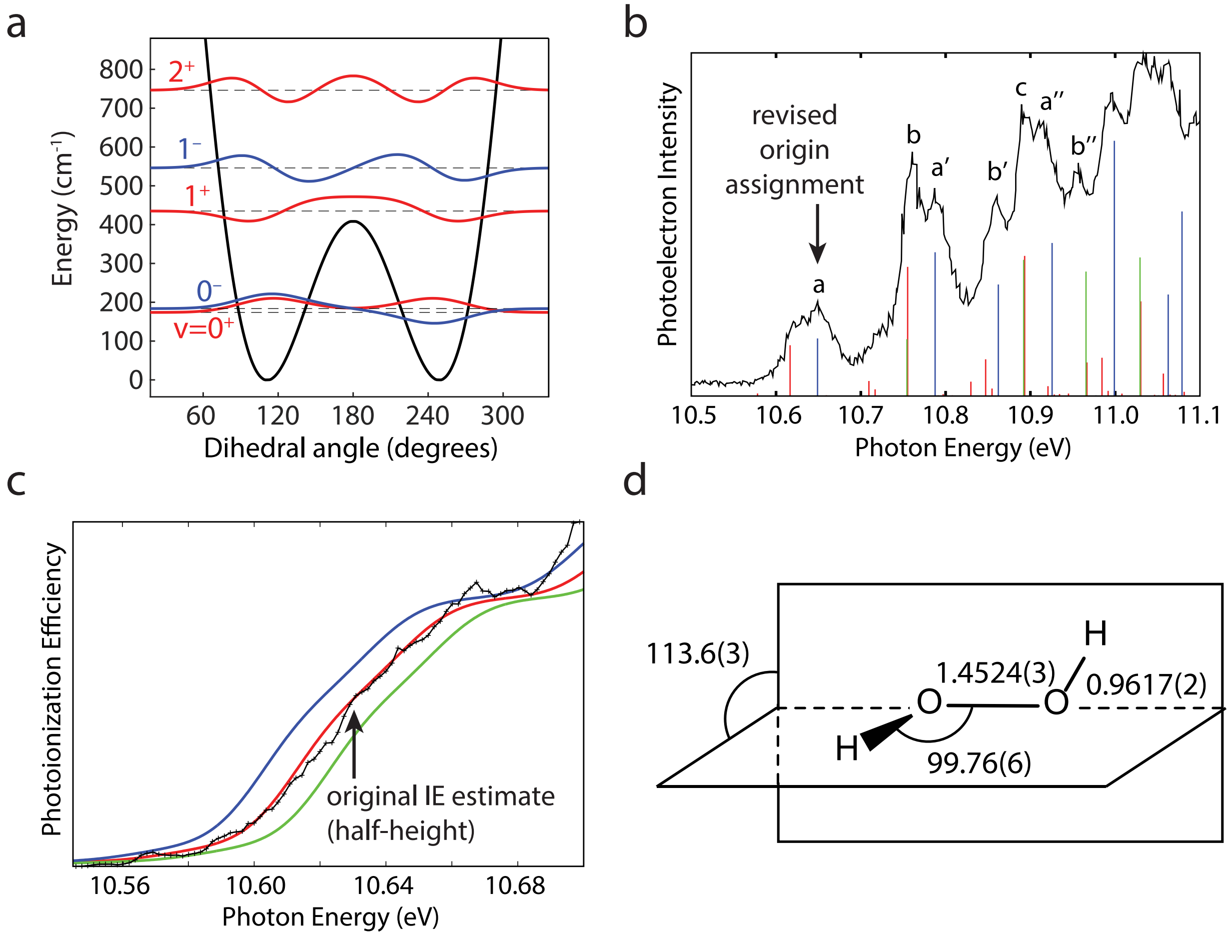

Figure 7.6: Potential energy, spectra, and equilibrium structure of H_2O_2. (a) The large-amplitude torsion angle is delocalized over a double-well potential energy curve. The ground torsional state has two tunneling components, $v = 0^+$ and 0^- split by 11 cm^{-1}. (b) The TPES spectrum from Ref. [294] (black) together with the simulated stick spectrum (this work). Blue features originate from the 0^+ ground state, green features from 0^-, and red features from higher torsional states $(1^+, 1^-, 2^+, \ldots)$. The stick spectrum was simulated at a vibrational temperature of 200 K. (c) PIE curve from Ref. [296] (black), along with integrals of the simulated spectrum (at 300 K). The three simulated curves are shown assuming an IE of 10.635 eV (blue), 10.645 eV (red), and 10.655 eV (green), without including effects from rotational contour shifts (see text). The original IE estimate at the half-height of the PIE step is indicated. (d) The semi-experimental equilibrium geometry of H_2O_2. Bond lengths are in Å, and angles are in degrees. (Figures b, c adapted with permission from P. B. Changala et al., *J. Phys. Chem. A*, 121:8799 (2017). Copyright 2017 American Chemical Society; Figure d reused with permission from J. Baraban et al., *J. Mol. Spectrosc.*, 343:92 (2018). Copyright 2018 Elsevier).

respectively. Together with a new *ab initio* IE calculated as part of this work (see Ref. [197] for details), a revised ATcT analysis results in a final composite IE value of 10.641 ± 0.006 eV. This value ends up being very similar to the previous best ATcT estimate (10.637 ± 0.006 eV [295]), but this appears to be due to a fortuitous cancellation of the corrections associated with the vibrational hot band analysis and rotational contour shifts.

During the course of this work, it was realized that the equilibrium structure of H_2O_2 had surprisingly never been completely determined [301–303], despite sufficient spectroscopic data being available [304–308]. The main challenge is the large difference between the equilibrium r_e structure and the effective ground state r_0 structure, making it critical to account for effects of large-amplitude zero-point torsional motion [303, 309]. We calculated the rovibrational zero-point corrections using the same methods as above for the H_2O_2 IE study. Semi-experimental rotational constants ($B^{\mathrm{se}}_{\mathrm{eq}}$) were determined by subtracting the *ab initio* zero-point motion correction from the measured ground state constants for HOOH, HOOD, and DOOD [304–308]. Figure 7.6d shows the semi-experimental equilibrium geometry fitted to the $B^{\mathrm{se}}_{\mathrm{eq}}$ values [196]. Without the inclusion of zero-point motion corrections, the fitted HOOH dihedral angle is 6° larger, illustrating the important effects of large-amplitude torsional motion. It is interesting to note that the equilibrium OH bond length in H_2O_2 (0.9617(2) Å) is much closer to that of H_2O (0.9578(1) Å [310]) than the OH radical (0.969628(9) Å [311]), consistent with the fact that the hybridization in H_2O_2 is more similar to that in H_2O than to OH.

7.3.4 The molecular structure of *gauche*-1,3-butadiene, C_4H_6

The Diels–Alder cycloaddition reaction between a conjugated diene and a dienophile is one of the most important ring-forming reactions in chemistry [312]. The classic example is the addition of 1,3-butadiene, $H_2C{=}CH{-}CH{=}CH_2$, and ethylene, $H_2C{=}CH_2$, to form cyclohexene,

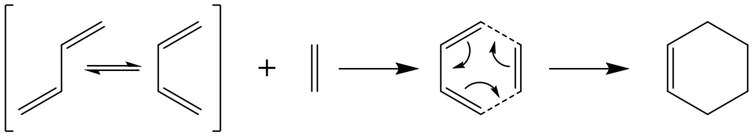

Although the *trans* isomer of butadiene is the thermodynamically most stable, it must isomerize to a *cis* conformation before proceeding through the aromatically stabilized, pericyclic planar transition state. The planarity of *cis*-butadiene itself, however, has not been established. In fact, a number of quantum chemical studies [313–317] and gas-phase Raman experiments [318–320] have led to the conclusion that "*cis*"-butadiene actually exhibits a non-planar *gauche* geometry [321], yet a definitive structural characterization of this molecule has remained elusive.

In another joint theoretical-experimental collaboration with the McCarthy and Patterson groups, a combination of sensitive microwave techniques and high accuracy rovibrational calculations has been used to conclusively show that *cis*-butadiene possesses a non-planar *gauche* equilibrium geometry and undergoes facile tunneling interconversion between its two enantiomeric forms [198]. Prior attempts to measure the microwave spectrum of *gauche*-butadiene have been unsuccessful due to multiple experimental challenges. First, the *gauche* conformer lies 2.93 kcal mol^{-1} above the more stable *trans* conformer [322]. At room temperature this translates into a relative population of only about 1%. Second, it possesses a very small dipole moment (ca. 0.09 D) leading to weak rotational transitions, the frequencies of which are sensitive to the C=C–C=C torsional angle τ (Fig. 7.7a). These experimental challenges were overcome with a combination of cavity-enhanced FTMW combined with a supersonic expansion and chirped-pulse FTMW in a cryogenic buffer gas cell (similar to the buffer gas cell apparatus used for the frequency comb spectroscopy described in this thesis). Further experimental details can be found in Ref. [198].

Spectral searches were initially guided by high-level *ab initio* calculations. With 10 atoms and

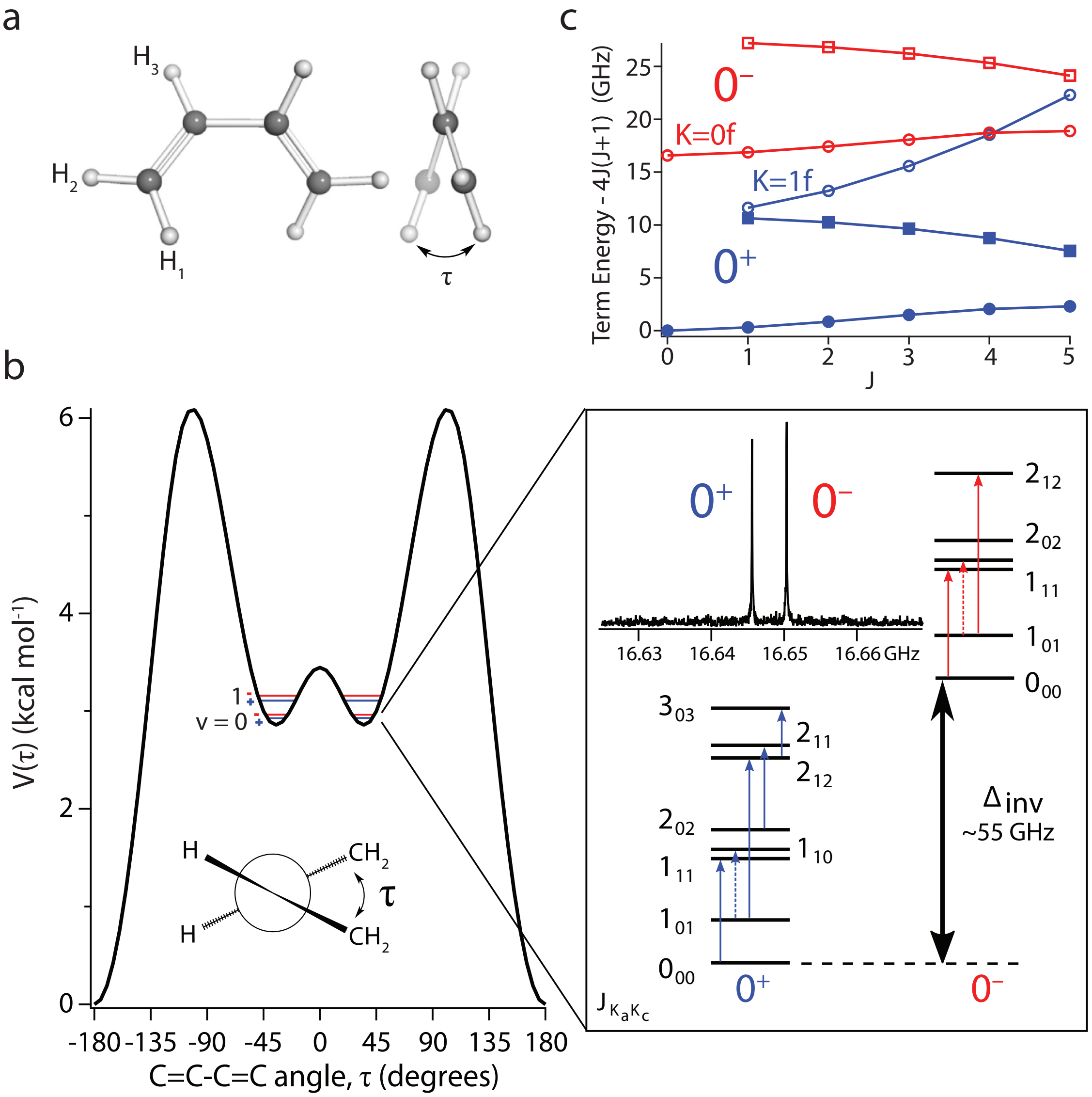

Figure 7.7: Structure and rovibrational energy levels of *gauche*-butadiene. (a) The C=C–C=C torsional dihedral angle of the butadiene carbon backbone is labeled τ. (b) The torsion potential energy curve has a global minimum at the *trans* geometry ($\tau = 180°$) and two symmetry-equivalent local minima at the *gauche* geometry ($\tau \approx \pm 35°$). The expanded view shows the rotational sublevels of the ground state tunneling doublet and the allowed pure rotational transitions. The dashed arrows indicate the transitions shown in the measured inset spectrum. The 0^+ and 0^- manifolds are separated in energy by the tunneling frequency Δ_{inv}. (c) Reduced rotational term energy plot of the ground state tunneling doublet for d_6 butadiene. The $K = 1f$ manifold of the 0^+ tunneling component crosses the $K = 0f$ manifold of the 0^- tunneling component at $J = 4$ resulting in magnified Coriolis perturbations. $E^+/O^+/E^-/O^-$ rovibrational symmetries are represented by filled circles/open circles/open squares/filled squares, respectively. (Figures reused with permission from J. Baraban et al. *Angew. Chem. Int. Ed.*, 57:1821 (2018).)

24 vibrational modes, butadiene is too large for a brute-force direct-product DVR grid calculation. We therefore turned to the rotational curvilinear VMP2 method to calculate accurate rovibrational parameters. We constructed a full-dimensional FC-CCSD(T)/ANO1 PIP PES and the associated curvilinear reaction path coordinate system. The *gauche* form of butadiene has a double-well potential energy curve along the τ torsion angle as shown in Fig. 7.7b. The ground vibrational state splits into $v = 0^+$ and 0^- tunneling components. Both tunneling components support an independent manifold of rotational sub-levels, and transitions within these appear as closely spaced doublets in the microwave spectrum. Rotational constant predictions calculated via rotational VMP2 guided targeted spectroscopic searches, which soon led to the observation of transitions near the predicted frequencies. The observed transitions were used to fit rotational constants for several isotopologues of *gauche*-butadiene. These measured rotational constants were finally corrected with theoretical zero-point motion shifts to determine the semi-experimental equilibrium structure summarized in Table 7.1. The fitted dihedral angle of $\tau = 33.8(13)^\circ$ unambiguously establishes the non-planarity of *gauche*-butadiene.

Table 7.1: Semi-experimental equilibrium geometry of *gauche*-butadiene. Bond lengths are in Å, and angles are in degrees. Numbers in brackets [ ] are fixed to *ab initio* values (see Ref. [198] for details).

Parameter	Value
r(C–C)	1.48(2)
r(C=C)	1.33(1)
$\angle$C–C=C	124.1(5)
$\angle$C=C–C=C (τ)	33.8(13)
r(C–H$_1$)	1.08(1)
$\angle$H$_1$–C=C	123(2)
$\angle$H$_1$–C=C–C	2(1)
r(C–H$_2$)	[1.07983]
$\angle$H$_2$–C=C	118(1)
$\angle$H$_2$–C=C–H$_3$	[2.410]
r(C–H$_3$)	1.083(5)
$\angle$H$_3$–C–C	116.2(6)
$\angle$H$_3$–C–C=C	−146.4(7)

Microwave transitions between the $v = 0^+$ and 0^- tunneling components are symmetry forbidden, so that the $0^+/0^-$ tunneling splitting Δ_{inv} cannot be directly probed. Multi-state rotational VMP2 calculations, however, reveal that the two tunneling components interact via a $C \times (J_a J_c + J_c J_a)$-type Coriolis term, with an interaction constant $C = 20 - 30$ MHz depending on the isotopologue. This interaction results in the largest spectroscopic perturbations near crossing-points of the $0^+/0^-$ rotational manifolds (Fig. 7.7c). By a careful fit of the microwave transition frequencies to an interacting two-state model, both the tunneling frequency Δ_{inv} and the Coriolis interaction coefficient C can be determined. Table 7.2 shows the results of this analysis for the fully deuterated d_6 isotopologue. The excellent agreement between the observed and calculated tunneling parameters is indicative of the robust zeroth-order treatment that curvilinear VSCF provides. A similar tunneling-Coriolis interaction mechanism has also been used to analyze the recently identified microwave spectrum of *gauche*-isoprene, a subtituted butadiene derivative [323].

Table 7.2: Tunneling parameters of d_6-*gauche*-butadiene. Δ_{inv} is the tunneling inversion splitting (the energy difference between the $v = 0^+$ and 0^- vibrational states). C is the coefficient of the $(J_a J_c + J_c J_a)$ Coriolis interaction operator.

Parameter	Expt.	Calc.
Δ_{inv} / cm^{-1}	0.55	0.58
C / MHz	23.4	23.3

At first glance, the non-planar geometry of *gauche*-butadiene might be justified by invoking repulsive steric interactions between the terminal hydrogen atoms. Wiberg et al. have recently suggested, however, that upon closer examination this effect is probably too weak to account for the observed structure [324]. Instead, one must consider terminal π-interactions. At the planar *cis* configuration, 1,4-π interactions are Hückel antiaromatic, destabilizing the molecule, while at twisted geometries the π system has a Möbius topology, stabilizing the π-electron system. A detailed study of a large number of heterodienes shows that this mechanism is consistent with the observed effects [324]. This is an excellent example of new insights into molecular interactions inspired by the precise structural information made available by the combination of high resolution spectroscopy and high level rovibrational theory [182].

7.4 Conclusions

This chapter has highlighted several applications of high-accuracy rovibrational calculations to the spectroscopy of complex polyatomic molecules. Each of these examples featured floppy molecules that exhibit highly anharmonic, large-amplitude nuclear motion. Direct-product DVR grid techniques provide a flexible, numerically exact method to treat these systems, but they are restricted to relatively small molecules. Curvilinear rotational-VMP2 provides quantitative predictions via a less expensive perturbative approach. For large systems, like butadiene, there are few, if any, comparable alternative methods.

The high quality zeroth-order picture of curvilinear VSCF suggests it may be useful for applications beyond pure spectroscopy. We are currently exploring extensions to it to study quantum reaction dynamics and resonance states via complex scaling [325–329], as well as thermodynamical properties such as partition functions with thermal variants [330]. It may be possible to combine the benefits of curvilinear VSCF with other techniques. For example, the VSCF Hamiltonian could be used for pre-conditioned spectral transformations with iterative diagonalization methods [205, 211] or to generate an importance sampling trial function for diffusion Monte Carlo techniques [331,332]. Ultimately, a good zeroth-order picture that accurately captures the physics of strong anharmonicity forms an excellent starting point for a variety of nuclear motion calculations.

Bibliography

[1] Quack, M. and Merkt, F., eds. Handbook of High-resolution Spectroscopy. John Wiley & Sons (2011).

[2] Udem, T., Holzwarth, R., and Hänsch, T. W. Optical frequency metrology. Nature, 416(6877):233–237 (2002).

[3] Cundiff, S. T. and Ye, J. Femtosecond optical frequency combs. Rev. Mod. Phys., 75(1):325–342 (2003).

[4] Stowe, M. C., Thorpe, M. J., Pe'er, A., Ye, J., Stalnaker, J. E., Gerginov, V., and Diddams, S. A. Direct frequency comb spectroscopy. Adv. At. Mol. Opt. Phy., 55:1–60 (2008).

[5] Thorpe, M. and Ye, J. Cavity-enhanced direct frequency comb spectroscopy. Appl. Phys. B, 91(3-4):397–414 (2008).

[6] Adler, F., Thorpe, M. J., Cossel, K. C., and Ye, J. Cavity-enhanced direct frequency comb spectroscopy: technology and applications. Ann. Rev. Anal. Chem., 3:175–205 (2010).

[7] Weichman, M. L., Changala, P. B., Ye, J., Chen, Z., Yan, M., and Picqué, N. Broadband molecular spectroscopy with optical frequency combs. J. Mol. Spectrosc., 355:66–78 (2019).

[8] Foreman, S. M., Jones, D. J., and Ye, J. Flexible and rapidly configurable femtosecond pulse generation in the mid-IR. Opt. Lett., 28(5):370–371 (2003).

[9] Erny, C., Moutzouris, K., Biegert, J., Kühlke, D., Adler, F., Leitenstorfer, A., and Keller, U. Mid-infrared difference-frequency generation of ultrashort pulses tunable between 3.2 and 4.8 μm from a compact fiber source. Opt. Lett., 32(9):1138–1140 (2007).

[10] Gambetta, A., Ramponi, R., and Marangoni, M. Mid-infrared optical combs from a compact amplified Er-doped fiber oscillator. Opt. Lett., 33(22):2671–2673 (2008).

[11] Adler, F., Cossel, K. C., Thorpe, M. J., Hartl, I., Fermann, M. E., and Ye, J. Phase-stabilized, 1.5 W frequency comb at 2.8–4.8 μm. Opt. Lett., 34(9):1330–1332 (2009).

[12] Ruehl, A., Gambetta, A., Hartl, I., Fermann, M. E., Eikema, K. S. E., and Marangoni, M. Widely-tunable mid-infrared frequency comb source based on difference frequency generation. Opt. Lett., 37(12):2232–2234 (2012).

[13] Gambetta, A., Coluccelli, N., Cassinerio, M., Gatti, D., Laporta, P., Galzerano, G., and Marangoni, M. Milliwatt-level frequency combs in the 8-14 μm range via difference frequency generation from an Er:fiber oscillator. Opt. Lett., 38(7):1155–1157 (2013).

[14] Heckl, O. H., Bjork, B. J., Winkler, G., Changala, P. B., Spaun, B., Porat, G., Bui, T. Q., Lee, K. F., Jiang, J., Fermann, M. E., Schunemann, P. G., and Ye, J. Three-photon absorption in optical parametric oscillators based on OP-GaAs. Opt. Lett., 41(22):5405–5408 (2016).

[15] Lee, K. F., Hensley, C. J., Schunemann, P. G., and Fermann, M. E. Midinfrared frequency comb by difference frequency of erbium and thulium fiber lasers in orientation-patterned gallium phosphide. Opt. Express, 25(15):17411–17416 (2017).

[16] Iwakuni, K., Porat, G., Bui, T. Q., Bjork, B. J., Schoun, S. B., Heckl, O. H., Fermann, M. E., and Ye, J. Phase-stabilized 100 mW frequency comb near 10 μm. Appl. Phys. B, 124(7):128 (2018).

[17] Gordon, I., Rothman, L., Hill, C., Kochanov, R., Tan, Y., Bernath, P., Birk, M., Boudon, V., Campargue, A., Chance, K., Drouin, B., Flaud, J.-M., Gamache, R., Hodges, J., Jacquemart, D., Perevalov, V., Perrin, A., Shine, K., Smith, M.-A., Tennyson, J., Toon, G., Tran, H., Tyuterev, V., Barbe, A., Császár, A., Devi, V., Furtenbacher, T., Harrison, J., Hartmann, J.-M., Jolly, A., Johnson, T., Karman, T., Kleiner, I., Kyuberis, A., Loos, J., Lyulin, O., Massie, S., Mikhailenko, S., Moazzen-Ahmadi, N., Müller, H., Naumenko, O., Nikitin, A., Polyansky, O., Rey, M., Rotger, M., Sharpe, S., Sung, K., Starikova, E., Tashkun, S., Auwera, J. V., Wagner, G., Wilzewski, J., Wcisło, P., Yu, S., and Zak, E. The HITRAN2016 molecular spectroscopic database. J. Quant. Spectrosc. Radiat. Transf., 203:3–69 (2017).

[18] Bunker, P. R. and Jensen, P. Molecular Symmetry and Spectroscopy. NRC Research Press, Ottawa, Canada, 2nd edition (1998).

[19] White, J. U. Long Optical Paths of Large Aperture. J. Opt. Soc. Am., 32(5):285–288 (1942).

[20] Herriott, D. R. and Schulte, H. J. Folded Optical Delay Lines. Appl. Opt., 4(8):883–889 (1965).

[21] Gagliardi, G. and Loock, H.-P., eds. Cavity-Enhanced Spectroscopy and Sensing. Springer (2014).

[22] Gohle, C., Stein, B., Schliesser, A., Udem, T., and Hänsch, T. W. Frequency Comb Vernier Spectroscopy for Broadband, High-Resolution, High-Sensitivity Absorption and Dispersion Spectra. Phys. Rev. Lett., 99(26):263902 (2007).

[23] Drever, R. W. P., Hall, J. L., Kowalski, F. V., Hough, J., Ford, G. M., Munley, A. J., and Ward, H. Laser phase and frequency stabilization using an optical resonator. Appl. Phys. B, 31(2):97–105 (1983).

[24] Adler, F., Masłowski, P., Foltynowicz, A., Cossel, K. C., Briles, T. C., Hartl, I., and Ye, J. Mid-infrared Fourier transform spectroscopy with a broadband frequency comb. Opt. Express, 18(21):21861–72 (2010).

[25] Maslowski, P., Lee, K. F., Johansson, A. C., Khodabakhsh, A., Kowzan, G., Rutkowski, L., Mills, A. A., Mohr, C., Jiang, J., Fermann, M. E., and Foltynowicz, A. Surpassing the path-limited resolution of Fourier-transform spectrometry with frequency combs. Phys. Rev. A, 93(2):021802 (2016).

[26] Foltynowicz, A., Ban, T., Masłowski, P., Adler, F., and Ye, J. Quantum-Noise-Limited Optical Frequency Comb Spectroscopy. Phys. Rev. Lett., 107(23):233002 (2011).

[27] Changala, P. B., Spaun, B., Patterson, D., Doyle, J. M., and Ye, J. Sensitivity and resolution in frequency comb spectroscopy of buffer gas cooled polyatomic molecules. Appl. Phys. B, 122(12):292 (2016).

[28] Changala, P. B., Weichman, M. L., Lee, K. F., Fermann, M. E., and Ye, J. Rovibrational quantum state resolution of the C_{60} fullerene. Science, 363:49–54 (2019).

[29] Fleisher, A. J., Bjork, B. J., Bui, T. Q., Cossel, K. C., Okumura, M., and Ye, J. Mid-Infrared Time-Resolved Frequency Comb Spectroscopy of Transient Free Radicals. J. Phys. Chem. Lett., 5(13):2241–2246 (2014).

[30] Bjork, B. J., Bui, T. Q., Heckl, O. H., Changala, P. B., Spaun, B., Heu, P., Follman, D., Deutsch, C., Cole, G. D., Aspelmeyer, M., Okumura, M., and Ye, J. Direct frequency comb measurement of OD + CO $\rightarrow$ DOCO kinetics. Science, 354:444–448 (2016).

[31] Bui, T. Q., Bjork, B. J., Changala, P. B., Heckl, O. H., Spaun, B., and Ye, J. OD + CO $\rightarrow$ D + CO_2 branching kinetics probed with time-resolved frequency comb spectroscopy. Chem. Phys. Lett., 683:91–95 (2017).

[32] Bui, T. Q., Bjork, B. J., Changala, P. B., Nguyen, T. L., Stanton, J. F., Okumura, M., and Ye, J. Direct measurements of DOCO isomers in the kinetics of OD + CO. Science Advances, 4(1):eaao4777 (2018).

[33] Iwakuni, K., Bui, T. Q., Niedermeyer, J. F., Sukegawa, T., and Ye, J. Comb-resolved spectroscopy with immersion grating in long-wave infrared. Opt. Express, 27(3):1911 (2019).

[34] Shirasaki, M. Large angular dispersion by a virtually imaged phased array and its application to a wavelength demultiplexer. Opt. Lett., 21(5):366 (1996).

[35] Xiao, S. and Weiner, A. M. 2-D wavelength demultiplexer with potential for $\geq$1000 channels in the C-band. Opt. Express, 12(13):2895 (2004).

[36] Diddams, S. A., Hollberg, L., and Mbele, V. Molecular fingerprinting with the resolved modes of a femtosecond laser frequency comb. Nature, 445(7128):627–630 (2007).

[37] Thorpe, M. J., Adler, F., Cossel, K. C., de Miranda, M. H., and Ye, J. Tomography of a supersonically cooled molecular jet using cavity-enhanced direct frequency comb spectroscopy. Chem. Phys. Lett., 468(1-3):1–8 (2009).

[38] Spaun, B., Changala, P. B., Patterson, D., Bjork, B. J., Heckl, O. H., Doyle, J. M., and Ye, J. Continuous probing of cold complex molecules with infrared frequency comb spectroscopy. Nature, 533:517–520 (2016).

[39] Messer, J. K. and De Lucia, F. C. Measurement of Pressure-Broadening Parameters for the CO-He System at 4 K. Phys. Rev. Lett., 53(27):2555–2558 (1984).

[40] Patterson, D., Tsikata, E., and Doyle, J. M. Cooling and collisions of large gas phase molecules. Phys. Chem. Chem. Phys., 12(33):9736–41 (2010).

[41] Patterson, D. and Doyle, J. M. Cooling molecules in a cell for FTMW spectroscopy. Mol. Phys., 110:1757–1766 (2012).

[42] Piskorski, J., Patterson, D., Eibenberger, S., and Doyle, J. M. Cooling, spectroscopy and non-sticking of trans-stilbene and Nile Red. 15:3800–4 (2014).

[43] Tobin, A. G., Sedgley, D. W., Batzer, T. H., and Call, W. R. Evaluation of charcoal sorbents for helium cryopumping in fusion reactors. J. Vac. Sci. Technol. A, 5(1):101–105 (1987).

[44] Sedgley, D. W., Tobin, A. G., Batzer, T. H., and Call, W. R. Characterization of charcoals for helium cryopumping in fusion devices. J. Vac. Sci. Technol. A, 5(4):2572–2576 (1987).

[45] Hutzler, N. R., Parsons, M. F., Gurevich, Y. V., Hess, P. W., Petrik, E., Spaun, B., Vutha, A. C., DeMille, D., Gabrielse, G., and Doyle, J. M. A cryogenic beam of refractory, chemically reactive molecules with expansion cooling. Phys. Chem. Chem. Phys., 13(42):18976–85 (2011).

[46] Hutzler, N. R., Lu, H.-I., and Doyle, J. M. The buffer gas beam: an intense, cold, and slow source for atoms and molecules. Chem. Rev., 112(9):4803–27 (2012).

[47] Stycast 2850FT Technical Data Sheet. `http://www.hitek-ltd.co.uk/media/downloads/5284/Stycast%202850%20FT%20Cat%209%2011%2023LV%20and%2024LV%20(2013).pdf`. Accessed: March 20, 2019.

[48] Tennyson, J., Bernath, P. F., Brown, L. R., Campargue, A., Császár, A. G., Daumont, L., Gamache, R. R., Hodges, J. T., Naumenko, O. V., Polyansky, O. L., Rothman, L. S., Vandaele, A. C., Zobov, N. F., Al Derzi, A. R., Fábri, C., Fazliev, A. Z., Furtenbacher, T., Gordon, I. E., Lodi, L., and Mizus, I. I. IUPAC critical evaluation of the rotational–vibrational spectra of water vapor, Part III: Energy levels and transition wavenumbers for $H_2{}^{16}O$. J. Quant. Spectrosc. Radiat. Transf., 117:29–58 (2013).

[49] Olson, W. B., Maki, A. G., and Lafferty, W. J. Tables of N_2O absorption lines for the calibration of tunable infrared lasers from 522 cm^{-1} to 657 cm^{-1} and from 1115 cm^{-1} to 1340 cm^{-1}. J. Phys. Chem. Ref. Data, 10(4):1065–1084 (1981).

[50] Camy-Peyret, C., Flaud, J. M., Mahmoudi, A., Guelachvili, G., and Johns, J. W. C. Line positions and intensities in the ν_2 band of D_2O improvied pumped D_2O laser frequencies. Int. J. Infrared Millimeter Waves, 6(3):199–233 (1985).

[51] Changala, P. B. and Baraban, J. H. Ab initio effective rotational and rovibrational Hamiltonians for non-rigid systems via curvilinear second order vibrational Møller–Plesset perturbation theory. J. Chem. Phys., 145:174106 (2016).

[52] Sørensen, G., Pedersen, T., Dreizler, H., Guarnieri, A., and Cox, A. P. Microwave spectra of nitromethane and D3-nitromethane. J. Mol. Struct., 97:77–82 (1983).

[53] Sørensen, G. and Pedersen, T. Symmetry and microwave spectrum of nitromethane. Stud. Phys. Theor. Chem., 23:219–236 (1983).

[54] Barnes, W. L. Measurement and Analysis of the ν_3 Band of Methane. J. Chem. Phys., 56(10):5160 (1972).

[55] Rohart, F. Microwave spectrum of nitromethane internal rotation Hamiltonian in the low barrier case. J. Mol. Spectrosc., 57(2):301–311 (1975).

[56] Hazra, A., Ghosh, P., and Kshirsagar, R. Fourier Transform Infrared Spectrum and Rotational Structure of the A-Type 917.5 cm^{-1} Band of Nitromethane. J. Mol. Spectrosc., 164(1):20–26 (1994).

[57] Hazra, A. and Ghosh, P. Assignment of the $m \neq 0$ Transitions in the ν_4 Band of Nitromethane by the Symmetric Top Approximation Method. J. Mol. Spectrosc., 173(1):300–302 (1995).

[58] Pal, C., Hazra, A., Ghosh, P. N., and Kshirsagar, R. High resolution Fourier transform infrared spectrum and vibration-rotation analysis of the B-type 1584 cm^{-1} band of nitromethane. J. Mol. Struct., 407(2-3):165–170 (1997).

[59] Dawadi, M. B., Degliumberto, L., Perry, D. S., Mettee, H. D., and Sams, R. L. High-resolution infrared spectroscopy of the asymmetric NO stretch band of jet-cooled nitromethane and assignment of the lowest four torsional states. J. Mol. Spectrosc., 343:85–91 (2018).

[60] Dawadi, M. B., Twagirayezu, S., Perry, D. S., and Billinghurst, B. E. High-resolution Fourier transform infrared synchrotron spectroscopy of the NO_2 in-plane rock band of nitromethane. J. Mol. Spectrosc., 315:10–15 (2015).

[61] McKean, D. and Watt, R. Vibrational spectra of nitromethanes and the effects of internal rotation. J. Mol. Spectrosc., 61(2):184–202 (1976).

[62] Cavagnat, D. and Lespade, L. Internal dynamics contributions to the CH stretching overtone spectra of gaseous nitromethane NO_2CH_3. J. Chem. Phys., 106(19):7946 (1997).

[63] Hill, J. R., Moore, D. S., Schmidt, S. C., and Storm, C. B. Infrared, Raman, and coherent anti-Stokes Raman spectroscopy of the hydrogen/deuterium isotopomers of nitromethane. J. Phys. Chem., 95(8):3037–3044 (1991).

[64] Watson, J. K. G. Aspects of quartic and sextic centrifugal effects on rotational energy levels. In J. Durig, ed., Vibrational Spectra and Structure, Vol. 6, chapter 1. Elsevier, Amsterdam (1977).

[65] Halonen, M., Halonen, L., Callegari, A., and Lehmann, K. K. Molecular Beam Infrared Spectrum of Nitromethane in the Region of the First C-H Stretching Overtone. J. Phys. Chem. A, 102(46):9124–9128 (1998).

[66] Tannenbaum, E., Myers, R. J., and Gwinn, W. D. Microwave Spectra, Dipole Moment, and Barrier to Internal Rotation of CH_3NO_2 and CD_3NO_2. J. Chem. Phys., 25:42 (1956).

[67] Wu, K. and Simon, H. Thick-Restart Lanczos Method for Large Symmetric Eigenvalue Problems. SIAM J. Matrix Anal. Appl., 22:602–616 (2000).

[68] Light, J. C. and Carrington Jr., T. Discrete-Variable Representations and their Utilization. Adv. Chem. Phys., 114:263 (2000).

[69] Puzzarini, C., Stanton, J. F., and Gauss, J. Quantum-chemical calculation of spectroscopic parameters for rotational spectroscopy. Int. Rev. Phys. Chem., 29(2):273–367 (2010).

[70] Mills, I. M. Vibration-Rotation Structure in Asymmetric- and Symmetric-Top Molecules. In K. N. Rao and C. W. Mathews, eds., Molecular Spectroscopy: Modern Research, chapter 3.2, pages 115–140. Academic Press, New York (1972).

[71] Watson, J. K. G. Simplification of the molecular vibration-rotation Hamiltonian. Mol. Phys., 15:479–490 (1968).

[72] Bowman, J. M. Self-consistent field energies and wavefunctions for coupled oscillators. J. Chem. Phys., 68:608–610 (1978).

[73] Bowman, J. M. The self-consistent-field approach to polyatomic vibrations. Acc. Chem. Res., 19(7):202–208 (1986).

[74] Gerber, R. B. and Ratner, M. A. Self-Consistent-Field Methods for Vibrational Excitations in Polyatomic Systems. Adv. Chem. Phys., 70:97–132 (1988).

[75] Møller, C. and Plesset, M. S. Note on an Approximation Treatment for Many-Electron Systems. Phys. Rev., 46(7):618–622 (1934).

[76] Norris, L. S., Ratner, M. A., Roitberg, A. E., and Gerber, R. B. Møller–Plesset perturbation theory applied to vibrational problems. J. Chem. Phys., 105:11261–11267 (1996).

[77] Wang, X., Carter, S., and Bowman, J. M. Pruning the Hamiltonian Matrix in MULTIMODE: Test for C_2H_4 and Application to CH_3NO_2 Using a New Ab Initio Potential Energy Surface. J. Phys. Chem. A, 119(47):11632–11640 (2015).

[78] Tennyson, J. Astronomical Spectroscopy. World Scientific (Europe), 3rd edition (2019).

[79] Ziurys, L. M. Millimeter and Submillimeter Wave Spectroscopy and Astrophysical Applications. In Handbook of High-resolution Spectroscopy. John Wiley & Sons, Ltd (2011).

[80] Tielens, A. Interstellar Polycyclic Aromatic Hydrocarbon Molecules. Annu. Rev. Astron. Astrophys., 46(1):289–337 (2008).

[81] Nesbitt, D. J. and Field, R. W. Vibrational Energy Flow in Highly Excited Molecules: Role of Intramolecular Vibrational Redistribution. J. Phys. Chem., 100(31):12735–12756 (1996).

[82] Pirali, O., Goubet, M., Huet, T. R., Georges, R., Soulard, P., Asselin, P., Courbe, J., Roy, P., and Vervloet, M. The far infrared spectrum of naphthalene characterized by high resolution synchrotron FTIR spectroscopy and anharmonic DFT calculations. Phys. Chem. Chem. Phys., 15:10141–50 (2013).

[83] Albert, S., Albert, K. K., Lerch, P., and Quack, M. Synchrotron-based highest resolution Fourier transform infrared spectroscopy of naphthalene ($C_{10}H_8$) and indole (C_8H_7N) and its application to astrophysical problems. Faraday Discuss., 150 (2011).

[84] Hewett, K. B., Shen, M., Brummel, C. L., and Philips, L. A. High resolution infrared spectroscopy of pyrazine and naphthalene in a molecular beam. J. Chem. Phys., 100:4077 (1994).

[85] Majewski, W. and Meerts, W. Near-UV spectra with fully resolved rotational structure of naphthalene and perdeuterated naphthalene. J. of Mol. Spectrosc., 104:271–281 (1984).

[86] Joo, D.-L., Takahashi, R., O'Reilly, J., Katô, H., and Baba, M. High-Resolution Spectroscopy of Jet-Cooled Naphthalene: the 0^0_0 and 33^1_0 Bands of the $\tilde{A}^1B_{1u} \leftarrow \tilde{X}^1A_g$ Transition. J. Mol. Spectrosc., 215:155–159 (2002).

[87] Pirali, O., Boudon, V., Oomens, J., and Vervloet, M. Rotationally resolved infrared spectroscopy of adamantane. J. Chem. Phys., 136(2):024310 (2012).

[88] Brumfield, B. E., Stewart, J. T., and McCall, B. J. Extending the limits of rotationally resolved absorption spectroscopy: pyrene. J. Phys. Chem. Lett., 3(15):1985–1988 (2012).

[89] Pirali, O., Boudon, V., Carrasco, N., and Dartois, E. Rotationally resolved IR spectroscopy of hexamethylenetetramine (HMT) $C_6N_4H_{12}$. Astron. Astrophys., 561:A109 (2014).

[90] Pirali, O. and Boudon, V. Synchrotron-based Fourier transform spectra of the ν_{23} and ν_{24} IR bands of hexamethylenetetramine $C_6N_4H_{12}$. J. Mol. Spectrosc., 315:37–40 (2015).

[91] Coveleskie, R. A., Dolson, D. A., and Parmenter, C. S. A direct view of intramolecular vibrational redistribution in S_1 *p*-difluorobenzene. J. Chem. Phys., 72:5774–5775 (1980).

[92] Hopkins, J. B., Langridge-Smith, P. R. R., and Smalley, R. E. Ground state vibrational randomization in alkylbenzenes. J. Chem. Phys., 78(6):3410–3414 (1983).

[93] Parmenter, C. S. and Stone, B. M. The methyl rotor as an accelerating functional group for IVR. J. Chem. Phys., 84(8):4710–4711 (1986).

[94] McIlroy, A. and Nesbitt, D. J. Vibrational mode mixing in terminal acetylenes: High-resolution infrared laser study of isolated J states. J. Chem. Phys., 92(4):2229–2243 (1990).

[95] McIlroy, A. and Nesbitt, D. J. Large amplitude skeletal isomerization as a promoter of intramolecular vibrational relaxation in CH stretch excited hydrocarbons. J. Chem. Phys., 101(5):3421 (1994).

[96] Lehmann, K. K., Pate, B. H., and Scoles, G. On the measurement of the rate of intramolecular vibrational energy redistribution via high resolution molecular beam optothermal spectroscopy. Laser Chem., 11:237 (1991).

[97] Lederman, S. M., Runnels, J. H., and Marcus, R. A. Densities of vibrational states of given symmetry species and their use in statistical estimates involving Coriolis and anharmonic effects. J. Phys. Chem., 87:4364–4367 (1983).

[98] Quack, M. On the densities and numbers of rovibronic states of a given symmetry species: Rigid and nonrigid molecules, transition states, and scattering channels. J. Chem. Phys., 82:3277 (1985).

[99] Pechukas, P. Comment on "Densities of vibrational states of given symmetry species". J. Phys. Chem., 88(4):828–828 (1984).

[100] Baer, T. and Hase, W. L. <u>Unimolecular Reaction Dynamics</u>. Oxford University Press, New York (1996).

[101] Sellers, H., Pulay, P., and Boggs, J. E. Theoretical prediction of vibrational spectra. 2. Force field, spectroscopically refined geometry, and reassignment of the vibrational spectrum of naphthalene. J. Am. Chem. Soc., 107(23):6487–6494 (1985).

[102] Mitra, S. S. and Bernstein, H. J. Vibrational spectra of naphthalene-d0 , -α-d4 , and -d8 molecules. Can. J. Chem., 37(3):553–562 (1959).

[103] Jensen, J. O. Vibrational frequencies and structural determination of adamantane. Spectrochim. Acta A, 60(8-9):1895–905 (2004).

[104] Ramachandran, G. and Manogaran, S. Vibrational spectra of adamantanes $X_{10}H_{16}$ and diamantanes $X_{14}H_{20}$ (X=C, Si, Ge, Sn): A theoretical study. THEOCHEM, 766(2-3):125–135 (2006).

[105] Jenkins, T. and Lewis, J. A Raman study of adamantane ($C_{10}H_{16}$), diamantane ($C_{14}H_{20}$) and triamantane ($C_{18}H_{24}$) between 10 K and room temperatures. Spectrochim. Acta A, 36(3):259–264 (1980).

[106] Schettino, V., Pagliai, M., Ciabini, L., and Cardini, G. The Vibrational Spectrum of Fullerene C_{60}. J. Phys. Chem. A, 105(50):11192–11196 (2001).

[107] Osawa, E. Superaromaticity. Kagaku, 25:854–863 (1970).

[108] Davidson, R. A. Spectral analysis of graphs by cyclic automorphism subgroups. Theo. Chim. Acta, 58(3):193–231 (1981).

[109] Bochvar, D. A. and Gal'pern, E. G. . Proc. Acad. Sci. USSR, 209:239–241 (1973).

[110] Stankevich, I. V., Nikerov, M. V., and Bochvar, D. A. The Structural Chemistry of Crystalline Carbon: Geometry, Stability, and Electronic Spectrum. Russ. Chem. Rev., 53(7):640–655 (1984).

[111] Kroto, H. W., Heath, J. R., O'Brien, S. C., Curl, R. F., and Smalley, R. E. C_{60}: Buckminsterfullerene. Nature, 318(6042):162–163 (1985).

[112] Kroto, H. Symmetry, space, stars and C_{60}. Rev. Mod. Phys., 69(3):703–722 (1997).

[113] Ajie, H., Alvarez, M. M., Anz, S. J., Beck, R. D., Diederich, F., Fostiropoulos, K., Huffman, D. R., Kraetschmer, W., Rubin, Y., Schriver, K. E., Sensharma, D., and Whetten, R. L. Characterization of the soluble all-carbon molecules C_{60} and C_{70} . J. Phys. Chem., 94(24):8630–8633 (1990).

[114] Taylor, R., Hare, J. P., Abdul-Sada, A. K., and Kroto, H. W. Isolation, separation and characterisation of the fullerenes C_{60} and C_{70}: the third form of carbon. J. Chem. Soc. Chem. Commun., 0(20):1423 (1990).

[115] Krätschmer, W., Lamb, L. D., Fostiropoulos, K., and Huffman, D. R. Solid C_{60}: a new form of carbon. Nature, 347(6291):354–358 (1990).

[116] Krätschmer, W., Fostiropoulos, K., and Huffman, D. R. The infrared and ultraviolet absorption spectra of laboratory-produced carbon dust: evidence for the presence of the C_{60} molecule. Chem. Phys. Lett., 170(2-3):167–170 (1990).

[117] Yannoni, C. S., Johnson, R. D., Meijer, G., Bethune, D. S., and Salem, J. R. Carbon-13 NMR study of the C_{60} cluster in the solid state: molecular motion and carbon chemical shift anisotropy. J. Phys. Chem., 95(1):9–10 (1991).

[118] Yannoni, C. S., Bernier, P. P., Bethune, D. S., Meijer, G., and Salem, J. R. NMR determination of the bond lengths in C_{60}. J. Am. Chem. Soc., 113(8):3190–3192 (1991).

[119] Hedberg, K., Hedberg, L., Bethune, D. S., Brown, C. A., Dorn, H. C., Johnson, R. D., and De Vries, M. Bond lengths in free molecules of buckminsterfullerene, C_{60}, from gas-phase electron diffraction. Science, 254(5030):410–412 (1991).

[120] Liu, S., Lu, Y.-J., Kappes, M. M., and Ibers, J. A. The Structure of the C_{60} Molecule: X-Ray Crystal Structure Determination of a Twin at 110 K. Science, 254(5030):408–410 (1991).

[121] Parker, S. F., Bennington, S. M., Taylor, J. W., Herman, H., Silverwood, I., Albers, P., and Refson, K. Complete assignment of the vibrational modes of C_{60} by inelastic neutron scattering spectroscopy and periodic-DFT. Phys. Chem. Chem. Phys., 13(17):7789 (2011).

[122] Pintschovius, L. Neutron studies of vibrations in fullerenes. Rep. Prog. Phys., 59(4):473–510 (1996).

[123] The vibrational Raman spectra of purified solid films of C_{60} and C_{70}. Chem. Phys. Lett., 174(3-4):219–222 (1990).

[124] Bethune, D. S., Meijer, G., Tang, W. C., Rosen, H. J., Golden, W. G., Seki, H., Brown, C. A., and de Vries, M. S. Vibrational Raman and infrared spectra of chromatographically separated C_{60} and C_{70} fullerene clusters. Chem. Phys. Lett., 179(1-2):181–186 (1991).

[125] Prassides, K., John, T., Dennis, S., Hare, J. P., Tomkinson, J., Kroto, H. W., Taylor, R., and Walton, D. R. Inelastic neutron scattering spectrum of the fullerene C_{60}. Chem. Phys. Lett., 187(5):455–458 (1991).

[126] Cappelletti, R. L., Copley, J. R. D., Kamitakahara, W. A., Li, F., Lannin, J. S., and Ramage, D. Neutron measurements of intramolecular vibrational modes in C_{60}. Phys. Rev. Lett., 66(25):3261–3264 (1991).

[127] Affholter, K. A., Henderson, S. J., Wignall, G. D., Bunick, G. J., Haufler, R. E., and Compton, R. N. Structural characterization of C_{60} and C_{70} fullerenes by small-angle neutron scattering. J. Chem. Phys., 99(11):9224–9229 (1993).

[128] Sassara, A., Zerza, G., and Chergui, M. Phosphorescence of C_{60} in rare gas matrices. Chem. Phys. Lett., 261:213–220 (1996).

[129] Sassara, A., Zerza, G., Chergui, M., and Leach, S. Absorption Wavelengths and Bandwidths for Interstellar Searches of C_{60} in the $2400-4100$ ÅRegion. Astrophys. J. Supp. Ser., 135(2):263–273 (2001).

[130] Sogoshi, N., Kato, Y., Wakabayashi, T., Momose, T., Tam, S., DeRose, M. E., and Fajardo, M. E. High-Resolution Infrared Absorption Spectroscopy of C_{60} Molecules and Clusters in Parahydrogen Solids. J. Phys. Chem. A, 104(16):3733–3742 (2000).

[131] Iglesias-Groth, S., Cataldo, F., and Manchado, A. Infrared spectroscopy and integrated molar absorptivity of C_{60} and C_{70} fullerenes at extreme temperatures. Mon. Not. R. Astron. Soc., 413(1):213–222 (2011).

[132] Brieva, A. C., Gredel, R., Jäger, C., Huisken, F., and Henning, T. C_{60} as a probe for astrophysical environments. Astrophys. J., 826(2):122 (2016).

[133] Absorption spectroscopy of C_{60} molecules isolated in helium droplets. Chem. Phys. Lett., 276:393–398 (1997).

[134] Wang, X.-B., Ding, C.-F., and Wang, L.-S. High resolution photoelectron spectroscopy of C_{60}^{-}. J. Chem. Phys., 110(17):8217 (1999).

[135] Wang, X.-B., Woo, H.-K., and Wang, L.-S. Vibrational cooling in a cold ion trap: Vibrationally resolved photoelectron spectroscopy of cold C_{60}^{-} anions. J. Chem. Phys., 123(5):051106 (2005).

[136] Huang, D.-L., Dau, P. D., Liu, H.-T., and Wang, L.-S. High-resolution photoelectron imaging of cold C_{60}^{-} anions and accurate determination of the electron affinity of C_{60}. J. Chem. Phys., 140(22):224315 (2014).

[137] Cami, J., Bernard-Salas, J., Peeters, E., and Malek, S. E. Detection of C_{60} and C_{70} in a young planetary nebula. Science, 329(5996):1180–2 (2010).

[138] Sellgren, K., Werner, M. W., Ingalls, J. G., Smith, J. D. T., Carleton, T. M., and Joblin, C. C_{60} in reflection nebulae. Astrophys. J., 722(1):L54–L57 (2010).

[139] Campbell, E. K., Holz, M., Gerlich, D., and Maier, J. P. Laboratory confirmation of C_{60}^{+} as the carrier of two diffuse interstellar bands. Nature, 523(7560):322–323 (2015).

[140] Campbell, E. K. and Maier, J. P. Perspective: C_{60}^{+} and laboratory spectroscopy related to diffuse interstellar bands. J. Chem. Phys., 146(16):160901 (2017).

[141] Maier, J. P. and Campbell, E. K. Fullerenes in Space. Angew. Chem. Int. Ed., 56(18):4920–4929 (2017).

[142] Gelessus, A., Thiel, W., and Weber, W. Multipoles and Symmetry. J. Chem. Ed., 72(6):505 (1995).

[143] Dorney, A. and Watson, J. Forbidden rotational spectra of polyatomic molecules. J. Mol. Spectrosc., 42(1):135–148 (1972).

[144] Orlandi, G. and Negri, F. Electronic states and transitions in C_{60} and C_{70} fullerenes. Photochem. Photobiol. Sci., 1(5):289–308 (2002).

[145] Haufler, R. E., Chai, Y., Chibante, L. P. F., Fraelich, M. R., Weisman, R. B., Curl, R. F., and Smalley, R. E. Cold molecular beam electronic spectrum of C_{60} and C_{70}. J. Chem. Phys., 95(3):2197–2199 (1991).

[146] Haufler, R., Wang, L.-S., Chibante, L., Jin, C., Conceicao, J., Chai, Y., and Smalley, R. Fullerene triplet state production and decay: R2PI probes of C_{60} and C_{70} in a supersonic beam. Chem. Phys. Lett., 179:449–454 (1991).

[147] Stewart, J. T., Brumfield, B. E., Gibson, B. M., and McCall, B. J. Inefficient Vibrational Cooling of C_{60} in a Supersonic Expansion. ISRN Phys. Chem., 2013:1–10 (2013).

[148] Hansen, K., Müller, R., Hohmann, H., and Campbell, E. Stability of clusters of fullerenes. Z. Phys. D, 40(1-4):361–364 (1997).

[149] Hansen, K., Hohmann, H., Müller, R., and Campbell, E. E. B. Icosahedra of icosahedra: The stability of $(C_{60})_{13}$. J. Chem. Phys., 105(14):6088 (1998).

[150] di Lauro, C. Spectra of Spherical Top Molecules. In Rotational Structure in Molecular Infrared Spectra, pages 225–245. Elsevier (2013).

[151] Rumble, J. R., ed. CRC Handbook of Chemistry and Physics. CRC Press/Taylor & Francis, Boca Raton, FL, 99th edition (2018).

[152] Zare, R. N. Angular Momentum. John Wiley & Sons (1988).

[153] Bunker, P. R. and Jensen, P. Spherical top molecules and the molecular symmetry group. Mol. Phys., 97(1-2):255–264 (1999).

[154] Changala, P. B., Weichman, M. L., Lee, K. F., Fermann, M. E., and Ye, J. External data for "Rovibrational quantum state resolution of the C_{60} fullerene," Version 1, https://doi.org/10.7910/DVN/RVVAN6. Harvard Dataverse (2018).

[155] Weeks, D. E. and Harter, W. G. Rotation-vibration scalar coupling zeta coefficients and spectroscopic band shapes of buckminsterfullerene. Chem. Phys. Lett., 176:209–216 (1991).

[156] Hecht, K. T. Vibration-rotation energies of tetrahedral XY_4 molecules. J. Mol. Spectrosc., 5(1-6):390–404 (1961).

[157] Valiev, M., Bylaska, E. J., Govind, N., Kowalski, K., Straatsma, T. P., van Dam, H. J. J., Wang, D., Nieplocha, J., Apra, E., Windus, T. L., and de Jong, W. A. NWChem: a comprehensive and scalable open-source solution for large scale molecular simulations. Comput. Phys. Commun., 181:1477 (2010).

[158] Weeks, D. E. Isotopic and anharmonic perturbations to the dipole active vibrational modes of buckminsterfullerene. J. Chem. Phys., 96(10):7380–7393 (1992).

[159] Johnson, R. D., Meijer, G., and Bethune, D. S. C_{60} has icosahedral symmetry. J. Amer. Chem. Soc., 112(24):8983–8984 (1990).

[160] Boudon, V., Champion, J.-P., Gabard, T., Loëte, M., Michelot, F., Pierre, G., Rotger, M., Wenger, C., and Rey, M. Symmetry-adapted tensorial formalism to model rovibrational and rovibronic spectra of molecules pertaining to various point groups. J. Mol. Spectrosc., 228(2):620–634 (2004).

[161] Wigner, E. P. Group Theory and its Application to the Quantum Mechanics of Atomic Spectra. Academic Press, New York (1959).

[162] Harter, W. G. and Weeks, D. E. Rovibrational spectral fine structure of icosahedral molecules. Chem. Phys. Lett., 132(4-5):387–392 (1986).

[163] Harter, W. G. and Weeks, D. E. Rotation–vibration spectra of icosahedral molecules. I. Icosahedral symmetry analysis and fine structure. J. Chem. Phys., 90(9):4727–4743 (1989).

[164] Georgakilas, V., Perman, J. A., Tucek, J., and Zboril, R. Broad Family of Carbon Nanoallotropes: Classification, Chemistry, and Applications of Fullerenes, Carbon Dots, Nanotubes, Graphene, Nanodiamonds, and Combined Superstructures. Chem. Rev., 115(11):4744–4822 (2015).

[165] Harter, W. G. and Reimer, T. C. Nuclear spin weights and gas phase spectral structure of $^{12}C_{60}$ and $^{13}C_{60}$ buckminsterfullerene. Chem. Phys. Lett., 194(3):230–238 (1992).

[166] Chen, C. C. and Lieber, C. M. Synthesis of pure $^{13}C_{60}$ and determination of the isotope effect for fullerene superconductors. J. Amer. Chem. Soc., 114(8):3141–3142 (1992).

[167] Popov, A. A., Yang, S., and Dunsch, L. Endohedral Fullerenes. Chem. Rev., 113(8):5989–6113 (2013).

[168] Faist, J., Capasso, F., Sivco, D. L., Sirtori, C., Hutchinson, A. L., and Cho, A. Y. Quantum Cascade Laser. Science, 264:553–556 (1994).

[169] Curl, R. F., Capasso, F., Gmachl, C., Kosterev, A. A., McManus, B., Lewicki, R., Pusharsky, M., Wysocki, G., and Tittel, F. K. Quantum cascade lasers in chemical physics. Chem. Phys. Lett., 487:1–18 (2010).

[170] Faist, J., Gmachl, C., Capasso, F., Sirtori, C., Sivco, D. L., Baillargeon, J. N., and Cho, A. Y. Distributed feedback quantum cascade lasers. Appl. Phys. Lett., 70(20):2670–2672 (1997).

[171] Berden, G. and Engeln, R., eds. Cavity ring-down spectroscopy: techniques and applications. John Wiley & Sons (2009).

[172] Dahmani, B., Hollberg, L., and Drullinger, R. Frequency stabilization of semiconductor lasers by resonant optical feedback. Opt. Lett., 12(11):876 (1987).

[173] Laurent, P., Clairon, A., and Breant, C. Frequency noise analysis of optically self-locked diode lasers. IEEE J. Quantum Electron., 25(6):1131–1142 (1989).

[174] Ohshima, S. and Schnatz, H. Optimization of injection current and feedback phase of an optically self-locked laser diode. J. Appl. Phys., 71(7):3114–3117 (1992).

[175] Burkart, J., Romanini, D., and Kassi, S. Optical feedback stabilized laser tuned by single-sideband modulation. Opt. Lett., 38:2062 (2013).

[176] Briles, T. C., Yost, D. C., Cingöz, A., Ye, J., and Schibli, T. R. Simple piezoelectric-actuated mirror with 180 kHz servo bandwidth. Optics Express, 18(10):9739 (2010).

[177] Maisons, G., Carbajo, P. G., Carras, M., and Romanini, D. Optical-feedback cavity-enhanced absorption spectroscopy with a quantum cascade laser. Opt. Lett., 35:3607 (2010).

[178] Hamilton, D. J. and Orr-Ewing, A. J. A quantum cascade laser-based optical feedback cavity-enhanced absorption spectrometer for the simultaneous measurement of CH_4 and N_2O in air. Appl. Phys. B, 102:879–890 (2011).

[179] Gorrotxategi-Carbajo, P., Fasci, E., Ventrillard, I., Carras, M., Maisons, G., and Romanini, D. Optical-feedback cavity-enhanced absorption spectroscopy with a quantum-cascade laser yields the lowest formaldehyde detection limit. Appl. Phys. B, 110:309–314 (2013).

[180] Fasci, E., Coluccelli, N., Cassinerio, M., Gambetta, A., Hilico, L., Gianfrani, L., Laporta, P., Castrillo, A., and Galzerano, G. Narrow-linewidth quantum cascade laser at 8.6 μm. Opt. Lett., 39:4946 (2014).

[181] Ye, J., Ma, L.-S., and Hall, J. L. Ultrasensitive detections in atomic and molecular physics: demonstration in molecular overtone spectroscopy. J. Opt. Soc. Am. B, 15(1):6 (1998).

[182] Martin-Drumel, M., Baraban, J. H., Changala, P. B., Stanton, J. F., and McCarthy, M. C. The Hunt for Elusive Molecules: Insights from Joint Theoretical and Experimental Investigations. Chem.: Eur. J., 25(30):7243–7258 (2019).

[183] Bak, K. L., Gauss, J., Jørgensen, P., Olsen, J., Helgaker, T., and Stanton, J. F. The accurate determination of molecular equilibrium structures. J. Chem. Phys., 114(15):6548–6556 (2001).

[184] Pawłowski, F., Jørgensen, P., Olsen, J., Hegelund, F., Helgaker, T., Gauss, J., Bak, K. L., and Stanton, J. F. Molecular equilibrium structures from experimental rotational constants and calculated vibration–rotation interaction constants. J. Chem. Phys., 116(15):6482–6496 (2002).

[185] Pfeiffer, F., Rauhut, G., Feller, D., and Peterson, K. A. Anharmonic zero point vibrational energies: Tipping the scales in accurate thermochemistry calculations? J. Chem. Phys., 138(4):044311 (2013).

[186] Karton, A., Rabinovich, E., Martin, J. M. L., and Ruscic, B. W4 theory for computational thermochemistry: In pursuit of confident sub-kJ/mol predictions. J. Chem. Phys., 125(14):144108 (2006).

[187] Tajti, A., Szalay, P. G., Császár, A. G., Kállay, M., Gauss, J., Valeev, E. F., Flowers, B. A., Vázquez, J., and Stanton, J. F. HEAT: High accuracy extrapolated ab initio thermochemistry. J. Chem. Phys., 121(23):11599–11613 (2004).

[188] Born, M. and Oppenheimer, R. Zur Quantentheorie der Molekeln. Ann. Phys., 389:457–484 (1927).

[189] Spectroscopy of large amplitude vibrational motions, on the occasion of Jon Hougen's 80th birthday - Part I. In L.-H. Xu and I. Kleiner, eds., J. Mol. Spectrosc. vol 342, pages 1–138 (2017).

[190] Spectroscopy of large amplitude vibrational motions, on the occasion of Jon Hougen's 80th birthday - Part II. In L.-H. Xu and I. Kleiner, eds., J. Mol. Spectrosc. vol 343, pages 1–126 (2018).

[191] Barone, V. Anharmonic vibrational properties by a fully automated second-order perturbative approach. J. Chem. Phys., 122:014108 (2005).

[192] Oliveira, A. M., Lu, Y.-J., Lehman, J. H., Changala, P. B., Baraban, J. H., Stanton, J. F., and Lineberger, W. C. Photoelectron Spectroscopy of the Methide Anion: Electron Affinities of CH_3 and CD_3 and Inversion Splittings of CH_3^- and CD_3^-. J. Am. Chem. Soc., 137(40):12939–45 (2015).

[193] Reilly, N. J., Changala, P. B., Baraban, J. H., Kokkin, D. L., Stanton, J. F., and McCarthy, M. C. The ground electronic state of Si_2C: Rovibrational level structure, quantum monodromy, and astrophysical implications. J. Chem. Phys., 142:231101 (2015).

[194] McCarthy, M. C., Baraban, J. H., Changala, P. B., Stanton, J. F., Martin-Drumel, M.-A., Thorwirth, S., Gottlieb, C. A., and Reilly, N. J. Discovery of a Missing Link: Detection and Structure of the Elusive Disilicon Carbide Cluster. J. Phys. Chem. Lett., 6:2107–2111 (2015).

[195] Cernicharo, J., McCarthy, M. C., Gottlieb, C. A., Agúndez, M., Prieto, L. V., Baraban, J. H., Changala, P. B., Guélin, M., Kahane, C., Martin-Drumel, M. A., Patel, N. A., Reilly, N. J., Stanton, J. F., Quintana-Lacaci, G., Thorwirth, S., and Young, K. H. Discovery of SiCSi in IRC+10216: A Missing Link Between Gas and Dust Carriers of Si–C Bonds. Astrophys. J. Lett., 806(1):L3 (2015).

[196] Baraban, J. H., Changala, P. B., and Stanton, J. F. The equilibrium structure of hydrogen peroxide. J. Mol. Spectrosc., 343:92–95 (2018).

[197] Changala, P. B., Nguyen, T. L., Baraban, J. H., Ellison, G. B., Stanton, J. F., Bross, D. H., and Ruscic, B. Active Thermochemical Tables: The Adiabatic Ionization Energy of Hydrogen Peroxide. J. Phys. Chem. A, 121:8799–8806 (2017).

[198] Baraban, J. H., Martin-Drumel, M.-A., Changala, P. B., Eibenberger, S., Nava, M., Patterson, D., Stanton, J. F., Ellison, G. B., and McCarthy, M. C. The Molecular Structure of gauche-1,3-Butadiene: Experimental Establishment of Non-planarity. Angew. Chem. Int. Ed., 57(7):1821–1825 (2018).

[199] NITROGEN, Numerical and Iterative Techniques for Rovibronic Energies with General Internal Coordinates, a program by P. B. Changala, http://www.colorado.edu/nitrogen.

[200] Bowman, J. M., Carrington, T., and Meyer, H.-D. Variational quantum approaches for computing vibrational energies of polyatomic molecules. Mol. Phys., 106(16-18):2145–2182 (2008).

[201] Carrington, T. Perspective: Computing (ro-)vibrational spectra of molecules with more than four atoms. J. Chem. Phys., 146(12):120902 (2017).

[202] Bramley, M. J. and Carrington, T. A general discrete variable method to calculate vibrational energy levels of three- and four-atom molecules. J. Chem. Phys., 99(11):8519–8541 (1993).

[203] Lehoucq, R., Gray, S., Zhang, D.-H., and Light, J. Vibrational eigenstates of four-atom molecules: a parallel strategy employing the implicitly restarted Lanczos method. Comp. Phys. Comm., 109(1):15–25 (1998).

[204] Yu, H.-G. and Nyman, G. A spectral transform Krylov subspace iteration approach to quantum scattering. Chem. Phys. Lett., 298(1-3):27–35 (1998).

[205] Huang, S.-W. and Carrington, T. A new iterative method for calculating energy levels and wave functions. J. Chem. Phys., 112:8765 (2000).

[206] Lanczos, C. An Iteration Method for the Solution of the Eigenvalue Problem of Linear Differential and Integral Operators. J. Res. Natl. Bur. Stand., 45(255) (1950).

[207] Lill, J., Parker, G., and Light, J. Discrete variable representations and sudden models in quantum scattering theory. Chem. Phys. Lett., 89(6):483–489 (1982).

[208] Light, J. C., Hamilton, I. P., and Lill, J. V. Generalized discrete variable approximation in quantum mechanics. J. Chem. Phys., 82(3):1400 (1985).

[209] Colbert, D. T. and Miller, W. H. A novel discrete variable representation for quantum mechanical reactive scattering via the S-matrix Kohn method. J. Chem. Phys., 96:1982 (1992).

[210] Mátyus, E., Šimunek, J., and Császár, A. G. On the variational computation of a large number of vibrational energy levels and wave functions for medium-sized molecules. J. Chem. Phys., 131(7):074106 (2009).

[211] Poirier, B. and Carrington, T. Accelerating the calculation of energy levels and wave functions using an efficient preconditioner with the inexact spectral transform method. J. Chem. Phys., 114(21):9254 (2001).

[212] Wang, X.-G. and Carrington, T. A symmetry-adapted method for calculating energy levels with different symmetries from a single set of iterations. J. Chem. Phys., 114(4):1473 (2001).

[213] Leclerc, A. and Carrington, T. Calculating vibrational spectra with sum of product basis functions without storing full-dimensional vectors or matrices. J. Chem. Phys., 140(17):174111 (2014).

[214] Thomas, P. S., Carrington, T., Agarwal, J., and Schaefer, H. F. Using an iterative eigensolver and intertwined rank reduction to compute vibrational spectra of molecules with more than a dozen atoms: Uracil and naphthalene. J. Chem. Phys., 149(6):064108 (2018).

[215] Carrington, T. Using Iterative Eigensolvers to Compute Vibrational Spectra. pages 217–243. John Wiley & Sons, Ltd (2018).

[216] Eckart, C. Some Studies Concerning Rotating Axes and Polyatomic Molecules. Phys. Rev., 47:552–558 (1935).

[217] McCoy, A. B. and Sibert III, E. L. Perturbative calculations of vibrational (J=0) energy levels of linear molecules in normal coordinate representations. J. Chem. Phys., 95(5):3476 (1991).

[218] McCoy, A. B. and Sibert III, E. L. Perturbative Studies of the Vibrations of Polyatomic Molecules Using Curvilinear Coordinates. In Advances in Molecular Vibrations and Collision Dynamics, Vol. 1A, pages 255–282. JAI Press (1991).

[219] Pavlyuchko, A. I., Yurchenko, S. N., and Tennyson, J. A hybrid variational-perturbation calculation of the ro-vibrational spectrum of nitric acid. J. Chem. Phys., 142(9):094309 (2015).

[220] Pavlyuchko, A. I., Yurchenko, S. N., and Tennyson, J. Hybrid variational-perturbation method for calculating ro-vibrational energy levels of polyatomic molecules. Mol. Phys., 113:1559–1575 (2015).

[221] Carter, S., Culik, S. J., and Bowman, J. M. Vibrational self-consistent field method for many-mode systems: A new approach and application to the vibrations of CO adsorbed on Cu(100). J. Chem. Phys., 107(24):10458–10469 (1997).

[222] Christiansen, O. Møller–Plesset perturbation theory for vibrational wave functions. J. Chem. Phys., 119:5773–5781 (2003).

[223] Carter, S. and Handy, N. C. The vibrations of H_2O_2, studied by “multimode,” with a large amplitude motion. J. Chem. Phys., 113:987–993 (2000).

[224] Bowman, J. M., Huang, X., Handy, N. C., and Carter, S. Vibrational Levels of Methanol Calculated by the Reaction Path Version of MULTIMODE, Using an ab initio, Full-Dimensional Potential. J. Phys. Chem. A, 111:7317–7321 (2007).

[225] Horn, T. R., Gerber, R. B., and Ratner, M. A. Vibrational states of very floppy clusters: Approximate separability and the choice of good curvilinear coordinates for $XeHe_2$, I_2He. J. Chem. Phys., 91(3):1813–1823 (1989).

[226] Zuñiga, J., Bastida, A., Requena, A., and Hidalgo, A. Self-consistent-field calculation of vibrational bound states for triatomic molecules using transformed Jacobi coordinates. J. Phys. Chem., 95:2292–2297 (1991).

[227] Bounouar, M. and Scheurer, C. The impact of approximate VSCF schemes and curvilinear coordinates on the anharmonic vibrational frequencies of formamide and thioformamide. Chem. Phys., 347(1):194–207 (2008).

[228] Scribano, Y., Lauvergnat, D. M., and Benoit, D. M. Fast vibrational configuration interaction using generalized curvilinear coordinates and self-consistent basis. J. Chem. Phys., 133(9):094103 (2010).

[229] Strobusch, D. and Scheurer, C. Hierarchical expansion of the kinetic energy operator in curvilinear coordinates for the vibrational self-consistent field method. J. Chem. Phys., 135:124102 (2011).

[230] Strobusch, D. and Scheurer, C. The hierarchical expansion of the kinetic energy operator in curvilinear coordinates extended to the vibrational configuration interaction method. J. Chem. Phys., 135:144101 (2011).

[231] Van Vleck, J. H. On σ-Type Doubling and Electron Spin in the Spectra of Diatomic Molecules. Phys. Rev., 33:467–506 (1929).

[232] Lukka, T. J. and Kauppi, E. Seminumerical contact transformations: From internal coordinate rovibrational Hamiltonian to effective rotational Hamiltonians. Framework of the method. J. Chem. Phys., 103(15):6586 (1995).

[233] Field, R. W., Baraban, J. H., Lipoff, S. H., and Beck, A. R. Effective Hamiltonians for Electronic Fine Structure and Polyatomic Vibrations. In M. Quack and F. Merkt, eds., Handbook of High-Resolution Spectroscopy, page 1461. John Wiley & Sons, Chichester, UK (2011).

[234] Gordy, W. and Cook, R. L. Microwave Molecular Spectra. John Wiley & Sons, New York, 3rd edition (1984).

[235] Exact quantum molecular Hamiltonians. Mol. Phys., 72:1–31 (1991).

[236] Lukka, T. J. A simple method for the derivation of exact quantum-mechanical vibration-rotation Hamiltonians in terms of internal coordinates. J. Chem. Phys., 102:3945–3955 (1995).

[237] Lauvergnat, D. and Nauts, A. Exact numerical computation of a kinetic energy operator in curvilinear coordinates. J. Chem. Phys., 116(19):8560 (2002).

[238] Watson, J. K. G. The molecular vibration-rotation kinetic-energy operator for general internal coordinates. J. Mol. Spectrosc., 228:645–658 (2004).

[239] Mátyus, E., Czakó, G., and Császár, A. G. Toward black-box-type full- and reduced-dimensional variational (ro)vibrational computations. J. Chem. Phys., 130(13):134112 (2009).

[240] Fábri, C., Mátyus, E., and Császár, A. G. Rotating full- and reduced-dimensional quantum chemical models of molecules. J. Chem. Phys., 134(7):074105 (2011).

[241] Fábri, C., Mátyus, E., and Császár, A. G. Numerically constructed internal-coordinate Hamiltonian with Eckart embedding and its application for the inversion tunneling of ammonia. Spectrochim. Acta A, 119:84–9 (2014).

[242] Szalay, V. Aspects of the Eckart frame ro-vibrational kinetic energy operator. J. Chem. Phys., 143(6):064104 (2015).

[243] Podolsky, B. Quantum-Mechanically Correct Form of Hamiltonian Function for Conservative Systems. Phys. Rev., 32(5):812–816 (1928).

[244] Dirac, P. A. M. The Physical Interpretation of the Quantum Dynamics. Proc. Roy. Soc. A, 113:621–641 (1927).

[245] Mladenovic, M. Rovibrational Hamiltonians for general polyatomic molecules in spherical polar parametrization. I. Orthogonal representations. J. Chem. Phys., 112:1070 (2000).

[246] Gatti, F. and Iung, C. Exact and constrained kinetic energy operators for polyatomic molecules: The polyspherical approach. Phys. Rep., 484(1):1–69 (2009).

[247] Wilson Jr., E. B., Decius, J. C., and Cross, P. C. Molecular Vibrations. Dover, New York (1980).

[248] Kraka, E. Reaction path Hamiltonian and the unified reaction valley approach. Comp. Mol. Sci., 1(4):531–556 (2011).

[249] Nauts, A. and Chapuisat, X. The description of molecular large-amplitude motions in terms of curvilinear coordinates associated with the reaction path. Chem. Phys., 76(3):349–366 (1983).

[250] Miller, W. H., Handy, N. C., and Adams, J. E. Reaction path Hamiltonian for polyatomic molecules. J. Chem. Phys., 72:99 (1980).

[251] Page, M. and McIver, J. W. On evaluating the reaction path Hamiltonian. J. Chem. Phys., 88:922 (1988).

[252] Jackels, C. F., Gu, Z., and Truhlar, D. G. Reaction-path potential and vibrational frequencies in terms of curvilinear internal coordinates. J. Chem. Phys., 102(8):3188 (1995).

[253] Szalay, V. Eckart ro-vibrational Hamiltonians via the gateway Hamilton operator: Theory and practice. J. Chem. Phys., 146(12):124107 (2017).

[254] Lauvergnat, D., Luis, J. M., Kirtman, B., Reis, H., and Nauts, A. Numerical and exact kinetic energy operator using Eckart conditions with one or several reference geometries: Application to HONO. J. Chem. Phys., 144(8):084116 (2016).

[255] Dymarsky, A. Y. and Kudin, K. N. Computation of the pseudorotation matrix to satisfy the Eckart axis conditions. J. Chem. Phys., 122(12):124103 (2005).

[256] Yachmenev, A. and Yurchenko, S. N. Automatic differentiation method for numerical construction of the rotational-vibrational Hamiltonian as a power series in the curvilinear internal coordinates using the Eckart frame. J. Chem. Phys., 143(1):014105 (2015).

[257] Krasnoshchekov, S. V., Isayeva, E. V., and Stepanov, N. F. Determination of the Eckart molecule-fixed frame by use of the apparatus of quaternion algebra. J. Chem. Phys., 140(15):154104 (2014).

[258] Raghavachari, K., Trucks, G. W., Pople, J. A., and Head-Gordon, M. A fifth-order perturbation comparison of electron correlation theories. Chem. Phys. Lett., 157(6):479–483 (1989).

[259] Dunning, T. H. Gaussian basis sets for use in correlated molecular calculations. I. The atoms boron through neon and hydrogen. J. Chem. Phys., 90(2):1007 (1989).

[260] Almlöf, J. and Taylor, P. R. General contraction of Gaussian basis sets. I. Atomic natural orbitals for first- and second-row atoms. J. Chem. Phys., 86(7):4070 (1987).

[261] McCaslin, L. and Stanton, J. Calculation of fundamental frequencies for small polyatomic molecules: a comparison between correlation consistent and atomic natural orbital basis sets. Mol. Phys., 111(9-11):1492–1496 (2013).

[262] CFOUR, Coupled-Cluster techniques for Computational Chemistry, a quantum-chemical program package by J.F. Stanton, J. Gauss, M.E. Harding, P.G. Szalay with contributions from A.A. Auer, R.J. Bartlett, U. Benedikt, C. Berger, D.E. Bernholdt, Y.J. Bomble, L. Cheng, O. Christiansen, M. Heckert, O. Heun, C. Huber, T.-C. Jagau, D. Jonsson, J. Jusélius, K. Klein, W.J. Lauderdale, F. Lipparini, D.A. Matthews, T. Metzroth, L.A. Mück, D.P. O'Neill, D.R. Price, E. Prochnow, C. Puzzarini, K. Ruud, F. Schiffmann, W. Schwalbach, C. Simmons, S. Stopkowicz, A. Tajti, J. Vázquez, F. Wang, J.D. Watts and the integral packages MOLECULE (J. Almlöf and P.R. Taylor), PROPS (P.R. Taylor), ABACUS (T. Helgaker, H.J. Aa. Jensen, P. Jørgensen, and J. Olsen), and ECP routines by A. V. Mitin and C. van Wüllen. For the current version, see http://www.cfour.de.

[263] Braams, B. J. and Bowman, J. M. Permutationally invariant potential energy surfaces in high dimensionality. Int. Rev. Phys. Chem., 28(4):577–606 (2009).

[264] Gong, J. Z., Matthews, D. A., Changala, P. B., and Stanton, J. F. Fourth-order vibrational perturbation theory with the Watson Hamiltonian: Report of working equations and preliminary results. J. Chem. Phys., 149(11):114102 (2018).

[265] Squires, R. R. Gas-phase carbanion chemistry. Acc. Chem. Res., 25(10):461–467 (1992).

[266] DePuy, C. H., Gronert, S., Barlow, S. E., Bierbaum, V. M., and Damrauer, R. The gas-phase acidities of the alkanes. J. Am. Chem. Soc., 111(6):1968–1973 (1989).

[267] Špirko, V. and Bunker, P. The inversion potential and rotation-inversion energy levels of H_3O^+ and CH_3^-. J. Mol. Spectrosc., 95:226–235 (1982).

[268] Ellison, G. B., Engelking, P. C., and Lineberger, W. C. An experimental determination of the geometry and electron affinity of methyl radical. J. Am. Chem. Soc., 100:2556–2558 (1978).

[269] Graul, S. T. and Squires, R. R. Gas-phase reactions of the methyl anion. J. Am. Chem. Soc., 111:892–899 (1989).

[270] Mitchell, S. E., Conklin, P. M., and Farley, J. W. First observation of autodetachment lifetimes of methide, CH_3^-. J. Chem. Phys., 118:11017 (2003).

[271] Schwenke, D. W. A theoretical study of the ro-vibrational spectrum of the X state of CH_3. Spectrochim. Acta A, 55(3):731–738 (1999).

[272] Cleeton, C. E. and Williams, N. H. Electromagnetic Waves of 1.1 cm Wave-Length and the Absorption Spectrum of Ammonia. Phys. Rev., 45:234–237 (1934).

[273] Gordon, J. P., Zeiger, H. J., and Townes, C. H. The Maser—New Type of Microwave Amplifier, Frequency Standard, and Spectrometer. Phys. Rev., 99:1264–1274 (1955).

[274] Yu, S., Drouin, B. J., Pearson, J. C., and Pickett, H. M. Terahertz Spectroscopy and Global Analysi of H_3O^+. Astrophys. J. Suppl. S., 180(1):119–124 (2009).

[275] Rajamäki, T., Miani, A., and Halonen, L. Six-dimensional ab initio potential energy surfaces for H_3O^+ and NH_3: Approaching the sub-wavenumber accuracy for the inversion splittings. J. Chem. Phys., 118(24):10929–10938 (2003).

[276] McCarthy, M. C., Gottlieb, C. A., and Cernicharo, J. Building blocks of dust: A coordinated laboratory and astronomical study of the archtype AGB carbon star IRC+10216. Journal of Molecular Spectroscopy, 356:7–20 (2019).

[277] Zetterling, C.-M., ed. Process Technology for Silicon Carbide Devices. IET, The Institution of Engineering and Technology, Michael Faraday House, Six Hills Way, Stevenage SG1 2AY, UK (2002).

[278] Photolysis experiments on SiC mixed clusters: From silicon carbide clusters to silicon-doped fullerenes. J. Chem. Phys., 110:6927–6938 (1999).

[279] Takano, S., Saito, S., and Tsuji, T. Silicon Chemistry in the Outer Envelope of IRC-10216: The Detailed Distribution of SiC_2. Publ. Astron. Soc. Japan, 44:469–480 (1992).

[280] Spielfiedel, A., Carter, S., Feautrier, N., Chambaud, G., and Rosmus, P. Theoretical Study of the Electronic States of Si_2C. J. Phys. Chem., 100:10055–10061 (1996).

[281] Barone, V., Jensen, P., and Minichino, C. Vibro-rotational analysis of Si_2C from an ab initio potential energy surface. A comparison between perturbative and variational methods. J. Mol. Spectrosc., 154:252–264 (1992).

[282] Koput, J. Ab Initio Potential Energy Surface and Vibration-Rotation Energy Levels of Disilicon Carbide, CSi_2. J. Mol. Spectrosc., 342:83–91 (2017).

[283] Bunker, P. R. Quasilinear and Quasiplanar Molecules. Ann. Rev. Phys. Chem., 34:59–75 (1983).

[284] Kafafi, Z. H., Hauge, R. H., Fredin, L., and Margrave, J. L. Infrared matrix isolation spectrum of the disilicon carbide (Si_2C) molecule. J. Phys. Chem., 87:797–800 (1983).

[285] Presilla-Márquez, J. D. and Graham, W. R. M. Fourier transform vibrational spectroscopy of Si_2C in solid Ar. J. Chem. Phys., 95:5612–5617 (1991).

[286] Steglich, M. and Maier, J. P. Electronic transitions of jet-cooled SiC_2, Si_2C_2 ($n = 1-3$), Si_3C_n ($n = 1, 2$), AND SiC_6H_4 between 250 and 710 nm. The Astrophysical Journal, 801(2):119 (2015).

[287] Dixon, R. N. Higher vibrational levels of a bent triatomic molecule. Trans. Faraday Soc., 60:1363 (1964).

[288] Baraban, J. H., Changala, P. B., Mellau, G. C., Stanton, J. F., Merer, A. J., and Field, R. W. Spectroscopic characterization of isomerization transition states. Science, 350(6266):1338–1342 (2015).

[289] Child, M. Quantum monodromy and molecular spectroscopy. Contemp. Phys., 55:212–221 (2014).

[290] Cernicharo, J., Guélin, M., Agúndez, M., Pardo, J. R., Massalkhi, S., Fonfría, J. P., Velilla Prieto, L., Quintana-Lacaci, G., Marcelino, N., Marka, C., Navarro, S., and Kramer, C. IRC +10216 as a spectroscopic laboratory: improved rotational constants for SiC_2 , its isotopologues, and Si_2C. Astron. Astrophys., 618:A4 (2018).

[291] Witsch, D., Lutter, V., Breier, A. A., Yamada, K. M. T., Fuchs, G. W., Gauss, J., and Giesen, T. F. Infrared Spectroscopy of Disilicon-Carbide, Si_2C: The ν_3 Fundamental Band. J. Phys. Chem. A, 123(19):4168–4177 (2019).

[292] Ruscic, B., Pinzon, R. E., Morton, M. L., von Laszevski, G., Bittner, S. J., Nijsure, S. G., Amin, K. A., Minkoff, M., and Wagner, A. F. Introduction to Active Thermochemical Tables: Several “Key” Enthalpies of Formation Revisited. J. Phys. Chem. A, 108:9979–9997 (2004).

[293] Ruscic, B., Pinzon, R. E., von Laszewski, G., Kodeboyina, D., Burcat, A., Leahy, D., Montoy, D., and Wagner, A. F. Active Thermochemical Tables: thermochemistry for the 21st century. J. Phys. Conf. Ser., 16:561–570 (2005).

[294] Schio, L., Alagia, M., Dias, A. A., Falcinelli, S., Zhaunerchyk, V., Lee, E. P. F., Mok, D. K. W., Dyke, J. M., and Stranges, S. A Study of H_2O_2 with Threshold Photoelectron Spectroscopy (TPES) and Electronic Structure Calculations: Redetermination of the First Adiabatic Ionization Energy (AIE). J. Phys. Chem. A (2016).

[295] Ruscic, B. and Bross, D. H. Active Thermochemical Tables (ATcT) values based on version 1.122 of the Thermochemical Network. 2016; online at http://ATcT.anl.gov.

[296] Litorja, M. and Ruscic, B. A photoionization study of the hydroperoxyl radical, HO_2, and hydrogen peroxide, H_2O_2,. J. Electron Spectros. Relat. Phenomena, 97(1-2):131–146 (1998).

[297] Ashmore, F. S. and Burgess, A. R. Study of some medium size alcohols and hydroperoxides by photoelectron spectroscopy. J. Chem. Soc., Faraday Trans., 73:1247 (1977).

[298] Koput, J., Carter, S., and Handy, N. C. Ab initio prediction of the vibrational-rotational energy levels of hydrogen peroxide and its isotopomers. J. Chem. Phys., 115(18):8345–8350 (2001).

[299] Małyszek, P. and Koput, J. Accurate ab initio potential energy surface and vibration-rotation energy levels of hydrogen peroxide. J. Comp. Chem., 34(5):337–345 (2013).

[300] Stanton, J. F. and Gauss, J. Analytic energy derivatives for ionized states described by the equation-of-motion coupled cluster method. J. Chem. Phys., 101(10):8938–8944 (1994).

[301] Khachkuruzov, G. A. and Przhevalskii, I. N. Molecular constants of hydrogen peroxide. 4: Structural parameters. Opt. Spektrosk., 36(172-174) (1974).

[302] Cremer, D. and Christen, D. On the r_0- and r_e-structures of H_2O_2. J. Mol. Spectrosc., 74(3):480–482 (1979).

[303] Koput, J. On the structure and the torsional potential function of hydrogen peroxide. J. Mol. Spectrosc., 115:438–441 (1986).

[304] Helminger, P., Bowman, W. C., and De Lucia, F. C. A study of the rotational-torsional spectrum of hydrogen peroxide between 80 and 700 GHz. J. Mol. Spectrosc., 85(1):120–130 (1981).

[305] Bowman, W. C., De Lucia, F. C., and Helminger, P. The higher K_{-1} states of hydrogen peroxide. J. Mol. Spectrosc., 87:571–574 (1981).

[306] Hillman, J. J. On the submillimeter spectrum of hydrogen peroxide. J. Mol. Spectrosc., 95:236–238 (1982).

[307] Flaud, J. M., Johns, J. W., Lu, Z., Winnewisser, G., and Klein, H. The torsion-rotation spectrum of D_2O_2. Can. J. Phys., 79:367–374 (2001).

[308] Herberth, D., Baum, O., Pirali, O., Roy, P., Thorwirth, S., Yamada, K. M., Schlemmer, S., and Giesen, T. F. Far infrared Fourier-transform spectroscopy of mono-deuterated hydrogen peroxide HOOD. J. Quant. Spec. Rad. Transf., 113:1127–1133 (2012).

[309] Koput, J. An ab initio study on the equilibrium structure and torsional potential energy function of hydrogen peroxide. Chem. Phys. Lett., 236:516–520 (1995).

[310] Császár, A. G., Czakó, G., Furtenbacher, T., Tennyson, J., Szalay, V., Shirin, S. V., Zobov, N. F., and Polyansky, O. L. On equilibrium structures of the water molecule. J. Chem. Phys., 122(21):214305 (2005).

[311] Amano, T. Difference frequency laser spectroscopy of OH and OD: Simultaneous fit of the infrared and microwave lines. J. Mol. Spectrosc., 103:436–454 (1984).

[312] Diels, O. and Alder, K. Synthesen in der hydroaromatischen Reihe. Justus Liebigs Ann. Chem., 460:98–122 (1928).

[313] Rice, J. E., Liu, B., Lee, T. J., and McMichael Rohlfing, C. The structure of cis-butadiene. Chem. Phys. Lett., 161(3):277–284 (1989).

[314] Alberts, I. L. and Schaeffer, H. F. The second stable conformer of 1,3-butadiene. Geometry optimizations with configuration interaction and coupled cluster methods. Chem. Phys. Lett., 161(4-5):375–382 (1989).

[315] Guo, H. and Karplus, M. Ab initio studies of polyenes. I. 1,3-butadiene. J. Chem. Phys., 94:3679–3699 (1991).

[316] Panchenko, Y. N. and De Maré, G. R. Vibrational analysis of buta-1,3-diene and its deutero and 13C derivatives and some of their rotational isomers. J. Struct. Chem., 49:235–244 (2008).

[317] Feller, D. and Craig, N. C. High level ab initio energies and structures for the rotamers of 1,3-butadiene. J. Phys. Chem. A, 113:1601–7 (2009).

[318] Engeln, R., Consalvo, D., and Reuss, J. Evidence for a gauche minor conformer of 1,3-butadiene. Chem. Phys., 160:427–433 (1992).

[319] Boopalachandran, P., Craig, N., Groner, P., and Laane, J. Gas-phase Raman spectra and the potential energy function for the internal rotation of 1,3-butadiene and its isotopologues. J. Phys. Chem. A, 115:8920–7 (2011).

[320] Boopalachandran, P., Craig, N. C., and Laane, J. Gas-phase Raman spectra of s-trans- and s-gauche-1,3-butadiene and their deuterated isotopologues. J. Phys. Chem. A, 116:271–81 (2012).

[321] Krasnoshchekov, S. V., Craig, N. C., Boopalachandran, P., Laane, J., and Stepanov, N. F. Anharmonic Vibrational Analysis of the Infrared and Raman Gas-Phase Spectra of s-trans- and s-gauche-1,3-Butadiene. J. Phys. Chem. A, 119:10706–10723 (2015).

[322] Saltiel, J., Sears, D. F., and Turek, A. M. UV Spectrum of the High Energy Conformer of 1,3-Butadiene in the Gas Phase. J. Phys. Chem. A, 105:7569–7578 (2001).

[323] Porterfield, J. P., Westerfield, J. H., Satterthwaite, L., Patterson, D., Changala, P. B., Baraban, J. H., and McCarthy, M. C. Rotational Characterization of the Elusive gauche-Isoprene. J. Phys. Chem. Lett., 10:1981–1985 (2019).

[324] Wiberg, K. B., Rablen, P. R., and Baraban, J. H. Butadiene and Heterodienes Revisited. J. Org. Chem., 83:8473–8482 (2018).

[325] Reinhardt, W. P. Complex Coordinates in the Theory of Atomic and Molecular Structure and Dynamics. Ann. Rev. Phys. Chem., 33:223–255 (1982).

[326] Christoffel, K. M. and Bowman, J. M. Complex coordinate, self-consistent field calculations of vibrational resonance energies. J. Chem. Phys., 76:5370–5374 (1982).

[327] Seideman, T. and Miller, W. H. Transition state theory, Siegert eigenstates, and quantum mechanical reaction rates. J. Chem. Phys., 95(3):1768–1780 (1991).

[328] Rom, N., Ryaboy, V., and Moiseyev, N. Cumulative reaction probability by the complex coordinate scattering theory. J. Chem. Phys., 98:6327–6331 (1993).

[329] Ryaboy, V. and Moiseyev, N. Cumulative reaction probability from Siegert eigenvalues: Model studies. J. Chem. Phys., 98:9618–9623 (1993).

[330] Roy, T. K. and Prasad, M. D. A thermal self-consistent field theory for the calculation of molecular vibrational partition functions. J. Chem. Phys., 131:114102 (2009).

[331] McCoy, A. B. Diffusion Monte Carlo approaches for investigating the structure and vibrational spectra of fluxional systems. Int. Rev. Phys. Chem., 25:77–107 (2006).

[332] Petit, A. S. and McCoy, A. B. Diffusion Monte Carlo in internal coordinates. J. Phys. Chem. A, 117:7009–18 (2013).

[333] PGOPHER, A Program for Simulating Rotational, Vibrational and Electronic Spectra, C. M. Western, University of Bristol, http://pgopher.chm.bris.ac.uk.

[334] de Kerckhove Varent, D. Contribution a l'etude de la molecule de bromure de vinyle en spectroscopie hertzienne. II. Bromure de vinyle monodeutere et substitue en ^{13}C, second ordre du couplage quadripolaire, structure de la molecule. Ann. Soc. Sci. Brux., T84:277–292 (1970).

[335] Hayashi, M., Ikeda, C., and Inagusa, T. Microwave spectrum, structure, and nuclear quadrupole coupling constant tensor of vinyl bromide and iodide. J. Mol. Spectrosc., 139(2):299–312 (1990).

Appendix A

Infrared line lists

A.1 Nitromethane, CH_3NO_2

Tables A.1 and A.2 list the rovibrational transition frequencies for the $m = 0$ and $|m| = 1$ components, respectively, of the $\nu_3 + \nu_6$ band (Section 3.2.2). Tables A.3 and A.4 list the $m = 0$ transitions for the ν_1 and ν_{10o} bands (Section 3.2.3).

Table A.1: Line list for the 2953 cm^{-1} band ($m = 0$) of nitromethane, assigned as $\nu_3 + \nu_6$. Transitions are specified with the lower state ($''$) and upper state ($'$) asymmetric top quantum numbers J, K_a, and K_c. E'' (E') is the lower (upper) state energy in cm^{-1}. An offset of 2950 cm^{-1} has been subtracted from the IR line positions and upper state energies. "Component 1" and "component 2" refer to members of a mixed bright state/dark state doublet.

m''	J''	K_a''	K_c''	E''^a	m'	J'	K_a'	K_c'	Line Pos.	E'	Comment
0	2	2	0	2.421311	0	1	1	1	0.8969	3.3182	
0	2	0	2	1.549651	0	1	1	1	1.7690	3.3186	
0	0	0	0	0.000000	0	1	1	1	3.3184	3.3184	
0	2	2	1	2.327828	0	1	1	0	1.1362	3.4640	
0	1	0	1	0.547713	0	1	1	0	2.9161	3.4638	
0	3	2	1	4.322080	0	2	1	2	−0.0584	4.2637	
0	3	0	3	2.935110	0	2	1	2	1.3287	4.2638	
0	2	2	1	2.327828	0	2	1	2	1.9358	4.2637	
0	1	0	1	0.547713	0	2	1	2	3.7159	4.2636	
0	3	2	2	3.970934	0	2	1	1	0.7220	4.6929	
0	2	2	0	2.421311	0	2	1	1	2.2719	4.6932	
0	2	0	2	1.549651	0	2	1	1	3.1437	4.6934	
0	4	0	4	4.703276	0	3	1	3	0.8403	5.5436	component 1
0	3	2	2	3.970934	0	3	1	3	1.5730	5.5440	
0	2	0	2	1.549651	0	3	1	3	3.9944	5.5440	

(continued on next page)

---

[a] Ground state energies from Ref. [52].

Table A.1: (continued)

m''	J''	K''_a	K''_c	E''^a	m'	J'	K'_a	K'_c	Line Pos.	E'	Comment
0	4	0	4	4.703276	0	3	1	3	0.9769	5.6802	component 2
0	3	2	2	3.970934	0	3	1	3	1.7096	5.6805	
0	2	0	2	1.549651	0	3	1	3	4.1310	5.6806	
0	4	2	3	6.082186	0	3	1	2	0.3326	6.4148	component 1
0	3	2	1	4.322080	0	3	1	2	2.0930	6.4151	
0	3	0	3	2.935110	0	3	1	2	3.4799	6.4150	
0	2	2	1	2.327828	0	3	1	2	4.0869	6.4147	
0	4	2	3	6.082186	0	3	1	2	0.4721	6.5543	component 2
0	3	2	1	4.322080	0	3	1	2	2.2327	6.5547	
0	3	0	3	2.935110	0	3	1	2	3.6193	6.5544	
0	2	2	1	2.327828	0	3	1	2	4.2265	6.5544	weak
0	4	2	2	6.839377	0	3	3	1	0.6678	7.5072	
0	4	4	0	8.311898	0	3	3	1	−0.8046	7.5073	
0	3	2	2	3.970934	0	3	3	1	3.5361	7.5070	
0	2	2	0	2.421311	0	3	3	1	5.0860	7.5073	
0	4	4	1	8.295303	0	3	3	0	−0.7425	7.5528	
0	3	2	1	4.322080	0	3	3	0	3.2309	7.5530	
0	2	2	1	2.327828	0	3	3	0	5.2248	7.5526	
0	5	0	5	6.860890	0	4	1	4	0.4886	7.3495	
0	4	2	3	6.082186	0	4	1	4	1.2671	7.3493	
0	3	0	3	2.935110	0	4	1	4	4.4145	7.3496	
0	5	2	4	8.619788	0	4	1	3	−0.0580	8.5618	component 1, blended
0	4	2	2	6.839377	0	4	1	3	1.7222	8.5616	
0	4	0	4	4.703276	0	4	1	3	3.8584	8.5617	
0	3	2	2	3.970934	0	4	1	3	4.5908	8.5618	
0	5	2	4	8.619788	0	4	1	3	0.1185	8.7383	component 2
0	4	2	2	6.839377	0	4	1	3	1.8990	8.7383	
0	4	0	4	4.703276	0	4	1	3	4.0351	8.7384	
0	3	2	2	3.970934	0	4	1	3	4.7679	8.7388	
0	5	4	1	11.352928	0	4	3	2	−1.5563	9.7966	
0	5	2	3	9.856035	0	4	3	2	−0.0594	9.7966	
0	4	4	1	8.295303	0	4	3	2	1.5013	9.7966	
0	4	2	3	6.082186	0	4	3	2	3.7148	9.7969	
0	3	2	1	4.322080	0	4	3	2	5.4746	9.7967	
0	5	4	2	11.234530	0	4	3	1	−1.2089	10.0256	
0	4	4	0	8.311898	0	4	3	1	1.7136	10.0255	
0	4	2	2	6.839377	0	4	3	1	3.1866	10.0260	
0	3	2	2	3.970934	0	4	3	1	6.0545	10.0255	
0	6	0	6	9.409937	0	5	1	5	0.0883	9.4983	
0	5	2	4	8.619788	0	5	1	5	0.8783	9.4981	
0	4	0	4	4.703276	0	5	1	5	4.7953	9.4985	
0	6	2	5	11.560383	0	5	1	4	−0.3965	11.1639	component 1
0	5	2	3	9.856035	0	5	1	4	1.3077	11.1637	

(continued on next page)

---

[a] Ground state energies from Ref. [52].

Table A.1: (continued)

m''	J''	K''_a	K''_c	E''^a	m'	J'	K'_a	K'_c	Line Pos.	E'	Comment
0	5	0	5	6.860890	0	5	1	4	4.3030	11.1639	
0	4	2	3	6.082186	0	5	1	4	5.0816	11.1638	
0	6	2	5	11.560383	0	5	1	4	−0.2190	11.3414	component 2
0	5	2	3	9.856035	0	5	1	4	1.4853	11.3413	
0	5	0	5	6.860890	0	5	1	4	4.4808	11.3416	
0	4	2	3	6.082186	0	5	1	4	5.2591	11.3413	
0	6	4	2	15.137207	0	5	3	3	−2.5377	12.5996	
0	6	2	4	13.256243	0	5	3	3	−0.6579	12.5984	blended
0	5	4	2	11.234530	0	5	3	3	1.3649	12.5994	
0	5	2	4	8.619788	0	5	3	3	3.9795	12.5993	
0	4	2	2	6.839377	0	5	3	3	5.7600	12.5994	
0	6	4	3	14.743171	0	5	3	2	−1.5973	13.1459	blended
0	5	4	1	11.352928	0	5	3	2	1.7934	13.1463	
0	5	2	3	9.856035	0	5	3	2	3.2907	13.1467	
0	4	4	1	8.295303	0	5	3	2	4.8515	13.1468	
0	4	2	3	6.082186	0	5	3	2	7.0647	13.1468	
0	6	6	0	17.788197	0	5	5	1	−2.6539	15.1343	
0	5	4	2	11.234530	0	5	5	1	3.9001	15.1346	
0	4	4	0	8.311898	0	5	5	1	6.8224	15.1343	
0	6	6	1	17.786379	0	5	5	0	−2.6450	15.1414	
0	5	4	1	11.352928	0	5	5	0	3.7881	15.1411	
0	4	4	1	8.295303	0	5	5	0	6.8458	15.1411	
0	7	0	7	12.350829	0	6	1	6	−0.3695	11.9813	component 1
0	6	2	5	11.560383	0	6	1	6	0.4209	11.9812	
0	5	0	5	6.860890	0	6	1	6	5.1207	11.9816	
0	7	0	7	12.350829	0	6	1	6	−0.2185	12.1324	component 2, overlap
0	6	2	5	11.560383	0	6	1	6	0.5715	12.1319	
0	5	0	5	6.860890	0	6	1	6	5.2709	12.1318	
0	7	2	6	14.895396	0	6	1	5	−0.7442	14.1512	
0	6	2	4	13.256243	0	6	1	5	0.8948	14.1511	
0	6	0	6	9.409937	0	6	1	5	4.7417	14.1516	
0	5	2	4	8.619788	0	6	1	5	5.5319	14.1517	
0	7	2	5	17.012438	0	6	3	4	−1.1530	15.8594	
0	6	4	3	14.743171	0	6	3	4	1.1160	15.8591	
0	6	2	5	11.560383	0	6	3	4	4.2986	15.8590	
0	5	2	3	9.856035	0	6	3	4	6.0030	15.8591	
0	7	4	4	18.767500	0	6	3	3			
0	6	4	2	15.137207	0	6	3	3	1.7430	16.8802	
0	6	2	4	13.256243	0	6	3	3	3.6240	16.8802	
0	5	4	2	11.234530	0	6	3	3	5.6459	16.8805	weak
0	5	2	4	8.619788	0	6	3	3			
0	7	4	4	18.767500	0	6	3	3			
0	6	4	2	15.137207	0	6	3	3	1.6553	16.7925	

(continued on next page)

---

[a] Ground state energies from Ref. [52].

Table A.1: (continued)

m''	J''	K''_a	K''_c	E''^a	m'	J'	K'_a	K'_c	Line Pos.	E'	Comment
0	6	2	4	13.256243	0	6	3	3	3.5361	16.7924	overlap
0	5	4	2	11.234530	0	6	3	3			
0	5	2	4	8.619788	0	6	3	3			
0	7	6	1	21.948226	0	6	5	2	−3.2809	18.6673	
0	6	6	1	17.786379	0	6	5	2	0.8807	18.6671	
0	6	4	3	14.743171	0	6	5	2	3.9241	18.6673	
0	5	4	1	11.352928	0	6	5	2	7.3146	18.6675	
0	7	6	2	21.927772	0	6	5	1	−3.2034	18.7244	
0	6	6	0	17.788197	0	6	5	1	0.9366	18.7248	
0	6	4	2	15.137207	0	6	5	1	3.5872	18.7244	
0	5	4	2	11.234530	0	6	5	1	7.4901	18.7247	
0	8	0	8	15.683641	0	7	1	7	−0.7391	14.9445	blended
0	7	2	6	14.895396	0	7	1	7	0.0492	14.9445	
0	6	0	6	9.409937	0	7	1	7	5.5346	14.9445	
0	8	2	7	18.622625	0	7	1	6	−1.1604	17.4622	tentative
0	7	2	5	17.012438	0	7	1	6	0.4498	17.4623	
0	7	0	7	12.350829	0	7	1	6	5.1117	17.4625	
0	6	2	5	11.560383	0	7	1	6	5.9019	17.4623	
0	8	2	6	21.143107	0	7	3	5	−1.5966	19.5465	blended
0	7	4	4	18.767500	0	7	3	5	0.7782	19.5457	
0	7	2	6	14.895396	0	7	3	5	4.6502	19.5456	
0	6	2	4	13.256243	0	7	3	5	6.2896	19.5458	
0	7	4	3	19.614558	0	7	3	4	1.5684	21.1830	tentative
0	7	2	5	17.012438	0	7	3	4	4.1707	21.1832	
0	6	4	3	14.743171	0	7	3	4	6.4402	21.1834	
0	7	4	3	19.614558	0	7	3	4	1.3625	20.9771	tentative
0	7	2	5	17.012438	0	7	3	4	3.9658	20.9782	
0	6	4	3	14.743171	0	7	3	4	6.2355	20.9787	
0	8	8	0	30.831142	0	7	7	1	−4.5623	26.2688	very weak, blended
0	6	6	0	17.788197	0	7	7	1	8.4802	26.2684	
0	8	8	1	30.830978	0	7	7	0	−4.5623	26.2687	very weak, blended
0	7	6	1	21.948226	0	7	7	0	4.3211	26.2693	
0	6	6	1	17.786379	0	7	7	0	8.4830	26.2694	
0	9	0	9	19.408388	0	8	1	8	−1.1478	18.2606	tentative
0	7	0	7	12.350829	0	8	1	8	5.9091	18.2599	tentative

[a] Ground state energies from Ref. [52].

Table A.2: Line list for the 2953 cm^{-1} band ($|m| = 1$) of nitromethane, assigned as $\nu_3 + \nu_6$. Transitions are specified with the lower state ($''$) and upper state ($'$) J quantum number and τ, an energy ordering index for a given J and m (counting only non-zero spin-weighted levels). E'' (E') is the lower (upper) state energy in cm^{-1}. An offset of 2950 cm^{-1} has been subtracted from the IR line positions and upper state energies.

$\|m''\|$	J''	τ''	E''^{a}	$\|m'\|$	J'	τ'	Line Pos.	E'	Comment
1	3	1	7.545719	1	2	1	0.7904	8.3361	
1	2	1	6.459007	1	2	1			very weak
1	1	1	5.390459	1	2	1	2.9457	8.3361	
1	4	1	9.383413	1	3	1	0.3800	9.7634	
1	3	2	8.197563	1	3	1			
1	2	1	6.459007	1	3	1	3.3043	9.7633	
1	5	1	11.564673	1	4	1	0.0002	11.5648	
1	4	2	10.534994	1	4	1	1.0298	11.5648	
1	3	2	8.197563	1	4	1	3.3673	11.5648	
1	3	1	7.545719	1	4	1	4.0193	11.5650	
1	6	1	14.126832	1	5	1	−0.7197	13.4071	
1	5	2	13.134167	1	5	1	0.2729	13.4071	
1	4	1	9.383413	1	5	1	4.0240	13.4074	
1	7	1	17.076453	1	6	1	−1.0788	15.9976	
1	5	1	11.564673	1	6	1	4.4330	15.9976	
1	8	1	20.415573	1	7	1	−1.4281	18.9874	
1	7	2	19.500138	1	7	1	−0.5125	18.9876	
1	6	1	14.126832	1	7	1	4.8611	18.9879	

[a] Ground state energies from Ref. [52].

Table A.3: Line list for the ν_1 ($m = 0$) band of nitromethane. Transitions are specified with the lower state ($''$) and upper state ($'$) asymmetric top quantum numbers J, K_a, and K_c. E'' (E') is the lower (upper) state energy in cm^{-1}. An offset of 2970 cm^{-1} has been subtracted from the IR line positions and upper state energies.

J''	K''_a	K''_c	E''^{a}	J'	K'_a	K'_c	Line Pos.	E'
2	0	2	1.549651	1	0	1	2.4433	3.9930
0	0	0	0.000000	1	0	1	3.9928	3.9928
3	0	3	2.935110	2	0	2	1.9923	4.9274
1	0	1	0.547713	2	0	2	4.3796	4.9273
4	0	4	4.703276	3	0	3	1.5774	6.2807
2	0	2	1.549651	3	0	3	4.7311	6.2807
5	0	5	6.860890	4	0	4	1.1802	8.0410
3	0	3	2.935110	4	0	4	5.1061	8.0412
6	0	6	9.409937	5	0	5	0.7647	10.1746
4	0	4	4.703276	5	0	5	5.4713	10.1746

(continued on next page)

[a] Ground state energies from Ref. [52].

Table A.3: (continued)

J''	K''_a	K''_c	E''^a	J'	K'_a	K'_c	Line Pos.	E'
7	0	7	12.350829	6	0	6	0.3615	12.7123
5	0	5	6.860890	6	0	6	5.8517	12.7126
8	0	8	15.683641	7	0	7	−0.0576	15.6260
6	0	6	9.409937	7	0	7	6.2160	15.6259
9	0	9	19.408388	8	0	8	−0.4740	18.9344
7	0	7	12.350829	8	0	8	6.5840	18.9348
10	0	10	23.525068	9	0	9	−0.8898	22.6353
8	0	8	15.683641	9	0	9	6.9517	22.6353
3	2	2	3.970934	2	2	1	1.4048	5.3757
2	2	0	2.421311	2	2	1	2.9544	5.3757
4	2	3	6.082186	3	2	2	1.0544	7.1366
3	2	1	4.322080	3	2	2	2.8151	7.1372
2	2	1	2.327828	3	2	2	4.8091	7.1369
5	2	4	8.619788	4	2	3	0.7016	9.3214
4	2	2	6.839377	4	2	3	2.4820	9.3214
3	2	2	3.970934	4	2	3	5.3505	9.3214
6	2	5	11.560383	5	2	4	0.3120	11.8724
5	2	3	9.856035	5	2	4	2.0167	11.8727
4	2	3	6.082186	5	2	4	5.7907	11.8729
7	2	6	14.895396	6	2	5	−0.0986	14.7968
6	2	4	13.256243	6	2	5	1.5397	14.7959
5	2	4	8.619788	6	2	5	6.1772	14.7970
8	2	7	18.622625	7	2	6	−0.5235	18.0991
7	2	5	17.012438	7	2	6	1.0869	18.0993
6	2	5	11.560383	7	2	6	6.5391	18.0995
9	2	8	22.741677	8	2	7	−0.9491	21.7926
8	2	6	21.143107	8	2	7	0.6497	21.7928
7	2	6	14.895396	8	2	7	6.8973	21.7927

[a] Ground state energies from Ref. [52].

Table A.4: Line list for the ν_{10o} ($m = 0$) band of nitromethane. Transitions are specified with the lower state ($''$) and upper state ($'$) asymmetric top quantum numbers J, K_a, and K_c. E'' (E') is the lower (upper) state energy in cm^{-1}. An offset of 3050 cm^{-1} has been subtracted from the IR line positions and upper state energies.

J''	K''_a	K''_c	E''^a	J'	K'_a	K'_c	Line Pos.	E'	Comment
2	2	1	2.3278	1	1	1	1.4118	3.7396	
1	0	1	0.5477	1	1	1	3.1916	3.7393	
2	2	0	2.4213	1	1	0	1.4628	3.8841	
0	0	0	0.0000	1	1	0	3.8837	3.8837	

(continued on next page)

[a] Ground state energies from Ref. [55].

Table A.4: (continued)

J''	K''_a	K''_c	E''^a	J'	K'_a	K'_c	Line Pos.	E'	Comment
3	2	2	3.9710	2	1	2	0.6791	4.6501	
2	0	2	1.5497	2	1	2	3.1001	4.6498	
3	2	1	4.3221	2	1	1	0.8052	5.1273	
2	2	1	2.3278	2	1	1	2.7992	5.1270	
1	0	1	0.5477	2	1	1	4.5793	5.1270	
4	2	3	6.0822	3	1	3	−0.0225	6.0597	
3	0	3	2.9351	3	1	3	3.1246	6.0597	
4	2	2	6.8395	3	1	2	0.0506	6.8901	
3	2	2	3.9710	3	1	2	2.9188	6.8898	
2	0	2	1.5497	3	1	2	5.3405	6.8902	
4	4	1	8.2954	3	3	1	−0.1496	8.1458	
3	2	1	4.3221	3	3	1	3.8235	8.1456	
2	2	1	2.3278	3	3	1	5.8179	8.1457	
4	4	0	8.3120	3	3	0	−0.1394	8.1726	
2	2	0	2.4213	3	3	0	5.7510	8.1723	
5	2	4	8.6197	4	1	4	−0.7495	7.8702	
4	0	4	4.7032	4	1	4	3.1674	7.8706	
5	2	3	9.8561	4	1	3	−0.7800	9.0761	
4	2	3	6.0822	4	1	3	2.9936	9.0758	
3	0	3	2.9351	4	1	3	6.1409	9.0760	
5	4	2	11.2347	4	3	2	−0.7982	10.4365	
4	2	2	6.8395	4	3	2	3.5968	10.4363	
3	2	2	3.9710	4	3	2	6.4652	10.4362	
5	4	1	11.3531	4	3	1	−0.7575	10.5956	
4	4	1	8.2954	4	3	1			
3	2	1	4.3221	4	3	1	6.2729	10.5950	
6	2	5	11.5602	5	1	5	−1.5864	9.9738	weak
5	0	5	6.8608	5	1	5	3.1128	9.9736	overlapped with $6_{15} \leftarrow 6_{25}$
6	2	5	11.5602	5	1	5	−1.7127	9.8475	
5	0	5	6.8608	5	1	5	2.9866	9.8474	
6	2	4	13.2562	5	1	4	−1.5958	11.6604	
5	2	4	8.6197	5	1	4	3.0410	11.6607	
4	0	4	4.7032	5	1	4	6.9572	11.6604	
6	4	3	14.7434	5	3	3	−1.4608	13.2826	
5	2	3	9.8561	5	3	3	3.4258	13.2819	
4	2	3	6.0822	5	3	3	7.2000	13.2822	
6	4	2	15.1375	5	3	2	−1.3996	13.7379	
5	4	2	11.2347	5	3	2			very weak
4	2	2	6.8395	5	3	2	6.8982	13.7377	
6	6	1	17.7865	5	5	1	−1.7785	16.0080	blended, weak
4	4	1	8.2954	5	5	1	7.7114	16.0068	
6	6	0	17.7884	5	5	0	−1.7791	16.0093	blended, weak
4	4	0	8.3120	5	5	0	7.6973	16.0093	

(continued on next page)

[a] Ground state energies from Ref. [55].

Table A.4: (continued)

J''	K_a''	K_c''	E''^a	J'	K_a'	K_c'	Line Pos.	E'	Comment
7	2	6	14.8950	6	1	6			
6	0	6	9.4096	6	1	6	3.0763	12.4859	(no comb. diff. found)
7	2	5	17.0123	6	1	5	−2.3396	14.6727	
6	2	5	11.5602	6	1	5	3.1128	14.6730	see $5_{15} \leftarrow 5_{05}$
5	0	5	6.8608	6	1	5	7.8122	14.6730	
7	4	4	18.7676	6	3	4	−2.1202	16.6474	
6	2	4	13.2562	6	3	4	3.3910	16.6472	
5	2	4	8.6197	6	3	4	8.0271	16.6468	
7	4	3	19.6150	6	3	3	−2.0864	17.5286	
6	4	3	14.7434	6	3	3			
5	2	3	9.8561	6	3	3	7.6718	17.5279	
7	2	6	14.8950	7	1	6	3.3472	18.2422	
6	0	6	9.4096	7	1	6	8.8327	18.2423	

[a] Ground state energies from Ref. [55].

A.2 Naphthalene, $C_{10}H_8$

Table A.5: Line list for the ν_{29} band of naphthalene. Transitions are specified with the lower state ($''$) and upper state ($'$) asymmetric top quantum numbers J, K_a, and K_c. Line positions are given in cm^{-1}.

J''	K_a''	K_c''	J'	K_a'	K_c'	Line Pos.
1	0	1	1	1	0	3064.5194
1	0	1	2	1	2	3064.4017
1	1	0	1	0	1	3064.6690
1	1	0	2	2	1	3064.2528
1	1	1	0	0	0	3064.7279
1	1	1	2	0	2	3064.5172
2	0	2	1	1	1	3064.6708
2	0	2	2	1	1	3064.5063
2	0	2	3	1	3	3064.3481
3	0	3	3	1	2	3064.4839
3	0	3	4	1	4	3064.2969
3	1	2	3	0	3	3064.7039
3	1	2	3	2	1	3064.4141
3	1	2	4	2	3	3064.1400
3	1	3	2	0	2	3064.8398
3	1	3	3	2	2	3064.3515
3	1	3	4	0	4	3064.3646
3	2	1	2	1	2	3065.0374
8	0	8	7	1	7	3065.0889
8	0	8	8	1	7	3064.2144
8	0	8	9	1	9	3064.0293
8	1	8	7	0	7	3065.0972
8	1	8	8	2	7	3064.1656
8	1	8	9	0	9	3064.0332
8	2	6	8	1	7	3064.8343
8	2	6	8	3	5	3064.3302
8	2	6	9	3	7	3063.7335
9	0	9	8	1	8	3065.1466
9	0	9	9	1	8	3064.1433
9	0	9	10	1	10	3063.9680
9	1	8	8	2	7	3065.1692
9	1	8	9	2	7	3064.2996
9	1	8	10	2	9	3063.8850
9	1	9	8	0	8	3065.1533
9	1	9	9	2	8	3064.1138
9	1	9	10	0	10	3063.9724

(continued on next page)

Table A.5: (continued)

J''	K_a''	K_c''	J'	K_a'	K_c'	Line Pos.	J''	K_a''	K_c''	J'	K_a'	K_c'	Line Pos.
3	2	1	3	1	2	3064.7743	9	2	7	9	1	8	3064.8850
3	2	1	4	3	2	3063.9725	9	2	7	9	3	6	3064.3341
4	0	4	3	1	3	3064.8222	9	2	7	10	3	8	3063.7039
4	0	4	4	1	3	3064.4500	10	0	10	9	1	9	3065.2060
4	0	4	5	1	5	3064.2470	10	0	10	10	1	9	3064.0759
4	1	4	3	0	3	3064.8909	10	0	10	11	1	11	3063.9096
4	1	4	4	2	3	3064.3267	10	1	9	9	2	8	3065.2435
4	1	4	5	0	5	3064.2925	10	1	9	10	0	10	3065.1025
4	2	2	4	1	3	3064.7658	10	1	9	10	2	8	3064.2364
4	2	2	4	3	1	3064.2657	10	1	9	11	2	10	3063.8360
4	2	2	5	3	3	3063.9096	10	2	8	10	1	9	3064.9458
4	3	1	3	2	2	3065.2256	10	2	8	10	3	7	3064.3234
4	3	1	4	2	2	3064.9241	10	2	8	11	3	9	3063.6748
4	3	1	5	4	2	3063.7607	10	2	9	9	1	8	3065.2970
5	0	5	4	1	4	3064.8940	10	2	9	10	1	10	3065.1220
5	0	5	5	1	4	3064.4041	10	2	9	10	3	8	3064.1169
5	0	5	6	1	6	3064.1955	10	2	9	11	1	10	3063.8679
5	1	4	4	2	3	3064.8170	11	0	11	10	1	10	3065.2650
5	1	4	5	0	5	3064.7827	11	0	11	11	1	10	3064.0113
5	1	4	5	2	3	3064.4220	11	0	11	12	1	12	3063.8503
5	1	4	6	2	5	3064.0499	11	1	10	10	2	9	3065.3122
5	1	5	4	0	4	3064.9396	11	1	10	11	0	11	3065.1663
5	1	5	5	2	4	3064.2950	11	1	10	11	2	9	3064.1655
5	1	5	6	0	6	3064.2236	11	1	10	12	2	11	3063.7834
5	2	3	5	1	4	3064.7658	11	1	11	10	0	10	3065.2660
5	2	3	5	3	2	3064.2802	11	1	11	11	2	10	3063.9994
5	2	3	6	3	4	3063.8542	11	1	11	12	0	12	3063.8503
5	3	2	4	2	3	3065.3033	11	2	10	10	1	9	3065.3446
5	3	2	5	2	3	3064.9089	11	2	10	11	3	9	3064.0738
5	3	2	6	4	3	3063.6914	11	2	10	12	1	11	3063.8019
5	3	3	4	2	2	3065.2799	12	0	12	11	1	11	3065.3226
5	3	3	5	2	4	3064.9507	12	0	12	12	1	11	3063.9465
5	3	3	6	4	2	3063.6880	12	0	12	13	1	13	3063.7897
6	1	5	5	2	4	3064.9107	12	1	11	11	2	10	3065.3763
6	1	5	6	0	6	3064.8387	12	1	11	12	2	10	3064.0906
6	1	5	6	2	4	3064.4118	12	1	11	13	2	12	3063.7271
6	1	5	7	2	6	3064.0101	12	1	12	11	0	11	3065.3226
6	2	5	5	1	4	3065.1368	12	1	12	12	2	11	3063.9401
6	2	5	6	1	6	3064.9290	12	1	12	13	0	13	3063.7897
6	2	5	6	3	4	3064.2260	13	0	13	12	1	12	3065.3810
6	2	5	7	1	6	3064.1843	13	0	13	13	1	12	3063.8849
6	2	5	7	3	4	3063.7038	13	0	13	14	1	14	3063.7296
7	0	7	6	1	6	3065.0268	13	1	12	12	2	11	3065.4386
7	0	7	7	1	6	3064.2825	13	1	12	13	0	13	3065.2883

(continued on next page)

Table A.5: (continued)

J''	K_a''	K_c''	J'	K_a'	K_c'	Line Pos.	J''	K_a''	K_c''	J'	K_a'	K_c'	Line Pos.
7	0	7	8	1	8	3064.0862	13	1	12	14	2	13	3063.6706
7	1	6	6	2	5	3065.0019	13	1	13	12	0	12	3065.3810
7	1	6	7	0	7	3064.9024	13	1	13	13	2	12	3063.8809
7	1	6	7	2	5	3064.3887	13	1	13	14	0	14	3063.7296
7	1	6	8	2	7	3063.9715	13	2	11	12	3	10	3065.4484
7	1	7	6	0	6	3065.0419	13	2	11	13	3	10	3064.2002
7	1	7	7	2	6	3064.2130	13	2	11	14	3	12	3063.5742
7	1	7	8	0	8	3064.0943	13	2	12	12	1	11	3065.4482
7	2	5	7	1	6	3064.7970	13	2	12	13	3	11	3063.9725
7	2	5	7	3	4	3064.3164	13	2	12	14	1	13	3063.6747
7	2	5	8	3	6	3063.7670	14	0	14	13	1	13	3065.4385
7	3	4	6	2	5	3065.4827	14	0	14	14	1	13	3063.8224
7	3	4	7	2	5	3064.8698	14	0	14	15	1	15	3063.6694
7	3	4	7	4	3	3064.1352	14	1	14	13	0	13	3065.4385
7	3	4	8	4	5	3063.5621	14	1	14	14	2	13	3063.8209
							14	1	14	15	0	15	3063.6694

A.3 Buckminsterfullerene, C_{60}

A line list of the assigned R-branch transitions of the 8.5 μm band of C_{60}, as well as the raw spectrum itself, is located in a permanent online data repository [154].

Appendix B

Spectroscopic constants of the ν_3 band of vinyl bromide

Table B.1 below contains the fitted spectroscopic parameters for the ν_3 band of vinyl bromide (see Fig. 2.1). The fit was performed using the standard Watson A-reduced quartic Hamiltonian [64] and nuclear quadrupole hyperfine terms with the PGOPHER program [333].

Table B.1: Effective Hamiltonian fits for the ν_3 band of $CH_2CH^{79}Br$ and $CH_2CH^{81}Br$. The standard Watson A-reduced quartic Hamiltonian (I^r representation) was used to fit the measured transition frequencies. All values are given in cm^{-1}, except for χ_{aa}, χ_{bb-cc}, and $|\chi_{ab}|$, which are given in MHz. All ground state ($v = 0$) constants are taken from Ref. [334], again except for χ_{aa}, χ_{bb-cc}, and $|\chi_{ab}|$, which are taken from Ref. [335]. Values in [ ] brackets are held fixed during the fit. 1σ uncertainties are specified in parentheses; for ν_0 values, the uncertainty corresponds to the estimated absolute frequency accuracy of our calibration procedure.

		^{79}Br		^{81}Br	
Parameter		Ground state	ν_3	Ground state	ν_3
ν_0		0	3027.4152(10)	0	3027.4041(10)
A		1.810093	1.804461(7)	1.809641	1.804053(9)
B		0.1388471	0.1387183(4)	0.1380359	0.1379096(5)
C		0.1288373	0.1286733(5)	0.1281362	0.1279755(5)
Δ_J	$\times10^7$	0.534	0.520(12)	0.528	0.553(13)
Δ_{JK}	$\times10^5$	−0.10216	−0.1188(29)	−0.10146	−0.1018(47)
Δ_K	$\times10^4$	0.4223	0.1624(40)	0.4206	0.2835(51)
δ_J	$\times10^8$	0.57	[0.57]	0.57	[0.57]
δ_K	$\times10^6$	0.3922	[0.3922]	0.3841	[0.3841]
χ_{aa}		470.98	469.55(237)	393.58	394.13(237)
χ_{bb-cc}		37.04	31.59(733)	30.86	22.68(716)
$\|\chi_{ab}\|$		246.14	[246.14]	204.17	[204.17]
RMS error$\times10^4$			2.20		2.24

Appendix C

Icosahedral symmetry and spherical tensor operators

This appendix summarizes key results from a group theoretical analysis of icosahedral C_{60}.

C.1 Icosahedral character table and correlations

Table C.1 reproduces the character table of the icosahedral I_h molecular symmetry group (adapted from Table A-16 of Ref. [18]). It is useful to note that I_h is a direct product group of I and the inversion group $\{E, i\}$. I is the icosahedral rotation group, containing only the pure rotation symmetry operations of the icosahedron. Transformation properties of the symmetric top

Table C.1: Character table for the I_h(M) molecular symmetry group of C_{60}. "ϕ" is the equivalent rotation angle corresponding to the given group element class. The symmetries of the body-fixed angular momentum operators ($J_{x,y,z}$) and dipole moment operators (x, y, z) are indicated. The lab frame dipole moment operators each belong to the symmetry given by Γ^*, the parity-antisymmetric irreducible representation (A_u for I_h).

I_h:	E	$12C_5$	$12C_5^2$	$20C_3$	$15C_2$	i	$12S_{10}^3$	$12S_{10}$	$20S_6$	15σ :	
ϕ:	0	$\frac{2\pi}{5}$	$\frac{4\pi}{5}$	$\frac{2\pi}{3}$	π	0	$\frac{2\pi}{5}$	$\frac{4\pi}{5}$	$\frac{2\pi}{3}$	π :	
A_g:	1	1	1	1	1	1	1	1	1	1 :	
A_u:	1	1	1	1	1	−1	−1	−1	−1	−1 :	Γ^*
T_{1g}:	3	η^+	η^-	0	−1	3	η^+	η^-	0	−1 :	(J_x, J_y, J_z)
T_{1u}:	3	η^+	η^-	0	−1	−3	$-\eta^+$	$-\eta^-$	0	1 :	(x, y, z)
T_{2g}:	3	η^-	η^+	0	−1	3	η^-	η^+	0	−1 :	
T_{2u}:	3	η^-	η^+	0	−1	−3	$-\eta^-$	$-\eta^+$	0	1 :	
G_g:	4	−1	−1	1	0	4	−1	−1	1	0 :	
G_u:	4	−1	−1	1	0	−4	1	1	−1	0 :	
H_g:	5	0	0	−1	1	5	0	0	−1	1 :	
H_u:	5	0	0	−1	1	−5	0	0	1	−1 :	

Note: $\eta^\pm = (1 \pm \sqrt{5})/2$.

rotational wavefunctions $|Jkm\rangle$ can be determined by recognizing that they transform as the the irreducible representation (irrep) $D^{(J)}$ of the rotation group SO(3), and then correlating between $D^{(J)}$ and the irreps of I, which is a subgroup of SO(3). This is facilitated by the fact that the character of $D^{(J)}$ under a symmetry element is determined solely by the angle of the equivalent rotation (ϕ in Table C.1) via

$$\chi^{(J)}(\phi) = \frac{\sin\left((J+\frac{1}{2})\phi\right)}{\sin(\phi/2)}. \tag{C.1}$$

Once the characters of $D^{(J)}$ are determined, the reduction in terms of the irreps of I is straightforward. These results are summarized in Table C.2 (and have been derived previously by others; see, for example, Table 3 of Ref. [153]). The correlations between irreps of SO(3) and I determine much of the fundamental structure of C_{60}. For example, the fact that the lowest non-vanishing multipole moment of C_{60} is the hexacontatetrapole (64-pole) is due to the fact that the first $D^{(J>0)}$ that correlates to A is for $J = 6$ ($2^6 = 64$). These correlations are also critical in determining nuclear spin statistics and the spherical tensor properties of rovibrational effective Hamiltonians for C_{60}.

Table C.2: Correlation of irreps $D^{(J)}$ of the SO(3) rotation group to those of I, the icosahedral rotation group. For $J = 30n + \mathrm{mod}(J, 30)$, the representation is equal to that of $\mathrm{mod}(J, 30)$ plus $n \times (1A + 3T_1 + 3T_2 + 4G + 5H)$.

J	:	A	T_1	T_2	G	H
0	:	1				
1	:		1			
2	:					1
3	:			1	1	
4	:				1	1
5	:		1	1		1
6	:	1	1		1	1
7	:		1	1	1	1
8	:			1	1	2
9	:		1	1	2	1
10	:	1	1	1	1	2
11	:		2	1	1	2
12	:	1	1	1	2	2
13	:		1	2	2	2
14	:		1	1	2	3
15	:	1	2	2	2	2
16	:	1	2	1	2	3
17	:		2	2	2	3
18	:	1	1	2	3	3
19	:		2	2	3	3
20	:	1	2	2	2	4
21	:	1	3	2	3	3
22	:	1	2	2	3	4
23	:		2	3	3	4
24	:	1	2	2	4	4
25	:	1	3	3	3	4
26	:	1	3	2	3	5
27	:	1	3	3	4	4
28	:	1	2	3	4	5
29	:		3	3	4	5
30	:	2	3	3	4	5

Appendix D

Spherical top R selection rule

In this appendix, we derive the R selection rule introduced in Section 5.3.3 for the case of a linear dipole moment function. Then we discuss the basis of this rule in terms of both a simple physical picture and some general arguments based on icosahedral symmetry and the Wigner-Eckart theorem.

D.1 Explicit derivation for linear dipole moment operator

Let $\{q_x, q_y, q_z\}$ be triply degenerate vibrational coordinates for an IR active fundamental. Their conjugate momenta are $\{p_x, p_y, p_z\}$, with $[q_x, p_x] = i$, $[q_x, p_y] = 0$, etc. The molecule body-fixed frame components of the vibrational angular momentum are

$$\ell_x = q_y p_z - q_z p_y \tag{D.1}$$

and cyclic permutations thereof. The commutation relations between the components of the vibrational angular momentum and the coordinates are

$$[\ell_z, q_x] = i q_y, \tag{D.2}$$

$$[\ell_z, q_y] = -i q_x, \tag{D.3}$$

$$[\ell_z, q_z] = 0, \tag{D.4}$$

and cyclic permutations thereof.

The body-fixed dipole moment can be expanded to first order in the triply degenerate vibrational coordinates

$$\vec{\mu}_{\mathrm{bf}} \propto \begin{pmatrix} q_x \\ q_y \\ q_z \end{pmatrix}. \tag{D.5}$$

The lab-fixed dipole moment is related to the body-fixed one by

$$\vec{\mu}_{\mathrm{L}} = S^{-1} \cdot \vec{\mu}_{\mathrm{bf}}, \tag{D.6}$$

where the direction cosine matrix S^{-1} is, in terms of the standard Euler angles,

$$S^{-1} = \begin{pmatrix} c\theta c\phi c\chi - s\phi s\chi & -c\theta c\phi s\chi - s\phi c\chi & s\theta c\phi \\ c\theta s\phi c\chi + c\phi s\chi & -c\theta s\phi s\chi + c\phi c\chi & s\theta s\phi \\ -s\theta c\chi & s\theta s\chi & c\theta \end{pmatrix}. \tag{D.7}$$

(Cosine and sine are abbreviated as c and s, respectively.)

We now compute the commutators of the components of the vibrational and total angular momentum with $\vec{\mu}_{\mathrm{L}}$. We begin with the z component of the vibrational angular momentum:

$$
\begin{aligned}
[\ell_z, \vec{\mu}_{\mathrm{L}}] &= [\ell_z, S^{-1} \cdot \begin{pmatrix} q_x \\ q_y \\ q_z \end{pmatrix}] \\
&= S^{-1} \cdot [\ell_z, \begin{pmatrix} q_x \\ q_y \\ q_z \end{pmatrix}] \\
&= S^{-1} \cdot \begin{pmatrix} iq_y \\ -iq_x \\ 0 \end{pmatrix} \\
&= i \begin{pmatrix} q_y(c\theta c\phi c\chi - s\phi s\chi) + q_x(c\theta c\phi s\chi + s\phi c\chi) \\ q_y(c\theta s\phi c\chi + c\phi s\chi) + q_x(c\theta s\phi s\chi - c\phi c\chi) \\ -q_y(s\theta c\chi) - q_x(s\theta s\chi) \end{pmatrix} .
\end{aligned}
\tag{D.8}
$$

We now evaluate the commutator with the z component of the total angular momentum

$J_z = -i\partial_\chi$:

$$\begin{aligned}
[J_z, \vec{\mu}_\mathrm{L}] &= [-i\partial_\chi, S^{-1} \cdot \vec{\mu}_\mathrm{bf}] \\
&= -i[\partial_\chi, S^{-1}] \cdot \vec{\mu}_\mathrm{bf} \\
&= -i \begin{pmatrix} -c\theta c\phi s\chi - s\phi c\chi & -c\theta c\phi c\chi + s\phi s\chi & 0 \\ -c\theta s\phi s\chi + c\phi c\chi & -c\theta s\phi c\chi - c\phi s\chi & 0 \\ +s\theta s\chi & s\theta c\chi & 0 \end{pmatrix} \cdot \vec{\mu}_\mathrm{bf} \\
&= -i \begin{pmatrix} -c\theta c\phi s\chi - s\phi c\chi & -c\theta c\phi c\chi + s\phi s\chi & 0 \\ -c\theta s\phi s\chi + c\phi c\chi & -c\theta s\phi c\chi - c\phi s\chi & 0 \\ +s\theta s\chi & s\theta c\chi & 0 \end{pmatrix} \cdot \begin{pmatrix} q_x \\ q_y \\ q_z \end{pmatrix} \\
&= i \begin{pmatrix} q_x(c\theta c\phi s\chi + s\phi c\chi) + q_y(c\theta c\phi c\chi - s\phi s\chi) \\ q_x(c\theta s\phi s\chi - c\phi c\chi) + q_y(c\theta s\phi c\chi + c\phi s\chi) \\ -q_x(s\theta s\chi) - q_y(s\theta c\chi) \end{pmatrix}
\end{aligned} \tag{D.9}$$

We can now see that

$$[\ell_z, \vec{\mu}_\mathrm{L}] = [J_z, \vec{\mu}_\mathrm{L}] \tag{D.10}$$

and therefore

$$[R_z, \vec{\mu}_\mathrm{L}] = [J_z - \ell_z, \vec{\mu}_\mathrm{L}] = 0. \tag{D.11}$$

It must be that R_x and R_y also have vanishing commutators with $\vec{\mu}_\mathrm{L}$ (our choice of body-fixed z axis was arbitrary to begin with), so that $\mathbf{R}^2 = R_x^2 + R_y^2 + R_z^2$ completely commutes with the lab frame dipole moment operator,

$$[\mathbf{R}^2, \vec{\mu}_\mathrm{L}] = 0, \tag{D.12}$$

and dipole transitions must therefore satisfy $\Delta R = 0$. The z component relation,

$$[R_z, \vec{\mu}_\mathrm{L}] = 0, \tag{D.13}$$

also implies $\Delta k_R = 0$, where k_R is the body-fixed z projection of $\mathbf{R}$.

D.2 A simple physical picture

We can approximate the carbon cage of C_{60} as a spherical elastic shell depicted in Fig. D.1a. A fixed point on the sphere is marked with a red dot. Vibrational motion deforms the surface and produces an oscillating dipole moment oriented along the direction of deformation (Fig. D.1b). The electric field of incident radiation exerts a torque on the oscillating vibrational dipole causing the deformation to rotate (Fig. D.1c), but leaving the orientation of the shell itself unchanged. The deformation is able to move along the surface of the sphere freely, like a traveling wave, without the body of the sphere moving. This can only occur because the deformation has no preferred orientatation.

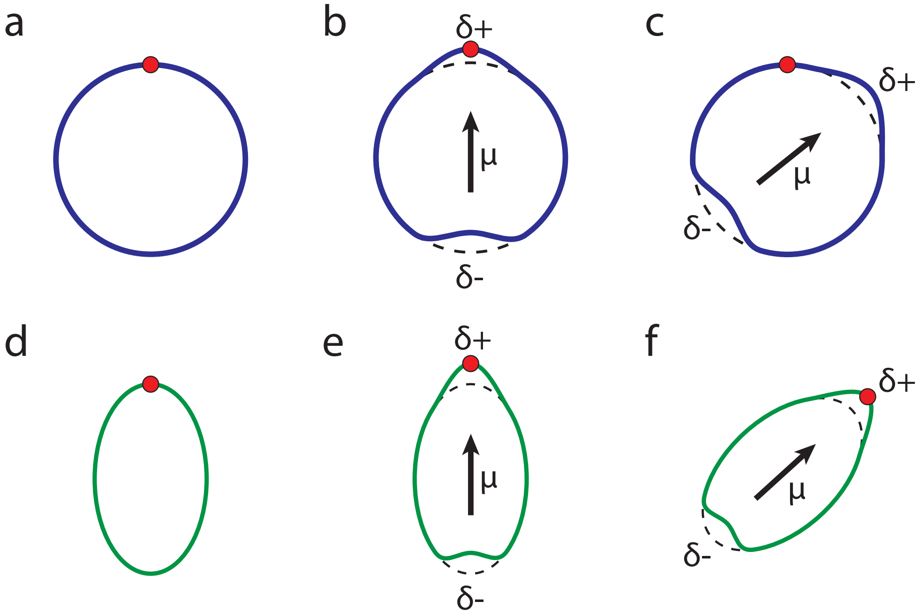

Figure D.1: A simple physical picture for the R selection rule. (a) A spherical shell is deformed, producing (b) an oscillating vibrational dipole. (c) Rotation of this dipole by an electric field rotates the deformation, but not the underlying spherical shell. (d) An aspherical shell can also be deformed, producing (e) a similar oscillating dipole along its long axis. (f) Rotation of this dipole requires that the entire body move, as the orientation of the vibration is fixed relative to the body-fixed frame.

The three-fold degeneracy of the T_{1u} IR active vibrations of C_{60} leads them to behave like the above deformation of a spherical shell. The vibrational angular momentum $\boldsymbol{\ell}$ is associated with the rotation of the deformation, while the "pure rotational" angular momentum $\mathbf{R}$ is associated with the rotation of the spherical frame itself. The vibrational dipole is a "slippery handle." Because it can rotate freely with respect to the frame, an electric field can only exert a torque on $\boldsymbol{\ell}$ and not $\mathbf{R}$. Spectroscopically, this translates to the $\Delta R = \Delta k_R = 0$ selection rules.

To help solidify this physical picture, consider the more common case of a less symmetrical molecule, illustrated as an oblong shell in Fig. D.1d. A vibrational deformation along the long axis of the shell again produces an oscillating vibrational dipole in the same direction (Fig. D.1e). Unlike the spherical case, however, this non-degenerate vibration has a definite preferred orientation with respect to the shell. Vibrations along the short axis occur at a different frequency, and so they cannot "resonantly" travel freely between the long and short axes. Electric radiation that torques the vibrational dipole moment must rotate the deformed shell as a whole (Fig. D.1f). Thus, in non-spherical molecules, vibrational excitations can occur with a simultaneous change in the angular momentum of the entire molecular frame. (An example of this type of oblong shell is a linear molecule such as acetylene, HCCH. The deformation along the long-axis would correspond to the antisymmetric CH stretching mode. Such a $\Sigma - \Sigma$ transition has $\Delta J = \pm 1$ selection rules.)

D.3 Spherical tensor operators and the Wigner-Eckart theorem

The R selection rule can also be understood in the general formalism of spherical tensor operators. The triply generate vibrational coordinates $\{q_x, q_y, q_z\}$ behave as a vector, i.e. the components of a proper rank-1 tensor, with respect to the $\mathrm{SO(3)_M}$ rotation group generated by the body-fixed components of $\mathbf{R}$. Therefore, in the linear dipole approximation $\vec{\mu}_{\mathrm{bf}} \propto (q_x, q_y, q_z)^T$ is also a rank-1 vector in $\mathrm{SO(3)_M}$. When rotating body-fixed quantities into the lab frame, we use the direction cosine matrix S^{-1} (Eq. D.7). Each row of S^{-1} itself transforms as a rank-1 vector in $\mathrm{SO(3)_M}$. Therefore, rotating the body-fixed dipole moment operator into the lab frame, Eq. D.6, amounts to performing three separate tensor couplings between a pair of rank-1 vectors to generate a rank-0 operator. Each row of S^{-1} is coupled with $\vec{\mu}_{\mathrm{bf}}$ to form a single lab frame component of $\vec{\mu}_{\mathrm{L}}$, each of which is a spherical rank-0 operator in $\mathrm{SO(3)_M}$. We can then make use of the Wigner-Eckart theorem [152,161], from which it follows that matrix elements of the form

$$\langle R, k_R, J, m|\hat{T}_q^{(k)}|R', k'_R, J', m'\rangle, \tag{D.14}$$

are zero unless $|R' - k| \leq R \leq R' + k$ and $k_R = k'_R + q$, where k and q are the rank and tensor component of the operator $\hat{T}_q^{(k)}$ in $\mathrm{SO}(3)_\mathrm{M}$. For the linear dipole approximation, each lab-frame component of $\vec{\mu}_\mathrm{L}$ is a spherical operator with $k = q = 0$, leading to the $\Delta R = \Delta k_R = 0$ selection rule.

Wait a minute, one might protest. *Isn't the lab-frame dipole moment operator $\vec{\mu}_\mathrm{L}$ a vector?* It is and it isn't. This is an excellent example of the difference between the $\mathrm{SO}(3)_\mathrm{M}$ and the $\mathrm{SO}(3)_\mathrm{L}$ rotation groups. $\mathrm{SO}(3)_\mathrm{M}$ is generated by the *body-fixed frame* components of $\mathbf{R}$, while $\mathrm{SO}(3)_\mathrm{L}$ is generated by the *lab frame* components of $\mathbf{J}$. Each lab frame component of $\vec{\mu}_\mathrm{L}$ is a rank-0 spherical tensor operator in $\mathrm{SO}(3)_\mathrm{M}$ (under the linear dipole approximation), while the three components together transform as a rank-1 vector operator in $\mathrm{SO}(3)_\mathrm{L}$. Electric dipole transitions therefore have $\Delta R = 0$ and $\Delta J = 0, \pm 1$ selection rules. The two rotation groups co-exist, providing complementary descriptions of the properties of spherical tensor operators.

We can now see that the "slipperiness" of the vibrational transition dipole for spherical tops in our simple physical picture above is associated with its rank-0 tensor properties. However, for icosahedral tops like C_{60}, the true molecular symmetry group is not quite $\mathrm{SO}(3)_\mathrm{M}$, but rather the lower symmetry icosahedral group I_h. Therefore, the lab frame dipole moment operators may have higher rank contributions that break the $\Delta R = 0$ selection rule. As can be seen in the I_h character table (Table C.1), the lab frame dipole moment operators each transform as A_u. Table C.2 indicates that A_u operators can have not only rank-0 contributions, but also rank-6, 10, 12, etc. Such higher rank contributions in $\vec{\mu}_\mathrm{L}$ must come from corresponding terms in the body-frame dipole moment operator $\vec{\mu}_\mathrm{bf}$, which transforms as T_{1u}. The linear approximation restricts $\vec{\mu}_\mathrm{bf}$ to transform as a rank-1 vector, but, in general, rank-5, 6, 7, ... contributions are possible. These high rank terms are expected to be small, making the $\Delta R = 0$ selection rule quite strong.